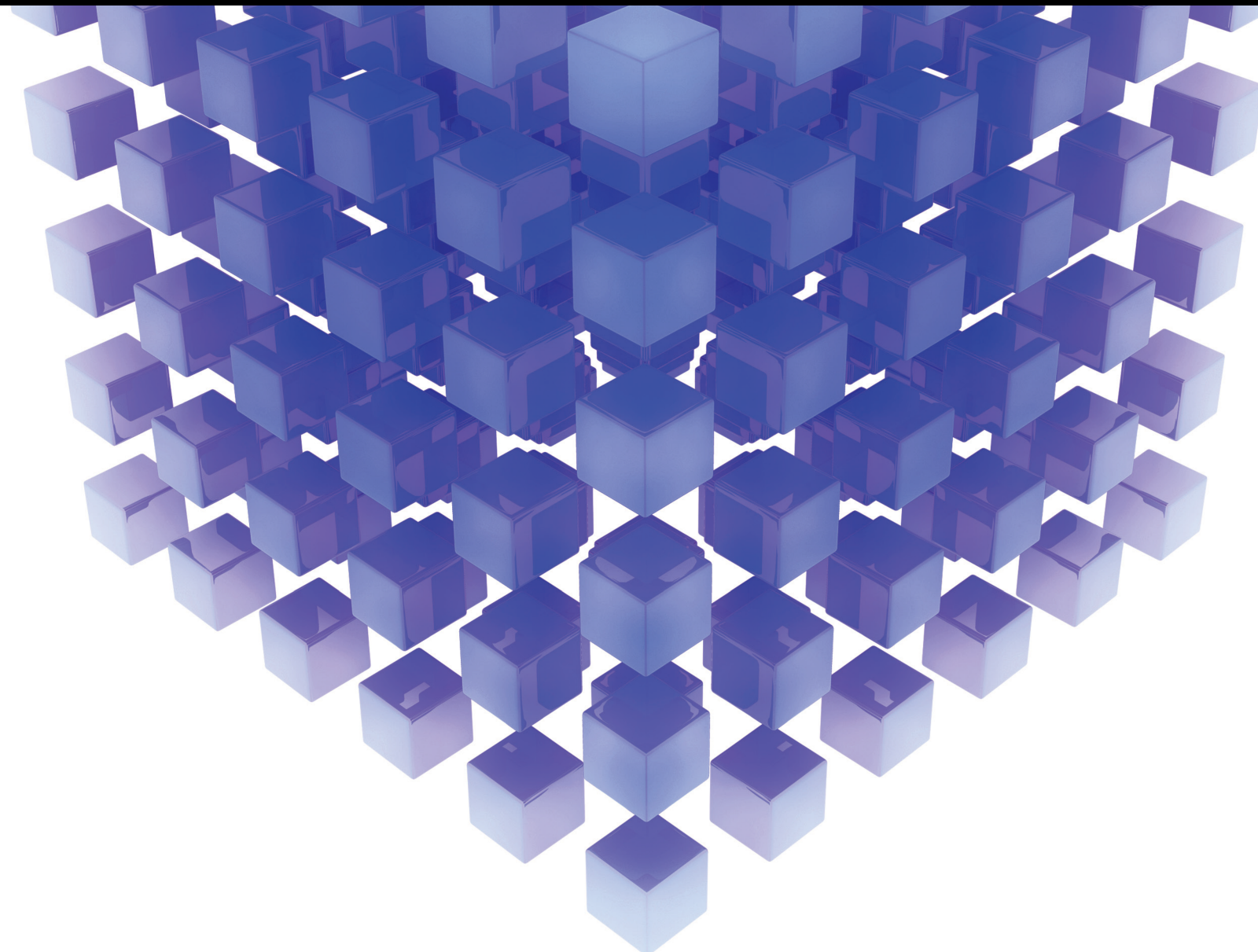


Optimal Design, Control, and Identification of Energy Conversion Systems

Lead Guest Editor: Francisco Beltran-Carbajal

Guest Editors: Ruben Tapia-Olvera, Antonio Valderrabano-Gonzalez, and Pablo Gomez





Optimal Design, Control, and Identification of Energy Conversion Systems

Mathematical Problems in Engineering

**Optimal Design, Control, and
Identification of Energy Conversion
Systems**


Lead Guest Editor: Francisco Beltran-Carbajal
Guest Editors: Ruben Tapia-Olvera, Antonio
Valderrabano-Gonzalez, and Pablo Gomez



Copyright © 2021 Hindawi Limited. All rights reserved.

This is a special issue published in “Mathematical Problems in Engineering.” All articles are open access articles distributed under the Creative Commons Attribution License, which permits unrestricted use, distribution, and reproduction in any medium, provided the original work is properly cited.

Chief Editor

Guangming Xie , China

Academic Editors

Kumaravel A , India
Waqas Abbasi, Pakistan
Mohamed Abd El Aziz , Egypt
Mahmoud Abdel-Aty , Egypt
Mohammed S. Abdo, Yemen
Mohammad Yaghoub Abdollahzadeh
Jamalabadi , Republic of Korea
Rahib Abiyev , Turkey
Leonardo Acho , Spain
Daniela Addessi , Italy
Arooj Adeel , Pakistan
Waleed Adel , Egypt
Ramesh Agarwal , USA
Francesco Aggogeri , Italy
Ricardo Aguilar-Lopez , Mexico
Afaq Ahmad , Pakistan
Naveed Ahmed , Pakistan
Elias Aifantis , USA
Akif Akgul , Turkey
Tareq Al-shami , Yemen
Guido Ala, Italy
Andrea Alaimo , Italy
Reza Alam, USA
Osamah Albahri , Malaysia
Nicholas Alexander , United Kingdom
Salvatore Alfonzetti, Italy
Ghous Ali , Pakistan
Nouman Ali , Pakistan
Mohammad D. Aliyu , Canada
Juan A. Almendral , Spain
A.K. Alomari, Jordan
José Domingo Álvarez , Spain
Cláudio Alves , Portugal
Juan P. Amezcua-Sanchez, Mexico
Mukherjee Amitava, India
Lionel Amodeo, France
Sebastian Anita, Romania
Costanza Arico , Italy
Sabri Arik, Turkey
Fausto Arpino , Italy
Rashad Asharabi , Saudi Arabia
Farhad Aslani , Australia
Mohsen Asle Zaem , USA

Andrea Avanzini , Italy
Richard I. Avery , USA
Viktor Avrutin , Germany
Mohammed A. Awadallah , Malaysia
Francesco Aymerich , Italy
Sajad Azizi , Belgium
Michele Bacciocchi , Italy
Seungik Baek , USA
Khaled Bahlali, France
M.V.A Raju Bahubalendruni, India
Pedro Balaguer , Spain
P. Balasubramaniam, India
Stefan Balint , Romania
Ines Tejado Balsera , Spain
Alfonso Banos , Spain
Jerzy Baranowski , Poland
Tudor Barbu , Romania
Andrzej Bartoszewicz , Poland
Sergio Baselga , Spain
S. Caglar Baslamisli , Turkey
David Bassir , France
Chiara Bedon , Italy
Azeddine Beghdadi, France
Andriette Bekker , South Africa
Francisco Beltran-Carbajal , Mexico
Abdellatif Ben Makhlof , Saudi Arabia
Denis Benasciutti , Italy
Ivano Benedetti , Italy
Rosa M. Benito , Spain
Elena Benvenuti , Italy
Giovanni Berselli, Italy
Michele Betti , Italy
Pietro Bia , Italy
Carlo Bianca , France
Simone Bianco , Italy
Vincenzo Bianco, Italy
Vittorio Bianco, Italy
David Bigaud , France
Sardar Muhammad Bilal , Pakistan
Antonio Bilotta , Italy
Sylvio R. Bistafa, Brazil
Chiara Boccaletti , Italy
Rodolfo Bontempo , Italy
Alberto Borboni , Italy
Marco Bortolini, Italy

Paolo Boscariol, Italy
Daniela Boso , Italy
Guillermo Botella-Juan, Spain
Abdesselem Boulkroune , Algeria
Boulaïd Boulkroune, Belgium
Fabio Bovenga , Italy
Francesco Braghin , Italy
Ricardo Branco, Portugal
Julien Bruchon , France
Matteo Bruggi , Italy
Michele Brun , Italy
Maria Elena Bruni, Italy
Maria Angela Butturi , Italy
Bartłomiej Błachowski , Poland
Dhanamjayulu C , India
Raquel Caballero-Águila , Spain
Filippo Cacace , Italy
Salvatore Caddemi , Italy
Zuowei Cai , China
Roberto Caldelli , Italy
Francesco Cannizzaro , Italy
Maosen Cao , China
Ana Carpio, Spain
Rodrigo Carvajal , Chile
Caterina Casavola, Italy
Sara Casciati, Italy
Federica Caselli , Italy
Carmen Castillo , Spain
Inmaculada T. Castro , Spain
Miguel Castro , Portugal
Giuseppe Catalanotti , United Kingdom
Alberto Cavallo , Italy
Gabriele Cazzulani , Italy
Fatih Vehbi Celebi, Turkey
Miguel Cerrolaza , Venezuela
Gregory Chagnon , France
Ching-Ter Chang , Taiwan
Kuei-Lun Chang , Taiwan
Qing Chang , USA
Xiaoheng Chang , China
Prasenjit Chatterjee , Lithuania
Kacem Chehdi, France
Peter N. Cheimets, USA
Chih-Chiang Chen , Taiwan
He Chen , China





















Kebing Chen , China
Mengxin Chen , China
Shyi-Ming Chen , Taiwan
Xizhong Chen , Ireland
Xue-Bo Chen , China
Zhiwen Chen , China
Qiang Cheng, USA
Zeyang Cheng, China
Luca Chiapponi , Italy
Francisco Chicano , Spain
Tirivanhu Chinyoka , South Africa
Adrian Chmielewski , Poland
Seongim Choi , USA
Gautam Choubey , India
Hung-Yuan Chung , Taiwan
Yusheng Ci, China
Simone Cinquemani , Italy
Roberto G. Citarella , Italy
Joaquim Ciurana , Spain
John D. Clayton , USA
Piero Colajanni , Italy
Giuseppina Colicchio, Italy
Vassilios Constantoudis , Greece
Enrico Conte, Italy
Alessandro Contento , USA
Mario Cools , Belgium
Gino Cortellessa, Italy
Carlo Cosentino , Italy
Paolo Crippa , Italy
Erik Cuevas , Mexico
Guozeng Cui , China
Mehmet Cunkas , Turkey
Giuseppe D'Aniello , Italy
Peter Dabnichki, Australia
Weizhong Dai , USA
Zhifeng Dai , China
Purushothaman Damodaran , USA
Sergey Dashkovskiy, Germany
Adiel T. De Almeida-Filho , Brazil
Fabio De Angelis , Italy
Samuele De Bartolo , Italy
Stefano De Miranda , Italy
Filippo De Monte , Italy

José António Fonseca De Oliveira
Correia , Portugal
Jose Renato De Sousa , Brazil
Michael Defoort, France
Alessandro Della Corte, Italy
Laurent Dewasme , Belgium
Sanku Dey , India
Gianpaolo Di Bona , Italy
Roberta Di Pace , Italy
Francesca Di Puccio , Italy
Ramón I. Diego , Spain
Yannis Dimakopoulos , Greece
Hasan Dinçer , Turkey
José M. Domínguez , Spain
Georgios Dounias, Greece
Bo Du , China
Emil Dumic, Croatia
Madalina Dumitriu , United Kingdom
Premraj Durairaj , India
Saeed Eftekhari Azam, USA
Said El Kafhali , Morocco
Antonio Elipse , Spain
R. Emre Erkmen, Canada
John Escobar , Colombia
Leandro F. F. Miguel , Brazil
FRANCESCO FOTI , Italy
Andrea L. Facci , Italy
Shahla Faisal , Pakistan
Giovanni Falsone , Italy
Hua Fan, China
Jianguang Fang, Australia
Nicholas Fantuzzi , Italy
Muhammad Shahid Farid , Pakistan
Hamed Faruqi, Iran
Yann Favennec, France
Fiorenzo A. Fazzolari , United Kingdom
Giuseppe Fedele , Italy
Roberto Fedele , Italy
Baowei Feng , China
Mohammad Ferdows , Bangladesh
Arturo J. Fernández , Spain
Jesus M. Fernandez Oro, Spain
Francesco Ferrise, Italy
Eric Feulvarch , France
Thierry Floquet, France















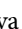








Eric Florentin , France
Gerardo Flores, Mexico
Antonio Forcina , Italy
Alessandro Formisano, Italy
Francesco Franco , Italy
Elisa Francomano , Italy
Juan Frausto-Solis, Mexico
Shujun Fu , China
Juan C. G. Prada , Spain
HECTOR GOMEZ , Chile
Matteo Gaeta , Italy
Mauro Gaggero , Italy
Zoran Gajic , USA
Jaime Gallardo-Alvarado , Mexico
Mosè Gallo , Italy
Akemi Gálvez , Spain
Maria L. Gandarias , Spain
Hao Gao , Hong Kong
Xingbao Gao , China
Yan Gao , China
Zhiwei Gao , United Kingdom
Giovanni Garcea , Italy
José García , Chile
Harish Garg , India
Alessandro Gasparetto , Italy
Stylianios Georgantzinou, Greece
Fotios Georgiades , India
Parviz Ghadimi , Iran
Ştefan Cristian Gherghina , Romania
Georgios I. Giannopoulos , Greece
Agathoklis Giaralis , United Kingdom
Anna M. Gil-Lafuente , Spain
Ivan Giorgio , Italy
Gaetano Giunta , Luxembourg
Jefferson L.M.A. Gomes , United Kingdom
Emilio Gómez-Déniz , Spain
Antonio M. Gonçalves de Lima , Brazil
Qunxi Gong , China
Chris Goodrich, USA
Rama S. R. Gorla, USA
Veena Goswami , India
Xunjie Gou , Spain
Jakub Grabski , Poland

Antoine Grall , France
George A. Gravvanis , Greece
Fabrizio Greco , Italy
David Greiner , Spain
Jason Gu , Canada
Federico Guarracino , Italy
Michele Guida , Italy
Muhammet Gul , Turkey
Dong-Sheng Guo , China
Hu Guo , China
Zhaoxia Guo, China
Yusuf Gurefe, Turkey
Salim HEDDAM , Algeria
ABID HUSSANAN, China
Quang Phuc Ha, Australia
Li Haitao , China
Petr Hájek , Czech Republic
Mohamed Hamdy , Egypt
Muhammad Hamid , United Kingdom
Renke Han , United Kingdom
Weimin Han , USA
Xingsi Han, China
Zhen-Lai Han , China
Thomas Hanne , Switzerland
Xinan Hao , China
Mohammad A. Hariri-Ardebili , USA
Khalid Hattaf , Morocco
Defeng He , China
Xiao-Qiao He, China
Yanchao He, China
Yu-Ling He , China
Ramdane Hedjar , Saudi Arabia
Jude Hemanth , India
Reza Hemmati, Iran
Nicolae Herisanu , Romania
Alfredo G. Hernández-Díaz , Spain
M.I. Herreros , Spain
Eckhard Hitzer , Japan
Paul Honeine , France
Jaromir Horacek , Czech Republic
Lei Hou , China
Yingkun Hou , China
Yu-Chen Hu , Taiwan
Yunfeng Hu, China
Can Huang , China
Gordon Huang , Canada
Linsheng Huo , China
Sajid Hussain, Canada
Asier Ibeas , Spain
Orest V. Iftime , The Netherlands
Przemyslaw Ignaciuk , Poland
Giacomo Innocenti , Italy
Emilio Insfran Pelozo , Spain
Azeem Irshad, Pakistan
Alessio Ishizaka, France
Benjamin Ivorra , Spain
Breno Jacob , Brazil
Reema Jain , India
Tushar Jain , India
Amin Jajarmi , Iran
Chiranjibe Jana , India
Łukasz Jankowski , Poland
Samuel N. Jator , USA
Juan Carlos Jáuregui-Correa , Mexico
Kandasamy Jayakrishna, India
Reza Jazar, Australia
Khalide Jbilou, France
Isabel S. Jesus , Portugal
Chao Ji , China
Qing-Chao Jiang , China
Peng-fei Jiao , China
Ricardo Fabricio Escobar Jiménez , Mexico
Emilio Jiménez Macías , Spain
Maolin Jin, Republic of Korea
Zhuo Jin, Australia
Ramash Kumar K , India
BHABEN KALITA , USA
MOHAMMAD REZA KHEDMATI , Iran
Viacheslav Kalashnikov , Mexico
Mathiyalagan Kalidass , India
Tamas Kalmar-Nagy , Hungary
Rajesh Kaluri , India
Jyotheeswara Reddy Kalvakurthi, India
Zhao Kang , China
Ramani Kannan , Malaysia
Tomasz Kapitaniak , Poland
Julius Kaplunov, United Kingdom
Konstantinos Karamanos, Belgium
Michal Kawulok, Poland

Irfan Kaymaz , Turkey
Vahid Kayvanfar , Qatar
Krzysztof Kecik , Poland
Mohamed Khader , Egypt
Chaudry M. Khalique , South Africa
Mukhtaj Khan , Pakistan
Shahid Khan , Pakistan
Nam-Il Kim, Republic of Korea
Philipp V. Kiryukhantsev-Korneev ,
Russia
P.V.V Kishore , India
Jan Koci , Czech Republic
Ioannis Kostavelis , Greece
Sotiris B. Kotsiantis , Greece
Frederic Kratz , France
Vamsi Krishna , India
Edyta Kucharska, Poland
Krzysztof S. Kulpa , Poland
Kamal Kumar, India
Prof. Ashwani Kumar , India
Michal Kunicki , Poland
Cedrick A. K. Kwuimy , USA
Kyandoghere Kyamakya, Austria
Ivan Kyrchei , Ukraine
Márcio J. Lacerda , Brazil
Eduardo Lalla , The Netherlands
Giovanni Lancioni , Italy
Jaroslaw Latalski , Poland
Hervé Laurent , France
Agostino Lauria , Italy
Aimé Lay-Ekuakille , Italy
Nicolas J. Leconte , France
Kun-Chou Lee , Taiwan
Dimitri Lefebvre , France
Eric Lefevre , France
Marek Lefik, Poland
Yaguo Lei , China
Kauko Leiviskä , Finland
Ervin Lenzi , Brazil
ChenFeng Li , China
Jian Li , USA
Jun Li , China
Yueyang Li , China
Zhao Li , China































Zhen Li , China
En-Qiang Lin, USA
Jian Lin , China
Qibin Lin, China
Yao-Jin Lin, China
Zhiyun Lin , China
Bin Liu , China
Bo Liu , China
Heng Liu , China
Jianxu Liu , Thailand
Lei Liu , China
Sixin Liu , China
Wanquan Liu , China
Yu Liu , China
Yuanchang Liu , United Kingdom
Bonifacio Llamazares , Spain
Alessandro Lo Schiavo , Italy
Jean Jacques Loiseau , France
Francesco Lolli , Italy
Paolo Lonetti , Italy
António M. Lopes , Portugal
Sebastian López, Spain
Luis M. López-Ochoa , Spain
Vassilios C. Loukopoulos, Greece
Gabriele Maria Lozito , Italy
Zhiguo Luo , China
Gabriel Luque , Spain
Valentin Lychagin, Norway
YUE MEI, China
Junwei Ma , China
Xuanlong Ma , China
Antonio Madeo , Italy
Alessandro Magnani , Belgium
Toqeer Mahmood , Pakistan
Fazal M. Mahomed , South Africa
Arunava Majumder , India
Sarfranz Nawaz Malik, Pakistan
Paolo Manfredi , Italy
Adnan Maqsood , Pakistan
Muazzam Maqsood, Pakistan
Giuseppe Carlo Marano , Italy
Damijan Markovic, France
Filipe J. Marques , Portugal
Luca Martinelli , Italy
Denizar Cruz Martins, Brazil

Francisco J. Martos , Spain
Elio Masciari , Italy
Paolo Massioni , France
Alessandro Mauro , Italy
Jonathan Mayo-Maldonado , Mexico
Pier Luigi Mazzeo , Italy
Laura Mazzola, Italy
Driss Mehdi , France
Zahid Mehmood , Pakistan
Roderick Melnik , Canada
Xiangyu Meng , USA
Jose Merodio , Spain
Alessio Merola , Italy
Mahmoud Mesbah , Iran
Luciano Mescia , Italy
Laurent Mevel , France
Constantine Michailides , Cyprus
Mariusz Michta , Poland
Prankul Middha, Norway
Aki Mikkola , Finland
Giovanni Minafò , Italy
Edmondo Minisci , United Kingdom
Hiroyuki Mino , Japan
Dimitrios Mitsotakis , New Zealand
Ardashir Mohammadzadeh , Iran
Francisco J. Montáns , Spain
Francesco Montefusco , Italy
Gisele Mophou , France
Rafael Morales , Spain
Marco Morandini , Italy
Javier Moreno-Valenzuela , Mexico
Simone Morganti , Italy
Caroline Mota , Brazil
Aziz Moukrim , France
Shen Mouquan , China
Dimitris Mourtzis , Greece
Emiliano Mucchi , Italy
Taseer Muhammad, Saudi Arabia
Ghulam Muhiuddin, Saudi Arabia
Amitava Mukherjee , India
Josefa Mula , Spain
Jose J. Muñoz , Spain
Giuseppe Muscolino, Italy
Marco Mussetta , Italy

Hariharan Muthusamy, India
Alessandro Naddeo , Italy
Raj Nandkeolyar, India
Keivan Navaie , United Kingdom
Soumya Nayak, India
Adrian Neagu , USA
Erivelton Geraldo Nepomuceno , Brazil
AMA Neves, Portugal
Ha Quang Thinh Ngo , Vietnam
Nhon Nguyen-Thanh, Singapore
Papakostas Nikolaos , Ireland
Jelena Nikolic , Serbia
Tatsushi Nishi, Japan
Shanzhou Niu , China
Ben T. Nohara , Japan
Mohammed Nouari , France
Mustapha Nourelfath, Canada
Kazem Nouri , Iran
Ciro Núñez-Gutiérrez , Mexico
Włodzimierz Ogryczak, Poland
Roger Ohayon, France
Krzysztof Okarma , Poland
Mitsuhiro Okayasu, Japan
Murat Olgun , Turkey
Diego Oliva, Mexico
Alberto Olivares , Spain
Enrique Onieva , Spain
Calogero Orlando , Italy
Susana Ortega-Cisneros , Mexico
Sergio Ortobelli, Italy
Naohisa Otsuka , Japan
Sid Ahmed Ould Ahmed Mahmoud , Saudi Arabia
Taoreed Owolabi , Nigeria
EUGENIA PETROPOULOU , Greece
Arturo Pagano, Italy
Madhumangal Pal, India
Pasquale Palumbo , Italy
Dragan Pamučar, Serbia
Weifeng Pan , China
Chandan Pandey, India
Rui Pang, United Kingdom
Jürgen Pannek , Germany
Elena Panteley, France
Achille Paolone, Italy

George A. Papakostas , Greece
Xosé M. Pardo , Spain
You-Jin Park, Taiwan
Manuel Pastor, Spain
Pubudu N. Pathirana , Australia
Surajit Kumar Paul , India
Luis Payá , Spain
Igor Pažanin , Croatia
Libor Pekař , Czech Republic
Francesco Pellicano , Italy
Marcello Pellicciari , Italy
Jian Peng , China
Mingshu Peng, China
Xiang Peng , China
Xindong Peng, China
Yuexing Peng, China
Marzio Pennisi , Italy
Maria Patrizia Pera , Italy
Matjaz Perc , Slovenia
A. M. Bastos Pereira , Portugal
Wesley Peres, Brazil
F. Javier Pérez-Pinal , Mexico
Michele Perrella, Italy
Francesco Pesavento , Italy
Francesco Petrini , Italy
Hoang Vu Phan, Republic of Korea
Lukasz Pieczonka , Poland
Dario Piga , Switzerland
Marco Pizzarelli , Italy
Javier Plaza , Spain
Goutam Pohit , India
Dragan Poljak , Croatia
Jorge Pomares , Spain
Hiram Ponce , Mexico
Sébastien Poncet , Canada
Volodymyr Ponomaryov , Mexico
Jean-Christophe Ponsart , France
Mauro Pontani , Italy
Sivakumar Poruran, India
Francesc Pozo , Spain
Aditya Rio Prabowo , Indonesia
Anchasa Pramuanjaroenkij , Thailand
Leonardo Primavera , Italy
B Rajanarayan Prusty, India

Krzysztof Puszynski , Poland
Chuan Qin , China
Dongdong Qin, China
Jianlong Qiu , China
Giuseppe Quaranta , Italy
DR. RITU RAJ , India
Vitomir Racic , Italy
Carlo Rainieri , Italy
Kumbakonam Ramamani Rajagopal, USA
Ali Ramazani , USA
Angel Manuel Ramos , Spain
Higinio Ramos , Spain
Muhammad Afzal Rana , Pakistan
Muhammad Rashid, Saudi Arabia
Manoj Rastogi, India
Alessandro Rasulo , Italy
S.S. Ravindran , USA
Abdolrahman Razani , Iran
Alessandro Reali , Italy
Jose A. Reinoso , Spain
Oscar Reinoso , Spain
Haijun Ren , China
Carlo Renno , Italy
Fabrizio Renno , Italy
Shahram Rezapour , Iran
Ricardo Rianza , Spain
Francesco Riganti-Fulginei , Italy
Gerasimos Rigatos , Greece
Francesco Ripamonti , Italy
Jorge Rivera , Mexico
Eugenio Roanes-Lozano , Spain
Ana Maria A. C. Rocha , Portugal
Luigi Rodino , Italy
Francisco Rodríguez , Spain
Rosana Rodríguez López, Spain
Francisco Rossomando , Argentina
Jose de Jesus Rubio , Mexico
Weiguo Rui , China
Rubén Ruiz , Spain
Ivan D. Rukhlenko , Australia
Dr. Eswaramoorthi S. , India
Weichao SHI , United Kingdom
Chaman Lal Sabharwal , USA
Andrés Sáez , Spain

Bekir Sahin, Turkey
Laxminarayan Sahoo , India
John S. Sakellariou , Greece
Michael Sakellariou , Greece
Salvatore Salamone, USA
Jose Vicente Salcedo , Spain
Alejandro Salcido , Mexico
Alejandro Salcido, Mexico
Nunzio Salerno , Italy
Rohit Salgotra , India
Miguel A. Salido , Spain
Sinan Salih , Iraq
Alessandro Salvini , Italy
Abdus Samad , India
Sovan Samanta, India
Nikolaos Samaras , Greece
Ramon Sancibrian , Spain
Giuseppe Sanfilippo , Italy
Omar-Jacobo Santos, Mexico
J Santos-Reyes , Mexico
José A. Sanz-Herrera , Spain
Musavarah Sarwar, Pakistan
Shahzad Sarwar, Saudi Arabia
Marcelo A. Savi , Brazil
Andrey V. Savkin, Australia
Tadeusz Sawik , Poland
Roberta Sburlati, Italy
Gustavo Scaglia , Argentina
Thomas Schuster , Germany
Hamid M. Sedighi , Iran
Mijanur Rahaman Seikh, India
Tapan Senapati , China
Lotfi Senhadji , France
Junwon Seo, USA
Michele Serpilli, Italy
Silvestar Šesnić , Croatia
Gerardo Severino, Italy
Ruben Sevilla , United Kingdom
Stefano Sfarra , Italy
Dr. Ismail Shah , Pakistan
Leonid Shaikhet , Israel
Vimal Shanmuganathan , India
Prayas Sharma, India
Bo Shen , Germany
Hang Shen, China

Xin Pu Shen, China
Dimitri O. Shepelsky, Ukraine
Jian Shi , China
Amin Shokrollahi, Australia
Suzanne M. Shontz , USA
Babak Shotorban , USA
Zhan Shu , Canada
Angelo Sifaleras , Greece
Nuno Simões , Portugal
Mehakpreet Singh , Ireland
Piyush Pratap Singh , India
Rajiv Singh, India
Seralathan Sivamani , India
S. Sivasankaran , Malaysia
Christos H. Skiadas, Greece
Konstantina Skouri , Greece
Neale R. Smith , Mexico
Bogdan Smolka, Poland
Delfim Soares Jr. , Brazil
Alba Sofi , Italy
Francesco Soldovieri , Italy
Raffaele Solimene , Italy
Yang Song , Norway
Jussi Sopanen , Finland
Marco Spadini , Italy
Paolo Spagnolo , Italy
Ruben Specogna , Italy
Vasilios Spitas , Greece
Ivanka Stamova , USA
Rafał Stanisławski , Poland
Miladin Stefanović , Serbia
Salvatore Strano , Italy
Yakov Strelniker, Israel
Kangkang Sun , China
Qiuqin Sun , China
Shuaishuai Sun, Australia
Yanchao Sun , China
Zong-Yao Sun , China
Kumarasamy Suresh , India
Sergey A. Suslov , Australia
D.L. Suthar, Ethiopia
D.L. Suthar , Ethiopia
Andrzej Swierniak, Poland
Andras Szekrenyes , Hungary
Kumar K. Tamma, USA

Yong (Aaron) Tan, United Kingdom
Marco Antonio Taneco-Hernández , Mexico
Lu Tang , China
Tianyou Tao, China
Hafez Tari , USA
Alessandro Tasora , Italy
Sergio Teggi , Italy
Adriana del Carmen Téllez-Anguiano , Mexico
Ana C. Teodoro , Portugal
Efstathios E. Theotokoglou , Greece
Jing-Feng Tian, China
Alexander Timokha , Norway
Stefania Tomasiello , Italy
Gisella Tomasini , Italy
Isabella Torricollo , Italy
Francesco Tornabene , Italy
Mariano Torrisi , Italy
Thang nguyen Trung, Vietnam
George Tsiatas , Greece
Le Anh Tuan , Vietnam
Nerio Tullini , Italy
Emilio Turco , Italy
Ilhan Tuzcu , USA
Efstratios Tzirtzilakis , Greece
FRANCISCO UREÑA , Spain
Filippo Ubertini , Italy
Mohammad Uddin , Australia
Mohammad Safi Ullah , Bangladesh
Serdar Ulubeyli , Turkey
Mati Ur Rahman , Pakistan
Panayiotis Vafeas , Greece
Giuseppe Vairo , Italy
Jesus Valdez-Resendiz , Mexico
Eusebio Valero, Spain
Stefano Valvano , Italy
Carlos-Renato Vázquez , Mexico
Martin Velasco Villa , Mexico
Franck J. Vernerey, USA
Georgios Veronis , USA
Vincenzo Vespri , Italy
Renato Vidoni , Italy
Venkatesh Vijayaraghavan, Australia

Anna Vila, Spain
Francisco R. Villatoro , Spain
Francesca Vipiana , Italy
Stanislav Vitek , Czech Republic
Jan Vorel , Czech Republic
Michael Vynnycky , Sweden
Mohammad W. Alomari, Jordan
Roman Wan-Wendner , Austria
Bingchang Wang, China
C. H. Wang , Taiwan
Dagang Wang, China
Guoqiang Wang , China
Huaiyu Wang, China
Hui Wang , China
J.G. Wang, China
Ji Wang , China
Kang-Jia Wang , China
Lei Wang , China
Qiang Wang, China
Qingling Wang , China
Weiwei Wang , China
Xinyu Wang , China
Yong Wang , China
Yung-Chung Wang , Taiwan
Zhenbo Wang , USA
Zhibo Wang, China
Waldemar T. Wójcik, Poland
Chi Wu , Australia
Qihong Wu, China
Yuqiang Wu, China
Zhibin Wu , China
Zhizheng Wu , China
Michalis Xenos , Greece
Hao Xiao , China
Xiao Ping Xie , China
Qingzheng Xu , China
Binghan Xue , China
Yi Xue , China
Joseph J. Yame , France
Chuanliang Yan , China
Xinggang Yan , United Kingdom
Hongtai Yang , China
Jixiang Yang , China
Mijia Yang, USA
Ray-Yeng Yang, Taiwan






Zaoli Yang , China
Jun Ye , China
Min Ye , China
Luis J. Yebra , Spain
Peng-Yeng Yin , Taiwan
Muhammad Haroon Yousaf , Pakistan
Yuan Yuan, United Kingdom
Qin Yuming, China
Elena Zaitseva , Slovakia
Arkadiusz Zak , Poland
Mohammad Zakwan , India
Ernesto Zambrano-Serrano , Mexico
Francesco Zammori , Italy
Jessica Zangari , Italy
Rafal Zdunek , Poland
Ibrahim Zeid, USA
Nianyin Zeng , China
Junyong Zhai , China
Hao Zhang , China
Haopeng Zhang , USA
Jian Zhang , China
Kai Zhang, China
Lingfan Zhang , China
Mingjie Zhang , Norway
Qian Zhang , China
Tianwei Zhang , China
Tongqian Zhang , China
Wenyu Zhang , China
Xianming Zhang , Australia
Xuping Zhang , Denmark
Yinyan Zhang, China
Yifan Zhao , United Kingdom
Debao Zhou, USA
Heng Zhou , China
Jian G. Zhou , United Kingdom
Junyong Zhou , China
Xueqian Zhou , United Kingdom
Zhe Zhou , China
Wu-Le Zhu, China
Gaetano Zizzo , Italy
Mingcheng Zuo, China

Contents




An Effective Harmonic Suppression Method Based on Linear Active Disturbance Rejection Control for Copper Electrowinning Rectifier

Yang Cui , Cheng Liu , Yanming Cheng , Mahmoud Al Shurafa , Ilkyoo Lee , and Jing Niu 
Research Article (15 pages), Article ID 9933558, Volume 2021 (2021)





Design Methodology for Interfacing DERs to Power Systems through VSC

A. Valderrabano-Gonzalez , F. Beltran-Carbajal , R. Tapia-Olvera , O. Aguilar-Mejia , and J. C. Rosas-Caro 
Research Article (10 pages), Article ID 5541375, Volume 2021 (2021)

Algebraic Parameter Identification of Nonlinear Vibrating Systems and Non Linearity Quantification Using the Hilbert Transformation

Luis Gerardo Trujillo-Franco , Gerardo Silva-Navarro , and Francisco Beltran-Carbajal 
Research Article (16 pages), Article ID 5595453, Volume 2021 (2021)




A Hybrid Method to Diagnose 3D Rotor Eccentricity Faults in Synchronous Generators Based on ALIF_PE and KFCM

Chao Zhang , Chuang-Jin He, Shuai Li, Yu-Ling He , Xiao-Long Wang , Xiang-Yu Liu , and Lun Cheng
Research Article (14 pages), Article ID 5513881, Volume 2021 (2021)

First and Second Law Evaluation of Multipass Flat-Plate Solar Air Collector and Optimization Using Preference Selection Index Method

Nguyen Thanh Luan and Nguyen Minh Phu 
Research Article (16 pages), Article ID 5563882, Volume 2021 (2021)

Design of Real-Time Control Based on DP and ECMS for PHEVs

Wei Wang , Zhenjiang Cai , and Shaofei Liu 
Research Article (12 pages), Article ID 6667614, Volume 2021 (2021)

Research Article

An Effective Harmonic Suppression Method Based on Linear Active Disturbance Rejection Control for Copper Electrowinning Rectifier

Yang Cui ¹, Cheng Liu ¹, Yanming Cheng ¹, Mahmoud Al Shurafa ¹,
Ilkyoo Lee ² and Jing Niu ³

¹College of Electrical and Information Engineering, Beihua University, Jilin, China

²Department of Electrical, Electronics & Control Engineering Kongju National University, Gongju, Republic of Korea

³Jilin Chemical Fiber Group Co., Ltd., Jilin, China

Correspondence should be addressed to Cheng Liu; liucheng@beihua.edu.cn

Received 9 March 2021; Revised 7 November 2021; Accepted 4 December 2021; Published 23 December 2021

Academic Editor: Antonio Valderrabano-Gonzalez

Copyright © 2021 Yang Cui et al. This is an open access article distributed under the Creative Commons Attribution License, which permits unrestricted use, distribution, and reproduction in any medium, provided the original work is properly cited.

Because the harmonics in the production process of copper electrowinning have an important impact on the electrical energy consumption, it is necessary to suppress the harmonics effectively. In this paper, a copper electrowinning rectifier with double inverse star circuit is selected as a study object in which a large number of harmonics mainly including the 5th, 7th, 11th, and 13th harmonics are generated and injected back into the power grid. The total harmonic distortion rate of the power grid is up to 29.19% before filtering. Therefore, a method combining the induction filtering method and the active filtering method is proposed to carry out comprehensive filtering. Simulation results demonstrate that the total harmonic distortion rate of the system decreases to 4.20%, which indicates that the proposed method can track the corresponding changes of harmonics when the load changes in real time and filter them out. In order to ensure and improve the effect of active filter, a current harmonic tracking control method based on linear active disturbance rejection control is proposed. Simulation results show that the total harmonic distortion rate decreases to 3.34%, which is also lower than that of hysteresis control. Compared with the conventional single filtering method, the new filtering method combining induction filtering with active filtering based on linear active disturbance rejection control in the copper electrowinning rectifier has obvious advantages.

1. Introduction

In recent years, copper and its alloy materials are widely used in various fields, and the demand of copper is increasing in many enterprises. As one of the basic technologies of copper production, copper electrolysis and electrowinning rectification technology has attracted more and more attention. With the continuous increase of the number and capacity of copper electrowinning rectifier units, the impact of the system on the power grid in industrial application is becoming more and more serious. A large number of harmonics are injected back into the power grid, which will directly affect the quality of copper production. It is very important to ensure the safe and stable operation and power quality of power grid system [1, 2]. Many researchers and

scholars at home and abroad have studied power quality problems, especially the research on current quality in power grid [3–6]. The use of a large number of power electronic converter equipment will directly produce harmonic and reactive power problems and affect the power quality of the grid [7–9]. The copper electrowinning rectifier is such a typical device.

The rectifying device of the copper electrowinning device consists of voltage regulating transformer and double inverse star rectifier, which is a typical low-voltage high-current nonlinear load. In the process of operation, turning on and off semiconducted thyristor can cause a distortion of the grid current and voltage. From the perspective of frequency domain, these waveforms contain not only the power frequency sinusoidal quantity but also some voltage or

current components [2] which are positive integral multiples of power frequency. These components are called harmonics whose existence will not only affect the production quality of the system but also affect the normal operation of other equipment in the same power supply system and even lead to safety accidents in the power system. Therefore, it is an urgent problem to control the harmonics to ensure the power quality and build a clean electrical environment.

Yuan et al. [10] conducted the harmonic suppression characteristic analysis of a phase-shifting reactor in a rectifier system. Takeshita et al. [11] presented the input current waveform control of the rectifier circuit which realizes simultaneously the high input power factor and the harmonic suppression of the receiving-end voltage and the source current under the distorted receiving-end voltage. Méndez et al. [12] designed an active high-power filter for the harmonic suppression in coils powered separately by 12-pulsed thyristor converters. Liu et al. [13] proposed a novel controllable inductive power filtering (CIPF) method to effectively eliminate the harmonics flowing through the transformer in the industrial DC power supply system. Liu et al. [14] proposed a novel power factor correction (PFC) controller based on proportional resonant for selective harmonic suppression of a UPS system. Ramesh and Habeebullah Sait [15] introduced harmonic removal in a switched capacitor multilevel inverter utilizing the artificial bee colony (ABC) method. In [16], an impedance reconstruction control method for the source PWM inverter was proposed, which improves the phase of the output sequence impedance of the source PWM inverter at high-frequency areas to effectively suppress the high-frequency oscillation of the island power system.

Wang et al. [17] proposed a frequency-domain harmonic model for 12-pulse series-connected thyristor-controlled rectifier under unbalanced supply voltage. Wiechmann et al. [18] proposed an optimized sequential control technique to improve converter's reactive power consumption presentation for copper electrowinning high-current rectifiers. In [19], a modified DPWM (MDPWM) scheme was proposed to regulate the neutral point voltage by using redundant clamping modes in high-frequency Vienna-type rectifiers. An et al. [20] simulated diode rectifier + FC filter scheme-based large electrolytic aluminum filter device. Mao et al. [9] used the filter with single tuning in a high-power thyristor rectifier as a medium-frequency furnace and high-frequency furnace for metal smelting. Dai et al. [21] proposed a comprehensive treatment scheme of "automatic switch single tuning passive filter + high voltage side series filter inductor" in medium frequency smelting furnace. Ma et al. and Li et al. [22, 23] applied the first-order linear active disturbance rejection controller (LADRC) to the current tracking control of a 10 kV line parallel hybrid active power filter, which can well deal with the contradiction between overshoot and rapidity, and the performance is better than the traditional PI controller, which verifies the effectiveness of the linear active disturbance rejection control strategy. In [24], aiming at the disadvantages of the grid side inverter of doubly fed induction generator, such as the complexity and poor stability, and the problems of the conventional PI

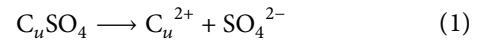
closed-loop control, such as poor stability and slow response speed, an ADRC control strategy was proposed, in which a resonance link is added to the linear state error feedback. Instead of PI control of current loop, it can suppress the low-order harmonics of grid connected current, improve the response speed of the system, and ensure smooth operation when the inverter is connected to the grid.

Analyzing above relevant researches on harmonic suppression methods for rectifier indicates that there are few special effective researches on harmonic suppression of high-power copper electrowinning rectifier. The effect of the conventional harmonic suppression method is not ideal. It is very important to study an effective harmonic suppression technology. Therefore, in this paper, an "induction filter + active filter" method is proposed to effectively suppress the harmonics. Moreover, the LADRC technology is added to the active filter current tracking control in active filter, which further improves the harmonic suppression effect.

2. Copper Electrowinning

2.1. Copper Electrowinning Process. In copper electrowinning production, cathode copper is produced through the leaching-extraction-electrowinning process; in the electrolyte, the insoluble lead-alloy plate (Pb-Ca-Sn) is used as the anode, and the thin copper starting sheet is used as the cathode. In essence, copper electrowinning is the process where copper ion is reduced by DC and deposited on the cathode [25, 26]. Main reactions are as follows.

The copper sulfate solution C_uSO_4 is decomposed into a copper ion Cu^{2+} and sulfate ion SO_4^{2-} in the applied electric field, and the process is expressed as



The copper ion obtains electrons on the cathode and is reduced to copper which is deposited on the cathode, and the process can be expressed as



2.2. Current Efficiency. According to Faraday's law, the theory is that copper of 1.1864×10^{-3} kg should be deposited on the cathode by DC of 1 ampere-hour. In fact, compared with the theoretical value, the actual amount of produced copper is decreased by impurities, oxidation and dissolution of cathode sediment, and electrode short circuit and leakage loss. In production practice, current efficiency is proposed to evaluate effective utilization of current, and it is the percentage ratio between the actual production of copper and theoretical production of the copper and is expressed by [27]

$$\eta = \frac{G}{q \cdot I \cdot t \cdot n} \times 100\%, \quad (3)$$

where η represents current efficiency in %, G represents actual production of copper in kg during t , q represents electrochemical equivalent of copper in 1.1864×10^{-3} kg/Ah,

I represents current intensity in A , t represents the time of electrowinning in hour, and n represents the number of electrowinning electrolytic tanks.

Current efficiency is an important technical and economic index of electrowinning copper production. In production practice, due to different specific conditions, the current efficiency of copper electroproduction is different, and effective measures should be taken to improve current efficiency.

2.3. DC Power Consumption. In copper electrowinning production, DC power consumption in kWh/kg is defined as the electricity used to produce copper of 1 kg in 1 hour, which is an important economic and technical index. DC power consumption is calculated by

$$W = \frac{v}{\eta \cdot q}, \quad (4)$$

where W represents DC power consumption in kWh/kg, v represents electrolytic tank voltage in V , and η represents current efficiency in %.

Formula (4) indicates that electrolytic tank voltage and current efficiency are the direct factors affecting energy consumption. In the industrial process, the voltage of conventional electrolytic tank voltage is in an approximate range of $1.8V \sim 2V$, and the electrolytic tank voltage will increase with the increase of current density; consequently, the power consumption will also increase. However, if low-current-density electrowinning is used, the output will be reduced, although the power consumption can be reduced in the electrowinning process. Therefore, the actual production situation of the factory should be taken into account when a current density is determined. At present, the current density of copper electrowinning used in the world is different, fluctuating in a range; the low one is approximately $100A/m^2$, and the high one is approximately $270A/m^2$.

3. Double Inverse Star Rectifying System for Copper Electrowinning Rectifier

3.1. Double Inverse Star Rectifying Circuit. With the continuous development of electrolysis, electroplating, electrolytic degreasing, and other industries, the demand for low-voltage and high-current DC power supply is increasing. Double inverse star rectifying circuit stands out among all kinds of circuits for its superior performance. It is a rectifying circuit composed of two three-phase half-wave circuits and a balance reactor, which is depicted in Figure 1.

Compared with the common six-phase half-wave rectifier circuit and three-phase six-pulse bridge rectifier circuit, the current effective value of the rectifier arm is smaller, and the capacity utilization rate is high. Adding the balance reactor can improve the reverse voltage drop, and the rectifier can parallel two output different instantaneous values of groups of three-phase half wave to supply power to the load. In the working process of double inverse star rectifier circuit, the rectifier is a nonlinear load, which will inevitably produce harmonics.

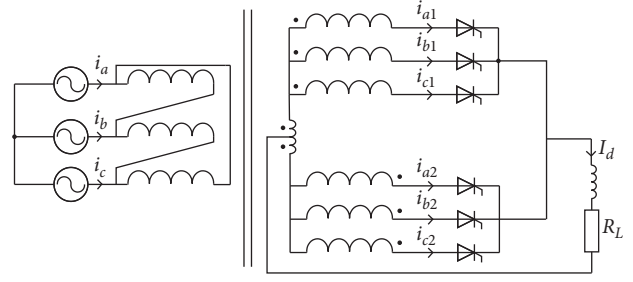


FIGURE 1: Structure diagram of double inverse star rectifying circuit.

The internal structure diagram of double inverse star transformer is illustrated in Figure 2. On the primary side of the transformer, the windings are connected according to the triangle structure, and the secondary side is composed of two-star structure windings with opposite directions. On the premise of meeting the safety requirements of industrial application, Figure 3 shows that the input three-phase grid voltages u_a, u_b, u_c are changed into six voltages u_{a1}, u_{b1}, u_{c1} and u_{a2}, u_{b2}, u_{c2} and there is a difference of 60° between them.

According to the internal structure and voltage vector relationship of double inverse star rectifier transformer, the corresponding mathematical model can be established. Firstly, the input three-phase grid voltage is set as

$$\begin{cases} u_a = U_m \sin(\omega t), \\ u_b = U_m \sin(\omega t - 2\pi/3), \\ u_c = U_m \sin(\omega t + 2\pi/3), \end{cases} \quad (5)$$

where U_m is defined as the magnitude of the grid voltage. According to the voltage vector relationship shown in Figure 3, the other two voltage equations can be obtained as follows:

$$\begin{cases} u_{a1} = U_n \sin(\omega t), \\ u_{b1} = U_n \sin(\omega t - 2\pi/3), \\ u_{c1} = U_n \sin(\omega t + 2\pi/3), \\ u_{a2} = U_n \sin(\omega t - \pi), \\ u_{b2} = U_n \sin(\omega t + \pi/3), \\ u_{ac2} = U_n \sin(\omega t - \pi/3), \end{cases} \quad (6)$$

where U_n is the amplitude of secondary voltage of the transformer. Assuming that the ratio of variation is k , the relationship between U_m and U_n satisfies

$$U_n = \frac{\sqrt{3}U_m}{k}. \quad (7)$$

3.2. Analysis of Characteristic Subharmonic Current. In order to analyze the types and contents of harmonics generated by the double inverse star rectifying transformer in the working process and effectively filter out the harmonics, it is assumed that both the grid voltage and the transformer are ideal. It can be seen from Figures 1 and 2 that the primary side current of the transformer can be represented by the secondary side current as

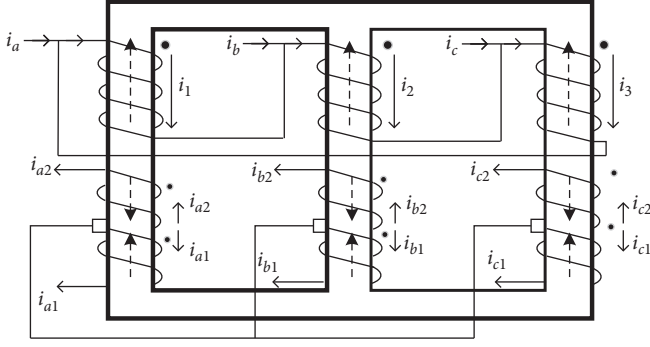


FIGURE 2: Internal structure diagram of double inverse star transformer.

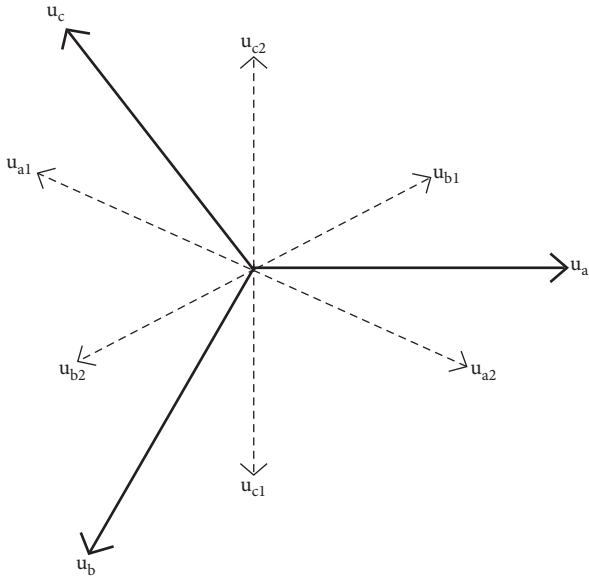


FIGURE 3: Vector relation of input and output voltages of transformer.

$$\begin{cases} i_1 = \frac{1}{k} (i_{a2} - i_{a1}), \\ i_2 = \frac{1}{k} (i_{b2} - i_{b1}), \\ i_3 = \frac{1}{k} (i_{c2} - i_{c1}). \end{cases} \quad (8)$$

The system input currents are obtained as

$$\begin{cases} i_a = i_1 - i_3, \\ i_b = i_3 - i_2, \\ i_c = i_2 - i_1. \end{cases} \quad (9)$$

By substituting (9) into (10), the expressions of system input current and secondary side current are obtained as

$$\begin{cases} i_a = \frac{1}{k} (i_{c1} - i_{c2} + i_{a2} - i_{a1}), \\ i_b = \frac{1}{k} (i_{b1} - i_{b2} + i_{c2} - i_{c1}), \\ i_c = \frac{1}{k} (i_{a1} - i_{a2} + i_{b2} - i_{b1}). \end{cases} \quad (10)$$

According to (11), it is difficult to analyze the input current. In this study, the load will be simplified to a constant current. It is difficult to determine the instantaneous voltage difference of three-phase half-wave output I_d , but its waveform is a triangular wave with three times the fundamental frequency. Since the balance reactor can make the rectifier system work independently with symmetry, the current can be supplied by two transformers equally, namely,

$$i_{d1} = i_{d2} = \frac{I_d}{2}. \quad (11)$$

In this paper, the switching function is introduced to study the current relationship between AC side and DC side directly. Taking the phase a_1 as an example, its switching function is $S_{a1} = i_{a1}/i_{d1}$ whose Fourier series expansion is

$$S_{a1} = \frac{1}{3} + \sum_{n=1}^{\infty} \left[\frac{\sin(2n\pi/3)}{n\pi} \cos n\omega t + \frac{1 - \cos(2n\pi/3)}{n\pi} \sin n\omega t \right]. \quad (12)$$

According to S_{a1} , Fourier series of phases b_1 and c_1 can be obtained, and then the expression of three-phase half-wave group I is expressed as

$$\begin{cases} S_{a1} = S_{a1} \angle 0, \\ S_{b1} = S_{a1} \angle -120^\circ, \\ S_{c1} = S_{a1} \angle +120^\circ. \end{cases} \quad (13)$$

On the basis of (14), the expression of three-phase half-wave group II can be obtained as

$$\begin{cases} S_{a2} = S_{a1} \angle +180^\circ, \\ S_{b2} = S_{b1} \angle +180^\circ, \\ S_{c2} = S_{c1} \angle +180^\circ. \end{cases} \quad (14)$$

The relationships between the switching function of each phase and its corresponding current input and output are as follows:

$$\begin{bmatrix} i_{a1} \\ i_{b1} \\ i_{c1} \end{bmatrix} = \begin{bmatrix} S_{a1} \\ S_{b1} \\ S_{c1} \end{bmatrix} i_{d1}, \quad (15)$$

$$\begin{bmatrix} i_{a2} \\ i_{b2} \\ i_{c2} \end{bmatrix} = \begin{bmatrix} S_{a2} \\ S_{b2} \\ S_{c2} \end{bmatrix} i_{d2}. \quad (16)$$

According to formulas (13)–(17), the Fourier series decomposition of each secondary side current is as follows:

$$\left\{ \begin{aligned} i_{a1} &= \frac{I_d}{2} \left\{ \frac{1}{3} + \sum_{n=1}^{\infty} \left[\frac{\sin(2n\pi/3)}{n\pi} \cos n\omega t + \frac{1 - \cos(2n\pi/3)}{n\pi} \sin n\omega t \right] \right\}, \\ i_{b1} &= \frac{I_d}{2} \left\{ \frac{1}{3} + \sum_{n=1}^{\infty} \left[\frac{\sin(2n\pi/3)}{n\pi} \cos n\left(\omega t - \frac{2\pi}{3}\right) + \frac{1 - \cos(2n\pi/3)}{n\pi} \sin n\left(\omega t - \frac{2\pi}{3}\right) \right] \right\}, \\ i_{c1} &= \frac{I_d}{2} \left\{ \frac{1}{3} + \sum_{n=1}^{\infty} \left[\frac{\sin(2n\pi/3)}{n\pi} \cos n\left(\omega t + \frac{2\pi}{3}\right) + \frac{1 - \cos(2n\pi/3)}{n\pi} \sin n\left(\omega t + \frac{2\pi}{3}\right) \right] \right\}, \end{aligned} \right. \quad (17)$$

$$\left\{ \begin{aligned} i_{a2} &= \frac{I_d}{2} \left\{ \frac{1}{3} + \sum_{n=1}^{\infty} (-1)^n \left[\frac{\sin 2n\pi/3}{n\pi} \cos n\omega t + \frac{1 - \cos 2n\pi/3}{n\pi} \sin n\omega t \right] \right\}, \\ i_{b2} &= \frac{I_d}{2} \left\{ \frac{1}{3} + \sum_{n=1}^{\infty} \left[\frac{\sin 2n\pi/3}{n\pi} \cos n\left(\omega t + \frac{\pi}{3}\right) + \frac{1 - \cos 2n\pi/3}{n\pi} \sin n\left(\omega t + \frac{\pi}{3}\right) \right] \right\}, \\ i_{c2} &= \frac{I_d}{2} \left\{ \frac{1}{3} + \sum_{n=1}^{\infty} \left[\frac{\sin 2n\pi/3}{n\pi} \cos n\left(\omega t - \frac{\pi}{3}\right) + \frac{1 - \cos 2n\pi/3}{n\pi} \sin n\left(\omega t - \frac{\pi}{3}\right) \right] \right\}. \end{aligned} \right. \quad (18)$$

It can be seen from (12), (18), and (19) that taking phase a as an example, its current expression is

$$\begin{aligned} i_a &= \sum_{n=1,2,3,\dots}^{\infty} R_n \sin(n\omega t), \\ R_n &= \frac{4I_d}{n\pi} \left[1 + \sin\left(\frac{1}{6}n\pi\right) \sin\left(\frac{1}{2}n\pi\right) \right]. \end{aligned} \quad (19)$$

It is obvious that the harmonic content in the power grid mainly contains $(6k \pm 1)$ times ($k = 1, 2, 3, \dots$) harmonics.

The electro-winning copper rectifier used in this paper is a double inverse star rectifying system, and its system parameters are summarized in Table 1.

According to Table 1, the parameters of the double inverse star rectifying simulation circuit are set. Figure 4 shows waveforms of output voltage and output current. Figure 5 shows waveforms of voltage and current measured on the power grid. Figure 6 shows the spectrum analysis diagram of harmonic measurement on the power grid.

Spectrum of harmonics in Figure 6 demonstrates that a large number of harmonics are generated and injected into the power grid in the rectifying process of double inverse star rectifier, and these harmonics are mainly the 5th, 7th, 11th, and 13th harmonics. Before filtering, the total measured distortion rate of the power grid is up to 29.19%.

4. Filtering Method Combining Active Filter with Inductive Filter

Because the induction filtering method can meet the requirements of the total harmonic distortion rate after filtering and the active power filtering method can meet

the requirements of tracking and filtering the harmonic changes in real time after the load changes, the two filtering methods are combined to carry out comprehensive filtering for the copper electrodeposited rectifying system.

A system diagram of combining the two filtering methods is shown in Figure 7, an induction filter is added to the transformer side, and the active power filter is added to the power grid side, which will make the electro-winning copper rectifier achieve a good filtering effect.

In the simulation process, the active filter is added at 0.02 s, the inductive filter is added at 0.06 s, and the SCR trigger angle is changed from 10° to 20° at 0.12 s, that is, when the load changes, the corresponding harmonic also changes. The simulation results are shown in Figures 8 and 9.

The corresponding harmonic spectrum is shown in Figure 9.

From the above simulation results, it can be seen that when the active filter is added at 0.02 s, the waveform has obvious changes and the filtering effect is good. When the induction filter is added at 0.06 s, the waveform is stable after one cycle, that is, the total harmonic distortion rate is 4.83% at 0.08 s, which basically meets the requirements of the power grid. When the load changes at 0.12 s, the total distortion rate rises to 8.07%, which indicates that the harmonic has changed. After a period of 0.16 s, the total distortion rate of the system decreases to 3.76%, which indicates that the filtering system can track the corresponding changes of harmonics when the load changes in real time and filter them out.

TABLE 1: Parameters of double inverse star rectifying system.

Parameters	Values
Input voltage	10 kV
Output voltage	60 ~ 80 V
Output current	10000 A
Transformer capacity	10 kVA
Frequency	50 Hz

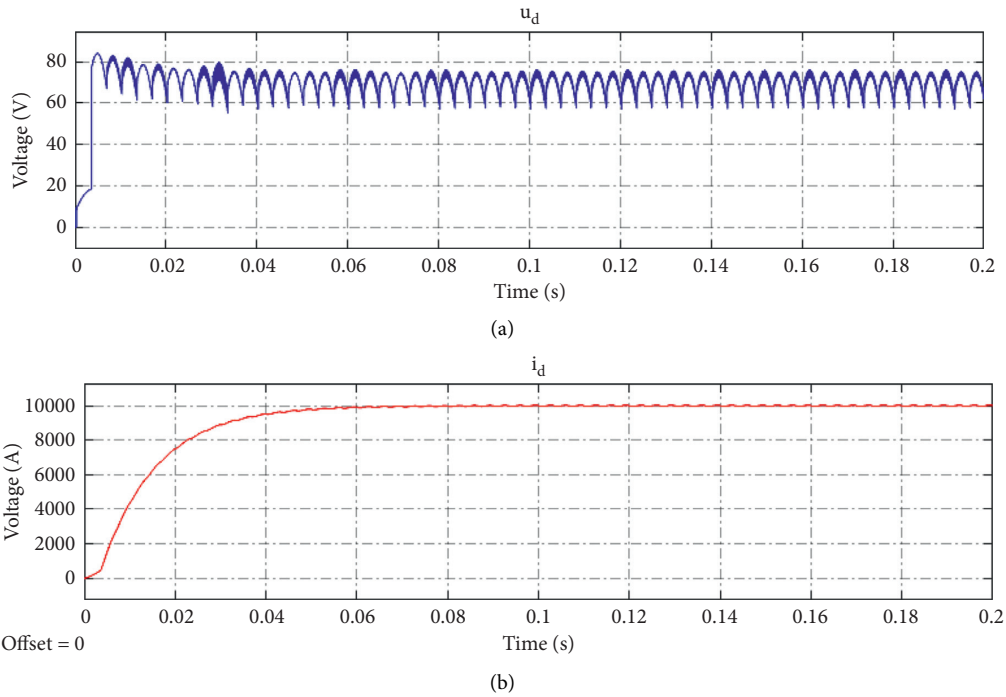


FIGURE 4: Waveforms of output voltage and output current.

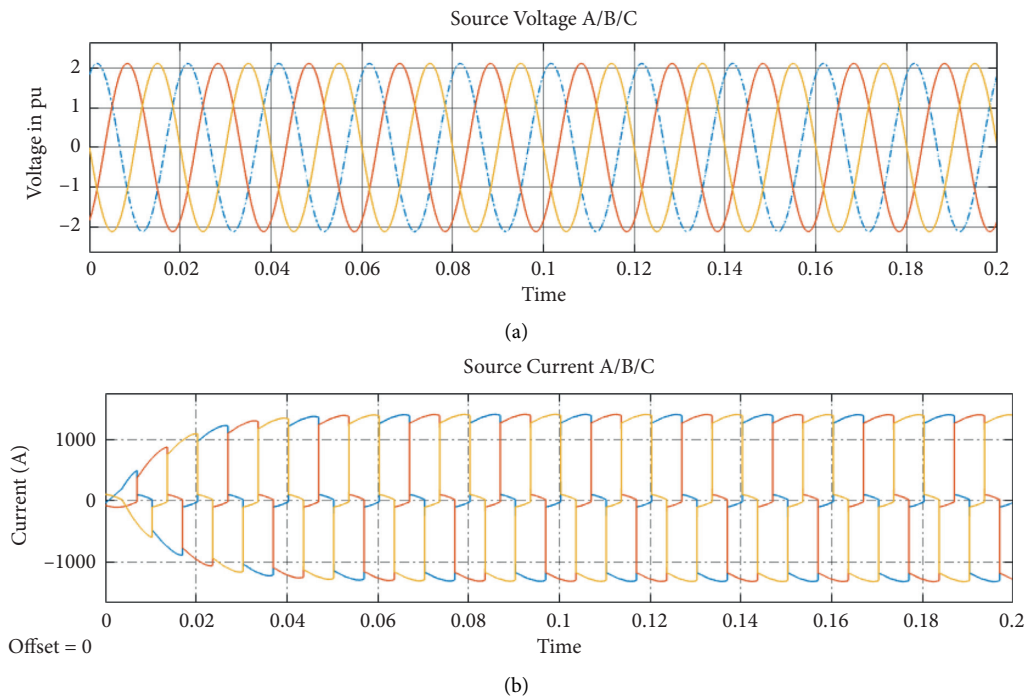


FIGURE 5: Waveforms of voltage and current measured on the power grid.

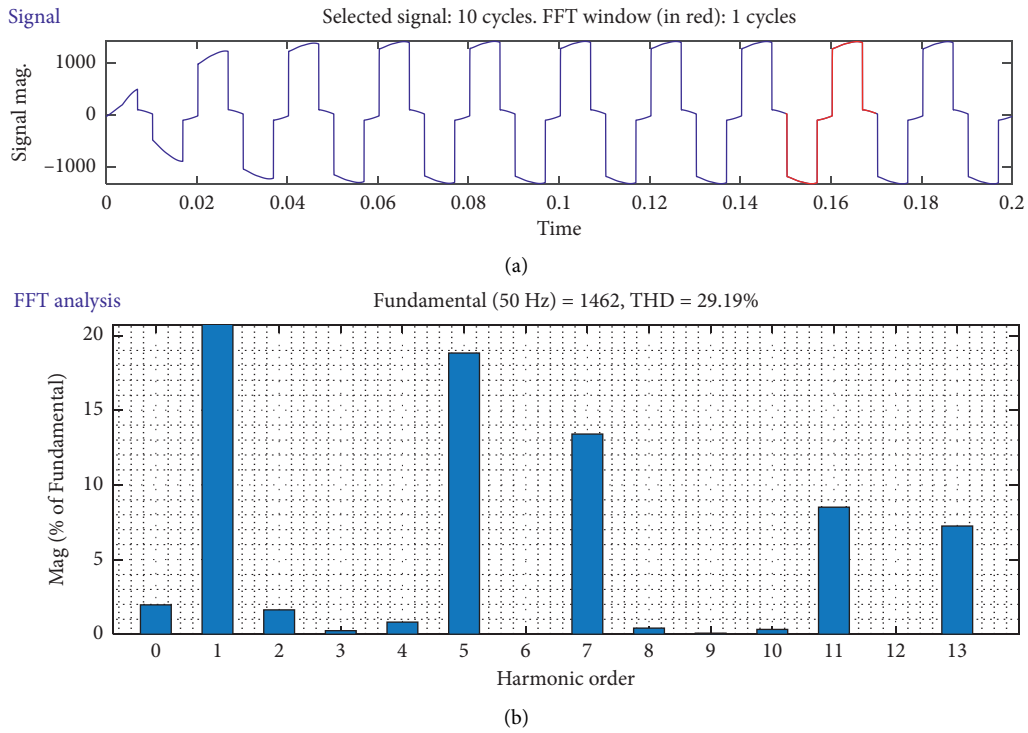


FIGURE 6: Spectrum of harmonic measurement on the power grid.

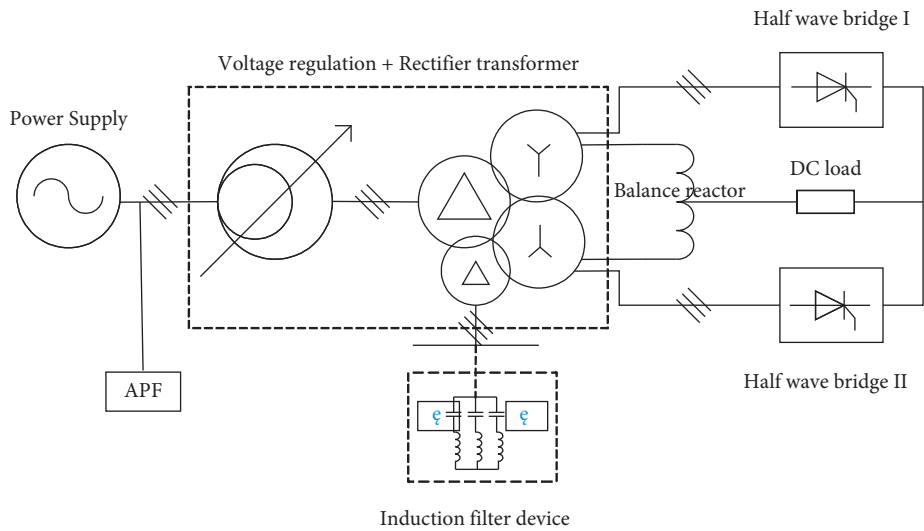


FIGURE 7: Filter system diagram of combination of induction filter and active filter.

5. Active Power Filter Based on Linear Active Disturbance Rejection Control

5.1. Construction of LADRC Applied in APF. In this paper, the current tracking control method of instantaneous value comparison is adopted. Although it has an obvious filtering effect, its tracking effect is limited by the choice of hysteresis loop width. If it is too large, the tracking effect is not good. If it is too small, the switching frequency is too high which results in higher power loss. Therefore, a new current tracking control method—linear active

disturbance rejection control (LADRC)—is introduced. The LADRC technology is an improvement of linearization based on active disturbance rejection control (ADRC). The key part is the linearization of the extended state observer (ESO). Compared with ADRC, the parameter tuning of ACRC is reduced, and the control process is relatively simple, which improves its practical value in the control process.

In this paper, the LADRC technology is applied in current tracking control, which means that ESO and control are linear, and the differential tracker is not needed in

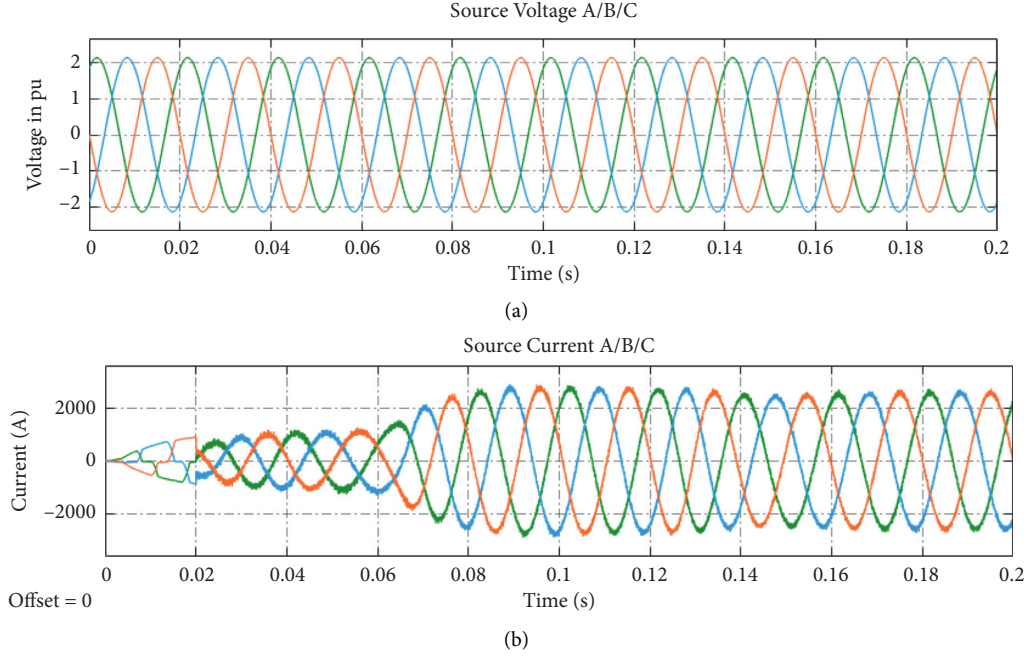


FIGURE 8: Harmonic current waveform on power grid side after combining induction filter and active filter.

practical application. The control block diagram of LADRC application in APF is shown in Figure 10, taking single-phase a as an example.

Figure 11 shows the internal structure block diagram of LADRC.

5.2. Design of Linear Expansion State Observer (LESO). In the entire LADRC system, the LESO is the most critical part. It can calculate each state quantity and disturbance value of the unknown model system according to the input data. For any given n -order unknown system, there is

$$y^{(n)}(t) = f(y^{(n-1)}(t), \dots, y(t), w(t)) + b_0 u(t), \quad (20)$$

where $y(t)$ represents the input signal of the system, the nonlinear dynamic characteristic of the system is $f(\bullet)$, $w(t)$ represents the external disturbance of the system, $u(t)$ represents the control input signal of the system, and b_0 represents the gain of the controller. In LACRC, $f(\bullet)$ is the expression of total disturbance. All state spaces of the system satisfy

$$\begin{cases} \dot{x}_1 = x_2, \\ \vdots, \\ \dot{x}_{n-1} = x_n, \\ \dot{x}_n = x_{n+1} + b_0 u, \\ \dot{x}_{n+1} = h(X, w), \\ y = x_1, \end{cases} \quad (21)$$

where, the state variable x_{n+1} , which is the total disturbance passing through the LESO, can be expressed as

$$x_{n+1} = f(y^{(n-1)}(t), \dots, y(t), w(t)). \quad (22)$$

Let

$$\dot{x}_{n+1} = h(X, w). \quad (23)$$

In this way, the original n -order system is expanded into a new $n+1$ -order linear system. The first-order linear ADRC is designed in this paper, and the state space of the system can be written as

$$\begin{cases} \dot{x}_1 = x_2 + b_0 u, \\ \dot{x}_2 = h(X, w), \\ y = x_1. \end{cases} \quad (24)$$

X is added to the system as an expanded state. For the convenience of design, the matrix form of (26) is

$$\begin{cases} \dot{x} = Ax + Bu + Eh, \\ y = Cx, \end{cases} \quad (25)$$

where $A = \begin{bmatrix} 0 & 1 \\ 0 & 0 \end{bmatrix}$, $B = \begin{bmatrix} b_0 \\ 0 \end{bmatrix}$, $E = \begin{bmatrix} 0 \\ 1 \end{bmatrix}$, and $C = [1 \ 0]$. $h = \dot{f}(\bullet)$ is the first derivative of the disturbance. The LESO of the system is written as

$$\begin{cases} \dot{z} = Az + Bu + L(y - \hat{y}), \\ \hat{y} = Cz, \end{cases} \quad (26)$$

where $L = \begin{bmatrix} \beta_1 \\ \beta_2 \end{bmatrix}$ is the gain of LESO.

By subtracting (27) from (28), the equation of state of observation error is obtained as

$$\dot{e} = A_e e + Eh, \quad (27)$$

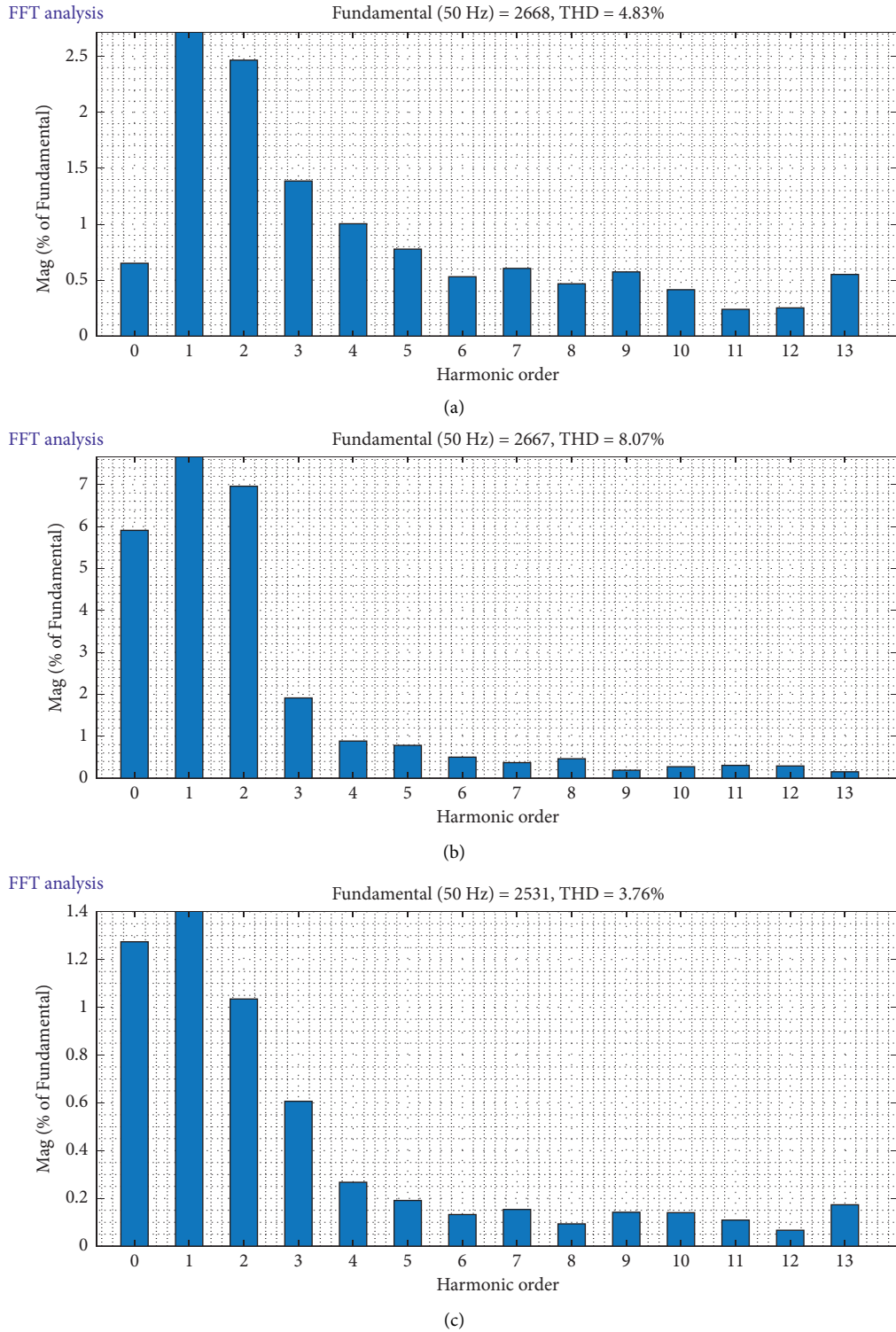


FIGURE 9: Harmonic spectrum after combining induction filter and active filter. (a) Total harmonic distortion rate at 0.08 s. (b) Total harmonic distortion rate at 0.12 s. (c) Total harmonic distortion rate at 0.16 s.

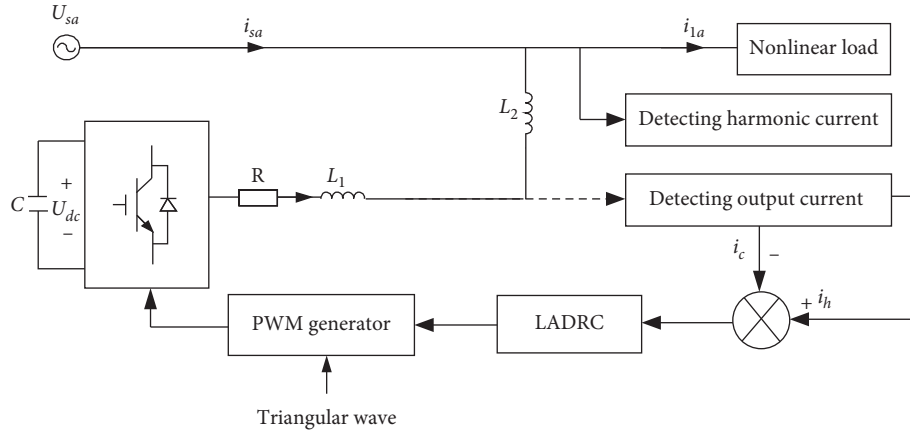


FIGURE 10: Control block diagram of LADRC applied in APF.

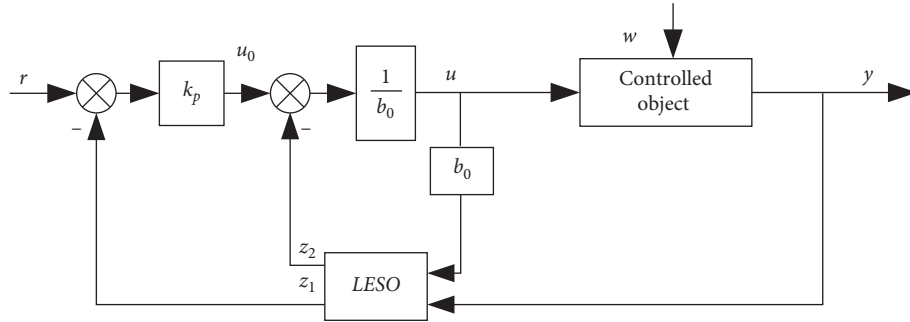


FIGURE 11: Structure block diagram of LADRC.

where $A_e = \begin{bmatrix} -\beta_1 & 1 \\ -\beta_2 & 0 \end{bmatrix}$.

If there is no steady-state error, the eigenvalues of the observation error characteristic matrix should be all in the left half of the plane, and the characteristic equation can be obtained as

$$\lambda(s) = s^2 + \beta_1 s + \beta_2. \quad (28)$$

When the bandwidth of the observer is fixed, if the following conditions are satisfied:

$$\lambda(s) = (s + \omega_0)^2, \quad (29)$$

the effect of the controller is best. According to formulas (30) and (31),

$$\begin{cases} \beta_1 = 2\omega_0, \\ \beta_2 = \omega_0^2. \end{cases} \quad (30)$$

The specific form of LESO is

$$\dot{z} = A_e z + [B \ L] \begin{bmatrix} u \\ y \end{bmatrix} = \begin{bmatrix} -\beta_1 & 1 \\ -\beta_2 & 0 \end{bmatrix} z + \begin{bmatrix} b_0 & 2\omega_0 \\ 0 & \omega_0^2 \end{bmatrix} \begin{bmatrix} u \\ y \end{bmatrix}. \quad (31)$$

Inputs of LESO are $u(t)$ and $y(t)$. The two system states z_1 and z_2 track y and expand the state x_2 , respectively.

5.3. Design of Linear State Error Feedback (LSEF). The main function of linear error feedback control rate is not only to preserve the advantages of integral link but also to avoid the error caused by integral transformation when designing parameters. Therefore, the disturbance compensation value $-z_2/b_0$ is required to replace the integral part of PID control in the design process. For the second-order and even higher-order system, although there is no integral term, it can still reflect the function of the integral. The LADRC system used in current tracking control is a first-order system in this paper, which does not need differential tracker. Therefore, we only need to use the control rate for P .

$$u_0 = k_p (r - y), \quad (32)$$

where u_0 is the error feedback control quantity and k_p represents the proportional constant. It can be seen from Figure 11 that the final error feedback control quantity is

$$u = \frac{u_0 - z_2}{b_0}. \quad (33)$$

For the convenience of frequency-domain analysis, Figure 11 can be transformed into Figure 12.

Figure 12 shows the transfer function in the frequency domain. The input signal of the controller is $R(s)$, and $Y(s)$ indicates the output signal. The disturbance signal is $W(s)$, and $P(s)$ indicates the controlled object model. The control

signal is $U(s)$, and $H(s)$ and $G(s)$ are the undetermined terms of the controller, respectively.

The control signal can be expressed as

$$U(s) = (R(s)H(s) - Y(s)) \times G(s). \quad (34)$$

Substituting (34) into (35) and performing Laplace transform, the following results are obtained:

$$U(s) = \frac{1}{b_0} (k_p) \times (R(s) - Y(s)) - Z_2(s). \quad (35)$$

The Laplace transform of (28) can be obtained as

$$Z(s) = \frac{1}{s^2 + \beta_1 s + \beta_2} \begin{bmatrix} b_0 s & \beta_1 s + \beta_2 \\ -\beta_2 b_0 & \beta_2 s \end{bmatrix} \begin{bmatrix} U(s) \\ Y(s) \end{bmatrix}. \quad (36)$$

Therefore,

$$Z_2(s) = \frac{-\beta_2 b_0 U(s) + \beta_2 s Y(s)}{s^2 + \beta_1 s + \beta_2}. \quad (37)$$

By substituting equation (39) into equation (38) and combining it with equation (37), the following results can be obtained:

$$\begin{cases} H(s) = \frac{k_p (s^2 + \beta_1 s + \beta_2)}{k_p s^2 + (k_p \beta_1 + \beta_2) s + k_p \beta_2}, \\ G(s) = \frac{k_p s^2 (k_p \beta_1 + \beta_2) s + k_p \beta_2}{b_0 (s^2 + \beta_1 s)}. \end{cases} \quad (38)$$

Let $k_p = \omega_c$, where ω_c is the bandwidth for the controller, and from experience, $\omega_0 = 3 \sim 5\omega_c$. By substituting equation (39) into equation (38), the following results can be obtained:

$$\begin{cases} H(s) = \frac{\omega_c (s^2 + 2\omega_0 s + \omega_0^2)}{\omega_c s^2 + (\omega_c 2\omega_0 + \omega_0^2) s + \omega_c \omega_0^2}, \\ G(s) = \frac{\omega_c s^2 + (\omega_c 2\omega_0 + \omega_0^2) s + \omega_c \omega_0^2}{b_0 (s^2 + 2\omega_0 s)}. \end{cases} \quad (39)$$

According to equation (41), the LADRC is a single-parameter controller. In this paper, $\omega_0 = 10$, $b_0 = 0.1$, $\beta_1 = 20$, $\beta_2 = 100$, and $k_p = 2$.

5.4. Convergence Analysis of Linear Extended State Observer. Taking the controlled object represented by equation (22) as an example, for the n -order controlled object represented by equation (23), the LESO is represented by

$$\begin{cases} \dot{z}_1 = z_2 - B_1(z_1 - y), \\ \vdots, \\ \dot{z}_n = z_{n+1} - B_n(z_1 - y) + bu, \\ \dot{z}_{n+1} = -B_{n+1}(z_1 - y). \end{cases} \quad (40)$$

The parameter of the observer is $L = [B_1, B_2, \dots, B_{n+1}]$ which is adjusted by pole assignment method.

Taking into account the general situation, if

$$[B_1, B_2, \dots, B_{n+1}] = [a_1 \omega_0, a_2 \omega_0^2, \dots, a_{n+1} \omega_0^{n+1}], \quad (\omega_0 > 0), \quad (41)$$

then the characteristic polynomial $s^3 + a_1 s^2 + a_2 s + a_3$ will satisfy the Herwitz criterion. In order to simplify the calculation process, setting $s^{n+1} + a_1 s^n + \dots + a_n s + a_{n+1} = (s + 1)^{n+1}$, then $a_i = (n + 1)! / i! (n + 1 - i)!$ can be obtained, $i = 1, 2, \dots, n + 1$. In this case, the characteristic polynomial of the LESO can be expressed as

$$\lambda(s) = (s + \omega_0)^{n+1}. \quad (42)$$

It is obvious that the undetermined parameter of the whole state observer is only ω_0 , setting $\tilde{x}_i = x_i - z_i$, $i = 1, 2, \dots, n + 1$. The estimation error of LESO can be obtained as

$$\begin{cases} \dot{\tilde{x}}_1 = \tilde{x}_2 - \omega_0 a_1 \tilde{x}_1, \\ \vdots \\ \dot{\tilde{x}}_{n-1} = \tilde{x}_n - \omega_0^{n-1} a_{n-1} \tilde{x}_1, \\ \dot{\tilde{x}}_n = \tilde{x}_{n+1} - \omega_0^n a_n \tilde{x}_1, \\ \dot{\tilde{x}}_{n+1} = h(x, w) - h(z, w) - \omega_0^{n+1} a_{n+1} \tilde{x}_1, \end{cases} \quad (43)$$

and let $\varepsilon_i = \tilde{x}_i / \omega_0^{i-1}$, $i = 1, 2, \dots, n + 1$. Then, equation (45) can be converted to

$$\dot{\varepsilon} = \omega_0 A \varepsilon + B \frac{h(x, w) - h(z, w)}{\omega_0^n}, \quad (44)$$

$$\text{where } A = \begin{bmatrix} -a_1 & 1 & 0 & \dots & 0 \\ -a_2 & 0 & 1 & \vdots & 0 \\ \vdots & \vdots & \ddots & \vdots & \vdots \\ -a_n & 0 & \dots & 0 & 1 \\ -a_{n+1} & 0 & \dots & 0 & 0 \end{bmatrix}, B = [0 \ 0 \ \dots \ 0 \ 1].$$

Because $a_i = (n + 1)! / i! (n + 1 - i)!$, matrix A satisfies the Herwitz criterion. LESO is convergent, when $h(x, w)$ satisfies Lipschitz continuity condition; that is to say, there exists $\omega_0 > 0$ to make $\lim_{t \rightarrow \infty} \tilde{x}_i = 0$, $i = 0, 1, 2, \dots, n + 1$.

Since matrix A satisfies the Herwitz criterion, there must be a positive definite matrix P such that

$$A^T P + P A = -I. \quad (45)$$

Matrix P selects Lyapunov function

$$V(\varepsilon) = \varepsilon^T P \varepsilon. \quad (46)$$

The derivation of equation (48) is obtained as

$$\dot{V}(\varepsilon) = -\omega_0 \|\varepsilon\|^2 + 2\varepsilon^T P B \frac{h(x, w) - h(z, w)}{\omega_0^n}. \quad (47)$$

Because $h(x, w)$ satisfies Lipschitz continuity condition for x_1, x_2, \dots, x_{n+1} , there must be a constant C , and for any x, z, w , there must exist

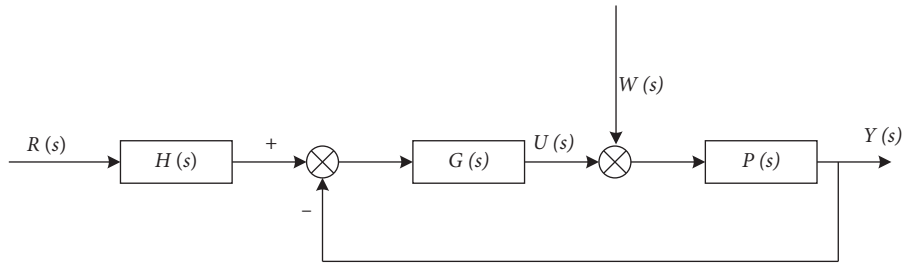


FIGURE 12: Block diagram of first-order LADRC.

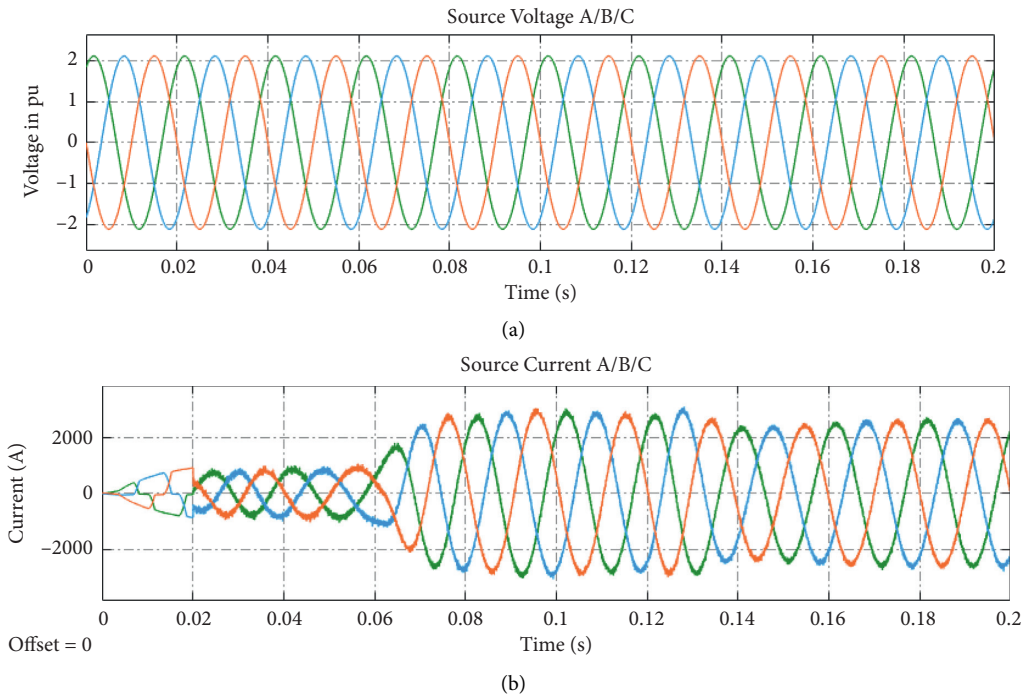


FIGURE 13: Voltage and current waveforms of three-phase power system using LADRC.

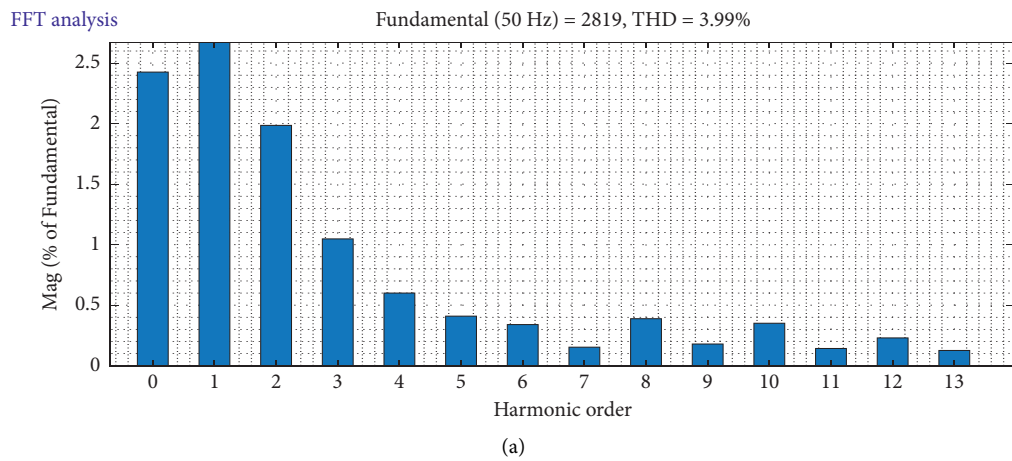


FIGURE 14: Continued.

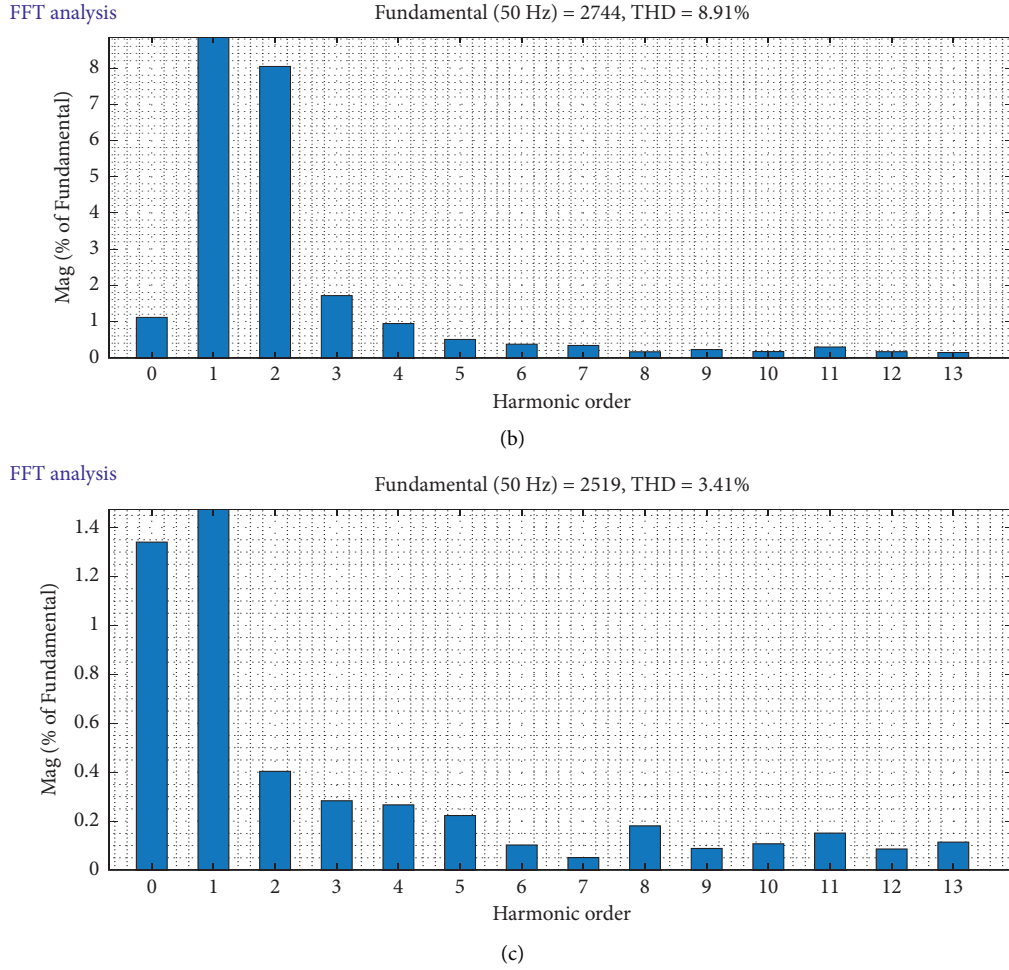


FIGURE 14: Harmonic spectrum after combining active filter with inductive filter method based on LADRC. (a) Total harmonic distortion at 0.08 s under the control of LADRC. (b) Total harmonic distortion at 0.12 s under the control of LADRC. (c) Total harmonic distortion at 0.16 s under the control of LADRC.

$$|h(x, \omega) - h(z, \omega)| \leq C \|x - z\|. \quad (48)$$

Equation (50) is further deduced as

$$2\varepsilon^T P B \frac{h(x, \omega) - h(z, \omega)}{\omega_0^n} \leq 2\varepsilon^T P B C \frac{\|x - z\|}{\omega_0^n}. \quad (49)$$

When $\omega_0 > 0$, there is

$$\frac{\|x - z\|}{\omega_0^n} = \frac{\|\tilde{x}\|}{\omega_0^n} = \frac{\left\| \sqrt{\varepsilon_1^2 + \varepsilon_2^2 \omega_0^2 + \dots + \varepsilon_{n+1}^2 \omega_0^{2n}} \right\|}{\omega_0^n} \leq \|\varepsilon\|, \quad (50)$$

where $C' = 1 + \|PBC\|^2$; in combination with (49) and (51), it can be obtained as

$$\dot{V}(\varepsilon) \leq -(\omega_0 - C') \|\varepsilon\|^2. \quad (51)$$

Therefore, if $\omega_0 > C'$, $\dot{V}(\varepsilon) \leq 0$, that is, $\lim_{t \rightarrow \infty} \tilde{x}_i = 0$, $i = 0, 1, 2, \dots, n+1$. That is to say, the pole assignment method is used to design the convergence of the LESO.

5.5. Harmonic Suppression with LADRC. On the basis of the filtering method combining active filter with inductive filter, the LADRC technology is applied in current tracking control in ARF, filtering effects of which are obtained by conducting simulation. Simulation results are obtained in Figures 13 and 14. The active filter is added at 0.02 s, the inductive filter is added at 0.06 s, and the SCR trigger angle changes from 10° to 20° at 0.12 s, that is, the load changes.

Comparison of total distortion rates between hysteresis control and LADRC is summarized in Table 2.

It can be seen from Table 2 that obviously the total harmonic distortion rate under the control of LADRC is 3.99% at 0.08 s, which is lower than that under hysteresis control; at 0.12 s, the trigger angle of SCR changes from 10° to 20° , that is, when the load changes, the harmonic also changes accordingly. After one cycle, the total harmonic distortion rate returns to 3.41%, which is also lower than that of hysteresis control. Therefore, the results verify that the harmonic suppression effect of LADRC is better than that of hysteresis tracking control.

TABLE 2: Comparison of total distortion rates.

Simulation time (s)	Total distortion rate (%)	
	Hysteresis control	LADRC
0.08	4.83	3.99
0.12	8.07	8.91
0.16	3.76	3.41

6. Conclusions

Since the induction filtering method can meet the requirements of the total harmonic distortion rate after filtering and the active power filtering method can meet the requirements of tracking and filtering the harmonic changes in real time when the load changes, in order to effectively suppress a large number of harmonics mainly including the 5th, 7th, 11th, and 13th harmonics generated during operation of a copper electro-winning rectifier with double inverse star circuit, firstly, this paper proposes a method combining the induction filtering method and the active filtering method to carry out comprehensive filtering. Simulation results indicate that the total distortion rate of the system decreases to 4.83% from 29.19% before filtering, which indicates that the proposed method can track the corresponding changes of harmonics when the load changes in real time and filter them out. Secondly, a current harmonic tracking control method based on LADRC is proposed to ensure and improve the effect of the active filter. Simulation results show that the total harmonic distortion rate can be decreased to 3.41%, which is also lower than that of hysteresis control. Compared with the conventional single filtering method, it is obvious that the proposed filtering method combining induction filtering with active filtering based on LADRC in the copper electro-winning rectifier has obvious advantages in setting parameter and debugging system.

Data Availability

The data used to support the findings of this study are available from the corresponding author upon request.

Conflicts of Interest

The authors declare that there are no conflicts of interest regarding the publication of this paper.

Acknowledgments

This study was supported by the Scientific Research Projects of the Jilin Provincial Development and Reform Commission (grant no. 2018C035-1), Development Plan Project of Jilin Provincial Science and Technology Department (grant nos. 20190101018JH, 20160101276JC, and 20150312040ZG), Scientific Research Projects of the Education Department of Jilin Province (grant no. JJKH20200044KJ), and Project of Beihua University (grant no. 201901012).

References

- [1] Z. Li, "Power quality and energy saving," *China Standardization*, vol. 12, pp. 7–9, 2010.
- [2] China Standardization Gb/114549-93, *Quality of Electric Energy Supply & Harmonics in Public Supply Network*, China standards Publishing House, Beijing China, 1994.
- [3] J. Wang, H. Y. Dong, and X. Guo, "Comprehensive evaluation method of power quality considering equipment compatibility," *Electric Engineering*, vol. 23, pp. 9–11+15, 2019.
- [4] H. P. Hang, Y. D. Ma, D. Zhang, D. Zhang, and H. Mao, "Simulation analysis of power quality of distributed power supply after grid connection based on active power filter," *Microcomputer Applications*, vol. 37, no. 1, pp. 165–167, 2021.
- [5] L. Zhou, Q. H. Jia, H. Y. Liu, F. Zhang, and Y. J. Qu, "Evaluation of power quality by fuzzy artificial neural network," *High Voltage Engineering*, vol. 9, pp. 66–99, 2007.
- [6] Z. H. Ning, L. F. Luo, Y. Li, Z. Zhiwen, Z. Zhiyu, and Z. Xiaohu, "Analysis of energy saving and harmonic power characteristics and its effects on electric energy measurement in high power rectifier system," *Transactions of China Electrotechnical Society*, vol. 27, no. 11, pp. 248–255, 2012.
- [7] P. Fang and L. N. Guo, "Harmonic analysis and suppression measures for rectifier power system in ionic membrane caustic," *Control and Instruments in Chemical Industry*, vol. 42, no. 1, pp. 96–100, 2015.
- [8] W. Zhao, A. Luo, J. Tang, and X. Deng, "Hybrid var compensator based on the coordinated operation of STATCOM and TSC," *Proceedings of the CSEE*, vol. 29, no. 19, pp. 92–98, 2009.
- [9] T. S. Mao, Y. J. Sun, and H. P. Zhou, "Smelter harmonic treatment examples," *Power Capacitor & Reactive Power Compensation*, vol. 33, no. 2, pp. 26–30+57, 2012.
- [10] D. Yuan, S. Wang, H. Zhang, X. Tao, J. Zhu, and Y. Guo, "The harmonic suppression characteristic analysis of a phase-shifting reactor in rectifier system," *IEEE Transactions on Magnetics*, vol. 51, no. 11, pp. 1–4, 2015.
- [11] T. Takeshita, H. Goto, T. Masuda, and N. Matsui, "Current waveform control of a high-power-factor rectifier circuit for harmonic suppression of voltage and current in a distribution system," *Electrical Engineering in Japan*, vol. 140, no. 4, pp. 62–71, 2002.
- [12] P. Méndez, I. Kirpichev, M. Blaumoser, M. Visiers, A. Agudo, and J. Iglesias, "High power IGBT bridge application for the harmonic suppression on the load side of the power supply system of the Spanish Stellarator TJ-II," *Fusion Engineering and Design*, vol. 75–79, pp. 123–126, 2005.
- [13] Q. Liu, Y. Li, S. Hu, and L. Luo, "Power quality improvement using controllable inductive power filtering method for industrial DC supply system," *Control Engineering Practice*, vol. 83, pp. 1–10, 2019.
- [14] B. Liu, J. J. Wu, J. Li, and J. Y. Dai, "A novel PFC controller and selective harmonics suppression," *International Journal of Electrical Power & Energy Systems*, vol. 44, no. 1, pp. 680–687, 2013.
- [15] A. Ramesh and H. Habeebullah Sait, "An approach towards selective harmonic elimination switching pattern of cascade switched capacitor twenty nine-level inverter using artificial bee colony algorithm," *Microprocessors and Microsystems*, vol. 79, Article ID 103292, 2020.
- [16] W. Wu, Z. Xie, Y. Chen et al., "Analysis and suppression of high-frequency oscillation between converter-based source

- and loads in an island power system,” *International Journal of Electrical Power & Energy Systems*, vol. 117, Article ID 105616, 2020.
- [17] Q. Wang, J. Wu, J. Gao et al., “Frequency-domain harmonic modeling and analysis for 12-pulse series-connected rectifier under unbalanced supply voltage,” *Electric Power Systems Research*, vol. 162, pp. 23–36, 2018.
- [18] E. P. Wiechmann, R. P. Burgos, and J. Holtz, “Sequential connection and phase control of a high-current rectifier optimized for copper electrowinning applications,” *IEEE Transactions on Industrial Electronics*, vol. 47, no. 4, pp. 734–743, 2000.
- [19] L. Zhang, R. Zhao, P. Ju et al., “A modified DPWM with neutral point voltage balance capability for three-phase Vienna rectifiers,” *IEEE Transactions on Power Electronics*, vol. 36, no. 1, pp. 263–273, 2021.
- [20] G. An, G. Y. Xu, and H. J. Dong, “Simulation de sign of MATLAB-based large electrolytic Aluminum filter device,” *Power Capacitor & Reactive Power Compensation*, vol. 5, no. 5, pp. 65–69, 2004.
- [21] S. J. Dai, J. H. Li, J. B. Liu, N. Li, Y. Shi, and W. N. Tan, “Harmonic suppression and reactive power compensation method at metal smelting factory,” *Power Capacitor & Reactive Power Compensation*, vol. 41, no. 5, pp. 12–16+22, 2020.
- [22] Y. J. Ma, J. Zhao, X. S. Zhou, and C. W. Tian, “A linear auto disturbance rejection controller for shunt hybrid active power filters and its stability analysis,” *Power System Technology*, vol. 36, no. 11, pp. 212–216, 2012.
- [23] D. Z. Li, W. L. Yu, and Q. B. Jin, “Stability region analysis of linear active disturbance rejection controllers for first order systems with time delay,” *Control Theory & Applications*, vol. 34, no. 9, pp. 1244–1249, 2017.
- [24] X. Q. Liang, S. An, and Z. Li, “A design of linear active disturbance rejection-improved control strategy for DFIG grid-side inverter,” *Computer Simulation*, vol. 37, no. 12, pp. 98–102, 2020.
- [25] P.-M. Hannula, M. K. Khalid, D. Janas, K. Yliniemi, and M. Lundström, “Energy efficient copper electrowinning and direct deposition on carbon nanotube film from industrial wastewaters,” *Journal of Cleaner Production*, vol. 207, pp. 1033–1039, 2019.
- [26] C. Chibwe and M. Tadie, “An experimental review of the physicochemical properties of copper electrowinning electrolytes,” *Mining, Metallurgy & Exploration*, vol. 38, no. 2, pp. 1225–1237, 2021.
- [27] J. Wu, Y. M. Cheng, C. Liu, I. k. Lee, and W. Huang, “A BP neural network based on ga for optimizing energy consumption of copper electrowinning,” *Mathematical Problems in Engineering*, vol. 2020, pp. 1–10, Article ID 1026128, 2020.

Research Article

Design Methodology for Interfacing DERs to Power Systems through VSC

A. Valderrabano-Gonzalez ¹, **F. Beltran-Carbajal** ², **R. Tapia-Olvera** ³,
O. Aguilar-Mejia ⁴, and **J. C. Rosas-Caro** ¹

¹Universidad Panamericana, Facultad de Ingeniería, Álvaro del Portillo 49, Zapopan, Jalisco 45010, Mexico

²Departamento de Energía, Universidad Autónoma Metropolitana, Unidad Azcapotzalco, Mexico City, Mexico

³Department of Electrical Energy, Universidad Nacional Autónoma de México, Mexico City, Mexico

⁴School Engineering, UPAEP University, Puebla 72410, Mexico

Correspondence should be addressed to A. Valderrabano-Gonzalez; avalder@up.edu.mx

Received 16 February 2021; Revised 4 June 2021; Accepted 15 October 2021; Published 31 October 2021

Academic Editor: David Bigaud

Copyright © 2021 A. Valderrabano-Gonzalez et al. This is an open access article distributed under the Creative Commons Attribution License, which permits unrestricted use, distribution, and reproduction in any medium, provided the original work is properly cited.

This paper presents a methodology to connect distributed energy resources via an 84-pulse voltage source converter to three-phase system grid or load of standard or nonstandard voltage values. Transfer function blocks are included to illustrate interfacing among converters. The main input-output values to be considered in the application are detailed and the system can be modified to be included in other systems without loss of generality. The definition of the reactive component for supporting grid or load variations without degrading the overall performance is carried by for the DC-DC converter. A control variable for reducing the DC gain is used to improve the settling time. Our proposal defines the capacitive and inductive component values for an operating point and gives the option to reduce them when adding smoothed variations and adaptive controllers.

1. Introduction

Voltage source converters (VSC) have been used for many years to adapt DC voltage to three-phase AC voltage load or interfacing to grid for improving power quality by reducing the conducted low-frequency phenomena described in [1]. They are encouraged to follow the attributes of the steady-state phenomena listed in [2]. In recent years, VSCs have been used to add compatibility for the interoperability between utility electric power systems (EPSs) and distributed energy resources (DERs) [3]. Topologies used for VSC vary from multilevel, pulse width modulation (PWM), and multipulse, and each one has some advantages over the others depending on the application. Because of that, combinations of topologies have been used for improving the response in particular applications, such as that described in [4] for sag, swell, three-phase failure, and motor startup and in [5] for large induction motor control. DC-link capacitor or battery energy storage systems (BESS) are

needed for an optimal operation of the system based on VSC [6, 7]. Low ripple or almost constant DC-link signals require bulky components leading to slow dynamic response of the system while maintaining the DC voltage under established parameters. Complex control routines or switching strategies for reducing these components are needed [8]. Maintaining the voltage level on the capacitor is another field of research, as we can get the energy from AC or DC sources and with different amplitudes. When high DC gain is required, quadratic converters can be used [9, 10], but low modifications on the DC input voltage can bring to large AC output voltage variations, which might require complex control strategies to operate [11]. Practical engineering applications require the system to work with the least amount of measurements possible, but the controllers have to be robust enough to parametric variation, nonmodeled dynamics, and disturbances, so, the system becomes high complex to model, even in a specific application [12, 13]. One of the hardest tasks for the power systems' designer is to

develop a set of component values for interfacing standard or nonstandard nominal system voltages of low and medium voltages with distributed energy resource connection [14, 15]. This paper defines a methodology for connecting an 84-pulse VSC to the grid or load specifying the needed DC voltage for it. As this voltage can be obtained from different sources, we are using the grid with standard or nonstandard values to build the AC-DC converter. The configuration is complemented by a simple buck-boost converter with a limited gain to avoid big voltage variations in the load. The VSC's output is defined by transformers' output and DC input, but we can select the transformers' ratio gain "n" to limit DC gain. Capacitive and inductive component values are chosen to limit the ripple, but by using programmed trajectories for smoothed transitions, the reduction of these components and settling time is granted. DER can be connected as the AC source when its output is AC or as the input to the buck-boost converter when its output is DC without changing the method. Simulations for a big load are included to verify the appropriateness of the proposal.

2. Methodology

This section deals with the voltage characteristics of the three-phase system to be converted to a DC signal using a noncontrolled three-phase full-wave rectifier. After that, the DC signal might need to be adapted in magnitude; for this, we use a buck-boost converter. Then, the DC signal is converted again to a three-phase quasi-sinusoidal signal using an 84-pulse voltage source converter. Lastly, this signal will be connected to the grid if the system is used as a StatCom or to the load if this works in an isolated system. This scheme is presented in Figure 1. This scheme illustrates the kind of converter required to adapt the power signals for feeding a load or give the energy back to the grid. The starting point would be associated to the type of distributed energy resource output voltage available.

In many cases, a single AC-AC converter is preferred over this three part cascaded converter, but the harmonic distortion obtained can be very high, and controlling it might be a hard task, reducing its capacity of use to a specific application. For the sake of simplicity, the variable names used on this section are detailed in Table 1.

2.1. Input AC-DC Converter. On this study, a balanced three-phase system with $v_{3\phi}$ of nominal RMS line voltage is used. For rectifying, it is needed to have a neutral point, so the phase peak voltage can be obtained by $V_m = v_{3\phi} \sqrt{2/3}$. Then, the phase voltage system is described by

$$\begin{aligned} v_a &= V_m \sin(\omega t), \\ v_b &= V_m \sin\left(\omega t - \frac{2\pi}{3}\right), \\ v_c &= V_m \sin\left(\omega t + \frac{2\pi}{3}\right). \end{aligned} \quad (1)$$

When this system is feeding a three-phase full wave rectifier for obtaining a DC signal, the average value V_{mean} and the root mean square V_{RMS} can be calculated by

$$V_{\text{mean}} = \frac{6}{\pi} \int_0^{\pi/6} (v_c - v_b) dt, \quad (2)$$

$$V_{\text{RMS}} = \sqrt{\left(\frac{6}{\pi} \int_0^{\pi/6} (v_c - v_b)^2 dt\right)}. \quad (3)$$

With these two values, it is possible to know the ripple factor (RF) on the rectified signal. This is a measure of how far is a DC signal from a constant value. This is obtained by

$$\text{RF} = \frac{\sqrt{V_{\text{RMS}}^2 - V_{\text{mean}}^2}}{V_{\text{mean}}}. \quad (4)$$

The lower RF on the output would bring better results in the DC-DC conversion, or it can be used to calculate a passive input filter.

When we manage control tasks for alternating currents, the usage of nonvarying signals reduces the computational effort, so it is important to use signals that are pure DC, and we can utilize the module of the three signals, defined by (5), as the reference:

$$V_{\text{module}} = \sqrt{v_a^2 + v_b^2 + v_c^2}. \quad (5)$$

Consider a balanced system, $V_{\text{module}} = V_m \sqrt{3/2}$, which is equal to the value of line voltage $v_{3\phi}$.

2.2. Output DC-AC Converter. When using an 84-pulse voltage source converter for obtaining the AC signal from the DC signal, we get the peak value of the three-phase staircase sinusoidal \vec{V}_m when the YY converter is at its maximum value, but $Y\Delta$ is at its minimum on the diagram of Figure 2.

Considering the converter structure defined in [5] and references therein,

$$\vec{V}_m = \frac{2n}{3} [2V_{\text{DC}} + a(3V_{\text{DC}})] + \frac{n}{\sqrt{3}} [2V_{\text{DC}} - a(3V_{\text{DC}})]. \quad (6)$$

This equation shows $(2n/3)$ as the gain of the six pulses YY transformers, $(n/\sqrt{3})$ as the gain of the $Y\Delta$ transformers, $(3V_{\text{DC}})$ as the amplitude of the seven-level inverter, $2V_{\text{DC}}$ is the central point or offset for the seven-level inverter, and a is the reinjection transformer ratio. The factor n is included in the case; we need to change the voltage output level in a fixed amount on the output transformers or add a coupling transformer with an integer transformer ratio. The factor $a = 0.5609$ is the optimized value to minimize the voltage THD, being according to IEEE Recommended Practice and Requirements for Harmonic Control in Electric Power Systems [16]. A strict reinjection transformer turns' ratio a is not obligated, as this factor can have 12.5% of variation to have a

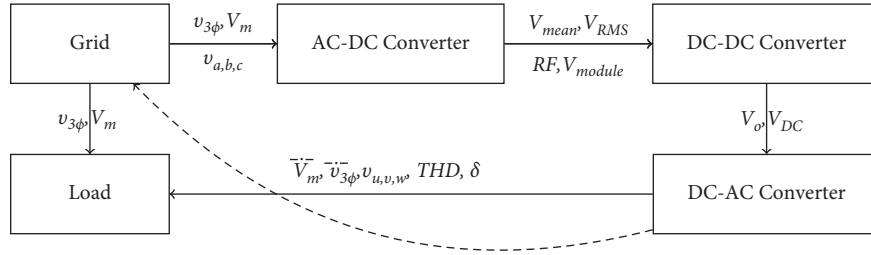


FIGURE 1: Block diagram of the proposal with variable names.

TABLE 1: Acronyms and abbreviations.

Parameters	Description	Unit
$v_{3\phi}$	Input grid RMS line to line voltage	V
V_m	Input grid phase voltage amplitude	V
$v_{a,b,c}$	Input grid phase voltage	V
V_{mean}	Full wave rectified average voltage	V
V_{RMS}	Full wave rectified RMS voltage	V
RF	Ripple on the rectified DC output	%
V_{module}	DC equivalent of a three-phase input voltage	V
V_{DC}	DC capacitor voltage for 7-level inverter	V
V_o	Capacitor chain voltage ($4V_{DC}$)	V
\bar{V}_m	Output VSC phase peak voltage amplitude	V
$\bar{v}_{3\phi}$	Output VSC RMS line to line voltage	V
a	Optimized reinjection transformer ratio	None
n	Integer factor for adjusting output transformers ratio	None
$v_{u,v,w}$	Output VSC phase voltage	V
v_{u_1,v_1,w_1}	Output VSC fundamental frequency phase voltage	V
δ	Phase shift among $v_{3\phi}$ and $v_{3\phi}^{0.0}$	rad
THD	Per phase output voltage total harmonic distortion	%

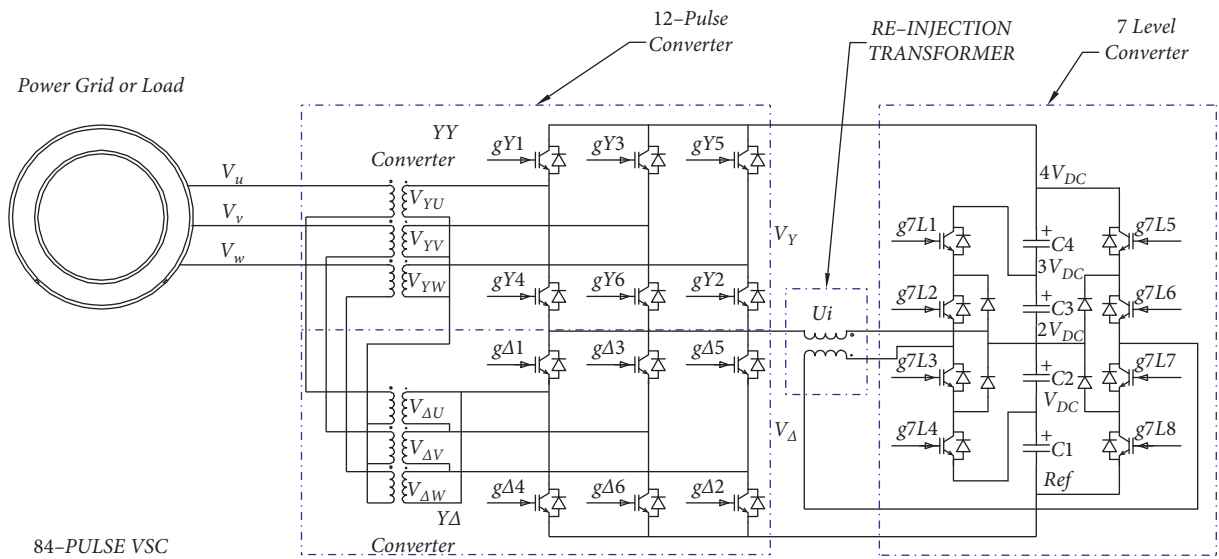


FIGURE 2: 84-pulse voltage source converter.

maximum THD lower than 3% when DC sources are used for the staircase signal generation [4].

The VSC phase voltage v_u can be calculated using the Fourier series of the staircase signal obtained at the VSC's

output [4], which is related to the VSC phase peak voltage amplitude $\dot{\bar{V}}_m$ by the following expression:

$$v_u = \sum_{m=1}^{\infty} V_{u(2m-1)} \sin((2m-1)\omega t),$$

$$V_{u(2m-1)} = \frac{4\dot{\bar{V}}_m}{3\pi(2m-1)} (A_{(2m-1)} + aB_{(2m-1)}),$$

$$A_{(2m-1)} = 2 + 2 \cos\left(\frac{1}{3}\pi(2m-1)\right) + 2\sqrt{3} \cos\left(\frac{1}{6}\pi(2m-1)\right),$$

$$B_{(2m-1)} = \sum_{i=0}^{20} C_i \cos\left(\frac{i}{42}\pi(2m-1)\right),$$

$$C_i = \left\{ \begin{array}{cccccccc} -3, & 1, & 1, & 1, & 1, & 1, & 1, & 1, \dots \\ -3\sqrt{3}, & \sqrt{3}-1, & \sqrt{3}-1, & \sqrt{3}-1, & \sqrt{3}-1, & \sqrt{3}-1, & \sqrt{3}-1, & \dots \\ -3, & -\sqrt{3}+2, & -\sqrt{3}+2, & -\sqrt{3}+2, & -\sqrt{3}+2, & -\sqrt{3}+2, & -\sqrt{3}+2, & \dots \end{array} \right\}.$$

In a similar way, v_v and v_w are obtained with a phase shift of $-2\pi/3$ rad and $2\pi/3$ rad, respectively. Figure 3 depicts the 84-pulse output used with this strategy.

The expected RMS line voltage for the VSC staircase signal to be connected to the point of common coupling (PCC) is

$$\dot{\bar{V}}_{3\phi} = \frac{2\sqrt{2}nV_{DC}\sqrt{-3\sqrt{3}a^2 + 6a^2 + 3\sqrt{3} + 6}}{3}, \quad (8)$$

where V_{DC} is the DC voltage of one capacitor or source of the ones connected in chain on the 7-level inverter, that is, the first part of the 84-pulse converter of Figure 2, and can be obtained with the next expression:

$$V_{DC} = \frac{\dot{\bar{V}}_{3\phi}}{2\sqrt{2}n\sqrt{-3\sqrt{3}a^2 + 6a^2 + 3\sqrt{3} + 6}}. \quad (9)$$

In a natural way, it can be noticed that it is needed to match the input voltage from the grid to the output voltage of the VSC affected by a gain. This gain can be obtained by a DC-DC converter that will be analyzed in Section 2.3, but it can drift the system to obtain a high DC gain. If we do not want to increase the DC components, we can take advantage of the transformers used on the VSC's output by modifying the transformer ratio by the factor $\{n, \}$ which can be obtained by

$$\text{ratio} = \frac{\dot{\bar{V}}_{3\phi}}{v_{3\phi}},$$

$$n = \begin{cases} 1 & \text{for } m = 1 \\ r - 1 & \text{for (ratio) } < 0.5 \\ r & \text{otherwise} \end{cases} \quad (10)$$

In this equation, "r" is the greatest integer less than or equal to "ratio."

The total harmonic distortion (THD) indicates how far is the shape of the generated staircase signal $v_{u,v,w}$, from a pure sinusoidal signal with the grid fundamental frequency. It can be computed by adding all the RMS ratios from single harmonic to the fundamental frequency signal or using the simplified version illustrated in (11), which is utilized for the data presented in this paper:

$$\text{THD} = \sqrt{\left(\frac{v_u}{v_{u_1}}\right)^2 - 1}, \quad (11)$$

where v_u represents the output VSC phase voltage and v_{u_1} is the output VSC fundamental frequency phase voltage.

2.3. DC-DC Converter Design. It is important to verify the input and output voltage levels to define the type of the DC-DC converter to be used. A great deal of converters to adapt

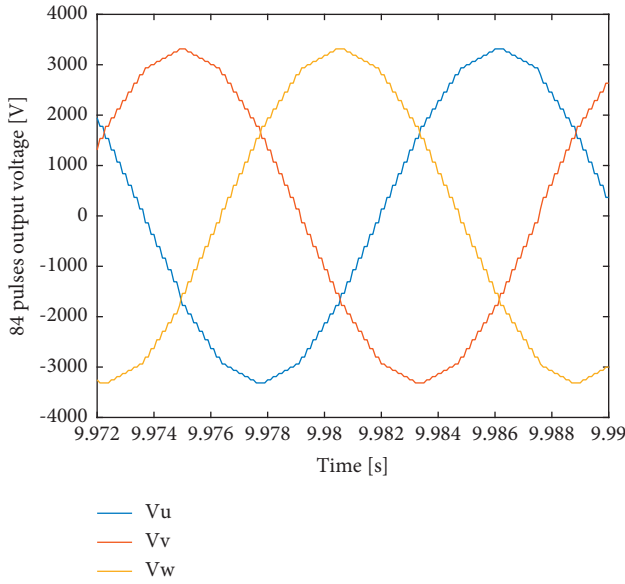


FIGURE 3: 84-pulse output voltage.

the DC voltage levels are available in the literature; many of them are encouraged to bring a high gain and are considered to step-up the voltage, but not all of them have the ability to step-down it. Among the ones with both attributes, Divya Navamani et al. [9] combine quadratic boosting with a multiplier cell, while Zhang et al. [10] merge one boost converter, one buck-boost converter, and one buck converter having a quadratic gain. In comparison, Hasanpour et al. [17] use a buck-boost converter along with a coupled inductor for increasing the voltage gain. As we are dealing with a rectified signal, we use V_{mean} (2) as input. The 7-level converter of Figure 2 goes up to $4V_{\text{DC}}$, so we use this voltage as the output V_o of the converter. This work deals with the combination of one buck and one boost converter on their basic configuration connected in cascade to increase the dynamic range conversion and be able to reduce or increase the output using a simple configuration, as depicted in Figure 4.

The switch S_1 , diode D_1 , and inductor L in the dashed box constitute the first part of the converter, forming a buck converter, while the second part, that is also the inductor L , switch S_2 , and diode D_2 in the dotted box, is forming the boost converter.

In order to design this DC to DC converter, it is needed to know the parameters and variables of the system where it will be immersed. Considering a balanced system, the power needed for the load will be generated in a balanced way, so the base impedance can be calculated from (12) as

$$Z_B = \frac{(v_{3\phi}(\text{line}))^2}{P_{3\phi}}. \quad (12)$$

This impedance is used for the capacitive and inductive component calculation.

The gain of these buck and boost converters considering continuous conduction mode (CCM) can be obtained by (13) and (14), respectively:

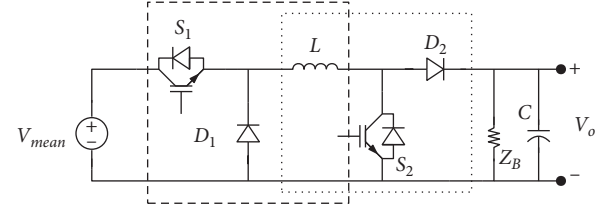


FIGURE 4: Positive output buck-boost converter.

$$\frac{V_o'}{V_{\text{mean}}} = D, \quad (13)$$

$$\frac{V_o}{V_o'} = \frac{1}{1-D}, \quad (14)$$

where D is the duty cycle of the switches. It is important to remember that the output voltage of the DC-DC converter will split to the four capacitors of the seven-level inverter of the 84-pulse voltage source converter, so $V_o = 4V_{\text{DC}}$. As both converters are connected in a cascaded way, using the expected interfacing gain, the equation that dominates the ratio output/input is

$$\frac{V_o}{V_{\text{mean}}} = \frac{D}{1-D}, \quad (15)$$

where $V_o = 4V_{\text{DC}}$ is the converter output voltage and V_{mean} is the source voltage. It is important to notice from (15) that when D is lower than 50%, the converter is functioning as a buck, with a transfer ratio close to a linear function; with $D = 50\%$, the output is equal to the input, and for larger values of D , the converter has a boost behavior, but it becomes highly nonlinear when D is larger than 70%, as depicted in Figure 5. For keeping the conversion ratio within the most linear part of the graphic, the proposal is to have $(1/3) < D < (2/3)$, which bonds the ratio output/input to $(1/2) < (V_o/V_{\text{mean}}) < 2$. If a higher ratio is expected, we will use n on the output transformers of the VSC.

At the moment of writing, there is a wide variation of switching times allowed on the available devices. We have chosen a low switching frequency $f_s = 20\text{KHz}$ in order for this strategy to work with most of the devices. D is the duty cycle defined as the time the switch is closed (t_{on}) in relation to the switching period ($T = (1/f_s)$):

$$D = \frac{t_{\text{on}}}{T}. \quad (16)$$

The controlling variable for the converter output voltage is going to be the duty cycle D , so it is convenient to represent (16) as the voltage transfer function:

$$D = \frac{V_o}{V_{\text{mean}} + V_o}. \quad (17)$$

The size of the capacitive and inductive components is obtained for continuous conduction mode, considering the motor load is requiring the nominal line current and the impedance as three times the the ratio between nominal voltage and current:

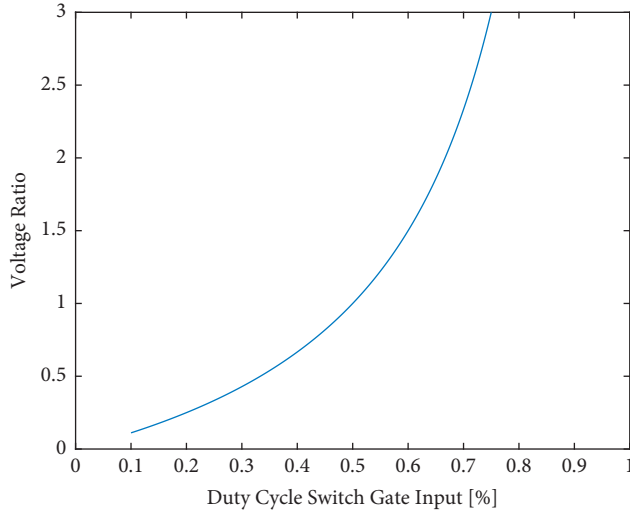


FIGURE 5: Buck-boost voltage ratio.

TABLE 2: Motor and grid parameters.

Parameters	Value	Unit
$P_{3\phi}$	500	HP
$v_{3\phi}$ (line)	2300	V_{RMS}
f_B	60	Hz
$i_{B(a,b,c)}$	93.6	A_{RMS}
from this		
Z_B	14.188	Ω

$$L = \frac{V_{\text{mean}} D}{f_s \Delta I_L}, \quad (18)$$

$$C = \frac{V_o D}{Z_B f_s \Delta V_C}.$$

On (18), ΔI_L and ΔV_C are the allowable variations on the inductor current and voltage capacitor and are selected as 1% of the nominal current and 1% of the rated voltage at the steady state.

3. Simulation Results

The proposed methodology is suitable to be used by DC or AC sources to be connected to AC grid or load. In order to test it, this paper uses a 500 HP, 2300 V_{RMS} , 60 Hz, three-phase induction motor as a load, and three-phase AC grid inputs of several levels. If the input was DC, the strategy would initiate from V_{mean} and follow the same steps. Base power and base voltage are selected, and all parameters and variables are normalized using these base quantities [18]. The main motor parameters for connection to the grid are described in Table 2 [5, 18]. Three different ways to feed the motor for free acceleration are described in the following sections.

3.1. Case 1: Free Acceleration and $n = 1$. Several standard and nonstandard nominal system input voltages are selected for this study [14, 15] and concentrated in Table 3 for easier reading. These voltages include 690 V_{RMS} used as the output voltage by the largest wind turbine manufacturers and utilized as $v_{3\phi}$ (V) on this proposal [19] and 900 V_{DC} as the output voltage for a photovoltaic system used as V_{mean} (V) which is normally used when power exceeds 10 kW [20]. Values of L and C are obtained according to Section 2.3, and THD is obtained using (11) after 10 seconds. As it is illustrated on this table, THD has no variations when $n = 1$.

The free acceleration plot for these cases is depicted in Figure 6. A faster response is observed when the ratio $(\bar{v}_{3\phi}/v_{3\phi}) \rightarrow 1$.

As illustrated in voltage profile (Figure 7), the behavior of the whole system is a second-order under damped system with base impedance Z_B constant, and components L and C change to have faster settling time. Again, the response is faster when the ratio $(\bar{v}_{3\phi}/v_{3\phi}) \rightarrow 1$.

3.2. Case 2: Free Acceleration and n Variant. By limiting the DC gain to $(1/2) < (V_o/V_{\text{mean}}) < 2$ as expressed in Section 2.3, we obtain the results of Table 4, with substantial improvement on the settling time for rotational speed and voltage profile, as observed in Figure 8 for the free acceleration and Figure 9 for the voltage profile. It can be inferred that it is recommended to limit the DC-DC gain. THD is also computed by using (11) after 10 seconds. It is observed that the THD increases when the value of n increases.

3.3. Case 3: Free Acceleration and Bézier Curve. If the VSC is intended to connect a motor, the rotor speed regulation tasks and starting up can be smoothed by using a Bézier curve for the voltage that shows a more convenient transition [21, 22]. The component values are the ones indicated in Table 5. This case presents a voltage trajectory given by

$$v_{a,b,c}^* = \begin{cases} 0 & \text{for } 0 \leq t \leq t_1 \\ v_{a,b,c} \mathfrak{B}_1 & \text{for } t_1 < t < t_2, \\ v_{a,b,c} & \text{for } t \geq t_2 \end{cases} \quad (19)$$

with Bézier curves

$$\mathfrak{B}_j = \sum_{k=1}^6 r_k \left(\frac{t - t_j}{t_{j+1} - t_j} \right)^{4+k}, \quad j = 1, 3, \quad (20)$$

where $r_1 = 252$, $r_2 = -1050$, $r_3 = 1800$, $r_4 = -1575$, $r_5 = 700$, $r_6 = -126$, $t_1 = 0$ s, and $t_2 = 0.5$ s.

The settling time for rotational speed and voltage profile is reduced, making the system faster. As it is illustrated in Table 5, THD increases as n increases. If the variation is bounded to 1% on voltage and current for the DC-DC converter, we can even reduce the value of the L and C to an optimum, which will be calculated on a new research. Figure 10 presents the free acceleration response, and Figure 11 is the voltage profile.

TABLE 3: Parameter values for case 1: Δ_{I_L} (1%), Δ_{V_C} (1%), $n = 1$, and $Z_B = 14.19\Omega$.

$v_{3\phi}$ (V)	V_{mean} (V)	$v_{3\phi}^{0-0}$ (V)	L (H)	C (F)	THD (%)
220	297.10	2300	0.0143896	0.000319495	2.43
440	594.21	2300	0.0263209	0.000292203	2.43
600	810.28	2300	0.0337927	0.000275112	2.43
690 (wind turbine)	931.83	2300	0.0376238	0.000266349	2.43
-- (PV array)	900.00	2300	0.0366445	0.000268589	2.43

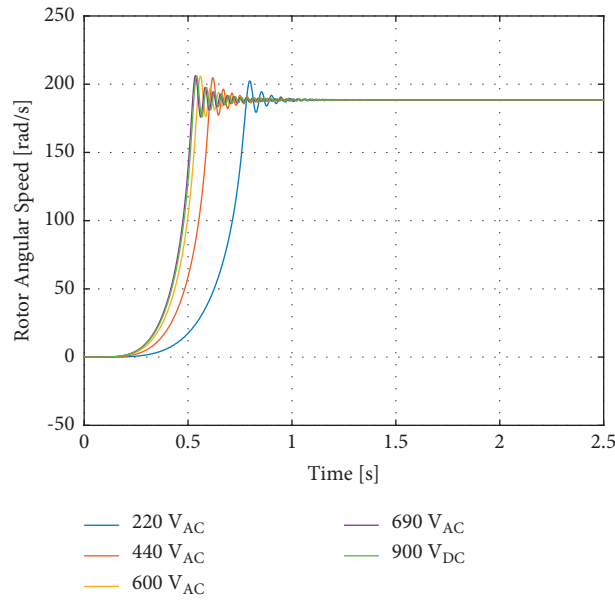


FIGURE 6: Rotational speed $n = 1$ (rad/s).

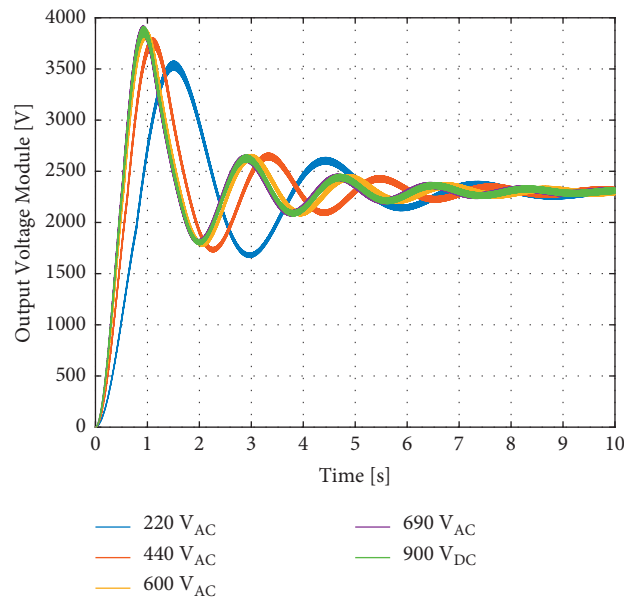


FIGURE 7: Voltage profile $n = 1$ (V).

TABLE 4: Parameter values for case 2: Δ_{I_L} (1%), Δ_{V_C} (1%), and $Z_B = 14.19\Omega$.

n	$v_{3\phi}$ (V)	V_{mean} (V)	$v_{3\phi}^{0-0}$ (V)	$L(H)$	$C(F)$	THD (%)
9	220	297.10	2300	0.000915092	$2.03179e - 05$	6.02
4	440	594.21	2300	0.00435048	$4.82972e - 05$	3.08
2	600	810.28	2300	0.013857	0.000112812	2.48
2	690 (wind turbine)	931.83	2300	0.0151196	0.000107036	2.48
2	-- (PV array)	900.00	2300	0.0148017	0.00010849	2.48

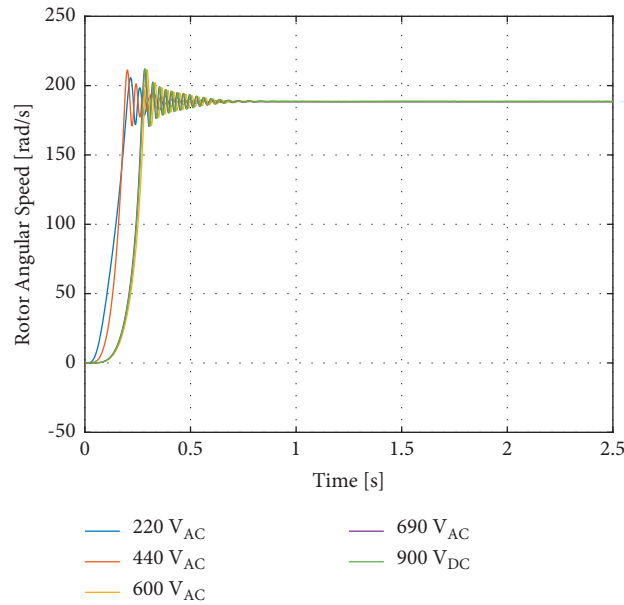


FIGURE 8: Rotational speed n variant (rad/s).

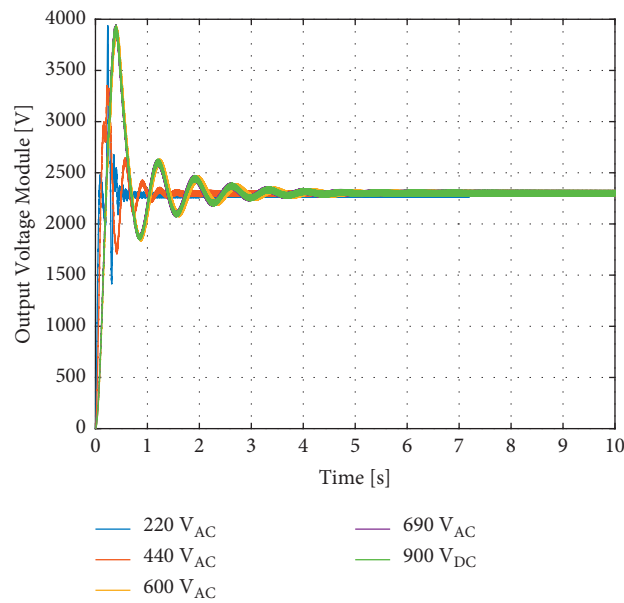


FIGURE 9: Voltage profile n variant (V).

TABLE 5: Parameter values for case 3: Δ_{I_L} (1%), Δ_{V_C} (1%), and $Z_B = 14.19\Omega$.

n	$v_{3\phi}$ (V)	V_{mean} (V)	$v^{0.0}_{3\phi}$ (V)	$L(H)$	$C(F)$	THD (%)
9	220	297.10	2300	0.000915092	$2.03179e - 05$	6.01
4	440	594.21	2300	0.00435048	$4.82972e - 05$	3.06
2	600	810.28	2300	0.013857	0.000112812	2.48
2	690 (wind turbine)	931.83	2300	0.0151196	0.000107036	2.48
2	-- (PV array)	900.00	2300	0.0148017	0.00010849	2.48

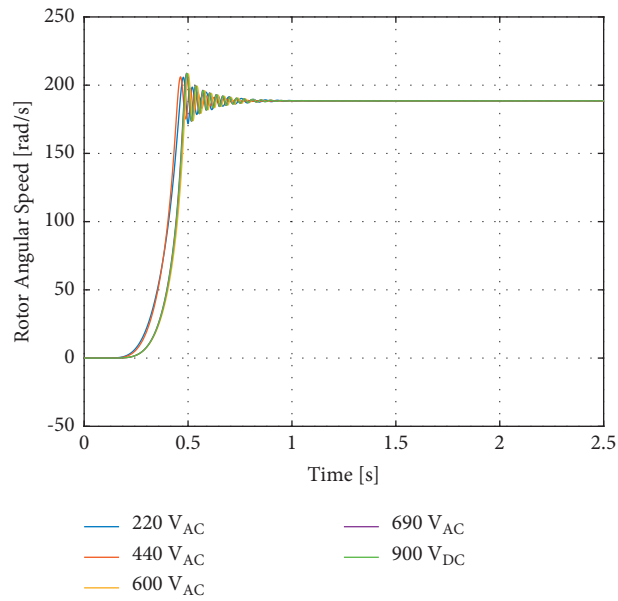


FIGURE 10: Rotational speed n variant and Bézier curve (rad/s).

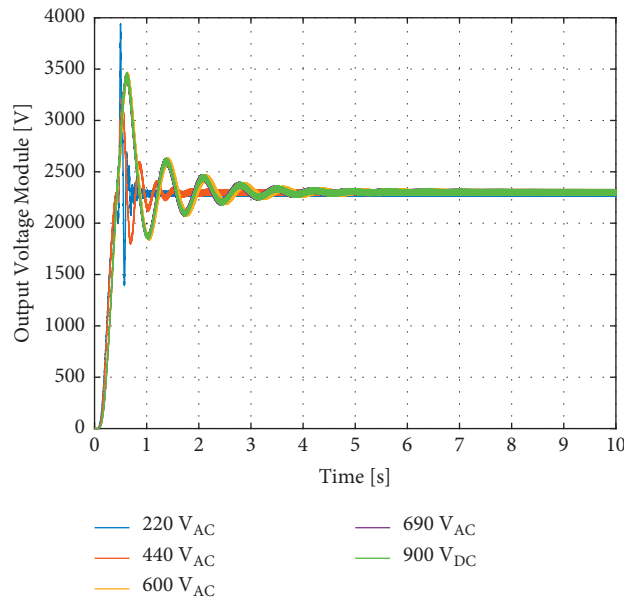


FIGURE 11: Voltage profile n variant and Bézier curve (V).

4. Conclusions

This proposal defines a straightforward methodology for calculating the DC-DC capacitive and inductive component values used for interfacing energy resources of different AC or DC voltage levels by using a VSC of 84 pulses. The strategy can be used also for driving AC motors or improving power quality on three-phase systems. The use of an 84-pulse voltage source converter at the point of common coupling allows to have low-voltage THD to accomplish standard limits. Defining the voltage transfer function in terms of n for the DC-AC converter gives the possibility of reducing the settling time to get the load expected characteristics, such as the speed of an induction motor. On this fashion, using a traditional buck-boost converter with a restricted operating range makes the interfacing between different voltage levels as an easy task. The nominal 1% of variation on the current and voltage for reactive components allows to obtain the initial values for base behavior. Bézier curves for smoothing behavior allow the reduction in the settling time and voltage ripple. As the ripple is reduced, further research will be conducted to reduce the capacitive and inductive components to optimum values and being within operating limits. Classical or modern control strategies for power, speed, or any variable required will be better achievable while using a power electronics interface with performance like the one of this proposal.

Data Availability

The data used to support the findings of this study are included within the article.

Conflicts of Interest

The authors declare that they have no conflicts of interest.

References

- [1] IEEE, *IEEE Recommended Practice for Monitoring Electric Power Quality*, Revision of IEEE Std 1159-2009, 2019.
- [2] IEC, *Electromagnetic Compatibility (EMC)-Part 2-5: Environment-Description and Classification of Electromagnetic Environments*, IEC, *Electromagnetic Compatibility*, 2017.
- [3] IEEE, *IEEE Standard for Interconnection and Interoperability of Distributed Energy Resources with Associated Electric Power Systems Interfaces*, IEEE Std 1547-2018, 2018.
- [4] A. Valderrábano and J. M. Ramirez, "DStatCom regulation by a fuzzy segmented PI controller," *Electric Power Systems Research*, vol. 80, no. 6, pp. 707–715, 2010.
- [5] F. Beltran-Carbajal, R. Tapia-Olvera, A. Valderrábano-Gonzalez, and I. Lopez-Garcia, "Adaptive neuronal induction motor control with an 84-pulse voltage source converter," *Asian Journal of Control*, vol. 23, no. 4, pp. 1603–1616, 2020.
- [6] T. Wu, Y. J. Zhang, and X. Tang, "A VSC-based BESS model for multi-objective OPF using mixed integer SOCP," *IEEE Transactions on Power Systems*, vol. 34, no. 4, pp. 2541–2552, 2019.
- [7] O. B. Adewuyi, R. Shigenobu, K. Ooya, T. Senjyu, and A. M. Howlader, "Static voltage stability improvement with battery energy storage considering optimal control of active and reactive power injection," *Electric Power Systems Research*, vol. 172, pp. 303–312, 2019.
- [8] I. Won, K. Lee, and Y. Cho, "An optimized switching scheme for DC-link current ripple reduction in three-level T-type inverter," in *Proceedings of the 2017 IEEE Applied Power Electronics Conference and Exposition (APEC)*, pp. 3415–3419, Tampa, FL, USA, March 2017.
- [9] J. Divya Navamani, K. Vijayakumar, and R. Jegatheesan, "Non-isolated high gain DC-DC converter by quadratic boost converter and voltage multiplier cell," *Ain Shams Engineering Journal*, vol. 9, no. 4, pp. 1397–1406, 2018.
- [10] N. Zhang, G. Zhang, K. W. See, and B. Zhang, "A single-switch quadratic buck-boost converter with continuous input port current and continuous output port current," *IEEE Transactions on Power Electronics*, vol. 33, no. 5, pp. 4157–4166, 2018.
- [11] A. B. K. Mukkapati, V. Krishnasamy, and R. Kaur, "Genetic algorithm assisted fixed frequency sliding mode controller for quadratic boost converter in fuel cell vehicle," *IET Electrical Systems in Transportation*, vol. 10, no. 1, pp. 81–88, 2020.
- [12] L. Liu, Y. Han, Y. Fang, M. Lin, and N. Shao, "Neural network dynamic surface backstepping control for the speed and tension system of reversible cold strip rolling mill," *Asian Journal of Control*, vol. 20, no. 4, pp. 1452–1463, 2018.
- [13] M. S. Zaky, "Robust chatter-free continuous VSC for the speed control of electrical motor drives using adaptive feedback gain," *Electric Power Systems Research*, vol. 140, pp. 786–796, 2016.
- [14] IEEE, *IEEE Recommended Practice for Electric Power Distribution for Industrial Plants*, IEEE Std 141-1993, 1994.
- [15] N. E. M. Association, *American National Standards Institute (ANSI) C84.1-2006, Voltage Ratings for Electric Power Systems and Equipment*, NEM Association, Rosslyn, VA, USA, 2006.
- [16] IEEE, *IEEE Recommended Practice and Requirements for Harmonic Control in Electric Power Systems*, IEEE Std 519-2014, Revision of IEEE Std 519-1992, 2014.
- [17] S. Hasanpour, A. Baghrmian, and H. Mojallali, "Analysis and modeling of a new coupled-inductor buck-boost DC-DC converter for renewable energy applications," *IEEE Transactions on Power Electronics*, vol. 35, no. 8, pp. 8088–8101, 2020.
- [18] C. Krause, O. Wasynczuk, and D. Sudhoff, *Analysis of Electric Machinery and Drive Systems*, IEEE Press Power Engineering Series, Piscataway, NJ, USA, 2002.
- [19] E. Tzen, "Wind-powered desalination-principles, configurations, design, and implementation," in *Renewable Energy Powered Desalination Handbook*, V. G. Gude, Ed., Butterworth-Heinemann, Oxford, UK, pp. 91–139, 2018.
- [20] A. Sace, *Technical Application Papers No. 10-photovoltaic Plants*, A Division of ABB SpALV Breakers, Zurich, Switzerland, 2010.
- [21] F. Beltran-Carbajal and G. Silva-Navarro, "Generalized nonlinear stiffness identification on controlled mechanical vibrating systems," *Asian Journal of Control*, vol. 21, no. 4, pp. 1–12, 2019.
- [22] M. B. Egerstedt and C. F. Martin, "A note on the connection between bezier curves and linear optimal control," *IEEE Transactions on Automatic Control*, vol. 49, no. 10, pp. 1728–1731, 2004.

Research Article

Algebraic Parameter Identification of Nonlinear Vibrating Systems and Non Linearity Quantification Using the Hilbert Transformation

Luis Gerardo Trujillo-Franco ¹, Gerardo Silva-Navarro ²,
and Francisco Beltran-Carbajal ³

¹Universidad Politecnica de Pachuca, Automotive Mechanical Engineering, Zempoala, Hidalgo, Mexico

²Centro de Investigacion y de Estudios Avanzados del IPN, Departamento de Ingenieria Electrica, Seccion de Mecatronica, Mexico City, Mexico

³Universidad Autónoma Metropolitana, Unidad Azcapotzalco, Departamento de Energía, Mexico City, Mexico

Correspondence should be addressed to Francisco Beltran-Carbajal; fbeltran@azc.uam.mx

Received 19 February 2021; Revised 2 June 2021; Accepted 14 June 2021; Published 23 June 2021

Academic Editor: Libor Pekař

Copyright © 2021 Luis Gerardo Trujillo-Franco et al. This is an open access article distributed under the Creative Commons Attribution License, which permits unrestricted use, distribution, and reproduction in any medium, provided the original work is properly cited.

A novel algebraic scheme for parameters' identification of a class of nonlinear vibrating mechanical systems is introduced. A nonlinearity index based on the Hilbert transformation is applied as an effective criterion to determine whether the system is dominantly linear or nonlinear for a specific operating condition. The online algebraic identification is then performed to compute parameters of mass and damping, as well as linear and nonlinear stiffness. The proposed algebraic parametric identification techniques are based on operational calculus of Mikusiński and differential algebra. In addition, we propose the combination of the introduced algebraic approach with signals approximation via orthogonal functions to get a suitable technique to be applied in embedded systems, as a digital signals' processing routine based on matrix operations. A satisfactory dynamic performance of the proposed approach is proved and validated by experimental case studies to estimate significant parameters on the mechanical systems. The presented online identification approach can be extended to estimate parameters for a wide class of nonlinear oscillating electric systems that can be mathematically modelled by the Duffing equation.

1. Introduction

Accurate fast parameter identification of vibrating mechanical systems constitutes an active research subject. Optimization algorithms, least squares, time series, statistical methods, spectral analysis, Volterra series, wavelets, and orthogonal functions have been used for development of parametric identification techniques [1–3]. In [4], optimization techniques, combined with classic control theory, have been introduced for system parameters' identification, and a special application for parameters' identification for active vibration absorption schemes is reported in [5] where the offline modal analysis are implemented in the presence of noise. A model for linear nonviscous damping and a time-

domain method for the identification of this parameter is proposed in [6]. In the context of nonlinear systems, a black box system identification technique based on co-evolutionary algorithms and neural networks is proposed in [7], and this approach is applied to a magnetorheological damper. As a process, system parameters' identification involves a sequence of systematic stages. The final of those stages involves the application of special tools such as specialized software that features several numerical methods for processing and analyzing the signals obtained from experimental tests applied to mechanical systems under the study. All of these efforts are conducted for achieving the final goal of building a mathematical model for the description of the dynamic behavior of a specific vibrating

mechanical system. Standard mathematical tools for identification purposes are methods used to analyze considerably large amounts of experimental data. As a result of this numerical analysis, the mathematical model of the system dynamics behavior is then built in terms of the determined or identified parameters. Classical mathematical modelling of vibrating systems is commonly based on linear assumptions on their dynamical behavior. In this way, it is possible to use basic and well-behaved approaches such as least squares and autoregressive models [3, 8–10]. Nevertheless, in modern materials and structural engineering, large displacements, geometrical restrictions, and complex behavior are now becoming common in modern mechanical structures resulting on inherent nonlinear phenomena. Hence, despite of numerous advantages of linearity assumptions on mechanical systems, there are cases where linear methods are not longer effective or even valid [3, 11, 12].

Nowadays, evident developments in computing sciences and great capabilities of modern and multitasking microprocessors and microcontrollers [13–15] open the doors to the possibility of applying novel and sophisticated numerical methods, which allow to perform interesting and before unacceptably, complicated online parameters' identification schemes for adaptive control [16]. Thus, complex problems, such as nonlinearities in mechanical systems, as that reported in [17], can be addressed by using mathematical tools, which in the past were purely theoretical and very hard to prove with experimental data, for the practical application of diverse nonlinear systems' identification schemes as the ones reported in [18–20], where the identification of the state equation in nonlinear systems is presented for two interesting simulation cases. These approaches are based on system signals' approximation by determining an analytical function \hat{g} that approximates the actual (unknown) system state equation g , with the form of \hat{g} including suitable basis functions that are relevant to the specific problem. Certainly, there are challenges and limitations in the use of microcontrollers in the context of strict real-time applications, given the inherent nature of their reduced instruction set architecture, called RISC, mainly in quadratic programming applications for optimization. However, in the present work, the use of these advanced digital systems in an algebraic identification scheme is proposed with satisfactory results.

In this work, we present an online algebraic identification method based on the important mathematical tools of Mikusiński's operational calculus, orthogonal functions' signal approximation, and application of Hilbert transforms, to compute the main physical parameters of a vibrating mechanical system, using measurements of its response under the action of exogenous forces. We use Hilbert transforms as an indicator of presence of nonlinearities, by using the properties of this linear transformation as reported in [8, 12]. On the contrary, we apply an algebraic approach to transform a complex calculus problem into an algebraic equation [21] in terms of the parameters to be identified; this equation has an iterated time integral structure, such that we

can take advantage of the orthogonal functions signal approximation in order to make compact and easier to perform iterated integrals [22, 23]. Analytical and experimental results are described to prove the effectiveness of the proposed algebraic scheme for online parameter estimation of the nonlinear vibrating system. The proposed algebraic identification scheme can be directly extended to estimate parameters for a wide class of nonlinear oscillating electric systems that can be mathematically modelled by the Duffing equation [24]. The main contributions of the present work are summarized as follows:

- (i) An algebraic method for online and time-domain identification of parameters for an important class of nonlinear vibrating systems is presented and evaluated in several experimental case studies
- (ii) The proposed algebraic estimation approach requires a small interval of time to provide accurate results
- (iii) Compared to other parameter identification methods, a significant reduction of the amount of data required for the estimation process is an important highlight
- (iv) The approximation of signals by means of orthogonal polynomials, in combination with the algebraic approach, provides robustness and simplifies the computation of iterated integrations

This paper is organized as follows. The class of nonlinear vibrating mechanical system considered for algebraic and online parameters estimation is described in Section 2. In addition, a nonlinearity detection method, based on the Hilbert transformation, is presented. The experimental verification of the proposed identification scheme is described in Section 3, where the performance of the algebraic identification approach is evaluated in two case studies. The nonlinearity detection method described in Section 2 is verified on both of the case studies. A combination of the algebraic estimation technique with the signals approximation using orthogonal polynomials is described in Section 4. The resulting technique represents an alternative to implement estimations of system parameters using buffered signals. Finally, main conclusions of the present study are described in Section 5.

2. Nonlinear Vibrating System

2.1. Mathematical Model of the Nonlinear Vibrating System. Consider the vibrating mechanical system shown in Figure 1. The inherent dynamic behavior of the vibrating mechanical system is determined by the parameters of mass m_i and nonlinear coupling elements that produce the forces F_{si} and F_{di} [22, 24]. Those nonlinear functions of displacements and velocities, x_i and \dot{x}_i , describe the nonlinear stiffness and nonlinear damping effects, respectively, and are defined as follows: where b_i denotes viscous damping and f_{ci} stands for the Coulomb friction coefficient, and the

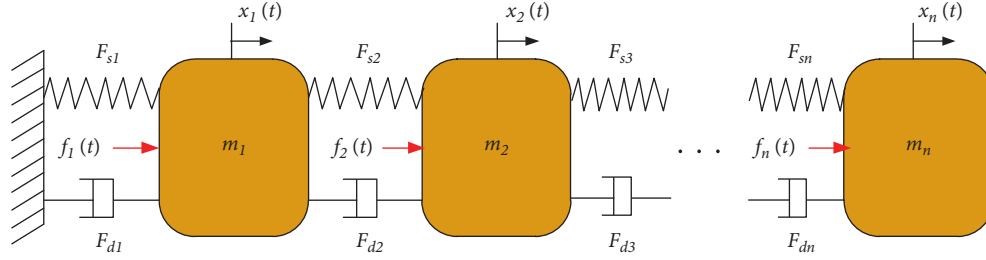


FIGURE 1: Schematic diagram of a general nonlinear mechanical system.

constants k_{ij} , $j = 1, 2, \dots, r$, with r a positive integer, represent polynomial stiffness coefficients. The function $\text{sgn}(\dot{x})$ is defined by

$$\begin{aligned} F_{si} &= k_{i1}(x_i - x_{i-1}) + k_{i2}(x_i - x_{i-1})^2 \\ &\quad + \dots + k_{ir}(x_i - x_{i-1})^r \\ &= \sum_{j=1}^r k_{ij}(x_i - x_{i-1})^j, \end{aligned} \quad (1)$$

$$\begin{aligned} F_{di} &= b_i(\dot{x}_i - \dot{x}_{i-1}) + f_{ci}\text{sgn}(\dot{x}_i), \\ i &= 1, 2, \dots, n, \quad x_0 \equiv 0, \end{aligned}$$

$$\text{sgn}(\dot{x}) = \begin{cases} 1, & \text{if } \dot{x} \geq 0, \\ -1, & \text{if } \dot{x} < 0 \end{cases}. \quad (2)$$

For each degree of freedom associated with the position coordinate x_i , the nonlinear system dynamics can be described by the set of coupled differential equations:

$$\begin{aligned} m_i \ddot{x}_i + F_{si} + F_{di} + b_{i+1}(\dot{x}_i - \dot{x}_{i+1}) \\ - \sum_{j=1}^r k_{i+1j}(x_{i+1} - x_i)^j = f_i, \quad i = 1, 2, \dots, n, \quad x_{n+1} \equiv 0. \end{aligned} \quad (3)$$

Thus, we can express the dynamic behavior of the nonlinear system shown in Figure 1 in the matrix form

$$\mathbf{M}\ddot{\mathbf{x}} + \mathbf{B}\dot{\mathbf{x}} + \mathbf{K}\mathbf{x} + \mathcal{Q}(\mathbf{y}, \dot{\mathbf{x}}) = \mathbf{f}(t), \quad (4)$$

where the vector $\mathbf{x} \in R^n$ denotes the physical displacements of the masses as a function of time t and the relative displacements $\mathbf{y} = [(x_2 - x_1), (x_3 - x_2), \dots, (x_{n+1} - x_n)]^T$, $\mathbf{f} \in R^n$ is an exogenous force vector, and the function $\mathcal{Q}(\mathbf{y}, \dot{\mathbf{x}}) \in R^n$ is a nonlinear restoring force, commonly depending on the displacements and velocities of the n degrees of freedom. The dynamic response of the linear part is determined for the mass, linear damping, and stiffness matrices: $\mathbf{M} \in R^{n \times n}$, $\mathbf{B} \in R^{n \times n}$, and $\mathbf{K} \in R^{n \times n}$. The nonlinear restoring force takes a structure such that

$$\mathcal{Q}(\mathbf{y}, \dot{\mathbf{x}}) = \mathbf{K}_2 \mathbf{y}^2 + \mathbf{K}_3 \mathbf{y}^3 + \dots + \mathbf{K}_r \mathbf{y}^r + \mathbf{F}_c \text{sgn}(\dot{\mathbf{x}}), \quad (5)$$

where $\mathbf{K}_j \in R^{n \times n}$ with $j = 2, 3, \dots, r$ are polynomial stiffness matrices and $\mathbf{F}_c \in R^{n \times n}$ is the Coulomb friction matrix. Equation (5) implies a piecewise operation such that $\mathbf{y}^r = [(x_2 - x_1)^r, (x_3 - x_2)^r, \dots, (x_{n+1} - x_n)^r]^T$. Now, it is

important and necessary to have an indicator of how important or dominant are the nonlinear terms over the global dynamic response of the mechanical system. In the next section, we present the application of a mathematical method for determining this influence in terms of a numerical indicator.

2.2. Nonlinearity Detection. There exist numerous methods for determining the influence of nonlinearities present in the system dynamics [12, 25, 26]. When assuming linear behavior on the system, it is possible to use basic approaches such as least squares and autoregressive models for control purposes [3, 27]. Despite of the numerous advantages of the linearity assumption on mechanical systems, there are cases where the linear methods are ineffective or inoperative. It is well known that the use of the Hilbert transform in the analysis of nonlinear systems is a well-founded tool [8, 12]. The Hilbert transform pairs, as described in [8], of an specific frequency response function $F(\omega)$, also known as system FRF, are defined as

$$\text{Re}(F(\omega)) = -\frac{1}{\pi} c p \int_{-\infty}^{\infty} \frac{\text{Im}(F(\omega))}{\omega - \omega_c} d\omega = H\{\text{Im}(F(\omega))\}, \quad (6)$$

$$\text{Im}(F(\omega)) = \frac{1}{\pi} c p \int_{-\infty}^{\infty} \frac{\text{Re}(F(\omega))}{\omega - \omega_c} d\omega = -H\{\text{Re}(F(\omega))\}, \quad (7)$$

where $H\{\}$ denotes the Hilbert transformation operator. The terms $\text{Re}(F(\omega))$ and $\text{Im}(F(\omega))$ denote the real and imaginary part of the complex function $F(\omega)$, respectively. The constant $c p$ denotes the Cauchy principal value of the integral, used by the singularity at $\omega = \omega_c$ into the integrand. Relations defined by (6) and (7) are not valid for nonlinear systems, and, as a consequence, the Hilbert transformation $H\{F(\omega)\}$ results in a distorted version of the original $F(\omega)$. This distortion is then used as a nonlinearity indicator, numerically quantifiable, that determines the level of nonlinear behavior of the system under analysis. The cross correlation coefficient is a numerical index used for this purpose:

$$\eta_{Hi} = \|X_{HF}(0)\|^2, \quad (8)$$

where $\|X_{HF}(0)\|$ is the normalized cross correlation coefficient defined by

$$X_{HF}(\Delta\omega) = \int_{-\infty}^{\infty} H(\omega)F(\omega + \Delta\omega)d\omega, \quad (9)$$

where $F(\omega)$ is the FRF of the system and $H(\omega)$ the Hilbert transform of $F(\omega)$. The numerical value η_{Hi} indicates nonlinearity in the system at a specific input amplitude. In this work, we use this index to study the presence of nonlinearities in the system under analysis, where, for a linear system, the expected value of η_{Hi} is precisely 1. Here, we consider a particular linearity criterion, as reported in [8]. Thus, we can consider a value of $0.9 \leq \eta \leq 1$ for a linearity assumption of the system. Values under 1 are considered as a clear indicative of nonlinear behavior of the system.

Remark 1. There are significant advances and improvements on the application of the Hilbert Transformation for the time-domain identification of the instantaneous frequency and damping ratios [8, 18]. Those developments and tools suggest the use of them for the implementation of linear and nonlinear systems' parameter estimation. However, we consider important to make clear to the reader that we are not using the Hilbert transformation-based methods to identify systems' parameters. We use the Hilbert transformation pairs (7) as a mathematical tool for the quantification of the nonlinear behavior of the system by analyzing its FRF.

3. Experimental Verification

3.1. First Case Study: One-Degree-of-Freedom Nonlinear Vibrating System. The experimental setup shown in Figure 2 is a configuration for a nonlinear vibrating system of one degree of freedom, where its corresponding schematic diagram is also depicted. The mechanical system consists of a mass carriage, attached to a nonlinear spring. The mass carriage has an antifriction ball bearing system, the mass carriage has a (rotary) high-resolution optical encoder to measure its actual position via cable-pulley system, where the effective resolution is 2266 pulses/cm.

The nonlinear spring shown in detail in Figure 3 presents a polynomial restoring behavior $F(\delta) = k_p\delta^3 + k\delta$, which is described by the experimental data chart, also shown in Figure 3. The numeric values of k_p and k were determined by applying a least squares curve fitting method to the experimental data, where their corresponding magnitudes are reported in Table 1.

The degree of freedom under analysis consists of one mass carriage connected to a fixed support by the nonlinear rubber elastic element described before. The mass carriage suspension has antifriction ball bearing systems such that we can neglect the dry friction. The mass carriage has a (rotary) high-resolution optical encoder to measure its actual position $x(t)$ via a cable-pulley system. The nonlinear differential equation that describes this dynamical system is given by

$$m\ddot{x} + b\dot{x} + q(x, \dot{x}) = f(t), \quad (10)$$

with

$$q(x, \dot{x}) = kx + k_p x^3. \quad (11)$$

3.2. Frequency Response Function (FRF) and Nonlinearity Index Calculation. The frequency analysis of the nonlinear mechanical system shown in Figure 4 was conducted by applying a harmonic sinusoidal swept $f(t) = A \sin[\omega(t)t]$, with a constant amplitude of $A = 2.96$ N and a time-varying frequency $\omega(t) = 1.25t$ Hz. The time-domain chart and the corresponding system response to the sinusoidal swept is shown in Figure 5.

The corresponding FRF is reported in Figure 4 where it is possible to observe a clear distortion on the Hilbert transform of the original FRF (on blue) at this particular amplitude of the input force, which is evident in the Argand (Real, Imag) chart, as depicted in Figure 4.

In order to evaluate the effects of the amplitude on the distortion produced by the Hilbert transformation over the original FRF, a set of sinusoidal sweeps, similar with the same frequency range and several different amplitudes were performed to the system. The effect of the amplitude on the nonlinearity index calculated according to equation (8) is reported in Figure 6. It is clear that the nonlinear effects are specially evident at amplitudes bigger than 2 N.

In previous works, time-domain system parameters' identification has been proposed and verified in experiments and numerical simulations [28, 29], which involves the use of operational calculus for the algebraic manipulation of differential equations (see [21]). The proposed identification scheme is robust and effective for both linear and nonlinear systems. In addition, the system parameters are estimated in a time-domain and online fashion by using measurements of the system input and output. In this work, we present experimental results of the evaluation of the algebraic approach on a particular experimental setup with geometric nonlinearities. For synthesis of online and time-domain parameter estimators, equation (10) is multiplied by $(\Delta t)^2 = (t - t_0)^2$ and then integrated by parts with respect to time yielding:

$$\begin{aligned} & m \left[2 \int_{t_0}^{(2)} x - 4 \int_{t_0}^{(2)} (\Delta t)x + (\Delta t)^2 x \right] \\ & + b \left[-2 \int_{t_0}^{(2)} (\Delta t)x + \int_{t_0}^{(2)} (\Delta t)^2 x \right] \\ & + k \int_{t_0}^{(2)} (\Delta t)^2 x + k_p \int_{t_0}^{(2)} (\Delta t)^2 x^3 = \int_{t_0}^{(2)} (\Delta t)^2 f(t), \end{aligned} \quad (12)$$

where $\int_0^{(n)} \phi(t)$ is used to denote iterated time integrals of the form:

$$\int_{t_0}^t \int_{t_0}^{\alpha_1} \dots \int_{t_0}^{\alpha_{n-1}} \phi(\alpha_n) d\alpha_n \dots d\alpha_1. \quad (13)$$

Notice that this expression does not depend on the system initial conditions of any involved function. Here, we have an expression for the system parameters m , b , k , and k_p . Notice that the system parameters appear algebraically in

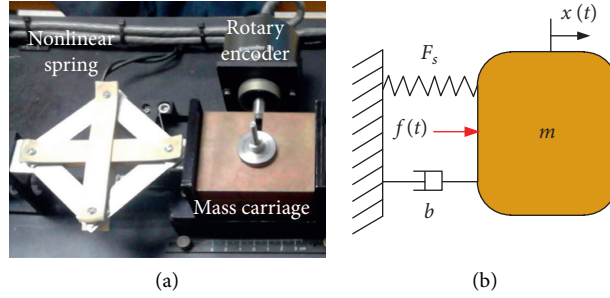


FIGURE 2: One degree-of-freedom nonlinear vibrating mechanical system and its corresponding schematic representation.

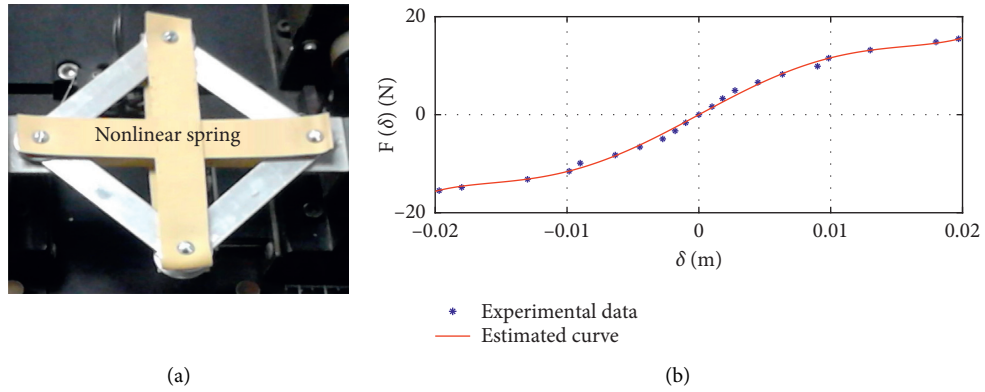


FIGURE 3: Nonlinear spring and its corresponding curve of force.

TABLE 1: System parameters.

Parameters	Value
m	2.53 kg
b	0 Ns/m
k	1272.1 N/m
k_p	-1.237×10^6 N/m ³

equation (12). The identification of the system parameters is achieved by the algebraic manipulation of equation (12) in order to express those parameters by a system of linear equations, whose solution is precisely the set of unknown terms [21, 29]. Hence,

$$\mathbf{A}\theta = \mathbf{D}, \tag{14}$$

where $\theta = [\hat{m}, \hat{b}, \hat{k}, \hat{k}_p]$ is the vector of the estimated parameters, \mathbf{A} and \mathbf{D} are, respectively, 4×4 and 4×1 matrices given by

$$\mathbf{A} = \begin{bmatrix} a_{11} & a_{12} & \dots & a_{14} \\ a_{21} & a_{22} & \dots & a_{24} \\ \vdots & \vdots & \ddots & \vdots \\ a_{41} & a_{42} & \dots & a_{44} \end{bmatrix}, \tag{15}$$

$$\mathbf{D} = \begin{bmatrix} d_1 \\ d_2 \\ \vdots \\ d_4 \end{bmatrix}.$$

The components $a_{i,j}$ and d_i are

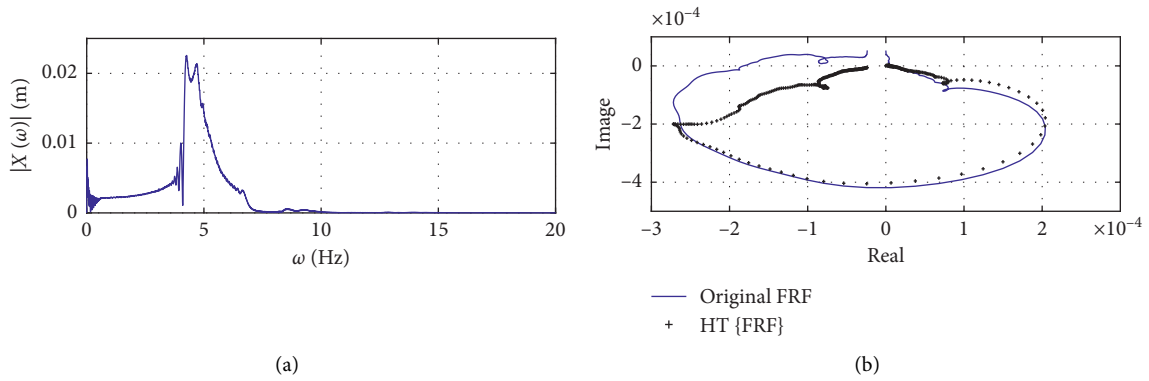


FIGURE 4: FRF of the system and its Hilbert transformation.

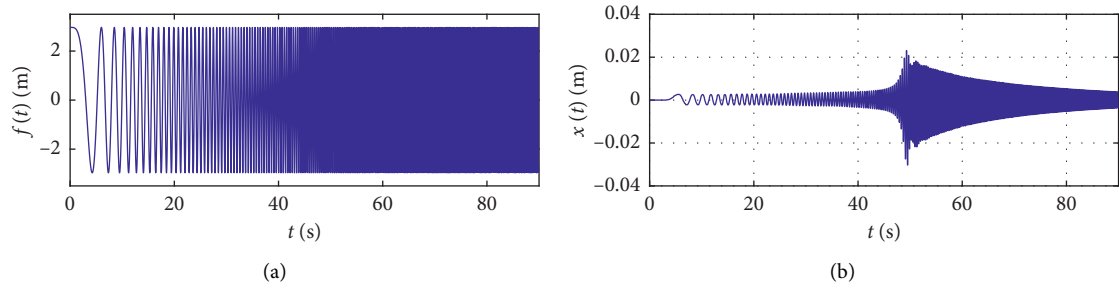


FIGURE 5: System response under sinusoidal swept excitation.

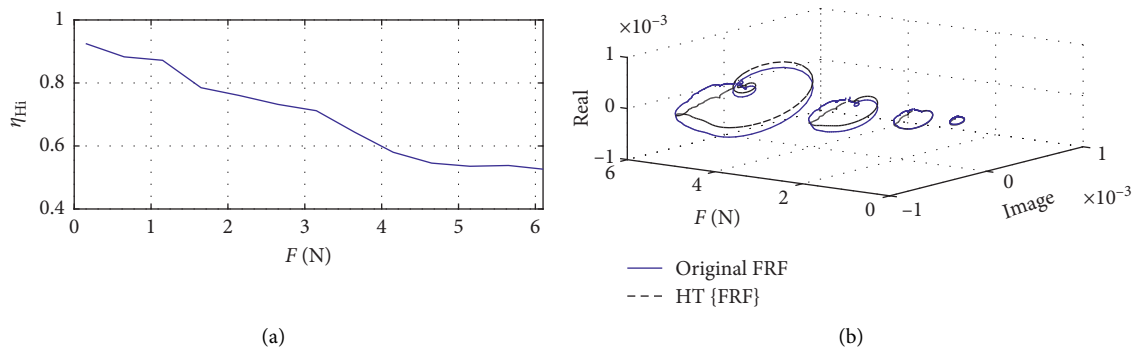


FIGURE 6: Effect of the amplitude on the nonlinearity index.

$$\begin{aligned}
a_{11} &= 2 \int_{t_0}^{(2)} x - 4 \int_{t_0} (\Delta t)x + (\Delta t)^2 x, \\
a_{12} &= -2 \int_{t_0}^{(2)} (\Delta t)x + \int_{t_0} (\Delta t)^2 x, \\
a_{13} &= \int_{t_0}^{(2)} (\Delta t)^2 x, \\
a_{14} &= \int_{t_0}^{(2)} (\Delta t)^2 x^3, \\
d_1 &= \int_{t_0}^{(2)} (\Delta t)^2 f.
\end{aligned} \tag{16}$$

The iterated integrations of equation (16) lead to the rest of the entries or components of the matrices \mathbf{A} and \mathbf{D} as follows:

$$\begin{aligned}
a_{kj} &= \int_{t_0} a_{k-1,j}, \\
d_k &= \int_{t_0} d_{k-1},
\end{aligned} \tag{17}$$

with $k = 2, \dots, 4$ and $j = 1, \dots, 4$. Hence,

$$\theta = (\mathbf{A})^{-1} \mathbf{D} = \frac{1}{\Delta} \begin{bmatrix} \Delta_1 \\ \vdots \\ \Delta_4 \end{bmatrix}. \tag{18}$$

Then, the estimations of the system parameters \hat{m} , \hat{b} , \hat{k} , and \hat{k}_p contained as components of the vector θ can be algebraically computed in some short window of time and without singularities by the estimators:

$$\hat{\theta}[i] = \text{sgn}(\Delta_i) \text{sgn}(\Delta) \frac{\int_{t_0}^{(2)} e^{-\gamma(t-t_0)} |\Delta_i|}{\int_{t_0}^{(2)} e^{-\gamma(t-t_0)} |\Delta|}, \quad i = 1, \dots, 4, \tag{19}$$

where $\gamma \geq 0$ is an invariant filtering and smoothing gain, as used in [29, 30]. Here, $\hat{\cdot}$ denotes estimate and “sgn” is a function defined in 2 which is only used to get the sign of the nonlinear stiffness parameter k_p .

For the experimental verification of the algebraic identification scheme, we use a step excitation force with an amplitude of 14 N and take measurements of the position of the mass carriage at a constant sampling period of 1 ms; both, the position signal $x(t)$ and algebraic identification are obtained through a high-speed DSP board into a standard PC running under Windows 10® and Matlab®/Simulink®. The parameters of the mechanical system are reported in Table 1. The excitation force $f(t)$ and the system response $x(t)$ are shown in Figure 7.

Online estimations of the parameters \hat{m} , \hat{b} , \hat{k} , and \hat{k}_p are shown in Figure 8. Notice that, the effective estimation of the system parameters is achieved in a considerably short period

of time (less than 200 ms). For the case of the estimation of the viscous damping, there is no reference for comparison due to the ineffectiveness of the traditional identification methods when are applied to this particular system.

The comparison and results are summarized in Table 2.

The estimations are practically similar to the actual values. The average values of the real-time estimated parameters are $\hat{m} = 2.55$ kg, $\hat{k} = 1290.34$ N/m, and $\hat{k}_p = -123.7 \times 10^4$ N/m³, which are good approximations to the actual values in spite of inherent unmodelled dynamics and noisy measurements.

3.3. Second Case Study: Two Degrees-of-Freedom Nonlinear Vibrating System. A two-degrees-of-freedom configuration is now shown in Figure 9, where the nonlinear springs have a similar behavior to the one degree of freedom configuration.

The actual system parameters are reported in Table 3. Similarly, small viscous damping was neglected. For the evaluation of the nonlinearity index, based on the Hilbert transformation, we analyze the system response to the sinusoidal swept, where the amplitude F is varied in the closed-time interval [0.1, 6.15] N, with 13 different measurements. In Figure 10, four measurements of the FRF and their corresponding Hilbert transformations in the Argand diagram are reported.

On the contrary, the nonlinearity index as a function of the input force amplitude is described in Figure 11. It can be confirmed that this system certainly exhibits high nonlinearities as far as the force input is increased. The corresponding Nyquist diagrams are shown in the right part of Figure 11. Here, we can observe a clear distortion on the Hilbert transforms for the original FRF (in blue), which is evident when the amplitude of the excitation force achieves a level of approximately 3 N.

We also compute the nonlinearity index based on the Hilbert transform as defined in (8) and (9).

For the case of two degrees of freedom, we can apply the online algebraic identification approach as in the case of the single-degree-of-freedom system with some adaptations that are reported in [29]. First, we can describe the system dynamics by the set of coupled differential equations, when the force applied to the second mass carriage or degree of freedom is zero ($f_2(t) \equiv 0$),

$$\begin{aligned}
m_1 \ddot{x}_1 + b_1 \dot{x}_1 + k_1 x_1 + k_{p1} x_1^3 + b_2 (\dot{x}_1 - \dot{x}_2) \\
+ k_2 (x_1 - x_2) - k_{p2} (x_2 - x_1)^3 = f_1,
\end{aligned} \tag{20}$$

$$\frac{b_2}{m_2} (\dot{x}_2 - \dot{x}_1) + \frac{k_2}{m_2} (x_2 - x_1) + \frac{k_{p2}}{m_2} (x_2 - x_1)^3 = -\ddot{x}_2. \tag{21}$$

For the construction of the online and time-domain estimators, equations (20) and (21) are first multiplied by $(\Delta t)^2 = (t - t_0)^2$ and then integrated by parts twice yielding

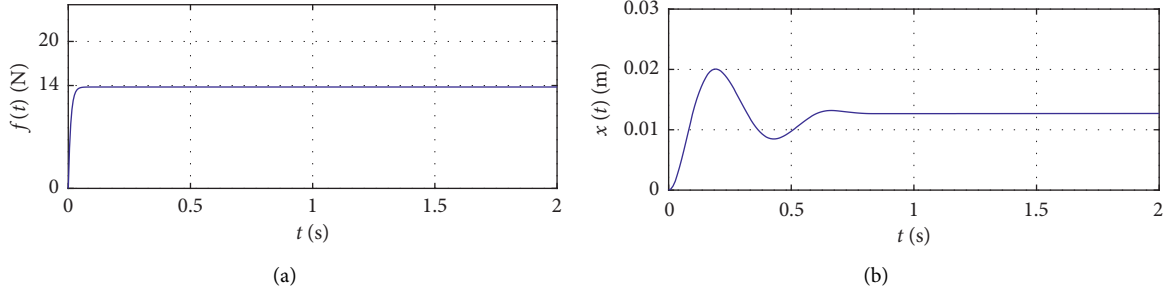


FIGURE 7: System response under step-type excitation: input force and transient response.

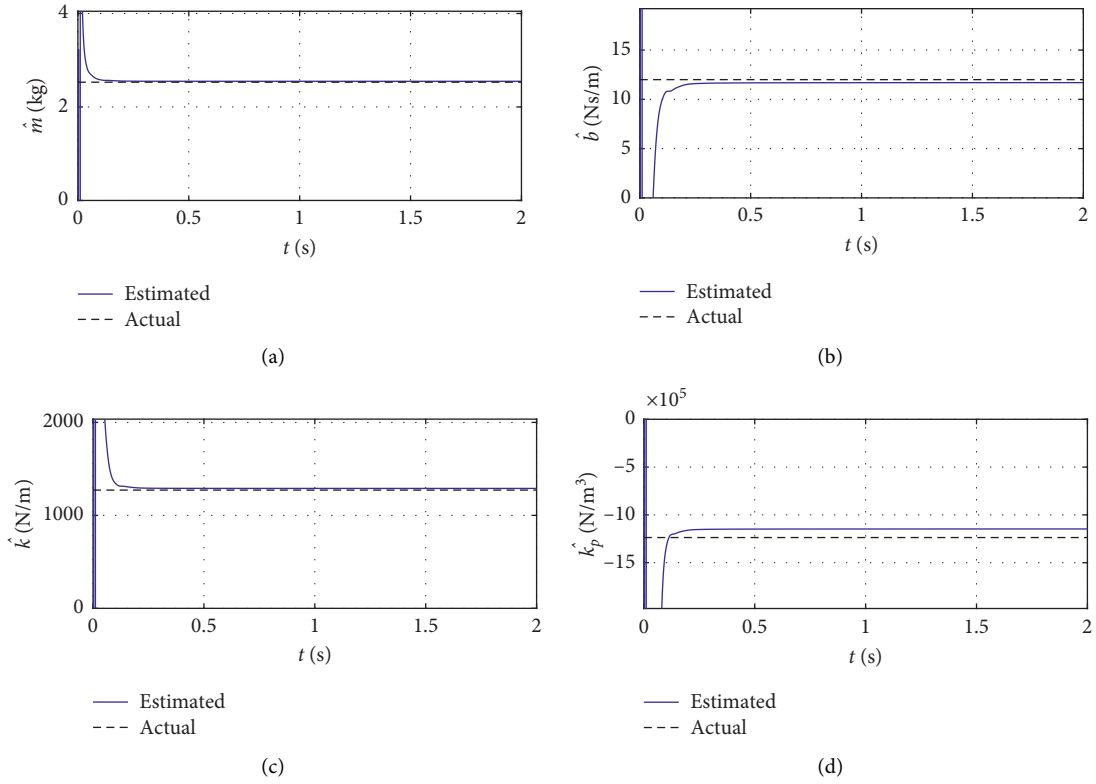


FIGURE 8: Online system parameters' identification.

$$\begin{aligned}
 & m_1 \left[2 \int_{t_0}^{(2)} x_1 - 4 \int_{t_0}^{(2)} (\Delta t) x_1 + (\Delta t)^2 x_1 \right] + b_1 \left[-2 \int_{t_0}^{(2)} (\Delta t) x_1 + \int_{t_0}^{(2)} (\Delta t)^2 x_1 \right] + k_1 \int_{t_0}^{(2)} (\Delta t)^2 x_1 \\
 & + k_{p1} \int_{t_0}^{(2)} (\Delta t)^2 x_1^3 + b_2 \left[-2 \int_{t_0}^{(2)} (\Delta t) (x_1 - x_2) + \int_{t_0}^{(2)} (\Delta t)^2 (x_1 - x_2) \right] + k_2 \int_{t_0}^{(2)} (\Delta t)^2 (x_1 - x_2) \\
 & - k_{p2} \int_{t_0}^{(2)} (\Delta t)^2 (x_2 - x_1)^3 = \int_{t_0}^{(2)} (\Delta t)^2 f_1(t),
 \end{aligned} \tag{22}$$

$$\begin{aligned}
 & \frac{b_2}{m_2} \left[-2 \int_{t_0}^{(2)} (\Delta t) (x_2 - x_1) + \int_{t_0}^{(2)} (\Delta t)^2 (x_2 - x_1) \right] + \frac{k_2}{m_2} \int_{t_0}^{(2)} (\Delta t)^2 (x_2 - x_1) \\
 & + \frac{k_{p2}}{m_2} \int_{t_0}^{(2)} (\Delta t)^2 (x_2 - x_1)^3 = \left[-2 \int_{t_0}^{(2)} x_2 + 4 \int_{t_0}^{(2)} (\Delta t) x_2 - (\Delta t)^2 x_2 \right],
 \end{aligned} \tag{23}$$

TABLE 2: Parameters' estimation summary.

Parameter	Actual	Estimated	Difference (%)
m kg	2.53	2.55	0.79
b Ns/m	—	12.47	—
k N/m	1272.1	1290.34	1.43
k_p Nm ⁻³	-123.7×10^4	-114.83×10^4	7.72

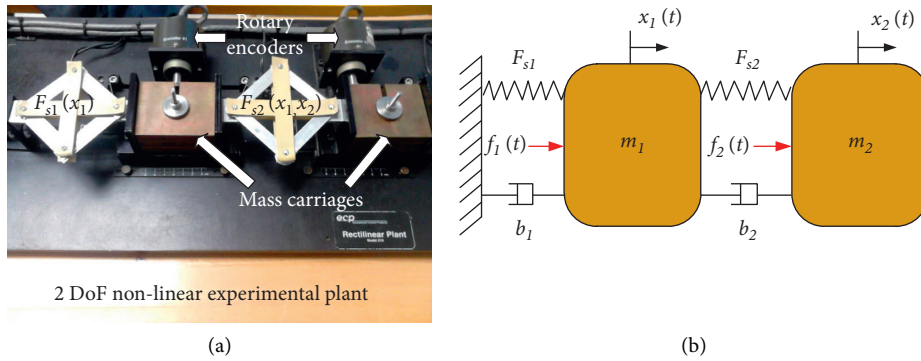


FIGURE 9: Two DOF vibrating mechanical system and its corresponding schematic representation.

TABLE 3: System parameters' 2DOF configuration.

Parameter	First DOF	Second DOF
m	2.35 kg	2.754 kg
b	—	—
k	1272.1 Nm ⁻¹	1570 Nm ⁻¹
k_p	-1.237×10^6 Nm ⁻³	-1.350×10^6 Nm ⁻³

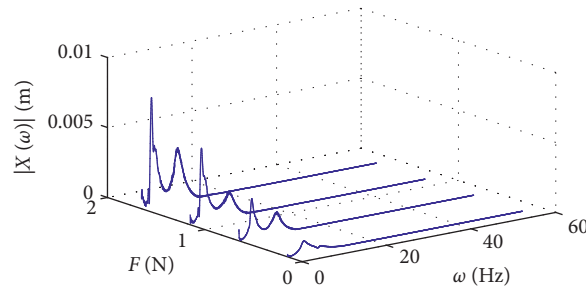


FIGURE 10: Two-degrees-of-freedom case, system FRF at different excitation amplitudes.

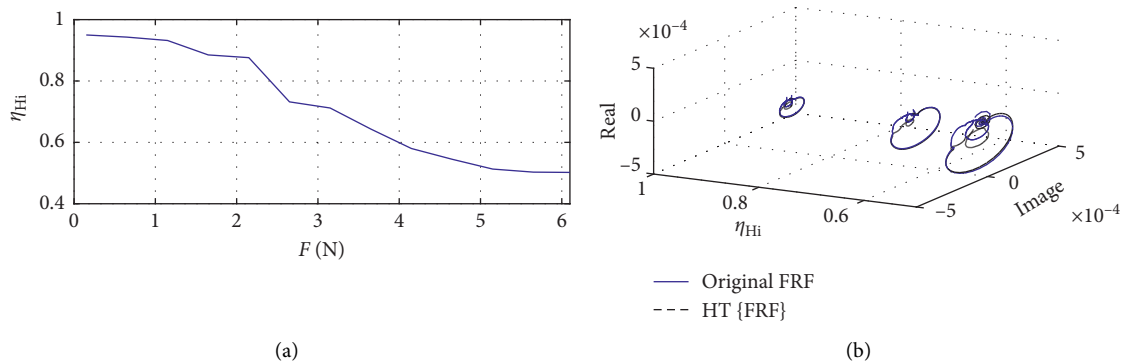


FIGURE 11: Nonlinearity index based on Hilbert transformation and Hilbert transformation of FRF distortion.

where $\int_0^{(n)} \phi(t)$ are iterated integrals such that: $\int_{t_0}^t \int_{t_0}^{\alpha_1} \dots \int_{t_0}^{\alpha_{n-1}} \phi(\alpha_n) d\alpha_n \dots d\alpha_1$, in the same way as the case of one degree of freedom. Here, we have expressions for the system parameters m_1 , b_1 , b_2 , k_1 , k_2 , k_{p1} , and k_{p2} ; these system parameters appear algebraically in equation (22). The identification of the system parameters for the case of two degrees of freedom is done by solving the algebraic equation (14) for each degree of freedom x_1 and x_2 . Hence, the two independent algebraic equations for the system parameter identification are

$$\mathbf{A}_1 \theta_1 = \mathbf{D}_1, \quad (24)$$

$$\mathbf{A}_2 \theta_2 = \mathbf{D}_2, \quad (25)$$

where $\theta_1 = [\widehat{m}_1, \widehat{b}_1, \widehat{k}_1, \widehat{k}_{p1}, \widehat{b}_2, \widehat{k}_2, \widehat{k}_{p2}]$ is the vector of the estimated parameters for the first degree of freedom x_1 and $\theta_2 = [\widehat{b}_2/m_2, \widehat{k}_2/m_2, \widehat{k}_{p2}/m_2]$ corresponds to the second degree of freedom x_2 . Notice that, we cannot obtain the value of m_2 directly because of the zero force applied to the second degree of freedom; however, the value of the parameter m_2 is easily obtained by using the estimations of some of the two parameters calculated with equation (25). The matrices \mathbf{A}_1 , \mathbf{D}_1 , \mathbf{A}_2 , and \mathbf{D}_2 are, respectively, 7×7 , 7×1 , 3×3 , and 3×1 , given by

$$\mathbf{A}_1 = \begin{bmatrix} a_{1(11)} & a_{1(12)} & \dots & a_{1(17)} \\ a_{1(21)} & a_{1(22)} & \dots & a_{1(27)} \\ \vdots & \vdots & \vdots & \vdots \\ a_{1(71)} & a_{1(72)} & \dots & a_{1(77)} \end{bmatrix},$$

$$\mathbf{D}_1 = \begin{bmatrix} d_{1(1)} \\ d_{1(2)} \\ \vdots \\ d_{1(7)} \end{bmatrix}, \quad (26)$$

$$\mathbf{A}_2 = \begin{bmatrix} a_{2(11)} & a_{2(12)} & a_{2(13)} \\ a_{2(21)} & a_{2(22)} & a_{2(23)} \\ a_{2(31)} & a_{2(32)} & a_{2(33)} \end{bmatrix},$$

$$\mathbf{D}_2 = \begin{bmatrix} d_{2(1)} \\ d_{2(2)} \\ d_{2(3)} \end{bmatrix}.$$

The components $a_{1(ij)}$ and $d_{1(i)}$ for the matrix \mathbf{A}_1 are

$$\begin{aligned} a_{1(11)} &= 2 \int_{t_0}^{(2)} x_1 - 4 \int_{t_0} (\Delta t) x_1 + (\Delta t)^2 x_1, \\ a_{1(12)} &= -2 \int_{t_0}^{(2)} (\Delta t) x_1 + \int_{t_0} (\Delta t)^2 x_1, \\ a_{1(13)} &= \int_{t_0}^{(2)} (\Delta t)^2 x_1, \\ a_{1(14)} &= \int_{t_0}^{(2)} (\Delta t)^2 x_1^3, \\ a_{1(15)} &= -2 \int_{t_0}^{(2)} (\Delta t) (x_1 - x_2) + \int_{t_0} (\Delta t)^2 (x_1 - x_2), \\ a_{1(16)} &= \int_{t_0}^{(2)} (\Delta t)^2 (x_1 - x_2), \\ a_{1(17)} &= \int_{t_0}^{(2)} (\Delta t)^2 (x_2 - x_1)^3, \\ d_{1(1)} &= \int_{t_0}^{(2)} (\Delta t)^2 f_1. \end{aligned} \quad (27)$$

The iterated integrations of equation (27) lead to the rest of the entries or components of the matrices \mathbf{A}_1 and \mathbf{D}_1 as follows:

$$\begin{aligned} a_{1(kj)} &= \int_{t_0} a_{1(k-1j)}, \\ d_{1(k)} &= \int_{t_0} d_{1(k-1)}, \end{aligned} \quad (28)$$

with $k = 2, \dots, 7$ and $j = 1, \dots, 7$. Likewise, the components $a_{2(ij)}$ and $d_{2(i)}$ for the matrix \mathbf{A}_2 are

$$\begin{aligned} a_{2(11)} &= -2 \int_{t_0}^{(2)} (\Delta t) (x_2 - x_1) + \int_{t_0} (\Delta t)^2 (x_2 - x_1), \\ a_{2(12)} &= \int_{t_0}^{(2)} (\Delta t)^2 (x_2 - x_1), \\ a_{2(13)} &= \int_{t_0}^{(2)} (\Delta t)^2 (x_2 - x_1)^3, \\ d_{2(1)} &= -2 \int_{t_0}^{(2)} x_2 + 4 \int_{t_0} (\Delta t) x_2 - (\Delta t)^2 x_2. \end{aligned} \quad (29)$$

The iterated integrations of equation (29) lead to the rest of the entries or components of the matrices \mathbf{A}_2 and \mathbf{D}_2 as follows:

$$\begin{aligned} a_{2(kj)} &= \int_{t_0} a_{2(k-1j)}, \\ d_{2(k)} &= \int_{t_0} d_{2(k-1)}, \end{aligned} \quad (30)$$

with $k = 2, 3$ and $j = 1, 2, 3$. Hence, we have two independent algebraic expressions for the identification of the two-degrees-of-freedom nonlinear mechanical system:

$$\begin{aligned} \theta_1 &= (\mathbf{A}_1)^{-1} \mathbf{D}_1 = \frac{1}{\Delta_1} \begin{bmatrix} \Delta_{1(1)} \\ \vdots \\ \Delta_{1(7)} \end{bmatrix}, \\ \theta_2 &= (\mathbf{A}_2)^{-1} \mathbf{D}_2 = \frac{1}{\Delta_2} \begin{bmatrix} \Delta_{2(1)} \\ \Delta_{2(2)} \\ \Delta_{2(3)} \end{bmatrix}. \end{aligned} \quad (31)$$

Then, the estimations of the system parameters $\hat{m}_2, \hat{b}_1, \hat{b}_2, \hat{k}_1, \hat{k}_2, \hat{k}_{p1},$ and \hat{k}_{p2} contained as components of the vectors θ_1 and θ_2 can be algebraically computed into some short window of time and without singularities by the estimators:

$$\hat{\theta}_1 [i] = \text{sgn}(\Delta_{1(i)}) \text{sgn}(\Delta_1) \frac{\int_{t_0}^{(2)} e^{-\gamma(t-t_0)} |\Delta_{1(i)}|}{\int_{t_0}^{(2)} e^{-\gamma(t-t_0)} |\Delta_1|}, \quad i = 1, \dots, 7, \quad (32)$$

$$\hat{\theta}_2 [i] = \text{sgn}(\Delta_{2(i)}) \text{sgn}(\Delta_2) \frac{\int_{t_0}^{(2)} e^{-\gamma(t-t_0)} |\Delta_{2(i)}|}{\int_{t_0}^{(2)} e^{-\gamma(t-t_0)} |\Delta_2|}, \quad i = 1, 2, 3, \quad (33)$$

where $\gamma \geq 0$ is an invariant filtering and smoothing gain. Here, $\hat{\cdot}$ denotes estimate and “sgn” is the function defined in equation (2) which is only used to get the sign of the nonlinear stiffness parameters \hat{k}_{p1} and \hat{k}_{p2} .

For experimental verification of the algebraic identification scheme, we use a step excitation force, applied to the first degree of freedom x_1 with an amplitude of 14 [N] and take measurements of the position of the two mass carriages x_1 and x_2 at a constant sampling period of 1 [ms]; both, the position signals $x_1(t)$ and $x_2(t)$ and the algebraic identification schemes (32) and (33) are obtained through a high-speed DSP board into a standard PC running under Windows 10® and Matlab®/Simulink®. The parameters of the mechanical system are reported in Table 1.

The performance of the algebraic identifiers (32) is shown in Figures 12 and 13. Notice that it takes less than a half of a second to have stable and accurate estimations of the system parameters. For the case of estimator (33), the fast and accurate estimations of the normalized (respect to m_2) parameters are depicted in Figure 13.

The excitation force $f_1(t)$ and the system responses, $x_1(t)$ and $x_2(t)$, are shown in Figure 14.

The results are summarized in Table 4.

4. Combination of Two Identification Techniques

The proposed online algebraic system parameters' identification scheme is suitable to be implemented in complex digital systems based on microprocessors with x86 architecture, such as desktop personal computers and portable computers (laptops) running hard or soft real-time operating systems as verified, shown and proven in the previous sections of this work. Nowadays, it is common to use embedded digital systems that contain a digital signal processors working in conjunction with native peripherals such as analogue-to-digital converters (ADC modules) and direct memory access (DMA) for the complete implementation of the digital system, see [13].

In this section, we propose a combination of two methods for the algebraic identification of the parameters of the nonlinear system studied in this work. We propose the use of the orthogonal functions' signal approximation for the calculation of the iterated integrals involved in the online algebraic identification approach. On the contrary, by combining the technique reported in [22] and the proposed algebraic scheme [29], we have a contribution to the implementation of a system parameters' identification technique designed to be applied on embedded digital systems, completely based on matrix operations compatible with DSP libraries available in 32 bits ARM micro-controllers, see [14, 15]. The flowchart of the process of system parameters' identification, for embedded systems, is depicted in Figure 15.

A set of functions are called orthogonal [22] in the interval $[a, b]$ if they satisfy

$$\begin{aligned} \int_a^b \phi_m(t) \phi_k(t) &= 0, & \text{if } m \neq k, \\ \int_a^b \phi_m(t) \phi_k(t) &= \text{constant} \neq 0, & \text{if } m = k. \end{aligned} \quad (34)$$

It is well known that, in a certain interval, it is possible to approximate a given function by a finite sum of orthogonal functions. Consider the matrix form of the coupled equations (20) and (21) that describe the dynamics of the nonlinear mechanical systems shown in Figure 9:

$$\mathbf{M}\ddot{\mathbf{x}} + \mathbf{B}\dot{\mathbf{x}} + \mathbf{K}\mathbf{x} + \mathbf{K}_p\mathbf{y}^3 = \mathbf{f}, \quad (35)$$

where $\mathbf{M} \in R^{2 \times 2}$, $\mathbf{B} \in R^{2 \times 2}$, and $\mathbf{K} \in R^{2 \times 2}$ are the mass, damping, and stiffness matrices, $\mathbf{K}_p \in R^{2 \times 2}$ is the nonlinear stiffness matrix, the vector $\mathbf{x} \in R^2$ denotes the physical displacements of the mass carriages, and the vector $\mathbf{y} \in R^2$ is defined as $\mathbf{y} = [(x_2 - x_1), -x_2]^T$, with the vector $\mathbf{y}^3 = [(x_2 - x_1)^3, -x_2^3]^T$. Finally, the exogenous force is represented in this particular experimental plant by the vector $\mathbf{f} \in R^2$ that, in this particular case, is $\mathbf{f} = [f(t) \ 0]$

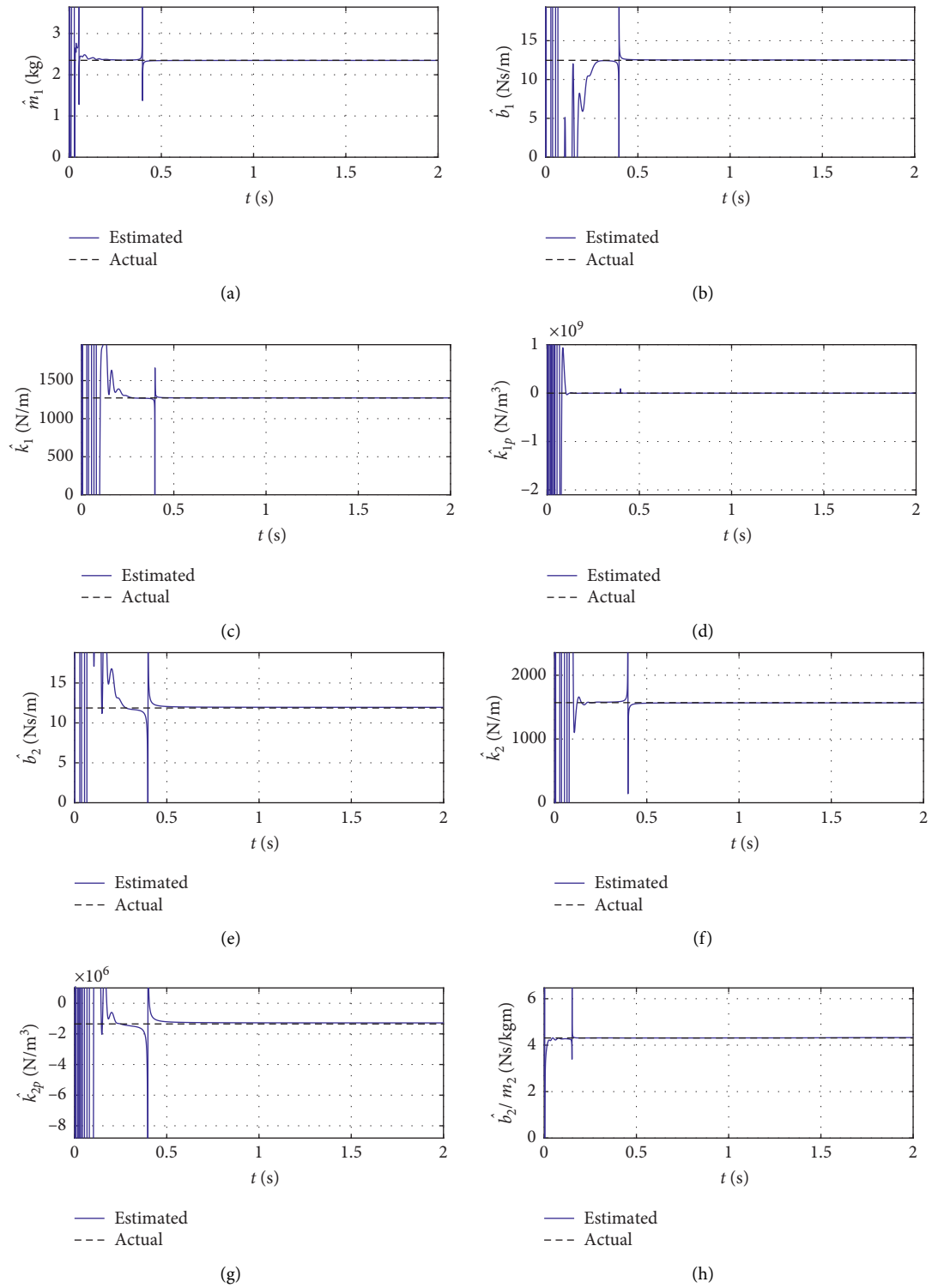


FIGURE 12: Online system parameters' identification 2DOF case.

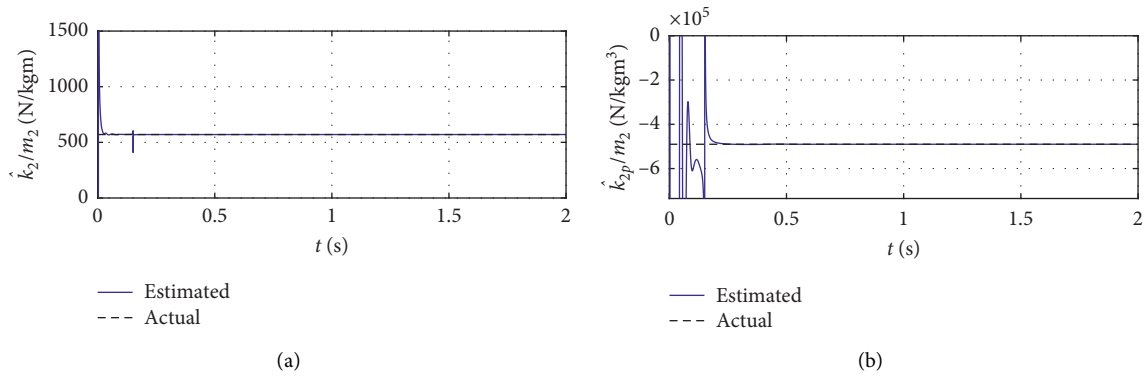


FIGURE 13: Online system parameters' identification 2DOF case, second degree of freedom.

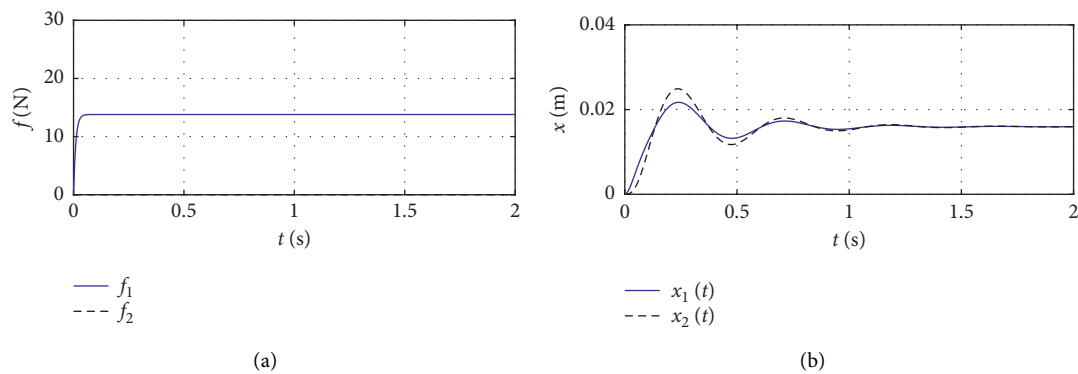


FIGURE 14: Two-degrees-of-freedom case.

TABLE 4: System parameters' estimation for the 2DOF configuration.

Parameters	Actual	Estimated	Difference (%)
m_1	2.53 kg	2.56 kg	1.19
b_1	—	12.48 Nsm ⁻¹	—
k_1	1272.1 Nm ⁻¹	1280.7 Nm ⁻¹	0.6
k_{p1}	-123.7×10^4 Nm ⁻³	-1304.7×10^4 Nm ⁻³	5.4
m_2	2.754 kg	2.80 kg	1.6
b_2	—	11.67 Ns ⁻¹	—
k_2	1570 Nm ⁻¹	1585 Nm ⁻¹	0.9
k_{p2}	-135.0×10^4 Nm ⁻³	-144.8×10^4 Nm ⁻³	7.2

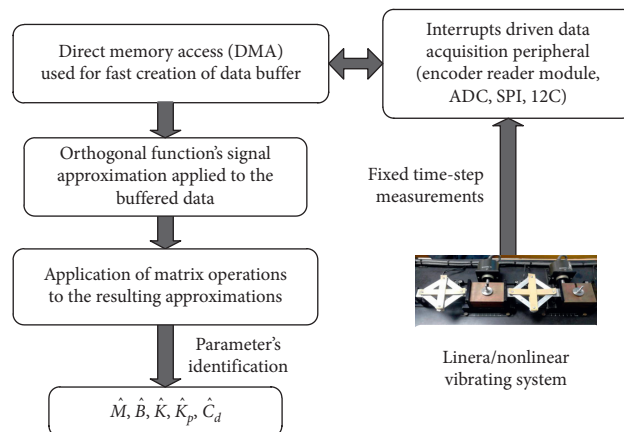


FIGURE 15: Flowchart of the combination of techniques as a buffered parameters' identification scheme.

TABLE 5: System parameters' estimation, using orthogonal functions' signal approximation.

Term	Estimated
$\bar{\mathbf{M}}$	$\begin{bmatrix} 2.57 & 0 \\ 0 & 2.75 \end{bmatrix}$
$\bar{\mathbf{B}}$	$\begin{bmatrix} 24.19 & -11.82 \\ -4.64 & 4.72 \end{bmatrix}$
$\bar{\mathbf{K}}$	$\begin{bmatrix} 2848.7 & -1575.2 \\ -571.96 & -576.4 \end{bmatrix}$
$\bar{\mathbf{K}}_p$	$1 \times 10^6 \begin{bmatrix} -1.23 & 1.355 \\ 0 & -0.51 \end{bmatrix}$

because the second degree of freedom is not actuated as described before. By dividing the second row of equation (36) by m_2 , one obtains

$$\bar{\mathbf{M}}\ddot{\mathbf{x}} + \bar{\mathbf{B}}\dot{\mathbf{x}} + \bar{\mathbf{K}}\mathbf{x} + \bar{\mathbf{K}}_p\mathbf{y}^3 = \bar{\mathbf{f}}, \quad (36)$$

where

$$\begin{aligned} \bar{\mathbf{M}} &= \begin{bmatrix} m_1 & 0 \\ 0 & 1 \end{bmatrix}, \\ \bar{\mathbf{B}} &= \begin{bmatrix} b_1 + b_2 & -b_2 \\ -\frac{b_2}{m_2} & \frac{b_2}{m_2} \end{bmatrix}, \\ \bar{\mathbf{K}} &= \begin{bmatrix} k_1 + k_2 & -k_2 \\ -\frac{k_2}{m_2} & \frac{k_2}{m_2} \end{bmatrix}, \\ \bar{\mathbf{K}}_p &= \begin{bmatrix} k_{p1} & -k_{p2} \\ 0 & \frac{k_{p2}}{m_2} \end{bmatrix}, \\ \bar{\mathbf{f}} &= \begin{bmatrix} f(t) \\ -\ddot{x}_2 \end{bmatrix}. \end{aligned} \quad (37)$$

Similarly, for the construction of the identifiers, by multiplying equation (37) by $(\Delta t)^2 = (t - t_0)^2$ and integrating it by parts two times, we have

$$\begin{aligned} &\bar{\mathbf{M}} \left[2 \int_{t_0}^{(2)} \mathbf{x} - 4 \int_{t_0} (\Delta t)\mathbf{x} + (\Delta t)^2\mathbf{x} \right] \\ &+ \bar{\mathbf{B}} \left[-2 \int_{t_0}^{(2)} (\Delta t)\mathbf{x} + \int_{t_0} (\Delta t)^2\mathbf{x} \right] \\ &+ \bar{\mathbf{K}} \int_{t_0}^{(2)} (\Delta t)^2\mathbf{x} + \bar{\mathbf{K}}_p \int_{t_0}^{(2)} (\Delta t)^2\mathbf{y}^3 = \int_{t_0}^{(2)} (\Delta t)^2\bar{\mathbf{f}}. \end{aligned} \quad (38)$$

The orthogonal functions approximation of the integrands of equation (38), in the corresponding matrix

representation by a sum of r orthogonal functions, is then given by

$$\begin{aligned} \Delta t^p \mathbf{x} &\cong \mathbf{X}_{p,(1,r)} \phi(t)_{(1,r)}, \\ \Delta t^2 \bar{\mathbf{f}} &\cong \mathbf{F}_{(1,r)} \phi(t)_{(1,r)}, \\ \Delta t^2 \mathbf{y}^3 &\cong \mathbf{Y}_{3,(1,r)} \phi(t)_{(1,r)}, \end{aligned} \quad (39)$$

where $p = 0, 1, 2$. Here, \mathbf{X} , \mathbf{Y}_3 , and \mathbf{F} are constant vectors with the coefficients of the orthogonal functions approximation of the integrands.

As reported in [22, 23], the orthogonal functions' signal approximation is useful in the solution of integral equations due to the property which allows to compute the iterated numerical integration as defined by the following matrix expression:

$$\int_{t_0}^{(n)} \phi(\tau) d\tau^n \cong \mathbf{P}^n \phi(t), \quad (40)$$

where $\mathbf{P} \in R^{r \times r}$ is the so-called operational matrix of integration with constant elements, whose values depend on the orthogonal basis used. $\phi(t) \in R^r$ is a vector called the vectorial basis of the orthogonal series. In [23], a unified method for the operational matrix of integration computing is reported for the most popular orthogonal functions basis for signal approximation, and therefore, we can compute numerically the iterated integral using this property. The substitution of equations (39) in (38) yields to

$$\begin{aligned} &\bar{\mathbf{M}} [2\mathbf{X}_0\phi(t)\mathbf{P}^2 - 4\mathbf{X}_1\phi(t)\mathbf{P} + \mathbf{X}_2\phi(t)] \\ &+ \bar{\mathbf{B}} [-2\mathbf{X}_1\phi(t)\mathbf{P}^2 + \mathbf{X}_2\phi(t)\mathbf{P}] \\ &+ \bar{\mathbf{K}}\mathbf{X}_2\phi(t)\mathbf{P}^2 + \bar{\mathbf{K}}_p\mathbf{Y}_3\phi(t)\mathbf{P}^2 = \mathbf{F}\phi(t)\mathbf{P}^2. \end{aligned} \quad (41)$$

Since we use a given orthogonal basis $\phi(t)$, we can equate this coefficients so that using equations (39) and (40), we obtain the following matrix equation:

$$\begin{bmatrix} \bar{\mathbf{M}} & \bar{\mathbf{B}} & \bar{\mathbf{K}} & \bar{\mathbf{K}}_p \end{bmatrix} \begin{bmatrix} 2\mathbf{X}_0\mathbf{P}^2 - 4\mathbf{X}_1\mathbf{P} + \mathbf{X}_2 \\ -2\mathbf{X}_1\mathbf{P}^2 + \mathbf{X}_2\mathbf{P} \\ \mathbf{X}_2\mathbf{P}^2 \\ \mathbf{Y}_3\mathbf{P}^2 \end{bmatrix} = \begin{bmatrix} \mathbf{F}\mathbf{P}^2 \end{bmatrix}. \quad (42)$$

Now, let us define

$$\begin{aligned} [\Theta]^T &= [\bar{\mathbf{M}} \bar{\mathbf{B}} \bar{\mathbf{K}} \bar{\mathbf{K}}_p], \\ [\mathbf{A}] &= \begin{bmatrix} 2\mathbf{X}_0\mathbf{P}^2 - 4\mathbf{X}_1\mathbf{P} + \mathbf{X}_2 \\ -2\mathbf{X}_1\mathbf{P}^2 + \mathbf{X}_2\mathbf{P} \\ \mathbf{X}_2\mathbf{P}^2 \\ \mathbf{Y}_3\mathbf{P}^2 \end{bmatrix}, \\ [\mathbf{B}] &= [\mathbf{F}\mathbf{P}^2]. \end{aligned} \quad (43)$$

Thus, in a compact way, we can write

$$[\Theta]^T [\mathbf{A}] = [\mathbf{B}]. \quad (44)$$

This last expression constitutes the algebraic problem from identification, solved by using singular value decomposition, which allows to introduce the concept of

pseudoinverse matrix, in order to solve the algebraic problem for the vector $[\Theta]$ as follows:

$$[\Theta] = [B][A]^T([A][A]^T)^{-1}. \quad (45)$$

The results of the parameters' estimation when the excitation force is $\bar{f} = [14 \ 0]^T [N]$ are reported in Table 5.

5. Conclusions

In the present contribution, a time-domain algebraic scheme for online parameter estimation for an important class of nonlinear vibrating mechanical systems was introduced. Experimental results to prove the effectiveness of the parameter estimation using real-time position measurements were described. The satisfactory online fast estimation of the system parameters, performed in less than a second, was confirmed as well. Hence, results reveal that the algebraic nonlinear parametric estimation constitutes an excellent alternative with a superior performance to conventional identification techniques. Experimental system configurations involving nonlinear stiffness modelled such as algebraic polynomials were presented. The nonlinearity exhibited in experimental configurations was of the geometric type. The algebraic approach can be extended to other type of nonlinearities, such as Coulomb friction, as long as they appear in an algebraic form in the system structure. Moreover, two different identification methods, taking advantage of particular capabilities in both of them, were properly combined. Computationally speaking, we have improved the algebraic approach in structure; that is, iterated time integrations can be computed by using a compact and clear matrix expression, which is quite well defined and robust due to the good structure of the operational matrix of integration in an algebraic sense; the pseudoinverse is always possible to be computed and the results are obtained in finite time and well bounded to mention some of them. However, parameter estimations are performed slower like a price to pay to achieve stability on calculations. Furthermore, the presented nonlinearity indicator is easy to program and test. From this study, it is recommended to make a good analysis of numerical methods applied to original data in order to have a good criterion for the final determination of presence of nonlinearities. We have considered a reasonable value of $\eta \leq 0.9$ to establish that a given vibrating system exhibits relevant nonlinear oscillating dynamics. Otherwise, vibrating system dynamics could be represented in terms of a linear mathematical model, where small parametric nonlinearities can be considered such as unknown disturbances.

Data Availability

The data used to support the findings of the study are available from the corresponding author upon request.

Conflicts of Interest

The authors declare that they have no conflicts of interest.

References

- [1] T. Söderström and P. Stoica, *System Identification*, Prentice-Hall, Hoboken, NJ, USA, 1989.
- [2] L. Ljung, *System Identification: Theory for the User*, Prentice-Hall, Hoboken, NJ, USA, 1987.
- [3] R. Isermann and M. Munchhof, *Identification of Dynamic Systems: An Introduction with Applications*, Springer-Verlag, Berlin, Germany, 2011.
- [4] R. Manikantan, S. Chakraborty, T. K. Uchida, and C. P. Vyasarayani, "Parameter identification in nonlinear mechanical systems with noisy partial state measurement using pid-controller penalty functions," *Mathematics*, vol. 8, pp. 1281–1292, 2020.
- [5] Y. Yi, S. Xing, and H. Yun, "Multidimensional system identification and active vibration control of a piezoelectric based sting system used in wind tunnel," *Shock and Vibration*, vol. 2020, Article ID 8856084, 15 pages, 2020.
- [6] R. Shen, X. Qian, and J. Zhou, "Identification of linear non-viscous damping with different kernel functions in the time domain," *Journal of Sound and Vibration*, vol. 487, Article ID 115623, 2020.
- [7] H. V. H. Ayala, D. Habineza, M. Rakotondrabe, and L. dos Santos Coelho, "Nonlinear black-box system identification through coevolutionary algorithms and radial basis function artificial neural networks," *Applied Soft Computing*, vol. 87, Article ID 105990, 2020.
- [8] M. Feldman, *Hilbert Transform Applications in Mechanical Vibration*, John Wiley & Sons, Chichester, UK, 2011.
- [9] M. Feldman, "Non-linear system vibration analysis using Hilbert transform--I. Free vibration analysis method "Free-vib"" *Mechanical Systems and Signal Processing*, vol. 8, no. 2, pp. 119–127, 1994.
- [10] G. Golub and C. V. Loan, "An analysis of the total least squares problem," *SIAM Journal on Numerical Analysis*, vol. 17, no. 6, pp. 883–893, 1980.
- [11] K. Worden and G. R. Tomlinson, *Nonlinearity in Structural Dynamics: Detection, Identification and Modelling*, Institute of Physics Publishing, Bristol, UK, 2001.
- [12] G. R. Tomlinson, "Developments in the use of the hilbert transform for detecting and quantifying non-linearity associated with frequency response functions," *Mechanical Systems and Signal Processing*, vol. 1, no. 2, pp. 151–171, 1987.
- [13] J. Yiu, *The Definitive Guide to ARM®CORTEX®-M3 and CORTEX®-M4 Processors*, Elsevier, Amsterdam, Netherlands, 2014.
- [14] W. Mucha, "Real-time finite element simulations on arm microcontroller," *Journal of Applied Mathematics and Computational Mechanics*, vol. 16, no. 1, pp. 109–116, 2017.
- [15] M. Alessandrini, G. Biagetti, P. Crippa, L. Falaschetti, L. Manoni, and C. Turchetti, "Singular value decomposition in embedded systems based on arm cortex-m architecture," *Electronics*, vol. 10, no. 1, 2020.
- [16] F. Beltran-Carbajal and G. Silva-Navarro, "Output feedback dynamic control for trajectory tracking and vibration suppression," *Applied Mathematical Modelling*, vol. 79, pp. 793–808, 2020.
- [17] O. Garcia-Perez, G. Silva-Navarro, and J. Peza-Solis, "Flexible-link robots with combined trajectory tracking and vibration control," *Applied Mathematical Modelling*, vol. 70, pp. 285–298, 2019.
- [18] V. Ondra, I. A. Sever, and C. W. Schwingshackl, "A method for detection and characterisation of structural non-linearities

- using the hilbert transform and neural networks,” *Mechanical Systems and Signal Processing*, vol. 83, pp. 210–227, 2017.
- [19] S. F. Masri, J. Caffrey, T. K. Caughey, A. W. Smyth, and A. Chassiakos, “Identification of the state equation in complex non-linear systems,” *International Journal of Non-Linear Mechanics*, vol. 39, pp. 111–1127, 2004.
- [20] I. A. Kougoumtzoglou and P. D. Spanos, “An identification approach for linear and nonlinear time-variant structural systems via harmonic wavelets,” *Mechanical Systems and Signal Processing*, vol. 37, pp. 338–352, 2013.
- [21] M. Fliess and H. Sira-Ramirez, “An algebraic framework for linear identification,” *ESAIM: Control, Optimization and Calculus of Variations*, vol. 9, pp. 151–168, 2003.
- [22] R. P. Pacheco and V. Steffen, “On the identification of non-linear mechanical systems using orthogonal functions,” *International Journal of Non-Linear Mechanics*, vol. 39, pp. 1147–1159, 2004.
- [23] J. I. Wu, C. h. Chen, and C. f. Chen, “A unified derivation of operational matrices for integration in systems analysis, information technology,” in *Proceedings of the International Conference on Coding and Computing*, pp. 436–442, Las Vegas, NV, USA, March 2000.
- [24] I. Kovacic and M. J. Brennan, *The Duffing Equation: Nonlinear Oscillators and Their Behaviour*, John Wiley & Sons, Hoboken, NJ, USA, 2011.
- [25] G. R. Tomlinson and I. Ahmed, “Hilbert transform procedures for detecting and quantifying non-linearity in modal testing,” *Meccanica*, vol. 22, no. 3, pp. 123–132, 1987.
- [26] M. Simon and G. Tomlinson, “Use of the hilbert transform in modal analysis of linear and non-linear structures,” *Journal of Sound and Vibration*, vol. 96, no. 4, pp. 421–436, 1984.
- [27] J. N. Juang, *Applied System Identification*, Prentice-Hall, Hoboken, NJ, USA, 1994.
- [28] L. G. Trujillo-Franco, G. Silva-Navarro, and F. Beltran-Carbajal, “Parameter estimation on nonlinear systems using orthogonal and algebraic techniques,” in *Proceedings of the Society for Experimental Mechanics Series, Society for Experimental Mechanics*, pp. 347–354, Springer, Cham, Switzerland, April 2016.
- [29] F. Beltran-Carbajal and G. Silva-Navarro, “Generalized nonlinear stiffness identification on controlled mechanical systems,” *Asian Journal of Control*, vol. 21, no. 3, pp. 1281–1292, 2019.
- [30] F. Beltran-Carbajal, G. Silva-Navarro, and L. G. Trujillo-Franco, “A sequential algebraic parametric identification approach for nonlinear vibrating mechanical systems,” *Asian Journal of Control*, vol. 19, no. 5, pp. 1–11, 2017.

Research Article

A Hybrid Method to Diagnose 3D Rotor Eccentricity Faults in Synchronous Generators Based on ALIF_PE and KFCM

Chao Zhang ¹, Chuang-Jin He,¹ Shuai Li,¹ Yu-Ling He ¹, Xiao-Long Wang ¹,
Xiang-Yu Liu ² and Lun Cheng³

¹Department of Mechanical Engineering and Hebei Key Laboratory of Electric Machinery Health Maintenance and Failure Prevention, North China Electric Power University, Baoding 071003, China

²State Grid Hebei Electric Power Research Institute, Shijiazhuang 050021, China

³State Grid Hebei Electric Power Supply Co., Ltd., Shijiazhuang 050022, China

Correspondence should be addressed to Yu-Ling He; heyuling1@163.com

Received 5 February 2021; Revised 3 May 2021; Accepted 24 May 2021; Published 1 June 2021

Academic Editor: Francisco Beltran-Carbajal

Copyright © 2021 Chao Zhang et al. This is an open access article distributed under the Creative Commons Attribution License, which permits unrestricted use, distribution, and reproduction in any medium, provided the original work is properly cited.

This paper proposed a new hybrid diagnosis method for the generator's 3D static eccentricity faults which include the axial eccentricity, the radial eccentricity, and the mixed eccentricity composed of the former two. Firstly, adaptive local iterative filtering (ALIF) method was used to decompose the vibration signals of the generator under eccentricity faults. Then, in order to figure out the intrinsic mode function (IMF) components with the upmost feature information, the correlation coefficient was calculated. Finally, the components' permutation entropy (PE) is extracted to construct the eigenvector matrix which can be used to input the kernel fuzzy C-means (KFCM) algorithm to obtain the result of clustering. The result indicates that the classification coefficient based on ALIF and KFCM behaves closer to 1, while the average fuzzy entropy (FE) is closer to 0, showing that this method is able to detect different eccentricity faults more accurately.

1. Introduction

As the center of electric system, generator is a typical high-speed rotating machine which is highly potential to suffer different faults such as rotor eccentricity or other mechanical failures from time to time [1, 2]. In order to realize the early detection and avoid losses, it is significant to explore high-efficiency methods in particular for each fault.

The typical faults of generator include rotor short circuit, stator short circuit, and air-gap eccentricity. Among them, eccentricity fault will lead to the change of air-gap magnetic field which would worsen the performances of generator and even damage the machine as a result of vibration, rotor bending, winding wear, and friction between stator and rotor [3]. Therefore, eccentricity fault detection is one of the important contents of generator fault diagnosis.

To detect the eccentricity faults, there are two common views: motor current signature analysis and vibration signals

[4]. Some scholars pay attention to the motor current signature analysis; for example, Taner Goktas et al. [5] dealt with the discernment of broken magnet and static eccentricity faults through the stator phase current. They analyzed stator electromotive force and phase current waveforms in detail to identify the discerning components and characterize their dynamic behaviors. The method was verified through both simulations and experiments. Attoui and Omeiri [6] proposed a new fractional-order controller (FOC) with a simple and practical design method which can ensure the stability of the nonlinear system in both healthy and faulty conditions. And they used an online fault diagnostic technique based on the spectral analysis of stator currents by a fast Fourier transform (FFT) algorithm in order to detect the stator and rotor faults.

Besides, the fault diagnosis methods based on the vibration signal are widely used in rolling bearing. However, it is also effective and worth researching in generator because it

can help us extract the fault feature. If we want to realize fault classification based on vibration signal, the study of signal processing technique is essential. In recent years, many scholars have been widely exploring the signal processing method. Encouragingly, a series of achievements have been obtained. For instance, in 1998, Huang et al. [7] proposed the empirical mode decomposition (EMD) method which can get the amplitude and frequency of signal by decomposing the nonstationary signal into several intrinsic mode function (IMF) components and combining with Hilbert transform.

However, about the EMD method, the problem of mode mixing is inevitable so that researchers spare no effort to overcome it. In 2009, Wu et al. [8, 9] combined the EMD method with the features of white Gaussian noise whose frequency distribution is uniform to solve this problem efficiently and they proposed ensemble empirical mode decomposition (EEMD) whose essence is to decompose the nonlinear and nonstationary multimodal signal from high frequency to low frequency into IMF components. The method shows a good decomposition effect. Xue et al. [10] used EEMD to decompose the ground-penetrating radar (GPR) signal into a series of IMFs and calculated the permutation entropy (PE) of each IMF to distinguish noise IMFs and target IMFs. Finally, they reconstructed the signal with target IMFs to remove the noise effectively.

Based on the research of the former scholars, M. A. Torres et al. [11] proposed complete ensemble empirical mode decomposition with adaptive noise (CEEMDAN) method which can add white noise to the signal adaptively according to the features and obtain the IMF components by calculating the only residual signal, so as to solve the problem of mode mixing and improve the efficiency of decomposition. It is widely introduced in the field of fault diagnosis. For instance, in order to solve the problem that the fault feature extraction is difficult because the vibration signal of rolling bearing is polluted by strong noise, Ji and Wang [12] proposed a CEEMDAN aided fast spectral kurtosis graph algorithm for fault diagnosis. The method decomposed the signal into multimodal components using the CEEMDAN algorithm and reconstructed the effective component by kurtosis value. The processing result of the algorithm indicated that the fault detection of bearing inner ring can be realized effectively.

With the purpose of realizing a better decomposition effect, people have also tried alternative methods. Cicone et al. [13] proposed the method of adaptive local iterative filtering (ALIF) based on the method of iterative filtering (IF) in 2016. In the process of iterative decomposition, the filter function of ALIF can alter different expressions with the signal changes; thus, the multimode signal can be decomposed into multiorder single components adaptively. Given its advantages, Tang and Pang [14] used ALIF to decompose the rotor fault vibration signal of turbogenerator sets to obtain several IMF components and then obtained the instantaneous frequency and amplitude of each IMF component through Hilbert transform. Finally, the fault type of the shafting was identified according to the time-frequency features of rotor vibration.

In order to represent the complexity of signal, entropy theory, including fuzzy entropy (FE), sample entropy (SE), PE, and approximate entropy (AE), is proposed and widely used in many fields of data analysis such as energy, material, and physiology [15, 16]. For example, Cao and Lin [17] proposed using inherent FE and its multiscale version, which employs EMD and fuzzy membership function to address the dynamic complexity in electroencephalogram (EEG) data.

In recent years, scholars have been trying to apply the entropy theory in fault diagnosis. As is known, feature extraction is one of the most important issues in mechanical fault diagnosis, which directly relates to the accuracy and the reliability of early fault prediction. Zhao et al. [18] used the EEMD method to decompose the vibration signal of bearing in generator and the correlation coefficient analysis method to determine three improved IMFs, which are close to the original signal. Then, they used the multiscale fuzzy theory to calculate the entropy values of the selected three IMFs in order to form a feature vector with the complexity measure, which is regarded as the inputs of the support vector machine (SVM) model for training and constructing an SVM classifier to recognize fault pattern. Their method can extract much feature information and effectively eliminate the impact of mode mixing. In 2016, Rostaghi and Azami [19] proposed dispersion entropy (DE), which not only has fast calculation speed but also is less affected by the mutation signal and takes into account the difference between the signal amplitude. As its application in generator, Wang et al. [20] distinguished the rotor short circuit and stator short circuit based on variational mode decomposition (VMD) and the refined composite multiscale dispersion entropy (RCMDE).

To characterize the complexity of the signal and quantify the signal features, in this paper, the PE algorithm is introduced which is proposed by Bandt and Pompe [21] to detect randomness and dynamic mutation. It has simple calculation, strong antinoise ability, and high sensitivity to signal changes. Subsequently, Ding and Zhang [22] used the Haar wavelet and PE method to denoise and extract fault eigenvalues. Then, they classified different gear faults according to the principle of different PE distribution corresponding to different faults. Moreover, Ren et al. [23] screened several inherent frequency band functions obtained by decomposing the hydrogenerator signal to achieve the purpose of denoising.

For further research, it is necessary to classify the fault feature information to realize the detection of different types of faults. Clustering is to classify a group of data with unknown distribution, merge data with the same properties into the same class or cluster, and divide data with different properties into different classes or clusters [24, 25]. The traditional fuzzy C-means (FCM) algorithm is relatively mature; on this basis, the kernel learning process was introduced in kernel fuzzy C-means (KFCM) algorithm which stuck out the feature differences by mapping the samples to high-dimensional space [26]. As for its application, Bi et al. [27] used VMD to decompose the signal of diesel engine and then selected the key

component whose maximum singular value would be calculated and input to KFCM to realize the classification of the faults of diesel engine. In addition, Zhang et al. [28] proposed a novel classifier that combined rough sets and SVM in the fault diagnosis for hydroelectric generator unit (HGU). They extracted the fault patterns lying in the overlapped region instead of classifying the patterns directly. Then, they defined the upper and lower approximations of each class on the basis of the rough set technique. Next, they calculated the reliability that they belong to a certain class for the fault patterns lying in the overlapped region. The results show that the proposed classifier can more properly describe the complex map between the faults and their symptoms.

With the development of artificial intelligence (AI) technology, some scholars spare no efforts to introduce AI technology to the field of fault classification; for example, Gao et al. [29] realized the classification of faults in rotor-bearing systems through AI model, which needs sufficient fault samples to have a better effect. They combined the finite element method (FEM) with generative adversarial networks (GANs) for rotor-bearing systems to expand fault samples so as to improve the accuracy. In addition, Wang et al. [30] proposed a method using deep belief networks (DBN) to detect multiple faults in axial piston pumps. For each individual fault, they calculated all the data indicators of the signals to construct samples. Then, they input the samples into DBNs to classify the multiple faults. With restricted Boltzmann machine (RBM) stacked layer by layer, DBNs can automatically learn fault features. These methods embodied the trend of intellectualization and automation.

Honestly, we suppose that the fault diagnosis would be more and more intelligent in the future. At the same time, clustering algorithm in fault diagnosis will probably develop in full swing. On the basis of this perspective, we proposed a new method that combines the PE method with ALIF and KFCM to meet the complicated feature extraction of nonlinear dynamics in generators in this paper. In fact, eccentricity fault is often not one-dimensional so that the diagnosis method focused on 3D faults shows huge potential. Besides, some other methods about eccentricity faults such as [31] focused on the degree of eccentricity faults rather than the type. Therefore, the method in this paper contributes ideas to diagnosis of the fault types just like the axial eccentricity, the radial eccentricity, and the mixed eccentricity composed of the former two. As presented in the following, the samples representing the same fault type are divided into a vivid cluster and we can easily recognize different fault types of generator.

The remainder of this paper is constructed as follows. The theoretical model and process of the proposed method are presented in Section 2 and Section 3, respectively, while the simulation and the experimental study of the proposed method are illustrated in Section 4. The results analysis is in Section 5. Finally, the brief conclusions drawn from the study are presented in Section 6.

2. Theoretical Model of the Proposed Method

The proposed method includes three parts, namely, the noise filtering based on ALIF, the PE calculation of the decomposed signal, and the clustering based on KFCM.

2.1. ALIF Filter. The filter function of ALIF can alter different expressions with the signal changes; thus, the multimode signal can also be decomposed into multiorder components adaptively [18]. The process of the ALIF algorithm includes inner loop and outer loop.

The function of the inner loop is to select each IMF component iteratively. The moving operator $\Gamma(z(t))$ can be obtained by

$$\Gamma(z(t)) = \int_{-l(z)}^{l(z)} z(t+\tau)\omega(\tau) d\tau, \quad (1)$$

where $\omega(t)$ is the filtering function and $l(z)$ is the filtering interval which can be written as

$$l(z) = 2 \left[\frac{N\lambda}{m} \right], \quad (2)$$

where $\lambda \in (1.6, 2)$, m is the number of extreme points, and N is the signal length.

The solution process of $\omega(t)$ is as follows.

Suppose that $h(x)$ and $g(x)$ are smooth differentiable functions and satisfy the following conditions on the interval $[a, b]$:

- (1) $g(a) = g(b) = 0, g(x) > 0$, for any $x \in (a, b)$
- (2) $h(a) < 0 < h(b)$

Then, the general form of the Fokker Planck equation is

$$\frac{\partial p}{\partial t} = -\delta \frac{\partial(h(x)p)}{\partial x} + \mu \frac{\partial^2(g^2(x)p)}{\partial x^2}, \quad (3)$$

where the value range of δ and μ is $(0, 1)$.

In (3), $\partial^2(g^2(x)p)/\partial x^2$ makes the solution $p(x)$ of the equation from the midpoint of the interval (a, b) to the endpoints a and b , and $-\partial(h(x)p)/\partial x$ makes $p(x)$ gather from the endpoints a and b to the center of the interval.

When the two mentioned are in balance, it has

$$-\delta \frac{\partial(h(x)p)}{\partial x} + \mu \frac{\partial^2(g^2(x)p)}{\partial x^2} = 0. \quad (4)$$

And the solution $p(x)$ of the equation now would be the filtering function $\omega(t)$, which satisfies

- (1) $p(x) \geq 0$ for any $x \in (a, b)$
- (2) $p(x) = 0$ for any $x \notin (a, b)$

The wave operator $\kappa(z(t))$ can be obtained by subtracting the original signal $z(t)$ by the moving operator $\Gamma(z(t))$ as

$$\kappa(z(t)) = z(t) - \Gamma(z(t)). \quad (5)$$

However, the iterative process will not be going on forever. Equation (6) is usually the condition to stop the

process. When E_i is less than the specified threshold, the inner loop iterative filtering will stop.

$$E_i = \frac{\|\kappa_{i,n} - \kappa_{i,n-1}\|_2}{\|\kappa_{i,n-2}\|_2} \quad (6)$$

The effect of outer loop is to stop the process of IMF extraction by inner loop.

When all IMF components are removed from the original signal $z(t)$ and the residual $r(t)$ shows obvious trend features, the outer loop will stop. The detailed process is illustrated in Figure 1.

2.2. Permutation Entropy. Permutation entropy is an appropriate complexity measure for chaotic time series, in particular in the presence of dynamical and observational noise [21].

Given its obvious superiority in reflecting small abrupt change behavior of system vibration response, PE is suitable for signal of mechanical equipment. The fundamental principle of the algorithm is as follows.

Construct a set of time series $\{x_i | i = 1, 2, \dots, N\}$; then, reconstruct the phase space. It has

$$X_i = [x_i, x_i + \tau, \dots, x_i + (m-1)\tau]. \quad (7)$$

where m is the embedding dimension and τ is the delay time.

Any X_i has $m!$ permutations. For any permutation w , $T(w)$ represents the number of times it appears; then, the probability of its occurrence is

$$P(w) = \frac{T(w)}{N - (m-1)\tau}. \quad (8)$$

Thus, PE can be defined as

$$H_{PE} = - \sum P(w) \ln P(w). \quad (9)$$

After normalization, it has

$$PE = \frac{H_{PE}}{\ln(m!)}. \quad (10)$$

The size of PE reflects the complexity and the randomness of the time-series signal. The larger PE means a more complicated time-series signal. The dimension m and the delay time τ will impact the calculation result during extracting the features by PE. If m is too small, the reconstructed vector contains too few states so that the algorithm will lose sense. However, if m is too large, the reconstruction of the phase space would homogenize the time series which would lead to long-time calculation and fewer details. The influence of the delay time τ is relatively smaller [21].

2.3. KFCM Cluster. Kernel fuzzy c -means (KFCM) clustering is a method to map the samples which are classified into high-dimensional space through nonlinear mapping of kernel space and then cluster after highlighting the differences of samples [31]. The nonlinear map Φ is defined as

$$\Phi_n x_k \longrightarrow \Phi(x_k) \in F, \quad (11)$$

where x_k is the original feature space sample, $x_k \in X$.

The clustering objective function of the KFCM algorithm can be expressed as

$$J_m = \sum_{i=1}^c \sum_{k=1}^n \mu_{ik}^m \|\Phi(x_k) - \Phi(v_i)\|^2, \quad (12)$$

where v_i is the clustering center, c is the number of clustering, n is the number of samples, μ_{ik} is the degree of membership, and m is the fuzzy weighted index.

At the same time, there is

$$\begin{aligned} \mu_{ik} \in [0, 1], \quad 0 < \sum_{k=1}^n \mu_{ik} < n, \quad (i = 1, \dots, c), \\ \sum_{i=1}^c \mu_{ik} = 1, \quad (k = 1, 2, \dots, n), \end{aligned} \quad (13)$$

where $K(x, y) = \Phi^T(x) \Phi(y)$ and can be further written as

$$K(x, y) = \exp\left[-\frac{\|x - y\|^2}{(2\sigma^2)}\right], \quad (14)$$

where σ is the Gaussian kernel parameter. Then, the Euclidean distance of kernel space is

$$\|\Phi(x_k) - \Phi(v_i)\|^2 = K(x_k, x_k) + K(v_i, v_i) - 2K(x_k, v_i). \quad (15)$$

According to equations (14) and (15) as well as the constraint condition, the degree of the membership and the clustering center can be calculated by

$$\begin{aligned} u_{ik} &= \frac{[1 - K(x_k, v_i)]^{-1/(m-1)}}{\sum_{j=1}^c [1 - K(x_k, v_j)]^{-1/(m-1)}}, \\ v_i &= \frac{\sum_{k=1}^n \mu_{ik}^m K(x_k, v_i) x_k}{\sum_{k=1}^n \mu_{ik}^m K(x_k, v_i)}. \end{aligned} \quad (16)$$

To analyze the clustering effect, the classification coefficient S and the average FE E are presented, which are defined, respectively, as

$$\begin{aligned} S &= \frac{1}{n} \sum_{i=1}^c \sum_{j=1}^n u_{ij}^2, \\ E &= -\frac{1}{n} \sum_{i=1}^c \sum_{j=1}^n u_{ij} \ln u_{ij}, \end{aligned} \quad (17)$$

where c is the number of categories, n is the number of samples, and u_{ij} is the degree of membership.

The classification coefficient S is used to express the fuzziness degree of the clustering result. If $S = 1$, the clustering result belongs to the hard partition; else if $S < 1$, it belongs to the fuzzy partition. Therefore, the closer S is to 1, the better the effect will be. The average FE indicates the uncertainty of the classification; for the hard partition, $E = 0$, while for the fuzzy partition, $E > 0$. Therefore, the effect will be better as E moves closer to 0 [32].

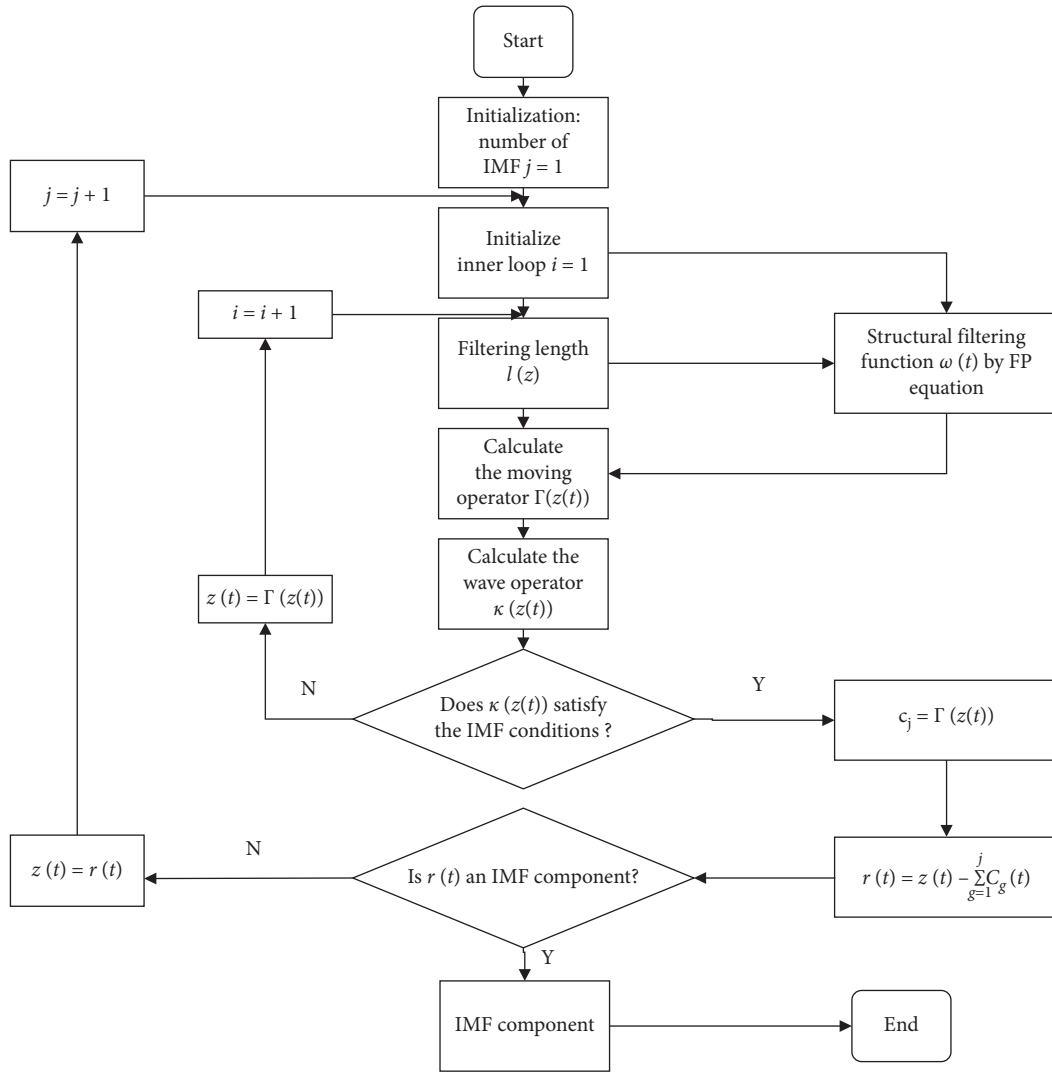


FIGURE 1: Process of outer loop.

3. Proposed Methodology

The hybrid method to diagnose 3D rotor eccentricity faults in synchronous generators based on ALIF PE and KFCM can be diagrammed in Figure 2. And the detailed process is introduced as follows.

Step 1. Decompose the signal data of training samples and testing samples using the ALIF method to obtain multiorder eigenmode components.

Step 2. Conduct correlation analysis between the original signal and the multiorder eigenmode components in order to get optimal mode components.

Step 3. Calculate the PE of the effective mode components as the feature vector so as to construct the training sample matrix and testing sample matrix.

Step 4. Input the training sample matrix to KFCM to obtain the center of clustering.

Step 5. Input the center of clustering and testing samples to KFCM together; then, we can get the result of clustering.

4. Simulation and Experiment Study

In this section, the simulating signal and the test data from the CS-5 prototype generator are employed to validate the proposed method. And, to get a comprehensive comparison, they are applied to some other popular methods including EEMD, CEEMDAN, and the clustering method based on FCM as well.

4.1. Application to Simulating Signal. The simulating signal is constructed as

$$x(t) = \sin(2 * 50\pi t) + \sin\left(2 * 100\pi t + \frac{\pi}{6}\right) + \sin\left(2 * 200\pi t + \frac{\pi}{3}\right) + \eta(t), \quad (18)$$

where $x(t)$ consists of three harmonic signals and the white Gaussian noise whose signal-to-noise ratio is 30 dB. Figure 3 illustrates the time domain waveform of the simulating signal, with the number of the sampling points 1000 and the sampling frequency of 1 kHz.

The results after decomposing by EEMD and CEEMDAN are shown in Figures 4 and 5, respectively. It is suggested from Figure 4 that IMF3 indicates an obvious mode mixing due to the impact of the white Gaussian noise, while in Figure 5, it shows that IMF3 and IMF 4 both have the endpoint effect. Therefore, both EEMD and CEEMD have defects.

The signal is also decomposed by ALIF, as illustrated in Figure 6. It shows that there are three IMF components and a residual r . The components IMF1, IMF2, and IMF3 correspond to the three sinusoidal components of 200 Hz, 100 Hz, and 50 Hz, respectively. Obviously, the three IMF components have neither the mode mixing nor the endpoint effect, suggesting the superior effect of ALIF against the traditional CEEMDAN and EEMD methods.

4.2. Comparison of Entropy Algorithms. Herein, we calculated the PE, DE, AE, and SE of the eccentricity faults signal and normal signal, respectively. Based on the entropy of normal signal, we obtained the difference between axial eccentricity, radial eccentricity, mixed eccentricity signal, and normal signal under corresponding entropy, respectively. The result is shown in Figure 7.

The result shows that the difference of PE between the three fault conditions and normal signal is the most obvious and the values are 0.542, 0.962, and 1.369, respectively. Therefore, it is easy to be distinguished based on the clear distribution. Finally, we chose PE as the indicator to detect the eccentricity faults.

4.3. Application to Experimental Signal

4.3.1. Method to Test the Vibration Signal. The experiment is carried out on the CS-5 prototype generator which has one pole-pair and a rated rotation of 3000 rpm, as shown in Figure 8(a). The rotor is kept stable with the foundation by the bearing blocks, while the stator can be moved along the radial direction and axial direction, respectively, to simulate the radial eccentricity, the axial eccentricity, and the mixed eccentricity, as illustrated in Figure 8(b). The movements are performed by 8 screws, with four for the radial and the other four for the axial shifts, and controlled by four dial indicators.

During the experiment, the excitation current was set to 2.5 A to output the phase voltage at 220 V, with three sliding rheostats of 500 Ω as the loads for the three phases. The vibration signals of the rotor and the stator are sampled through four accelerometers whose sensitivity is 10 mV/mm/s, with two for the radial vibration and the other two for

the axial vibration, as illustrated in Figure 8(c). The sampling frequency was set to 5000 Hz.

Four groups of experiments were taken, namely, the normal condition, the radial eccentricity of 0.2 mm (the radial air-gap length is 1.2 mm), the axial eccentricity of 2 mm, and the mixed eccentricity composed of the former two.

4.3.2. Fault Classification. EEMD, CEEMDAN, and ALIF methods are employed to decompose the vibration data, respectively. Taking the radial rotor vibration in the axial eccentricity case as an example, the decomposed results are illustrated in Figure 9. It shows that the results of EEMD and CEEMDAN are somewhat similar. The components E4, E5, C5, and C6 all indicate obvious mode mixing. However, the frequency range occupied by the first six components decomposed by ALIF is significantly refined, without any frequency mixing problem (E1~E6, C1~C6, and A1~A6 indicate amplitudes of mode components).

Since the IMF component with large correlation coefficient is able to well retain the fault features of the signal [32], in this paper, the correlation coefficients between the IMF components and the original signal are calculated, as listed in Table 1.

As indicated in Table 1, the correlation coefficients between the first three IMF components and the original signal are far greater than those of the other components. Therefore, it can be considered that most of the fault information is included in the first three IMF components. Consequently, IMF1 to IMF3 are selected to represent the original signal. In this paper, PE is used to extract the fault features of the IMF components for further clustering. The ALIF PE of the four signal types is calculated, respectively, as shown in Table 2.

Besides, we need to set delay time τ and dimension m to calculate PE. According to the change of PE at different delay times in Figure 10, it can be seen that the delay time τ has little influence on the calculation of time series. However, if the dimension m is too small, it is difficult to detect the dynamic mutation of the time series because there are too few states in the reconstructed sequence; if the value of m is too large, the calculation time is too long to reflect the subtle transformation of the time series. According to Bandt's suggestion [21], the value of m is 3~7. Combined with another research [33, 34], we set $m = 6$, $\tau = 1$, and a relatively good clustering effect is obtained.

As indicated in Table 2, the PE values of IMF1 to IMF3 are varied, suggesting that the complexities of them are different. Consequently, the eigenvectors composed of these permutation entropies should be also different, offering the possibility of hard classification.

5. Case Verification and Result Analysis

5.1. Case Setup. 20 groups of vibration data for each case (normal, radial eccentricity, axial eccentricity, and mixed

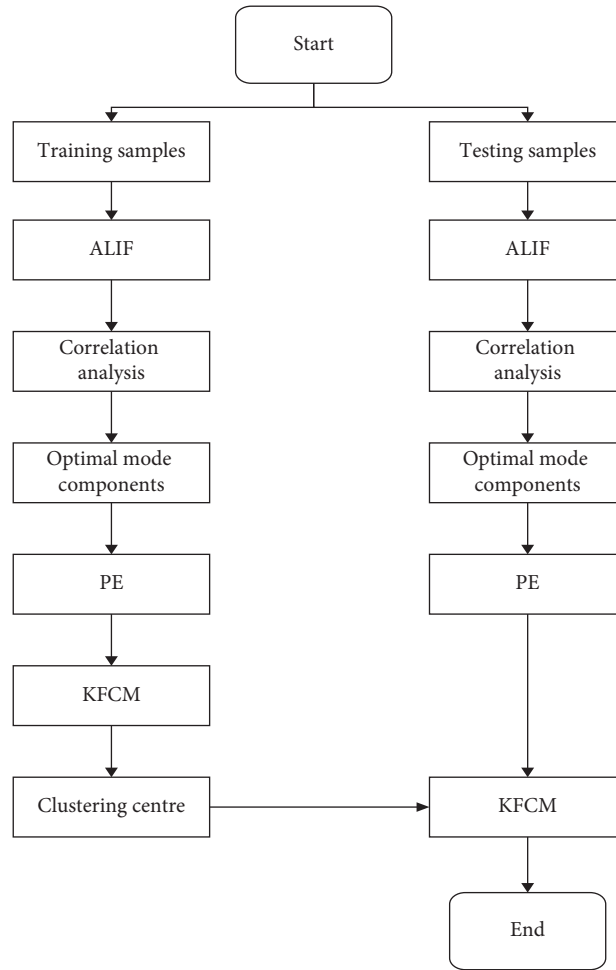


FIGURE 2: Process of the proposed method.

eccentricity) are taken continuously (10 groups for training and 10 groups for testing), and the points of each set are 2048.

EEMD, CEEMDAN, and ALIF methods are used to adaptively decompose the 20 sets of data and obtain the multiorder IMF components. Then, the correlation coefficients between each IMF and the original signal are calculated.

By calculating the PE of the first three IMF components, the eigenvector matrixes are obtained, with the forms of 3×40 .

Firstly, four clustering centers are obtained by clustering the eigenvector matrixes. Then the clustering centers as well as the eigenvector matrixes are applied with KFCM. Calculations are performed iteratively until the errors are less than the tolerance. The final results are illustrated in Figure 11.

5.2. Results Discussion. As illustrated in Figure 11(a), the data points are scattered around the cluster center. Moreover, the mixed eccentricity and the radial eccentricity faults cannot be distinguished. Therefore, EEMD does not offer a satisfactory effect.

Figure 11(b) shows the clustering effect of CEEMDAN. It is shown that the signal data points are clustered around the center, with the distribution compact. Compared with Figure 11(a), the clustering effect of this method is better than that of EEMD. It can basically realize the detection and classification of different eccentricity faults.

Figure 11(c) shows the effect of KFCM clustering based on ALIF. It is shown that the clustering centers of each case are far apart from each other and therefore can be distinguished clearly. What is more, the distances between two cluster centers are larger than those of the aforementioned two methods, showing an even better effect.

In order to compare the clustering effect of the above three algorithms more accurately, the classification coefficient S and the average FE E are employed, as shown in Table 3.

According to [32], the clustering effect of samples will be better if the classification coefficient S is closer to 1 and the average FE E is closer to 0. Obviously, the proposed method has the best clustering effect, while EEMD ranks the last.

In order to verify the superiority of the proposed method, the aforementioned eccentricity fault data are further analyzed for comparison with that FCM. The clustering result by ALIF-FCM is illustrated in Figure 11(d).

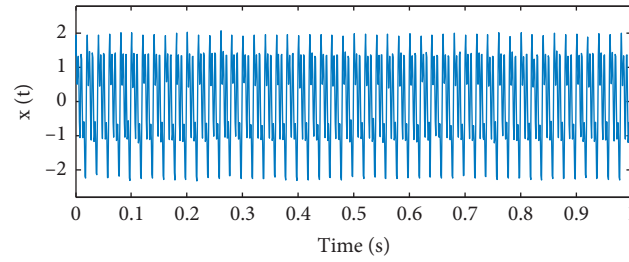


FIGURE 3: Simulating signal.

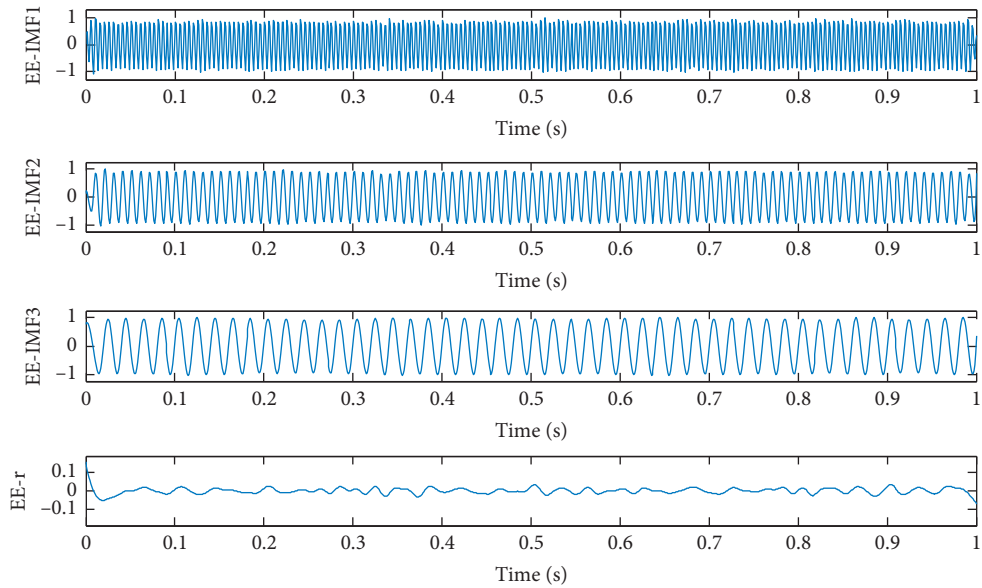


FIGURE 4: EEMD result of the simulating signal.

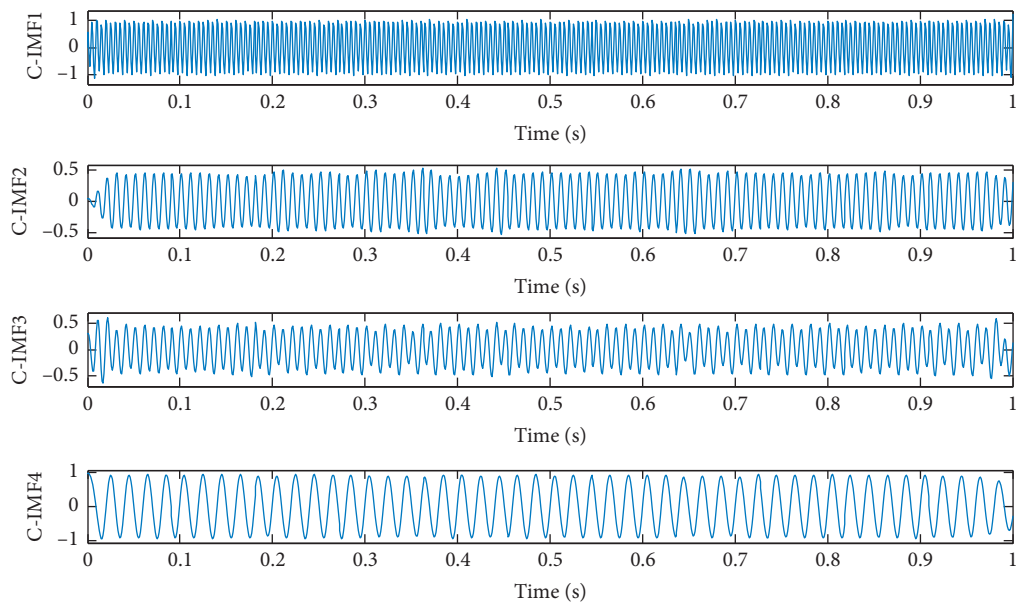


FIGURE 5: CEEMDAN result of the simulating signal.

As indicated in Figure 11(d), the mixed eccentricity and the normal operation signals are far away. The radial eccentricity and axial eccentricity fault signals are

relatively close while the distinction is clear. That means this method can realize the identification and division of different kinds of eccentricity faults. However, comparing

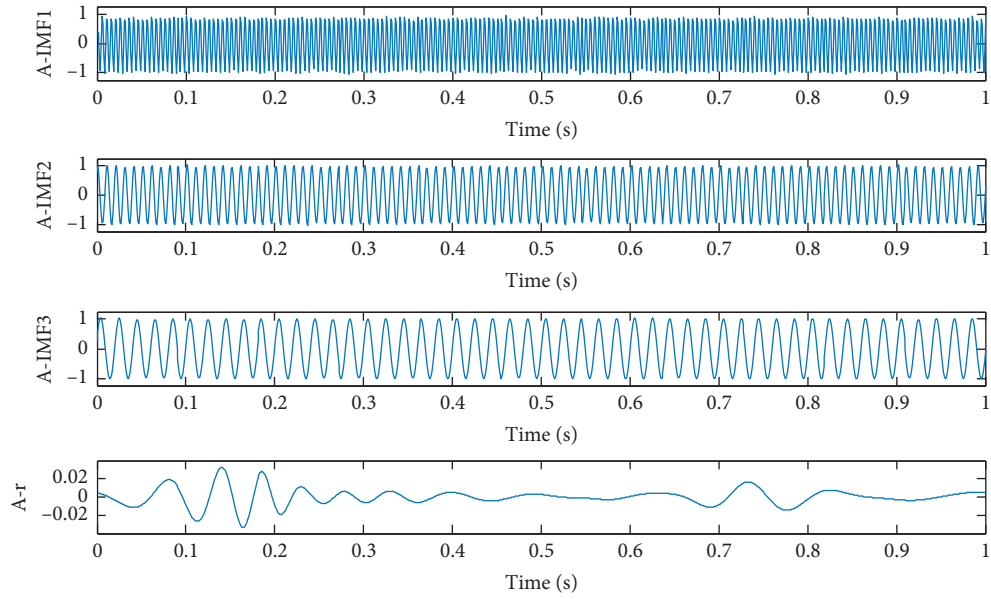


FIGURE 6: ALIF result of the simulating signal.

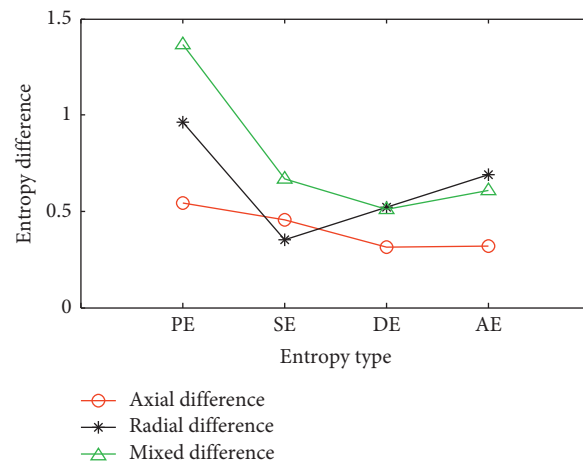
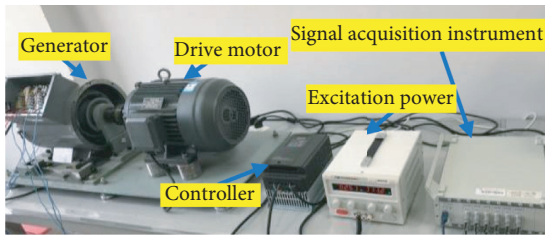
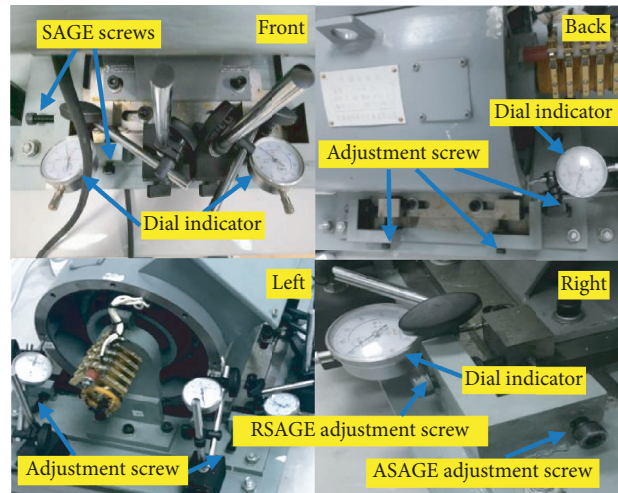


FIGURE 7: The differences of entropy.

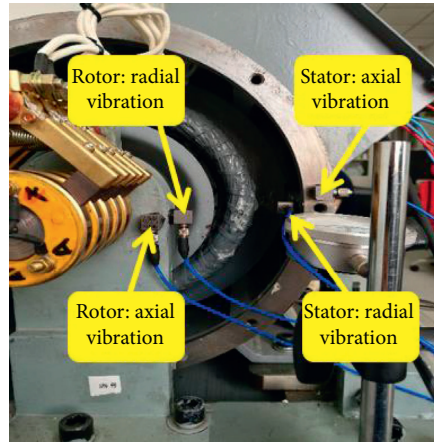


(a)



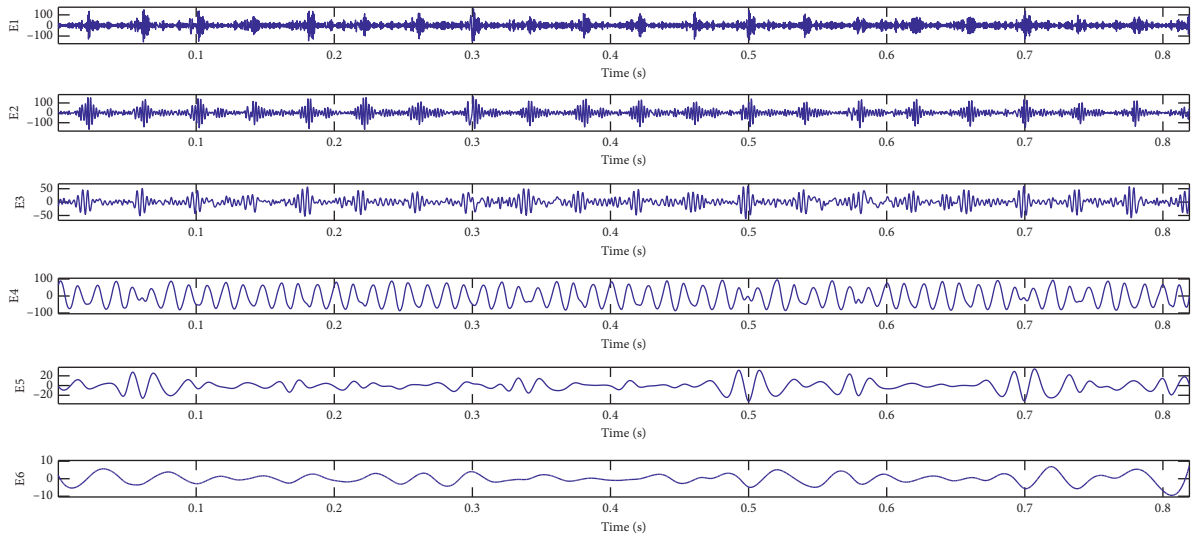
(b)

FIGURE 8: Continued.

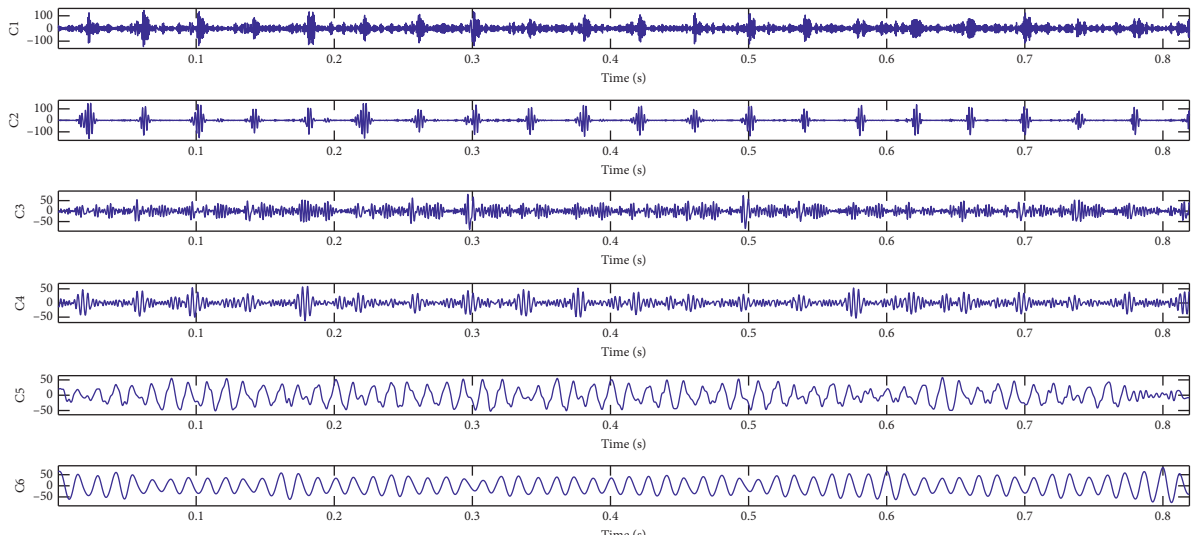


(c)

FIGURE 8: Method to test the vibration signal, (a) picture of experiment rig, (b) method to set radial and axial eccentricity, and (c) accelerometer setup.



(a)



(b)

FIGURE 9: Continued.

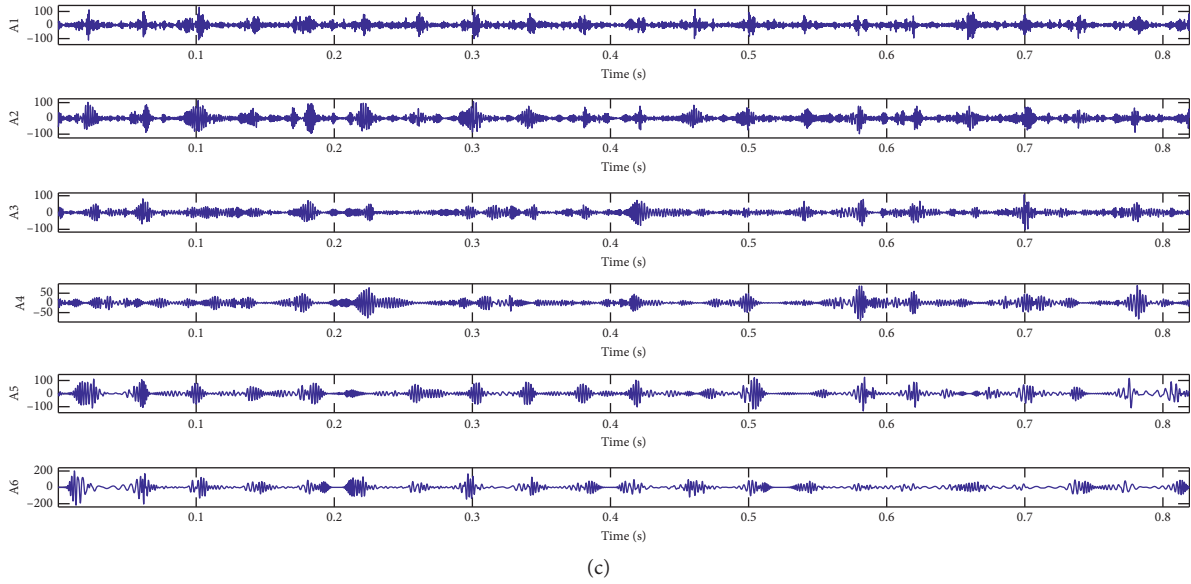


FIGURE 9: Decomposing results by three different methods, (a) signal decomposed by EEMD, (b) signal decomposed by CEEMDAN, and (c) signal decomposed by ALIF.

TABLE 1: Correlation coefficients between IMF components and the original signal.

Algorithm	Correlation coefficient				
	IMF1	IMF2	IMF3	IMF4	IMF5
EEMD	0.7942	0.3723	0.2253	0.0328	0.0155
CEEMDAN	0.7826	0.4265	0.2661	0.0623	0.0326
ALIF	0.7756	0.5127	0.2984	0.0927	0.0658

TABLE 2: Permutation entropy of the first three IMF components.

Signal type	Permutation entropy		
	IMF1	IMF2	IMF3
Normal	4.1653	2.7183	2.6223
Radial eccentricity	5.7926	5.0729	4.9135
Axial eccentricity	6.0456	5.9557	5.4241
Mixed eccentricity	5.8743	5.1811	4.8916

Figure 11(d) with 11(c), it is shown that the distribution of data points based on the KFCM clustering method is more compact, and the different signal intervals are more obvious.

In order to quantitatively compare the effects of FCM and KFCM, the classification coefficient S and the average FE E as well as the iteration times these two methods are calculated, as shown in Table 4. Obviously, although the KFCM

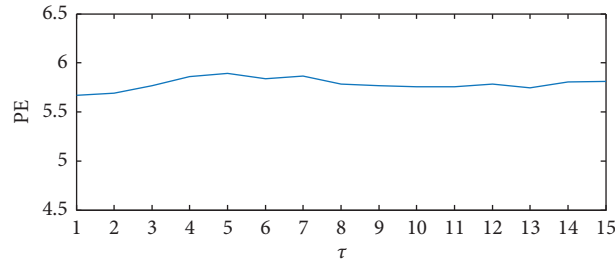


FIGURE 10: Permutation entropy (PE) at different delay times.

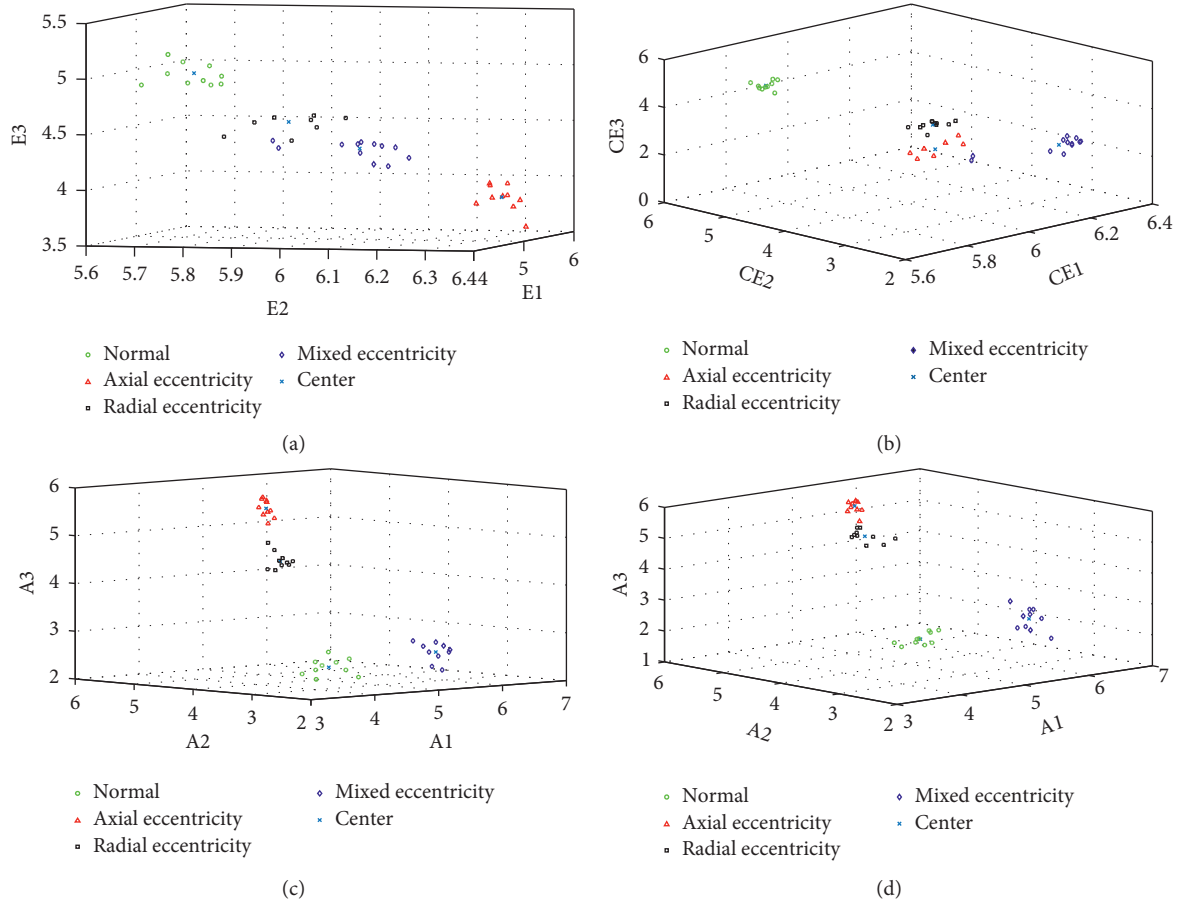


FIGURE 11: Cluster results by four different methods: (a) clustered by EEMD-KFCM, (b) clustered by CEEMDAN-KFCM, (c) clustered by ALIF-KFCM (this paper), and (d) clustered by ALIF-FCM.

TABLE 3: Clustering index of different methods.

Algorithm	Classification coefficient S	Average fuzzy entropy E
EEMD	0.7412	0.5186
CEEMDAN	0.8941	0.2188
ALIF-KFCM	0.9268	0.1758

TABLE 4: Clustering index of KFCM and FCM.

Algorithm	Classification coefficient S	Average fuzzy entropy E	Iteration times
FCM	0.9082	0.2067	12
KFCM	0.9268	0.1758	13

based method has one more interaction, it has a superior clustering effect since its S is closer to 1 while its E is closer to 0.

6. Conclusion

In this paper, we proposed a fault diagnosis method for the 3D eccentricity faults in synchronous generators based on ALIF-PE and KFCM. This method employs ALIF, which has a better effect than EEMD and CEEMDAN in avoiding the influence of mode mixing and endpoint effect, to decompose the vibration signal. In the meantime, the proposed method employs the PE and KFCM, which are superior to EEMD-KFCM, ALIF-KFCM, and CEEMDAN-KFCM in getting the classification coefficient S and the average FE E , to classify the fault types.

The index factors of the clustering effect, namely, the classification coefficient S and the average FE E of ALIF-KFCM, are 0.9268 and 0.1758, respectively. Comparing with the results by EEMD-KFCM ($S = 0.7412$ and $E = 0.5186$), the proposed ALIF-KFCM method improves 25.0% in S (the closer to 1, the better), while it improves 66.1% in E (the closer to 0, the better). Comparing with the results by CEEMDAN-KFCM ($S = 0.8941$ and $E = 0.2188$), the proposed method improves 3.66% in S and 19.7% in E . Comparing with the results by ALIF-FCM ($S = 0.9082$ and $E = 0.2067$), the proposed method improves 2.04% in S and 14.9% in E . Obviously, the proposed method is superior to these aforementioned methods.

The proposed method presents a qualified detection and classification of the 3D eccentricity faults, which includes the radial eccentricity, the axial eccentricity, and the mixed eccentricity composed of the former two. We focused on the type of static eccentricity faults rather than the degree. Based on its clear figure and intelligent effect, this method is potential for the application in the eccentricity fault monitoring and diagnosis.

In our next step work, we will focus on how to decrease the iteration times so that the proposed method can be performed more efficiently. In addition, we will try to analyze the diagnosis method under dynamic eccentricity fault and even the complex fault conditions including both eccentricity and interturn short circuit.

Data Availability

The data used to support the findings of this study are available from the corresponding author upon request.

Conflicts of Interest

The authors declare that there are no conflicts of interest regarding the publication of this paper.

Acknowledgments

This work was supported by the National Natural Science Foundation of China (51777074), the Hebei Provincial Natural Science Foundation (E2020502032), the Fundamental Research Funds for the Central Universities

(2020MS114 and 2018YQ03), and the Top Youth Talent Support Program of Hebei Province ([2018]-27).

References

- [1] Y.-L. He, W.-Q. Deng, G.-J. Tang, X.-L. Sheng, and S.-T. Wan, "Impact of different static air-gap eccentricity forms on rotor UMP of turbogenerator," *Mathematical Problems in Engineering*, vol. 2016, Article ID 5284815, 13 pages, 2016.
- [2] Y. He, Y. Zhang, Y. Meng, G. Tang, W. Deng, and H. Zhong, "Enhanced detection of characteristic vibration signal of generator based on self-adapted multi-scale top-hat transformation," *Recent Advances in Electrical & Electronic Engineering*, vol. 11, no. 1, pp. 418–424, 2018.
- [3] Y.-L. He, W.-Q. Deng, B. Peng et al., "Stator vibration characteristic identification of turbogenerator among single and composite faults composed of static air-gap eccentricity and rotor interturn short circuit," *Mathematical Problems in Engineering*, vol. 2016, Article ID 5971081, 14 pages, 2016.
- [4] X. Bao, "Review and prospect of air-gap eccentricity faults in induction machines," *Proceedings of the CSEE*, vol. 33, no. 6, pp. 93–100, 2013.
- [5] T. Goktas, M. Zafarani, and B. Akin, "Discernment of broken magnet and static eccentricity faults in permanent magnet synchronous motors," *IEEE Transactions on Energy Conversion*, vol. 31, no. 2, pp. 578–587, 2016.
- [6] I. Attoui and A. Omeiri, "Modeling, control and fault diagnosis of an isolated wind energy conversion system with a self-excited induction generator subject to electrical faults," *Energy Conversion and Management*, vol. 82, pp. 11–26, 2014.
- [7] N. E. Huang, Z. Shen, S. R. Long et al., "The empirical mode decomposition and the hilbert spectrum for nonlinear and non-stationary time series analysis," *Proceedings of the Royal Society of London. Series A: Mathematical, Physical and Engineering Sciences*, vol. 454, no. 1971, pp. 903–995, 1998.
- [8] Z. Wu and N. E. Huang, "Ensemble empirical mode decomposition: a noise assisted data analysis method," *Advances in Adaptive Data Analysis*, vol. 1, no. 1, pp. 1–41, 2009.
- [9] Z. Wu and N. E. Huang, "A study of the characteristics of white noise using the empirical mode decomposition method," *Proceedings of the Royal Society A: Mathematical, Physical and Engineering Sciences*, vol. 460, no. 2046, pp. 1597–1611, 2004.
- [10] W. Xue, X. Dai, J. Zhu, Y. Luo, and Y. Yang, "A noise suppression method of ground penetrating radar based on EEMD and permutation entropy," *IEEE Geoscience and Remote Sensing Letters*, vol. 16, no. 10, pp. 1625–1629, 2019.
- [11] M. E. Torres, M. A. Colominas, G. Schlott-Hauer et al., "A complete ensemble empirical mode decomposition with adaptive noise," in *Proceedings of the IEEE International Conference on Acoustics Speech and Signal Processing (ICASSP 2011)*, pp. 4144–4147, Prague, Czech Republic, May 2011.
- [12] N. Ji and L. Wang, "Bearing fault diagnosis based on fast spectral kurtosis graph algorithm aided by CEEMDAN," *Mechanical Engineer*, no. 1, pp. 76–79+82, 2020, in Chinese.
- [13] A. Ciccone, J. Liu, and H. Zhou, "Adaptive local iterative filtering for signal decomposition and instantaneous frequency analysis," *Applied and Computational Harmonic Analysis*, vol. 41, no. 2, pp. 384–411, 2016.
- [14] G.-J. Tang and B. Pang, "Fault diagnosis of a turbo-generator rotor based on ALIF-HT," *Journal of Chinese Society of Power Engineering*, vol. 37, no. 11, pp. 883–889, 2017.
- [15] J. S. Richman and J. Randall Moorman, "Physiological time-series analysis using approximate entropy and sample

- entropy,” *American Journal of Physiology- Heart and Circulatory Physiology*, vol. 278, pp. 2039–2049, 2000.
- [16] L.W. Zhong, “Entropy theory of distributed energy for internet of things,” *Nano Energy*, vol. 58, pp. 669–672, 2019.
- [17] Z. Cao and C.-T. Lin, “Inherent fuzzy entropy for the improvement of EEG complexity evaluation,” *IEEE Transactions on Fuzzy Systems*, vol. 26, no. 2, 2018.
- [18] H. Zhao, M. Sun, and X. Yang, “A new feature extraction method based on EEMD and multi-scale fuzzy entropy for motor bearing,” *Entropy*, vol. 19, no. 1, 2016.
- [19] M. Rostaghi and H. Azami, “A measure for time-series analysis,” *IEEE Signal Processing Letters*, vol. 23, no. 5, pp. 610–614, 2016.
- [20] T. Wang, *Research on Vibration Signal Feature Extraction Method of Generator under Interturn Short-Circuit Faults*, Degree thesis of North China Electric Power University, Beijing, China, 2020.
- [21] C. Bandt and B. Pompe, “Permutation entropy: a natural complexity measure for time series,” *Physical Review Letters*, vol. 88, no. 17, Article ID 174102, 2002.
- [22] W. Ding and Z. Zhang, “Fault identification method of transmission gear based on morphological wavelet and permutation entropy,” *Journal of Mechanical Transmission*, vol. 43, no. 10, pp. 165–168, 2019.
- [23] Y. Ren, S. Huangjin, L. Hu, X. Li, and H. Chen, “Research on denoising method of hydraulic turbine based on fourier decomposition and permutation entropy,” *Water Power*, vol. 46, no. 10, pp. 96–99, 2020.
- [24] J. Sun, J. Liu, and L. Zhao, “Clustering algorithms research,” *Journal of Software*, vol. 19, no. 1, pp. 48–61, 2008.
- [25] F. Wu and Y. Mao, “A novel fuzzy C-means algorithm based on k-d tree,” *Computer and Modernization*, vol. 11, pp. 1–5, 2015.
- [26] S. Sun, Q. Zhang, T. Du, J. Wang, and Y. Wang, “Study of evaluation method for low voltage conventional circuit breaker switching fault degree based on vibration signal,” *Proceedings of the CSEE*, vol. 37, no. 18, pp. 5473–5482, 2017.
- [27] F. Bi, D. Tang, L. Zhang, Li Xin, T. Ma, and Y. Xiao, “Diesel engine fault diagnosis algorithm based on VMD and KFCM,” *Journal of Vibration, Measurement & Diagnosis*, vol. 40, no. 5, pp. 853–858, 2020.
- [28] X. Zhang, J. Zhou, J. Guo, Q. Zou, and Z. Huang, “Vibrant fault diagnosis for hydroelectric generator units with a new combination of rough sets and support vector machine,” *Expert Systems with Applications*, vol. 39, no. 3, pp. 2621–2628, 2012.
- [29] Y. Gao, X. Liu, J. Xiang, and H. Huang, “A hybrid of FEM simulations and generative adversarial networks to classify faults in rotor-bearing systems,” *ISA Transactions*, vol. 108, pp. 356–366, 2021.
- [30] S. Wang, J. Xiang, Y. Zhong, and H. Tang, “A data indicator-based deep belief networks to detect multiple faults in axial piston pumps,” *Mechanical Systems and Signal Processing*, vol. 112, pp. 154–170, 2018.
- [31] Y. Chang, *Air-Gap Eccentricity Diagnosis for Introduction Motors Based on Vibration Analysis*, Degree thesis of Zhejiang University, Hangzhou, China, 2016.
- [32] J. C. Bezdek, “Cluster validity with fuzzy sets,” *Cybernetics and Systems*, vol. 3, no. 3, pp. 58–72, 1974.
- [33] G. Rao, “Method for optimal determination of parameters in permutation entropy algorithm,” *Journal of Vibration and Shock*, vol. 33, no. 1, pp. 188–193, 2014.
- [34] D. Q. Zhang and S. C. Chen, “Clustering incomplete data using kernel based fuzzy C means algorithm,” *Neural Processing Letters*, vol. 18, no. 3, pp. 155–162, 2003.

Research Article

First and Second Law Evaluation of Multipass Flat-Plate Solar Air Collector and Optimization Using Preference Selection Index Method

Nguyen Thanh Luan¹ and Nguyen Minh Phu ²

¹Faculty of Mechanical Engineering, Ho Chi Minh City University of Technology (HCMUT), VNU-HCM, Ho Chi Minh City, Vietnam

²Faculty of Heat and Refrigeration Engineering, Industrial University of Ho Chi Minh City (IUH), Ho Chi Minh City, Vietnam

Correspondence should be addressed to Nguyen Minh Phu; nguyenminhphu@iuh.edu.vn

Received 10 January 2021; Revised 28 February 2021; Accepted 18 March 2021; Published 28 March 2021

Academic Editor: Francisco Beltran-Carbajal

Copyright © 2021 Nguyen Thanh Luan and Nguyen Minh Phu. This is an open access article distributed under the Creative Commons Attribution License, which permits unrestricted use, distribution, and reproduction in any medium, provided the original work is properly cited.

In this paper, different flow configurations of multipass flat-plate air collectors are explored. Multiple passes are formed from glass cover, absorber plate, and back plate. Five types of air collectors were analysed and optimized with respect to maximum efficiencies and minimum cost. The analytical prediction of the heat exchanger, pressure loss, and efficiencies was presented. The effects of mass flow rate from 0.01 to 0.02 kg/s, air channel depth from 15 to 30 mm, and collector length from 1.5 to 2.5 m on different configurations were examined and compared. The results of the parametric study show that the triple-pass type has the greatest efficiency, whereas the smallest efficiency is of the single-pass type. Among double-pass types, the type with two glass covers and natural convection heat transfer achieved the highest effective and exergy efficiencies due to a reduction in the top loss. Double-pass type with single glass cover is not recommended from both energy and exergy standpoints. As the collector length increases, the effective efficiency decreases, but the exergy efficiency increases. The exergy performance of the triple-pass type can reach up to 5% at the air flow rate of 0.005 kg/s. Finally, multiobjective optimization using the preference selection index method is conducted with three targets including effective efficiency, exergy efficiency, and number of plates. Optimal results show that the triple-pass type with the lowest air flow rate and the longest length is the best. The effective and exergy efficiencies for the best case were found to be about 52.1% and 4.7%, respectively. However, this type with the highest flow rate and the shortest length is the worst.

1. Introduction

The national sustainable energy strategy always gives priority for developing renewable energy. Tropical countries like Vietnam promote solar energy conversion due to vast and stable radiation intensity during the year. The common types of solar thermal energy conversion are solar power, solar hot water, and solar hot air. The first two kinds have been developing stably and commercially for a long time, while the solar hot air has been researching. This continuous research is due to two major problems. Firstly, the thermal energy of hot air cannot be stored like hot water because the air specific heat and density are small compared to water. Secondly, the small thermal conductivity of the air results in a low

convection heat transfer coefficient. However, the application of solar air heater (SAH) is widespread for space heating [1], regeneration of desiccant [2], and drying of agricultural products [3]. Facing the needs and limitations of SAH, research on improving SAH performance is always paid attention [4]. Heat transfer improvement between the absorber plate and the air in the collector can be mentioned as the insertion of vortex generators [5], inclined plates [6], or roughness ribs on the absorber surface [7] to diminish the viscous sublayer close to the surface and create mixing of the primary and secondary flows.

Another measure is the collector duct divided into multiple air passes to reduce heat loss at the top of SAH because of the high temperature of the absorber plate.

Previously, Chandra et al. [8] established an analytical model and equivalent resistance method to calculate triple-pass air collector. Predictions from the two approaches were compared with experimental data to indicate discrepancies. Choudhury et al. [9] theoretically solved triple-pass air collector with single and double glass covers. They reported that low air flow rate and short collector length were the cost-effective solutions. Forson et al. [10] studied the theory and indoor experiment of double-duct SAH in the natural convection mode of air. They concluded that the collector efficiency decreased with increasing collector area. Ramadan et al. [11] have inserted a packed bed in the first pass of a double-pass SAH to increase the heat transfer surface. They recommend an air flow rate of less than 0.05 kg/s to achieve high efficiency. Sopian et al. [12] added porous media to the second pass of a double-pass SAH. This correction achieves collector efficiency up to 70% which is greater than the traditional single-pass SAH. Ramani et al. [13] expanded the study of double-pass SAH with the porous material configuration at the second pass. They claim that the collector efficiency is 25% higher than that of the double-pass SAH without porous and 35% higher than that of the single-pass SAH. Correction of the absorber surface to enhance heat transfer has been a concern for the past decade. El-Sebaï et al. [14] used a v-corrugated absorber surface in a double-duct SAH. They realized that the air temperature leaving the collector was 5% higher and the efficiency was 14% higher than the smooth absorber surface. A finned absorber plate in a double-pass SAH was proposed and examined by El-Sebaï et al. [15]. They reported that the optimum air flow rate was 0.0125 kg/s to achieve the maximum hydraulic thermal efficiency of 40%. Ho et al. [16] studied the effect of air recirculation fraction to the second pass in a wire mesh SAH. They reported that the optimal fraction was 0.5 for flat-plate collectors and 1 for wire mesh packed collectors. Yeh [17] studied to divide the airflow between the absorber plate and the back plate into multiple passes. The results showed that when the number of passes increased, the thermal efficiency increased, but the pressure loss penalty was not significant.

Recently, besides evaluating the energy efficiency and cost of multipass air collectors, the exergy efficiency estimation of the collector has been noted to fulfill the requirements needed for a thermal device. The exergy analysis is to quantify the availability of solar radiation which can be converted into its work potential and irreversibility due to exergy destruction. Velmurugan and Kalaivanan [18–21] studied the energy and exergy of multipass collectors with different configurations including ribbed, finned, wire mesh absorber plates. They reported that a mixed type of wire mesh in the second pass and fin in the first pass provides the highest energy and exergy efficiencies. Raj et al. [22] evaluated the exergy performance of a SAH under outdoor conditions. They concluded that the exergy efficiency increased with day time and mass flow rate due to the higher extracted useful energy. Abo-Elfadl [23] proposed 4E (energy, exergy, economic, and environmental) model to comprehensively investigate a double-pass SAH. They pointed out that finned SAH is the most feasible one in terms

of exergoeconomic point of view. Experimental studies on different modifications for multipass SAH have been performed to demonstrate their effectiveness [24–26]. In addition, with the development of numerical algorithms and computer processors, CFD (computational fluid dynamics) studies have been conducted to reduce the experimental time and costs [27–31]. More recently, Heydari et al. [32] proposed and numerically examined a novel helical airflow path around triangular channels. From the simulation results, the distributions of variables within the SAH such as velocity, pressure, and temperature are clarified to explain the mechanism of heat transfer enhancement and the potential for efficiency improvement. Multipass air collector applications for drying agricultural produce and integrating photovoltaic are also found in the literature [33–35].

Extensive review indicates that there is more variation in the multipass air collector to improve heat transfer such as wire mesh, porous, or fin. But in all, it is still based on a flat-plate collector with a certain number of passes. No previous works have been found to address the simultaneous comparison of multipass SAHs and multiobjective optimization to determine the most feasible collector. Therefore, this study focuses on evaluating the flat-plate collector with different number of glass covers, absorber plate, and back plate in order to examine all the possible passes of air. Energy, exergy, and optimization studies firmly confirm the pertinent type among the many configurations and major dimensions of air collectors through an analytical investigation coupled to an optimization method called multicriteria decision-making technique.

2. Model Formulation and Validation

Figure 1 shows the five types of flat-plate collectors that were investigated for energy, exergy, and optimization in this study. Type 1 consists of two glass covers, an absorber plate, and a back plate. The air travels from top to bottom via 3 passes. Type 2 consists of a glass cover, an absorber plate, and a back plate. Therefore, two passes can be created from these plates. Type 3 consists of two glass covers and one back plate where the air can travel through two passes. A four-plate configuration with two passes is seen in type 4, in which the air between the two glass covers is naturally convected. Type 5 consists of two glass covers and one absorber plate with the air blowing through single pass in order to compare with the multipass types of 1 to 4.

2.1. Thermohydraulic Modelling. The mathematical model is presented in this section with the following assumptions:

- (i) Flow is steady, incompressible, and one-dimensional (1D). In practical applications, such as convective drying, an air velocity was verified to obtain drying conditions. Thus, the airflow is assumed to be steady. The air velocity inside the solar air heater duct is moderate so that air temperature is high enough to serve a certain duty. Therefore, the airflow is considered incompressible. Variation of air pressure and temperature is along with duct length leading to the 1D flow consideration.

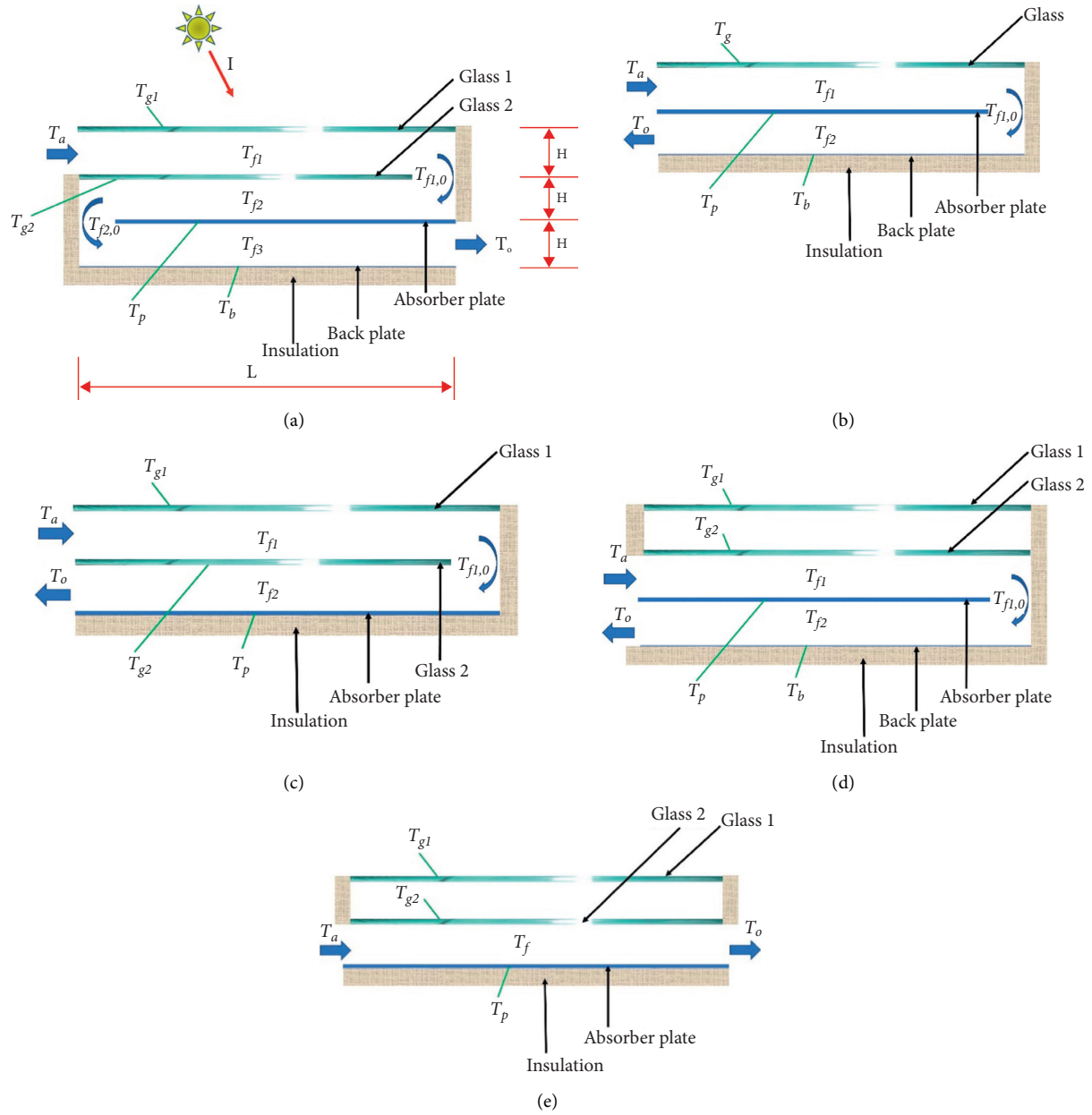


FIGURE 1: Configurations of solar air heater. (a) Type 1: triple-pass, double glass cover. (b) Type 2: double-pass, single glass cover. (c) Type 3: double-pass, double glass cover. (d) Type 4: double-pass, double glass cover. (e) Type 5: single-pass, double glass cover.

(ii) Thermal conduction in glass cover, absorber plate, and back plate is not considered due to their small thicknesses. The temperatures of these plates are homogeneous and equal to the average temperature. Multipoint temperature measurement on a plate is required in experiments, and the average temperature can be estimated by taking arithmetic mean [26].

(iii) The thermophysical properties of air, glass, and plates are constants because of low temperature change of a flat-plate air collector.

Equations (1)–(7) present the energy balance for type 1 as illustrated in Figure 2(a). Type 1 consists of 4 plates (2

glass covers, 1 absorber plate, and 1 back plate) and the fluid at 3 passes, so it takes seven equations to find seven corresponding temperatures. The thermal balance equation for the top glass cover is given below. The solar thermal energy absorption of the glass is equal to the amount of thermal energy released to the surrounding by convection and radiation, the heat transfer to the air in the first pass, and the heat transferred by radiation between the two glass covers [13]:

$$\alpha_g I = h_w(T_{g1} - T_a) + h_{r,g1,s}(T_{g1} - T_s) + h_{c,g1,f1}(T_{g1} - T_{f1}) + h_{r,g1,g2}(T_{g1} - T_{g2}). \quad (1)$$

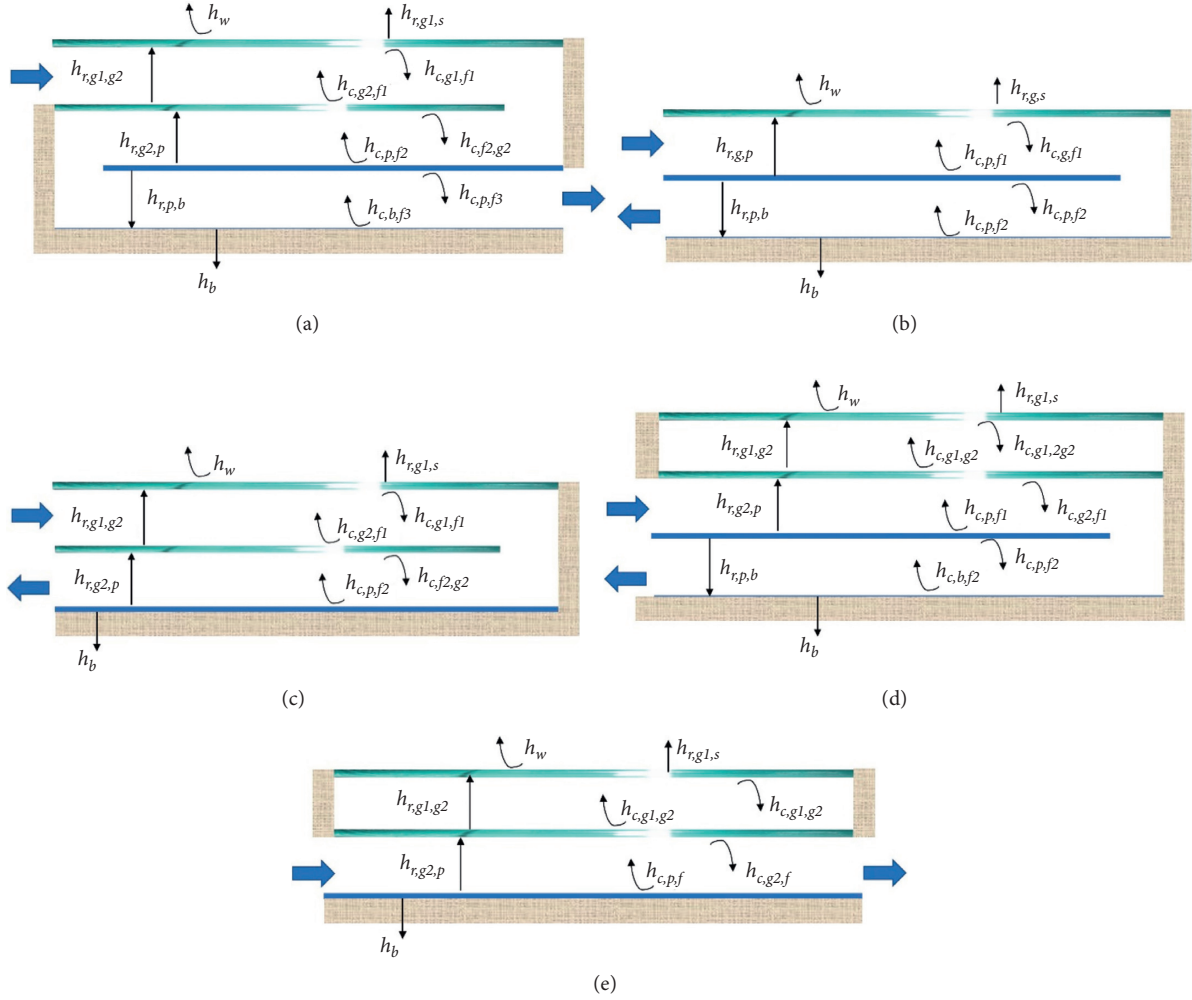


FIGURE 2: Energy balance diagram for plates and glass covers. (a) Type 1. (b) Type 2. (c) Type 3. (d) Type 4. (e) Type 5.

The air in the first pass receives heat from the two glass covers and increases its temperature. The temperature gradient can be approximated by the temperature difference between the inlet and outlet of the channel [16, 20]:

$$Q_1 = mc_p(T_{f1,o} - T_a) = Lbh_{c,g1,f1}(T_{g1} - T_{f1}) + Lbh_{c,g2,f1}(T_{g2} - T_{f1}). \quad (2)$$

The lower glass cover absorbs solar radiation equaled to the convection heat transfer with the airflows at first and second passes, and the radiant heat exchanges with the upper glass cover and the absorber plate:

$$\alpha_g \tau_g I = h_{c,g2,f1}(T_{g2} - T_{f1}) + h_{r,g1,g2}(T_{g2} - T_{g1}) + h_{c,f2,g2}(T_{g2} - T_{f2}) + h_{r,g2,p}(T_{g2} - T_p). \quad (3)$$

Thermal balance of fluid in the second pass is formed via convection heat transfer with the lower glass cover and absorber plate:

$$Q_2 = mc_p(T_{f2,o} - T_{f1,o}) = Lbh_{c,f2,g2}(T_{g2} - T_{f2}) + Lbh_{c,p,f2}(T_p - T_{f2}). \quad (4)$$

The heat gain from solar radiation of the absorber plate is balanced with the heat transferred to the fluid at the second and third passes and with the radiant heat transfer to the lower glass cover and back plate:

$$\alpha_p \tau_g^2 I = h_{c,p,f2}(T_p - T_{f2}) + h_{r,g2,p}(T_p - T_{g2}) + h_{c,p,f3}(T_p - T_{f3}) + h_{r,p,b}(T_p - T_b). \quad (5)$$

Thermal balance of fluid in the third pass is composed of convective heat transfer with absorber plate and back plate:

$$Q_3 = mc_p(T_{f3,o} - T_{f2,o}) = Lbh_{c,p,f3}(T_p - T_{f3}) + Lbh_{c,b,f3}(T_b - T_{f3}). \quad (6)$$

The back plate received thermal radiation from the absorber plate equilibrates with the convection heat exchange to the air in the third pass and the heat loss from the back plate to the environment:

$$h_{r,p,b}(T_p - T_b) = h_{c,b,f3}(T_b - T_{f3}) + h_b(T_b - T_a). \quad (7)$$

In the above equations, the fluid temperature (T_f) in a pass is taken as the average value of inlet and outlet

temperatures of the pass. This is due to the fact that the convective heat transfer coefficient (h_c) was developed based on the fluid bulk mean temperature.

$$\begin{aligned} T_{f1} &= 0.5(T_a + T_{f1,o}), \\ T_{f2} &= 0.5(T_{f2,0} + T_{f1,o}), \\ T_{f3} &= 0.5(T_o + T_{f2,o}). \end{aligned} \quad (8)$$

Equations (1)–(7) are rearranged in matrix form as follows:

$$\begin{bmatrix} S_{11} & -h_{c,g1,f1} & -h_{r,g1,g2} & 0 & 0 & 0 & 0 & 0 \\ Lbh_{c,g1,f1} & S_{22} & Lbh_{c,g2,f1} & 0 & 0 & 0 & 0 & 0 \\ -h_{r,g1,g2} & -h_{c,g2,f1} & S_{33} & -h_{c,f2,g2} & -h_{r,g2,p} & 0 & 0 & 0 \\ 0 & 4mc_p & Lbh_{c,f2,g2} & S_{44} & Lbh_{c,p,f2} & 0 & 0 & 0 \\ 0 & 0 & -h_{r,g2,p} & -h_{c,p,f2} & S_{55} & -h_{c,p,f3} & -h_{r,p,b} & 0 \\ 0 & 4mc_p & 0 & -4mc_p & -Lbh_{c,p,f3} & S_{66} & -Lbh_{c,b,f3} & 0 \\ 0 & 0 & 0 & 0 & h_{r,p,b} & h_{c,b,f3} & S_{77} & 0 \end{bmatrix} \begin{bmatrix} T_{g1} \\ T_{f1} \\ T_{g2} \\ T_{f2} \\ T_p \\ T_{f3} \\ T_b \end{bmatrix} = \begin{bmatrix} S_1 \\ S_2 \\ S_3 \\ S_4 \\ S_5 \\ S_6 \\ S_7 \end{bmatrix}, \quad (9)$$

where

$$\begin{aligned} S_{11} &= h_w + h_{r,g1,s} + h_{c,g1,g2} + h_{r,g1,g2}, \\ S_1 &= \alpha_g I + h_w T_a + h_{r,g1,s} T_s, \\ S_{22} &= -(2mc_p + Lbh_{c,g2,f1} + Lbh_{c,g1,f1}), \\ S_2 &= -2mc_p T_a, \\ S_{33} &= h_{c,g2,f1} + h_{r,g1,g2} + h_{c,g2,f2} + h_{r,g2,p}, \\ S_3 &= \alpha_g \tau_g I, \\ S_{44} &= -(2mc_p + Lbh_{c,f2,g2} + Lbh_{c,p,f2}), \\ S_4 &= 2mc_p T_a, \\ S_{55} &= h_{c,p,f2} + h_{r,g2,p} + h_{c,p,f3} + h_{r,p,b}, \\ S_5 &= \alpha_g \tau_g^2 I, \\ S_{66} &= 2mc_p + Lbh_{c,p,f3} + Lbh_{c,b,f3}, \\ S_6 &= 2mc_p T_a, \\ S_{77} &= -(h_{r,p,b} + h_{c,b,f3} + h_b), \\ S_7 &= -h_b T_a. \end{aligned} \quad (10)$$

The appendix presents the system of equations for determining the temperatures of the remaining types associated with the energy balance diagram in Figures 2(b)–2(e). From equation (9), it is possible to solve seven temperatures once the convection heat transfer coefficients and radiant heat transfer coefficients are specified. The convection heat transfer coefficient of the top glass cover with the ambient air is calculated from McAdams' equation as follows [36]:

$$h_w = 5.7 + 3.8V_w. \quad (11)$$

The forced convective heat transfer coefficient of the air in the collector is predicted using the Dittus–Boelter formula as follows [37]:

$$h_c = 0.023Re^{0.8}Pr^{0.4} \frac{k}{D_h}. \quad (12)$$

The natural convection heat transfer coefficient between 2 glass covers of types 4 and 5 is estimated by [20]

$$h_{c,g1,g2} = 1.25(T_{g2} - T_{g1})^{0.25}. \quad (13)$$

The radiant heat transfer coefficient from the top glass cover to the sky is evaluated by the following correlation:

$$h_{r,g,s} = \sigma \epsilon_g (T_g^2 + T_s^2)(T_g + T_s). \quad (14)$$

The sky temperature is calculated from the following equation [38]:

$$T_s = 0.0552T_a^{1.5}. \quad (15)$$

Generally, the radiant heat transfer coefficient between the two surfaces s_1 and s_2 is computed from their temperature and emissivity as follows [39]:

$$h_{r,s1,s2} = \sigma (T_{s1}^2 + T_{s2}^2) \frac{T_{s1} + T_{s2}}{(1/\epsilon_{s1}) + (1/\epsilon_{s2}) - 1}. \quad (16)$$

The conductive heat transfer coefficient from the back plate to surroundings is determined by

$$h_b = \frac{k_i}{t_i}. \quad (17)$$

The hydraulic diameter is defined as follows:

$$D_h = \frac{4Hb}{2(H+b)}. \quad (18)$$

The Reynolds number is given by

$$\text{Re} = \frac{2m}{\mu(b+H)} \quad (19)$$

The thermal efficiency, i.e., first law efficiency, is the ratio of the heat gain received by air through SAH to the solar radiation coming from the absorption surface:

$$\eta_I = \frac{Q}{LbI} \quad (20)$$

where Q is the useful heat gain received by the air: $Q = mc_p(T_o - T_a)$.

When reconfiguring a thermal device to improve its heat transfer, it is likely that pressure loss also increases. Therefore, it is necessary to evaluate hydraulic dissipated power. The pressure loss of the air through the collector is the sum of the pressure loss due to friction and the minor loss due to 180° return bend between successive passes:

$$\Delta P = \Delta P_{\text{smooth}} + \Delta P_{\text{bend}} \quad (21)$$

The frictional pressure loss is evaluated as

$$\Delta P_{\text{smooth}} = n_{\text{pass}} \rho f V^2 \frac{L}{D_h} \quad (22)$$

where f is the friction factor.

The friction factor can be calculated by [11]

$$f = 0.059 \text{Re}^{-0.2} \quad (23)$$

Minor pressure loss by 180° return bend can be estimated as

$$\Delta P_{\text{bend}} = (n_{\text{pass}} - 1) K_{\text{bend}} \rho \frac{V^2}{2} \quad (24)$$

where K_{bend} is minor loss coefficient for 180° return bend, $K_{\text{bend}} = 2.2$ [19].

The energy required to transport fluid against pressure loss is calculated as follows:

$$P_{\text{flow}} = m \frac{\Delta P}{\rho} \quad (25)$$

The difference between the useful heat gain and pumping power is attributed to effective efficiency as

$$\eta_{\text{eff}} = \frac{Q - (P_{\text{flow}}/C_o)}{LbI} \quad (26)$$

where C_o is the conversion factor considering the thermal energy equivalent of blower power, $C_o = 0.2$ [38].

2.2. Exergy-Based Modelling. The input exergy of the SAH is constituted by the air inflow and solar radiation source as follows [5, 38]:

$$\sum EX_{\text{inlet}} = IA_c \left[1 - \left(\frac{4}{3}\right) \left(\frac{T_a}{T_{\text{sun}}}\right) + \left(\frac{1}{3}\right) \left(\frac{T_a}{T_{\text{sun}}}\right)^4 \right] \quad (27)$$

where T_{sun} is the sun temperature, $T_{\text{sun}} = 4350$ K [38], and $A_c = Lb$ is the absorber plate area.

The exergy losses of a solar air heater have been derived into five components including optical loss, the loss due to heat transfer from the absorber plate to the environment, the loss due to solar radiation absorption of the absorber plate, the loss due to heat transfer from the absorber plate to the air, and the frictional loss of the air flowing in SAH. These qualities are quantified as follows:

(1) Optical exergy losses:

$$EX_{\text{loss,opt}} = IA_c (1 - \tau^{\eta_g} \alpha) \left[1 - \left(\frac{4}{3}\right) \left(\frac{T_a}{T_{\text{sun}}}\right) + \left(\frac{1}{3}\right) \left(\frac{T_a}{T_{\text{sun}}}\right)^4 \right] \quad (28)$$

(2) Exergy losses by convection and radiation heat transfer from the absorber plate to the environment:

$$EX_{\text{loss,Q,loss}} = U_L A_c (T_p - T_a) \left(1 - \frac{T_a}{T_p} \right) \quad (29)$$

where U_L is the total loss coefficient:

$$U_L = U_t + h_b \quad (30)$$

The heat loss from the top of each SAH is calculated by convection and radiation heat transfer coefficients above absorber plate as [38]

$$U_t = \left(\frac{1}{h_w + h_{r,g1,s}} + \frac{1}{h_{c,g2,f1} + h_{r,g1,g2}} + \frac{1}{h_{c,p,f2} + h_{r,g2,p}} \right)^{-1}, \text{ for type I and III,} \quad (31a)$$

$$U_t = \left(\frac{1}{h_w + h_{r,g,s}} + \frac{1}{h_{c,p,f1} + h_{r,g,p}} \right)^{-1}, \text{ for type II,} \quad (31b)$$

$$U_t = \left(\frac{1}{h_w + h_{r,g1,s}} + \frac{1}{h_{c,g1,g2} + h_{r,g1,g2}} + \frac{1}{h_{c,p,f1} + h_{r,g2,p}} \right)^{-1}, \text{ for type IV,} \quad (31c)$$

$$U_t = \left(\frac{1}{h_w + h_{r,g1,s}} + \frac{1}{h_{c,g1,g2} + h_{r,g1,g2}} + \frac{1}{h_{c,p,f} + h_{r,g2,p}} \right)^{-1}, \text{ for type V.} \quad (31d)$$

(3) Exergy losses by absorption of radiation by the absorber plate:

$$EX_{\text{loss},T_p,T_{\text{sun}}} = IA_c \tau^{n_g} \alpha \left[1 - \left(\frac{4}{3} \right) \left(\frac{T_a}{T_{\text{sun}}} \right) + \left(\frac{1}{3} \right) \left(\frac{T_a}{T_{\text{sun}}} \right)^4 - \left(1 - \frac{T_a}{T_p} \right) \right], \quad (32)$$

where n_g is the number of glass covers.

(4) Exergy losses by heat transfer to the working air:

$$EX_{\text{loss},T_p,T_f} = IA_c \eta_I T_a \left(\frac{1}{T_f} - \frac{1}{T_p} \right), \quad (33)$$

where T_f is the mean temperature of the working air, $T_f = 0.5(T_a + T_o)$.

(5) Frictional exergy losses of the working air:

$$EX_{\text{loss},\text{friction}} = \frac{m \Delta p T_a}{\rho T_f}. \quad (34)$$

The first two kinds of exergy losses are external losses. The remaining kinds are known as internal losses. The total exergy losses are determined by summing the above-mentioned exergy losses:

$$\begin{aligned} \sum EX_{\text{loss}} = & EX_{\text{loss,opt}} + EX_{\text{loss},Q_{\text{loss}}} + EX_{\text{loss},T_p,T_{\text{sun}}} \\ & + EX_{\text{loss},T_p,T_f} + EX_{\text{loss},\text{friction}}. \end{aligned} \quad (35)$$

The exergy efficiency can be calculated by summing the total exergy losses and input exergy as follows:

$$\eta_{\text{II}} = 1 - \frac{\sum EX_{\text{loss}}}{\sum EX_{\text{inlet}}}. \quad (36)$$

2.3. Preference Selection Index Method for Multiobjective Optimization. Choosing a final solution may involve multiobjective optimization. In this study, three objective functions were selected including maximum effective efficiency, maximum exergy yield, and minimum total number of plates. The total number of plates is composed of glass covers, absorber plate, and back plate. This is a parameter related to the capital cost of a multiple pass air collector so it should be minimal. There are many multiobjective optimization methods. The preference selection index (PSI) method is chosen in the current work due to its explicit approach, simplicity, and no need to choose weights [40, 41]. The method is the objective approach oriented to multicriteria decision-making which was recently devised by Mania and Bhatt [42]. Nowadays, the PSI method is widely applied in many fields [43].

The performance procedure of the PSI method can be summarised as follows [40, 41]:

Step 1: normalization of criteria

For criteria needed to be maximized, i.e., η_{eff} and η_{II} :

$$d_{i,\eta_{\text{eff}}} = \frac{\eta_{\text{eff}}^i}{\eta_{\text{eff}}^{\text{max}}}, \quad (37a)$$

$$d_{i,\eta_{\text{II}}} = \frac{\eta_{\text{II}}^i}{\eta_{\text{II}}^{\text{max}}}. \quad (37b)$$

For criterion needed to be minimized, i.e., total number of glass cover, absorber plate, and back plate:

$$d_{i,N_{\text{plate}}} = \frac{N_{\text{plate}}^{\text{min}}}{N_{\text{plate}}^i}, \quad (37c)$$

(i) where i is i^{th} case, there are 135 cases in the current study, and therefore, $i = 1$ to 135.

Step 2: find the mean value of an objective

$$\Delta_{\eta_{\text{eff}}} = \frac{1}{135} \sum_{i=1}^{135} d_{i,\eta_{\text{eff}}}, \quad (38a)$$

$$\Delta_{\eta_{\text{II}}} = \frac{1}{135} \sum_{i=1}^{135} d_{i,\eta_{\text{II}}}, \quad (38b)$$

$$\Delta_{N_{\text{plate}}} = \frac{1}{135} \sum_{i=1}^{135} d_{i,N_{\text{plate}}}. \quad (38c)$$

Step 3: compute the preference variation value

$$\chi_{\eta_{\text{eff}}} = \sum_{i=1}^{135} (d_{i,\eta_{\text{eff}}} - \Delta_{\eta_{\text{eff}}})^2, \quad (39a)$$

$$\chi_{\eta_{\text{II}}} = \sum_{i=1}^{135} (d_{i,\eta_{\text{II}}} - \Delta_{\eta_{\text{II}}})^2, \quad (39b)$$

$$\chi_{N_{\text{plate}}} = \sum_{i=1}^{135} (d_{i,N_{\text{plate}}} - \Delta_{N_{\text{plate}}})^2. \quad (39c)$$

Step 4: evaluate deviation of preference variation value

$$\theta_{\eta_{\text{eff}}} = 1 - \frac{\chi_{\eta_{\text{eff}}}}{135 - 1}, \quad (40a)$$

$$\theta_{\eta_{\text{II}}} = 1 - \frac{\chi_{\eta_{\text{II}}}}{135 - 1}, \quad (40b)$$

$$\theta_{N_{\text{plate}}} = 1 - \frac{\chi_{N_{\text{plate}}}}{135 - 1}. \quad (40c)$$

Step 5: estimate the overall preference value

$$\varepsilon_{\eta_{\text{eff}}} = \frac{\theta_{\eta_{\text{eff}}}}{\theta_{\eta_{\text{eff}}} + \theta_{\eta_{\text{II}}} + \theta_{N_{\text{plate}}}}, \quad (41a)$$

$$\varepsilon_{\eta_{\text{II}}} = \frac{\theta_{\eta_{\text{II}}}}{\theta_{\eta_{\text{eff}}} + \theta_{\eta_{\text{II}}} + \theta_{N_{\text{plate}}}}, \quad (41b)$$

$$\varepsilon_{N_{\text{plate}}} = \frac{\theta_{N_{\text{plate}}}}{\theta_{\eta_{\text{eff}}} + \theta_{\eta_{\text{II}}} + \theta_{N_{\text{plate}}}}. \quad (41c)$$

Step 6: calculate the preference selection index value for each case

$$\Omega_i = d_{i,\eta_{\text{eff}}} \varepsilon_{\eta_{\text{eff}}} + d_{i,\eta_{\text{II}}} \varepsilon_{\eta_{\text{II}}} + d_{i,N_{\text{plate}}} \varepsilon_{N_{\text{plate}}}. \quad (42)$$

Table 1 displays the input parameters entered into the mathematical model for all of the collector types examined. The above system of mathematical equations is solved in the Engineering Equation Solver (*F-chart* software) which specializes in solving system of nonlinear equations. Figure 3 shows the comparison of the calculated results from the current study with the published experimental results for collector types 4 and 5. It can be stated that the results in this study are slightly overestimated compared to the experimental results. This is because the predictions are limited as the above assumptions compared with the practical applications. However, analytical predictions coincide well with the experimental approaches. Verifications have been performed about heat transfer and hydraulics of single-pass and multipass SAHs. Confirmation on the prediction of the exergy analysis model was presented in our previous study [5]. It is not repeated here for the sake of brevity. Hence, the mathematical modelling was extended to the remaining types and carried out further evaluation for all collectors.

3. Results and Discussion

This section presents the effects of air mass flow rate (m), channel height (H), and collector length (L) on the energy and exergy performance of the types under consideration. Figures 4 and 5 consider the effect of mass flow rate while the collector geometry parameters are fixed. It can be observed in Figure 4 that the effective efficiency increases with the mass flow rate. As the flow rate increases, the intensity of the heat exchange increases, thus enhancing the useful heat gain of the air received from glass cover and plates. However, the

flow rate increases as a result of rising the pressure loss. But the pressure loss penalty is negligible due to air moving in the smooth channels. At high flow rates, the efficiency increases slightly because of remarkable pressure loss. It can be seen that type 1 (triple-pass SAH) has the highest performance and type 5 (single-pass SAH) has the lowest performance. This verifies that a multipass air collector reduces top loss and higher temperature rise of air because the air receives thermal energy from four plates (two glass covers, one absorber plate, and one back plate). The double-pass types have fairly close efficiencies in which type 4 reveals better performance because this type owns two glass covers in natural convection heat transfer, thus significantly reducing top loss. At a small flow rate, the triple-pass SAH (type 1) is nearly twice as efficient as the single-pass SAH (type 5). However, at a large flow rate, the effective efficiency of type 1 is only 20% higher than that of type 5 due to the long travel of the air inside the triple-pass SAH.

Figure 5 shows at low flow (less than 0.02 kg/s) the triple-pass collector earns the greatest exergy performance followed by double-pass and single-pass collectors. This is because the exergy loss decreases with the increase in the pass number. At low flow, a collector with a large pass number has a high exergy performance due to the higher temperature of the fluid and lower temperature of absorber plate reducing exergy losses. Among the double-pass types (types 2, 3, and 4), the single glass cover SAH (type 2) has the smallest exergy performance due to the highest exergy loss from the absorber plate to the environment. Exergy performance obtained the maximum value at a certain flow rate due to trade-off of increase in frictional exergy loss and a decrease in exergy loss by heat transfer from the absorber plate to the environment with mass flow rate. At high mass flow rates, the exergy performances of the double-pass SAHs seem to be identical. This means that the absorber plate temperature of the double-pass SAHs is almost the same leading to alike exergy losses at those flow rates.

Figures 6 and 7 show the energy and exergy performance of multipass SAH with collector length (L) at fixed air flow rate and channel height. It can be seen that the effective efficiency of air collectors decreases with increasing collector length. This is supposed due to the fact that the outlet air temperature does not increase linearly with the length. The fluid absorbs heat and increases its temperature along the flow path so that the longer length results in the lower temperature difference between the hot surface and the fluid. The small temperature difference causes an increase in useful heat gain by less than the order unity of the heat transfer length. At the same length, the effective efficiency increases with increasing the number of passes. For all double-pass types, type 4 is the best and type 2 is the worst as noted above. The triple-pass type has the largest slope because of the highest pressure loss. Contrary to the effective efficiency, the exergy efficiency increases with the collector length as can be seen in Figure 7. This is owing to the fact that the exergy loss due to heat transfer from the absorber plate to the fluid decreases because of the small temperature difference between the absorber plate and the airflow. Triple-pass SAH can achieve exergy performance of up to 5%. This is a very

TABLE 1: Input parameters.

Parameter	Symbol	Value	Unit
Solar radiation	I	1000	
Absorptivity of glass cover	α_g	0.06	W/m^2
Absorptivity of absorber plate	α_p	0.95	
Ambient temperature	T_a	306	K
Wind velocity	V_w	1.5	m/s
Emissivity of glass cover	ε_g	0.9	
Transmissivity of glass cover	τ_g	0.84	
Emissivity of absorber plate	ε_p	0.94	
Emissivity of back plate	ε_b	0.94	
Channel depth	H	15 to 30	mm
Collector length	L	1.5 to 2.5	m
Air mass flow rate	m	0.01 to 0.02	kg/s
Insulation thickness	t_i	0.05	m
Thermal conductivity of insulation	k_i	0.025	$W/m\ K$
Collector width	b	0.46	m

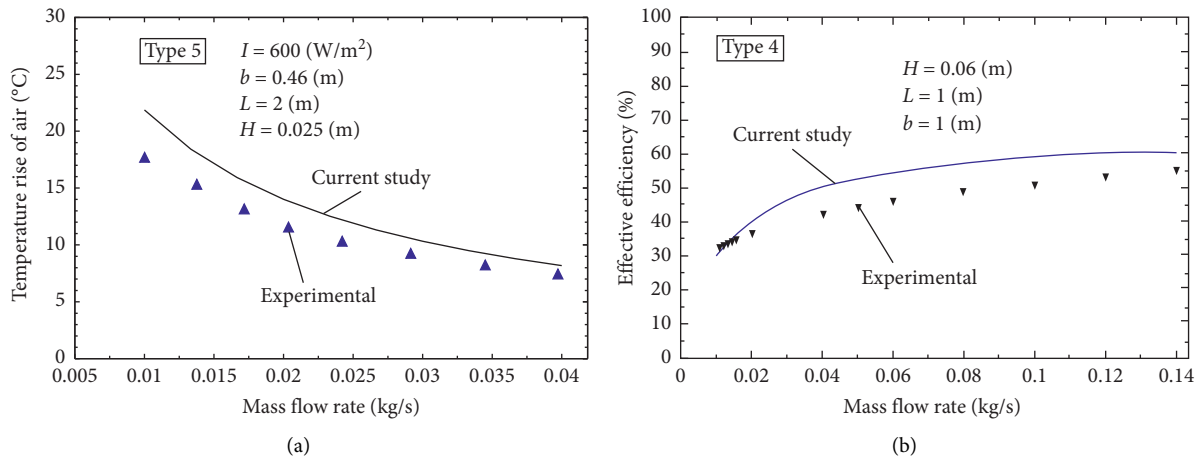


FIGURE 3: Verification of the current analytical results with experiments. (a) Comparison with experimental results [20] on type 5. (b) Comparison with experimental results [11] on type 4.

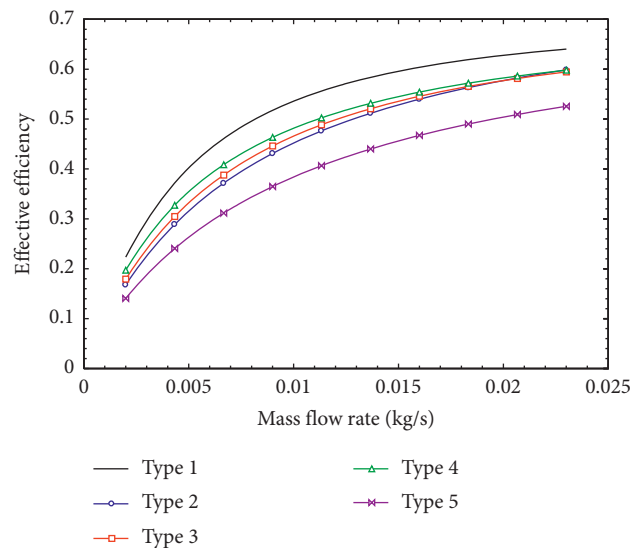


FIGURE 4: Effects of mass flow rate on effective efficiency.

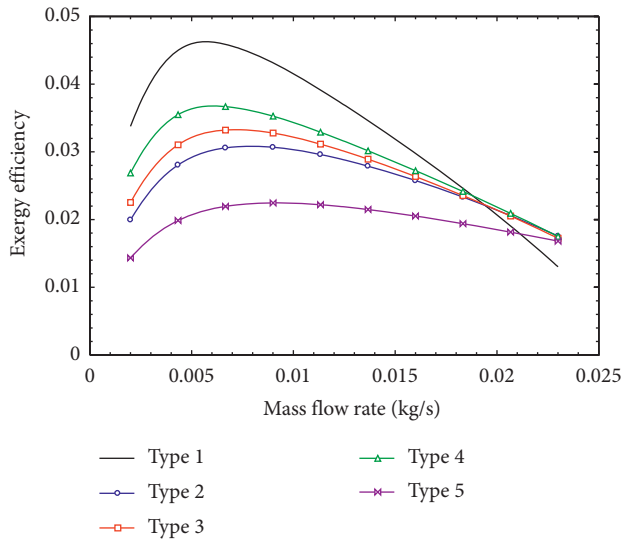


FIGURE 5: Effects of mass flow rate on exergy efficiency.

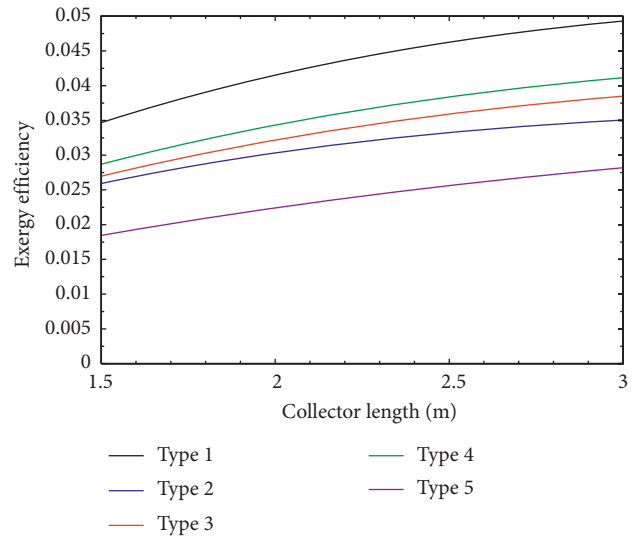


FIGURE 7: Effects of collector length on exergy efficiency.

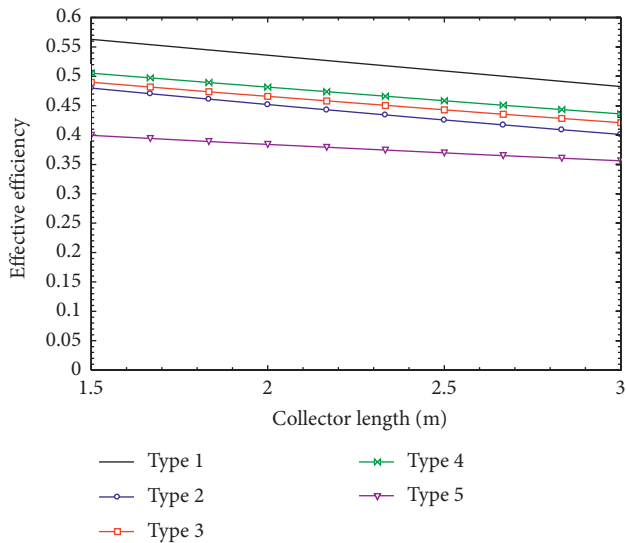


FIGURE 6: Effects of collector length on effective efficiency.

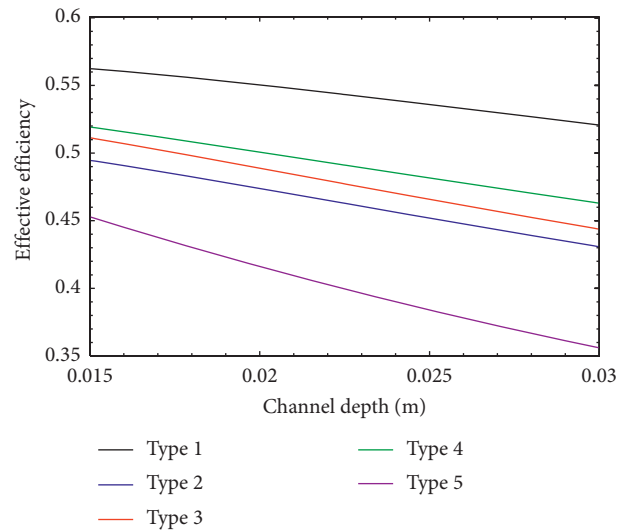


FIGURE 8: Effects of channel depth on effective efficiency.

encouraging performance for a solar air heater. As it is known, SAH's exergy efficiency is very low, say 2%, due to the great exergy destruction of converting solar radiation into heat [7].

The effect of channel depth (H) on effective and exergy efficiencies is shown in Figures 8 and 9 with fixed air flow rate and collector length. Increasing the channel depth reduces the velocity of air blowing through hot surfaces leading to low convection heat transfer coefficient. Also, the low air velocity increases the surface temperatures resulting in increased heat losses such as top loss and the loss from back plate to the environment. Increasing the temperature of the plates with the depth increases the exergy losses due to heat transfer to the fluid and heat loss. Hence, the exergy performance decreases with the increase in the air channel

depth as shown in Figure 9. However, it is worth noting that the exergy efficiency of the triple-pass SAH (type 1) reaches an extreme at the depth of 19 mm. This can be explained by the fact that at a depth of less than 19 mm, the fluid passing in the 3 passes reduces the temperature of the plates and the smallest top loss compared to other types. Thus, the exergy performance of the triple-pass type increases with the air channel depth from 15 mm to 19 mm.

The analysis above showed the influence of the design, operation parameters, and collector type on the performance. The characteristics of each collector and the maximum efficiencies have been indicated. To initialize the optimization for searching the final solution, in this study, there are 5 types of collector and 3 design and operation parameters including mass flow rate (range $m = 0.01 - 0.02$ kg/s), collector length

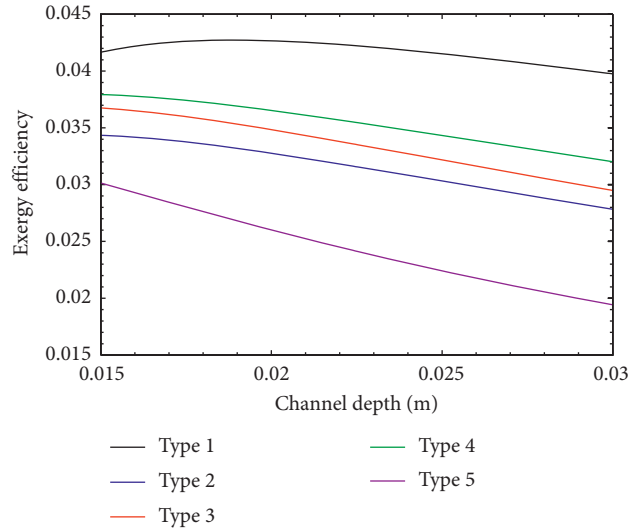


FIGURE 9: Effects of channel depth on exergy efficiency.

TABLE 2: Typical cases to be optimized using the PSI method.

Case, <i>i</i>	Type	Design parameters				Objectives	
		<i>m</i> , kg/s	<i>L</i> , m	<i>H</i> , m	η_{eff}	N_{plate}	η_{II}
1	1	0.01	1.5	0.02	0.5796	4	0.03562
2	1	0.01	1.5	0.025	0.5627	4	0.03469
3	1	0.01	1.5	0.03	0.5456	4	0.03316
4	1	0.01	2	0.02	0.5504	4	0.04266
5	1	0.01	2	0.025	0.5359	4	0.04152
6	1	0.01	2	0.03	0.5207	4	0.03975
7	1	0.01	2.5	0.02	0.5209	4	0.04733
8	1	0.01	2.5	0.025	0.509	4	0.04626
9	1	0.01	2.5	0.03	0.496	4	0.04446
10	1	0.015	1.5	0.02	0.6276	4	0.02198
11	1	0.015	1.5	0.025	0.6151	4	0.02459
12	1	0.015	1.5	0.03	0.6017	4	0.02516
13	1	0.015	2	0.02	0.607	4	0.0297
14	1	0.015	2	0.025	0.5958	4	0.03188
15	1	0.015	2	0.03	0.5835	4	0.03209
16	1	0.015	2.5	0.02	0.5854	4	0.03564
17	1	0.015	2.5	0.025	0.5759	4	0.03763
18	1	0.015	2.5	0.03	0.5648	4	0.03765
19	1	0.02	1.5	0.02	0.6513	4	0.005287
20	1	0.02	1.5	0.025	0.6424	4	0.01326
21	1	0.02	1.5	0.03	0.6321	4	0.01661
22	1	0.02	2	0.02	0.6359	4	0.01349
23	1	0.02	2	0.025	0.6278	4	0.02069
24	1	0.02	2	0.03	0.6181	4	0.02352
25	1	0.02	2.5	0.02	0.6195	4	0.01999
26	1	0.02	2.5	0.025	0.6125	4	0.02675
27	1	0.02	2.5	0.03	0.6036	4	0.02927

($L = 1.5 - 2.5$ m), and air channel height ($H = 20 - 30$ mm) each at three levels. Hence, there are 135 cases in total which need to select the best one. Typically, Table 2 presents 27 cases for type 1 with inputs and outputs.

Table 3 shows the calculated values from steps 3–5 of the PSI method for the objective functions under consideration. Table 4 exhibits selective 10 cases including 5 best cases (the

highest preference selection indices) and 5 worst cases (the smallest preference selection indices). It is confirmed that type 1 with lowest flow rate, maximum collector length, and moderate channel depth reaches the final optimal solution. This is also consistent with the statement in the above parametric study. Otherwise, type 1 with the largest airflow is the worst case. In addition, single-pass SAH (type 5) is also

TABLE 3: Values of χ , θ , and ε of objective functions.

Objectives	Preference variation value χ	Deviation of preference variation value θ	Overall preference value ε
Effective efficiency η_{Eff}	1.435	0.9893	0.3356
Exergy efficiency η_{II}	2.025	0.9849	0.3341
Number of plates N_{plate}	3.582	0.9733	0.3302

TABLE 4: Results of preference selection index Ω and ranking for 5 best cases (ranking 1 to 5) and 5 worst cases (ranking 131 to 135).

Case, i	Collector type	Air mass flow rate m , kg/s	Collector length L , m	Channel depth H , m	Objectives			Ω	Ranking
					η_{Eff}	N_{plate}	η_{II}		
7	1	0.01	2.5	0.02	0.5209	4	0.04733	0.8493	1
61	3	0.01	2.5	0.02	0.4629	3	0.03864	0.8423	2
70	3	0.015	2.5	0.02	0.5344	3	0.03273	0.8379	3
8	1	0.01	2.5	0.025	0.509	4	0.04626	0.8357	4
4	1	0.01	2	0.02	0.5504	4	0.04266	0.8319	5
120	5	0.015	1.5	0.03	0.4412	3	0.01501	0.6662	131
100	4	0.02	1.5	0.02	0.6125	4	0.01302	0.6571	132
114	5	0.01	2	0.03	0.356	3	0.01942	0.6531	133
111	5	0.01	1.5	0.03	0.3694	3	0.01589	0.6354	134
19	1	0.02	1.5	0.02	0.6513	4	0.005287	0.6231	135

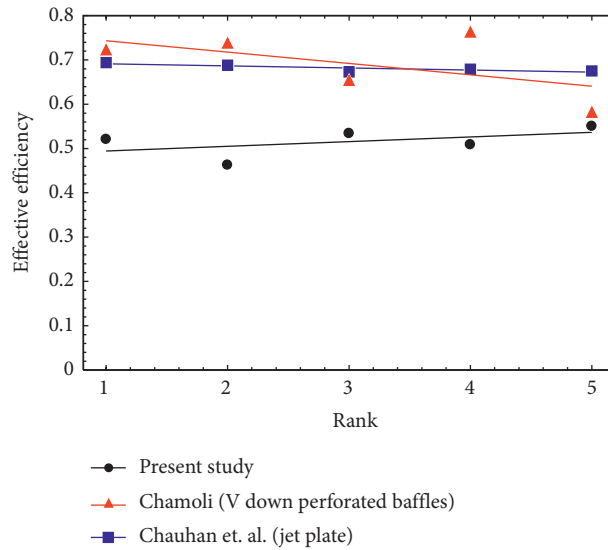


FIGURE 10: Comparison of five best cases of the present flat plate, jet plate [41], and V down perforated baffles on absorber plate [40].

three of five worst cases (cases 120, 114, and 111). From the PSI method, it can be concluded that types 1 and 3 with suitable geometry and operating parameters are the two SAHs that should be selected in multipass air collector configurations.

Figure 10 shows a comparison of optimal results from the PSI method for the objective function of effective efficiency. Two configurations compared to the current study were single-pass SAHs with impinging air jet plate [41] and V down perforated baffles on absorber plate [40]. It can be seen that the effective efficiency of flat-plate air collector in the present study is lower than that of collectors with special modification and insertion. This results in low convection heat transfer coefficient of a smooth duct compared to others. However, with the change of flow configuration to

types 1 (triple pass) or 3 (double pass), the flat-plate air collector can compete with other types. Especially at rank 5, the effective efficiency of triple-pass SAH is approximately equal to single-pass SAH with the roughness of V down perforated baffles.

4. Conclusions

The various configurations of the multipass flat-plate air collector have been analysed in this paper. The configurations include the number of passes from 1 to 3, and the number of glass covers is 1 or 2 with/without back plate. Independent parameters comprise collector length, air channel depth, and air mass flow rate to examine the efficiencies. Multiobjective optimization of the maximum

effective, exergy efficiencies, and minimum number of plates, i.e., glass cover, absorber plate, and back plate, were conducted using the preference selection index method. The main results are drawn as follows:

- (i) Triple-pass SAH has the highest effective efficiency followed by double-pass type and single-pass type. The efficiency of the triple-pass type is 30% higher than that of single-pass type. Among the double-pass types, type 4 obtained the largest effective efficiency.
- (ii) Exergy performance is maximum when the air flow rate is between 0.005 and 0.01 kg/s.
- (iii) The triple-pass type has the highest exergy performance that is twice as high as the single-pass type. Type 4 also yielded the biggest effective efficiency among the double-pass SAHs.
- (iv) Effective efficiency decreases when increasing the collector length. In contrast, exergy performance increases with the length.
- (v) As the collector depth increases, the effective efficiency decreases. The exergy performance of the triple-pass type is maximum at the collector depth of 19 mm. For other types, the exergy performance decreases when increasing the collector depth.

Adopting the multiobjective optimization, it is obviously confirmed that the triple-pass solar air heater is the best arrangement at low flow rate and the worst case at high flow rate. This is because at low flow rate, the effective efficiency and exergy efficiency of triple-pass type are quite large compared to other types. But at high flow rate, the exergy performance is too poor with a considerable investment cost.

Appendix

A. Thermal Transport Modelling for Solar Air Heater Types 2 to 5

A.1. Type 2. Glass cover

$$\alpha_g I = h_w (T_g - T_a) + h_{r,g,s} (T_g - T_s) + h_{c,g,f1} (T_g - T_{f1}) + h_{r,g,p} (T_g - T_p). \quad (\text{A.1})$$

Air in 1st pass

$$Q_1 = mc_p (T_{f1,o} - T_a) = Lbh_{c,g,f1} (T_g - T_{f1}) + Lbh_{c,p,f1} (T_p - T_{f1}). \quad (\text{A.2})$$

Absorber plate

$$\alpha_g \tau_g I = h_{c,p,f1} (T_p - T_{f1}) + h_{r,p,g} (T_p - T_g) + h_{c,p,f2} (T_p - T_{f2}) + h_{r,p,b} (T_p - T_b). \quad (\text{A.3})$$

Air in 2nd pass

$$Q_2 = mc_p (T_{f2,o} - T_{f1,o}) = Lbh_{c,p,f2} (T_p - T_{f2}) + Lbh_{c,b,f2} (T_b - T_{f2}). \quad (\text{A.4})$$

Back plate

$$h_{r,p,b} (T_p - T_b) = h_{c,b,f2} (T_b - T_{f2}) + h_b (T_b - T_a). \quad (\text{A.5})$$

A.2. Type 3. Upper glass cover

$$\alpha_g I = h_w (T_{g1} - T_a) + h_{r,g1,s} (T_{g1} - T_s) + h_{c,g1,f1} (T_{g1} - T_{f1}) + h_{r,g1,g2} (T_{g1} - T_{g2}). \quad (\text{A.6})$$

Air in 1st pass

$$Q_1 = mc_p (T_{f1,o} - T_a) = Lbh_{c,g1,f1} (T_{g1} - T_{f1}) + Lbh_{c,g2,f1} (T_{g2} - T_{f1}). \quad (\text{A.7})$$

Lower glass cover

$$\alpha_g \tau_g I = h_{c,g2,f1} (T_{g2} - T_{f1}) + h_{r,g1,g2} (T_{g2} - T_{g1}) + h_{c,f2,g2} (T_{g2} - T_{f2}) + h_{r,g2,p} (T_{g2} - T_p). \quad (\text{A.8})$$

Air in 2nd pass

$$\alpha_p \tau_g^2 I = h_{c,p,f2} (T_p - T_{f2}) + h_{r,g2,p} (T_p - T_{g2}) + h_b (T_p - T_a). \quad (\text{A.9})$$

A.3. Type 4. Upper glass cover

$$\alpha_g I = h_w (T_{g1} - T_a) + h_{r,g1,s} (T_{g1} - T_s) + (h_{c,g1,g2} + h_{r,g1,g2}) (T_{g1} - T_{g2}). \quad (\text{A.10})$$

Lower glass cover

$$\alpha_g \tau_g I = (h_{c,g1,g2} + h_{r,g1,g2}) (T_{g2} - T_{g1}) + h_{r,g2,p} (T_{g2} - T_p) + h_{c,g2,f} (T_{g2} - T_{f1}). \quad (\text{A.11})$$

Air in 1st pass

$$Q_1 = mc_p (T_{f1,o} - T_a) = Lbh_{c,g2,f1} (T_{g2} - T_{f1}) + Lbh_{c,p,f1} (T_p - T_{f1}). \quad (\text{A.12})$$

Absorber plate

$$\alpha_p \tau_g^2 I = h_{c,p,f1}(T_p - T_{f1}) + h_{r,g2,p}(T_p - T_{g2}) + h_{c,p,f2}(T_p - T_{f2}) + h_{r,p,b}(T_p - T_b). \quad (\text{A.13})$$

Air in 2nd pass

$$Q_2 = mc_p(T_{f2,o} - T_{f1,o}) = Lbh_{c,p,f2}(T_p - T_{f2}) + Lbh_{c,b,f2}(T_b - T_{f2}). \quad (\text{A.14})$$

Back plate

$$h_{r,p,b}(T_p - T_b) = h_{c,b,f2}(T_b - T_{f2}) + h_b(T_b - T_a). \quad (\text{A.15})$$

A.4. Type 5. Upper glass cover

$$\alpha_g I = h_w(T_{g1} - T_a) + h_{r,g1,s}(T_{g1} - T_s) + (h_{c,g1,g2} + h_{r,g1,g2})(T_{g1} - T_{g2}). \quad (\text{A.16})$$

Lower glass cover

$$\alpha_g \tau_g I = (h_{c,g1,g2} + h_{r,g1,g2})(T_{g2} - T_{g1}) + h_{r,g2,p}(T_{g2} - T_p) + h_{c,g2,f}(T_{g2} - T_f). \quad (\text{A.17})$$

Air

$$Q = mc_p(T_o - T_a) = Lbh_{c,g2,f}(T_{g2} - T_f) + Lbh_{c,p,f}(T_p - T_f). \quad (\text{A.18})$$

Absorber plate

$$\alpha_p \tau_g^2 I = h_{c,p,f}(T_p - T_f) + h_{r,g2,p}(T_p - T_{g2}) + h_b(T_p - T_a). \quad (\text{A.19})$$

Nomenclature

A_c :	Area of the absorber plate (m ²)
b :	Collector width (m)
c_p :	Specific heat at a constant pressure (J/kg-K)
D_h :	Hydraulic diameter (m)
EX:	Exergy (W)
f :	Friction factor
h :	Heat transfer coefficient (W/m ² -K)
H :	Channel depth (m)
I :	Solar radiation (W/m ²)
k :	Thermal conductivity (W/m-K)
L :	Collector length (m)
m :	Air mass flow rate (kg/s)
n_{glass} :	Number of glasses
n_{pass} :	Number of passes
N_{plate} :	Total number of plates (absorber plate, back plate, glass cover)
P :	Pressure (Pa)
Pr:	Prandtl number
Q :	Heat transfer rate (W)
Re:	Reynolds number

T :	Temperature (K)
t :	Thickness (m)
U_L :	Overall heat loss coefficient (W/m ² -K)
U_t :	Top loss coefficient (W/m ² -K)
V :	Velocity (m/s)

Greek symbols

α :	Absorptivity
ρ :	Air density (kg/m ³)
Δ :	Difference
μ :	Dynamic viscosity (Pa.s)
η :	Efficiency
ε :	Emissivity
Ω :	Preference selection index
σ :	Stefan constant
τ :	Transmissivity

Subscripts

a :	Ambient
b :	Back plate
c :	Convection
Eff:	Effective
f :	Fluid (air)
g :	Glass cover
I :	First law
i :	Insulation
II:	Second law
o :	Outlet
p :	Absorber plate
r :	Radiation
s :	Sky
w :	Wind.

Data Availability

No data were used to support this study.

Conflicts of Interest

The authors declare that they have no conflicts of interest.

Acknowledgments

This research is funded by the Vietnam National University Ho Chi Minh City (VNU-HCM) under grant number B2021-20-06.

References

- [1] K. A. Joudi and A. A. Farhan, "Greenhouse heating by solar air heaters on the roof," *Renewable Energy*, vol. 72, pp. 406–414, 2014.
- [2] S. Pramuang and R. H. B. Exell, "The regeneration of silica gel desiccant by air from a solar heater with a compound parabolic concentrator," *Renewable Energy*, vol. 32, no. 1, pp. 173–182, 2007.
- [3] T. Koyuncu, "Performance of various design of solar air heaters for crop drying applications," *Renewable Energy*, vol. 31, no. 7, pp. 1073–1088, 2006.
- [4] N. Minh Phu and N. Thanh Luan, "A review of energy and exergy analyses of a roughened solar air heater," *Journal of*

- Advanced Research in Fluid Mechanics and Thermal Sciences*, vol. 77, no. 2, pp. 160–175, 2020.
- [5] N. M. Phu, T. T. Bao, H. N. Hung, N. T. Tu, and N. Van Hap, “Analytical predictions of exergoeconomic performance of a solar air heater with surface roughness of metal waste,” *Journal of Thermal Analysis and Calorimetry*, 2020.
 - [6] N. T. Luan and N. M. Phu, “Thermohydraulic correlations and exergy analysis of a solar air heater duct with inclined baffles,” *Case Studies in Thermal Engineering*, vol. 21, Article ID 100672, 2020.
 - [7] N. M. Phu and N. Van Hap, “Performance evaluation of a solar air heater roughened with conic-curve profile ribs based on efficiencies and entropy generation,” *Arabian Journal for Science and Engineering*, vol. 45, no. 11, pp. 9023–9035, 2020.
 - [8] R. Chandra, N. P. Singh, and M. S. Sodha, “Thermal performance of a triple-pass solar air collector,” *Energy Conversion and Management*, vol. 30, no. 1, pp. 41–48, 1990.
 - [9] C. Choudhury, P. M. Chauhan, H. P. Garg, and S. N. Garg, “Cost-benefit ratio of triple pass solar air heaters,” *Energy Conversion and Management*, vol. 37, no. 1, pp. 95–116, 1996.
 - [10] F. K. Forson, M. A. A. Nazha, and H. Rajakaruna, “Experimental and simulation studies on a single pass, double duct solar air heater,” *Energy Conversion and Management*, vol. 44, no. 8, pp. 1209–1227, 2003.
 - [11] M. R. I. Ramadan, A. A. El-Sebaei, S. Aboul-Enein, and E. El-Bialy, “Thermal performance of a packed bed double-pass solar air heater,” *Energy*, vol. 32, no. 8, pp. 1524–1535, 2007.
 - [12] K. Sopian, M. A. Alghoul, E. M. Alfeqi, M. Y. Sulaiman, and E. A. Musa, “Evaluation of thermal efficiency of double-pass solar collector with porous-nonporous media,” *Renewable Energy*, vol. 34, no. 3, pp. 640–645, 2009.
 - [13] B. M. Ramani, A. Gupta, and R. Kumar, “Performance of a double pass solar air collector,” *Solar Energy*, vol. 84, no. 11, pp. 1929–1937, 2010.
 - [14] A. A. El-Sebaei, S. Aboul-Enein, M. R. I. Ramadan, S. M. Shalaby, and B. M. Moharram, “Investigation of thermal performance of double pass-flat and v-corrugated plate solar air heaters,” *Energy*, vol. 36, no. 2, pp. 1076–1086, 2011.
 - [15] A. A. El-Sebaei, S. Aboul-Enein, M. R. I. Ramadan, S. M. Shalaby, and B. M. Moharram, “Thermal performance investigation of double pass-finned plate solar air heater,” *Applied Energy*, vol. 88, no. 5, pp. 1727–1739, 2011.
 - [16] C.-D. Ho, C.-S. Lin, Y.-C. Chuang, and C.-C. Chao, “Performance improvement of wire mesh packed double-pass solar air heaters with external recycle,” *Renewable Energy*, vol. 57, pp. 479–489, 2013.
 - [17] Ho-M. Yeh, “Effect of pass number on collector efficiency in downward-type multipass solar air heaters,” *Journal of Applied Science and Engineering*, vol. 17, no. 2, 2014.
 - [18] P. Velmurugan and R. Kalaivanan, “Energy and exergy analysis of multi-pass flat plate solar air heater-an analytical approach,” *International Journal of Green Energy*, vol. 12, no. 8, pp. 810–820, 2014.
 - [19] P. Velmurugan and R. Kalaivanan, “Thermal performance studies on multi-pass flat-plate solar air heater with longitudinal fins: an analytical approach,” *Arabian Journal for Science and Engineering*, vol. 40, no. 4, pp. 1141–1150, 2015.
 - [20] P. Velmurugan and R. Kalaivanan, “Energy and exergy analysis of solar air heaters with varied geometries,” *Arabian Journal for Science and Engineering*, vol. 40, no. 4, pp. 1173–1186, 2015.
 - [21] P. Velmurugan and R. Kalaivanan, “Energy and exergy analysis in double-pass solar air heater,” *Sadhana*, vol. 41, no. 3, 2016.
 - [22] A. K. Raj, G. Kunal, M. Srinivas, and S. Jayaraj, “Performance analysis of a double-pass solar air heater system with asymmetric channel flow passages,” *Journal of Thermal Analysis and Calorimetry*, vol. 136, no. 1, pp. 21–38, 2018.
 - [23] S. Abo-Elfadl, M. S. Yousef, and H. Hassan, “Assessment of double-pass pin finned solar air heater at different air mass ratios via energy, exergy, economic, and environmental (4E) approaches,” *Environmental Science and Pollution Research*, vol. 28, 2020.
 - [24] H. Hassan and S. Abo-Elfadl, “Experimental study on the performance of double pass and two inlet ports solar air heater (SAH) at different configurations of the absorber plate,” *Renewable Energy*, vol. 116, pp. 728–740, 2018.
 - [25] D. K. Rabha, D. Pathak, R. Baruah, T. Kalita, and A. Sharma, “Experimental investigation of the performance of a double-pass unglazed transpired solar air heater,” in *Lecture Notes in Mechanical Engineering*, pp. 571–584, Springer, Singapore, 2019.
 - [26] S. Abo-Elfadl, H. Hassan, and M. F. El-Dosoky, “Study of the performance of double pass solar air heater of a new designed absorber: an experimental work,” *Solar Energy*, vol. 198, pp. 479–489, 2020.
 - [27] A. I. N. Korti, “Numerical 3-D heat flow simulations on double-pass solar collector with and without porous media,” *Journal of Thermal Engineering*, vol. 1, no. 1, p. 10, 2015.
 - [28] E. M. S. El-Said, “Numerical investigations of fluid flow and heat transfer characteristics in solar air collector with curved perforated baffles,” *Engineering Reports*, vol. 2, no. 4, 2020.
 - [29] A. Khanlari, A. Sözen, F. Afshari, C. Şirin, A. D. Tuncer, and A. Gungor, “Drying municipal sewage sludge with v-groove triple-pass and quadruple-pass solar air heaters along with testing of a solar absorber drying chamber,” *Science of The Total Environment*, vol. 709, Article ID 136198, 2020.
 - [30] A. D. Tuncer, A. Sözen, A. Khanlari, A. Amini, and C. Şirin, “Thermal performance analysis of a quadruple-pass solar air collector assisted pilot-scale greenhouse dryer,” *Solar Energy*, vol. 203, pp. 304–316, 2020.
 - [31] S. Singh, “Experimental and numerical investigations of a single and double pass porous serpentine wavy wiremesh packed bed solar air heater,” *Renewable Energy*, vol. 145, pp. 1361–1387, 2020.
 - [32] A. Heydari, M. Mesgarpour, and S. Wongwises, “Geometry optimization of double pass solar air heater with helical flow path,” *Solar Energy*, vol. 213, pp. 67–80, 2021.
 - [33] S. Kesavan, T. V. Arjunan, and S. Vijayan, “Thermodynamic analysis of a triple-pass solar dryer for drying potato slices,” *Journal of Thermal Analysis and Calorimetry*, vol. 136, no. 1, pp. 159–171, 2018.
 - [34] P. Sudhakar and M. Cheralathan, “Thermal performance enhancement of solar air collector using a novel V-groove absorber plate with pin-fins for drying agricultural products: an experimental study,” *Journal of Thermal Analysis and Calorimetry*, vol. 140, no. 5, pp. 2397–2408, 2019.
 - [35] M. M. Hegazy, A. El-Sebaei, M. R. Ramadan, S. Aboul-Enein, and A. E.-M. Khallaf, “Comparative study of three different designs of a hybrid PV/T double-pass finned plate solar air heater,” *Environmental Science and Pollution Research*, vol. 27, no. 26, pp. 32270–32282, 2020.
 - [36] W. H. McAdams, *Heat Transmission*, McGraw-Hill, New York, NY, USA, 3rd edition, 1954.
 - [37] F. W. Dittus and L. M. K. Boelter, *Heat Transfer in Automobile Radiators of the Tubular Type*, University of California Publications on Engineering, 1930.

- [38] M. M. Matheswaran, T. V. Arjunan, and D. Somasundaram, "Analytical investigation of solar air heater with jet impingement using energy and exergy analysis," *Solar Energy*, vol. 161, pp. 25–37, 2018.
- [39] J. A. Duffie and W. A. Beckman, *Solar Engineering of Thermal Processes*, John Wiley & Sons, Hoboken, NY, USA, 4th edition, 2013.
- [40] S. Chamoli, "Preference selection index approach for optimization of V down perforated baffled roughened rectangular channel," *Energy*, vol. 93, pp. 1418–1425, 2015.
- [41] R. Chauhan, T. Singh, N. S. Thakur, and A. Patnaik, "Optimization of parameters in solar thermal collector provided with impinging air jets based upon preference selection index method," *Renewable Energy*, vol. 99, pp. 118–126, 2016.
- [42] K. Maniya and M. G. Bhatt, "A selection of material using a novel type decision-making method: preference selection index method," *Materials & Design*, vol. 31, no. 4, pp. 1785–1789, 2010.
- [43] S. Mufazzal and S. M. Muzakkir, "Identification of optimal alternative as a prospective candidate for further design improvements using preference selection index method," in *Proceedings of the 2017 International Conference on Innovations in Control, Communication and Information Systems (ICICCI)*, Bangkok, Thailand, August 2017.

Research Article

Design of Real-Time Control Based on DP and ECMS for PHEVs

Wei Wang ¹, Zhenjiang Cai ¹, and Shaofei Liu ²

¹College of Mechanical and Electric Engineering, Hebei Agriculture University, Baoding 071001, China

²BAIC Motor Corporation Powertrain Center, Beijing 101106, China

Correspondence should be addressed to Wei Wang; wlovewj1314@163.com

Received 3 November 2020; Revised 7 January 2021; Accepted 19 January 2021; Published 3 February 2021

Academic Editor: ANTONIO VALDERRABANO-GONZALEZ

Copyright © 2021 Wei Wang et al. This is an open access article distributed under the Creative Commons Attribution License, which permits unrestricted use, distribution, and reproduction in any medium, provided the original work is properly cited.

A real-time control is proposed for plug-in-hybrid electric vehicles (PHEVs) based on dynamic programming (DP) and equivalent fuel consumption minimization strategy (ECMS) in this study. Firstly, the resulting controls of mode selection and series mode are stored in tables through offline simulation of DP, and the parallel HEV mode uses ECMS-based real-time algorithm to reduce the application of maps and avoid manual adjustment of parameters. Secondly, the feedback energy management system (FMES) is built based on feedback from SoC, which takes into account the charge and discharge reaction (CDR) of the battery, and in order to make full use of the energy stored in the battery, the reference SoC is introduced. Finally, a comparative simulation on the proposed real-time controller is conducted against DP, the results show that the controller has a good performance, and the fuel consumption value of the real-time controller is close to the value using DP. The engine operating conditions are concentrated in the low fuel consumption area of the engine, and when the driving distance is known, the SoC can follow the reference SoC well to make full use of the energy stored in the battery.

1. Introduction

Hybrid electric vehicles use at least two power sources, usually driven by an internal-combustion engine associated with a motor, in order to minimize the fuel consumption and/or emissions. The energy management of a PHEV is often divided into two categories. The first concerns global optimization based on offline simulation. In this case, the vehicle speed is regulated to follow a speed cycle using a torque at the wheel controller. Examples of such methods include Pontryagin's minimum principle [1, 2], dynamic programming (DP) [3–7], and genetic algorithm [8]. A second class of algorithms is real-time optimal control strategy that can be used to control a vehicle. Several algorithms have been proposed, some of which are based on rulers [9, 10] and Equivalent fuel Consumption Minimization Strategy (ECMS) [11–16], and others are approximate real-time control strategies based on DP [17–19]. ECMS has strong dynamic adaptability and can get similar results with DP in theory [20]; therefore, it has been extensively studied.

In this paper, a real-time control for PHEV based on DP and ECMS is studied. Real-time implementation has remained a major challenge in the design of complex control systems. To address this hurdle, simple and efficient models and fast optimization algorithms are developed. The real-time controllers must be simple in order to be implemented with limited computation and memory resources. Moreover, manual tuning of control parameters should be avoided to reduce the calibration work efforts. DP can obtain global optimal solutions, and ECMS can realize real-time computing and can theoretically get similar results with DP. This study combines the advantages of both to establish a real-time controller.

The contribution of the paper is to use the DP algorithm solving the optimal controls of driving cycle to establish the framework of FEMS. In order to fully utilize the potential of the battery, the charge and discharge reaction (CDR) of the battery is taken into account in the DP-based FEMS, and the reference SoC is introduced into the FEMS. The ECMS real-time algorithm is used for the parallel HEV mode to reduce the application of maps and avoid manual adjustment of parameters.

2. Hybrid Vehicle Modeling

For this study, two levels of modeling are considered. The first, called plant model (PM), shown in Figure 1, is used to simulate the vehicle over speed cycles [21]. It only represents the longitudinal behavior and is designed for the energetic-consumption simulation. It includes the following:

- Dynamic response of engine torque
- Motor model based on the characteristic map provided by the motor supplier
- Dedicated hybrid transmission (DHT) model (including the shift strategy)
- Full dynamic vehicle model
- High-voltage lithium battery model based on battery charge and discharge characteristics

An important part of PM is the fuel consumption model of engine. This is done only for fuel consumption using classical map and is validated according to real data results, as shown in Figure 2.

Based on this PM, a simplified model, called Energy Consumption Model (ECM), has been derived. The purpose of this paper is not the vehicle modeling, but control law synthesis. So, only ECM is used to derive the optimization algorithm. PM is omitted here, but PM is used for the simulation results at the end of this paper. Figure 1 is the simulation model of PHEV.

2.1. Energetic Consumption Modeling. The power flows of the PHEV and connections between components are shown in Figure 3. The vehicle has three energy converters, an internal-combustion engine (ENG), a drive electric motor (DEM) connected through a dedicated hybrid transmission (DHT), and a generator electric motor (GEM) as a generator connected to the engine via DHT. Both electric machines can work in both motoring and generating modes. The main component parameters of the powertrain are listed in Table 1.

As shown in Figure 3, the powertrain allows the vehicle to be driven in the following four modes:

- Mode 1: one-motor pure electric mode: only the DEM is connected to DHT.
- Mode 2: two-motor pure electric mode: the DEM and GEM are connected to DHT.
- Mode 3: series HEV: only the DEM is connected to DHT. The ENG and GEM work as an auxiliary power unit (APU), producing electric power.
- Mode 4: parallel HEV: all energy converters are connected to the DHT.

The following relations can be described as shown in Figure 3:

$$\omega_{wh}(k) = \frac{\omega_e(k)}{i_{gb}(n) \cdot i_{red}} = \frac{\omega_{gem}(k)}{i_{gem} \cdot i_{red}} = \frac{\omega_{dem}(k)}{i_{gb}(j) \cdot i_{red}}, \quad (1)$$

$$\begin{cases} P_m(k) = P_{gem}(k) + P_{dem}(k), \\ T_m(k) = \frac{i_{gem}}{i_{gb}(j)} T_{gem}(k) + T_{dem}(k), \end{cases} \quad (2)$$

$$T_{wh}(k) = i_{red} \eta_{red} \eta_{gb} (T_e(k) i_{gb}(n(k)) + T_m(k) i_{gb}(j(k))), \quad (3)$$

where n and j correspond to the engine transmission gear and the motor transmission gear, respectively.

3. Optimal Control Problem

The objective in energy management for hybrid vehicles is to minimize the cumulative fuel consumption, which is equivalent to minimizing the power consumption of the engine.

The battery is considered as a dynamical system, with the state of charge

$$x(k+1) = x(k) + P_{BT} \Delta t, \quad (4)$$

$$x(k+1) = x(k) + \eta_{BT} P_m(T_m(k), \omega_{dem}(k)) \Delta t. \quad (5)$$

From (1) and (3), formula (5) can be expressed as follows:

$$x(k+1) = x(k) + \eta_{BT} P_m(T_e(k), \omega_e(k)) \Delta t. \quad (6)$$

The objective function is

$$J = \sum_{k=0}^{N-1} \dot{m}_f(T_e(k), \omega_e(k)) \Delta t. \quad (7)$$

The speeds and torques of both engine and motor are limited by the following mechanical constraints.

Constraints on speeds:

$$\omega_{m_min} \leq \omega_m \leq \omega_{m_max}, \quad (8)$$

$$0 \leq \omega_e \leq \omega_{e_max}. \quad (9)$$

Constraints on torques:

$$T_{m_min} \leq T_m \leq T_{m_max}, \quad (10)$$

$$0 \leq T_e \leq T_{e_max}. \quad (11)$$

However, the constraints on state of charge are

$$x_{min} \leq x \leq x_{max}, \quad (12)$$

$$x(N) - x(0) = \Delta \text{SoC}. \quad (13)$$

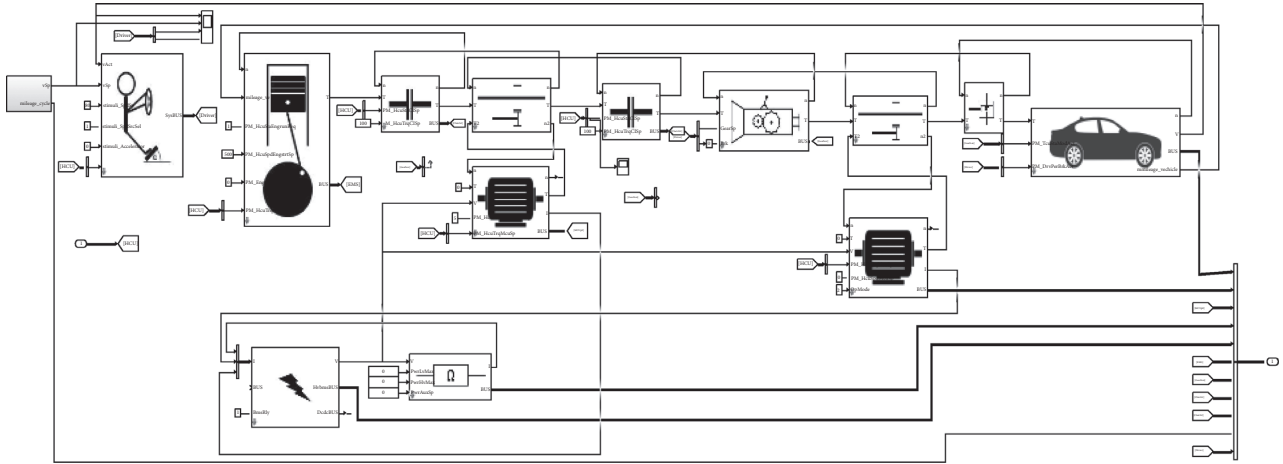


FIGURE 1: Simulation model of PHEV in MATLAB-Simulink.

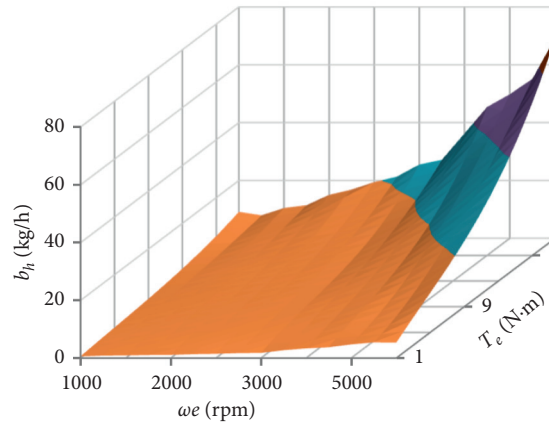


FIGURE 2: Fuel consumption map.

With ΔSoC , the desired electric energy consumption over the speed cycle is called overall SoC variation.

The relationships between the different torques and speeds, (2)–(4), allow writing the constraints (8) and (11) as

$$T'_{e_min}(k) \leq T_e(k) \leq T'_{e_max}(k), \quad (14)$$

where

$$T'_{e_min} = \max \left\{ 0, \frac{(T_{wh}(k)/i_{red}\eta_{red}\eta_{gb}) - T_{m_max}(k)i_{gb}(j(k))}{i_{gb}(n(k))} \right\}, \quad (15)$$

$$T'_{e_max} = \min \left\{ T_{e_max}, \frac{(T_{wh}(k)/i_{red}\eta_{red}\eta_{gb}) - T_{m_min}(k)i_{gb}(j(k))}{i_{gb}(n(k))} \right\}. \quad (16)$$

For a given gear ratio i_{gb} , T'_{e_min} and T'_{e_max} define the interval of admissible values for engine torque. Several cases may happen, as follows:

$T'_{e_min} = T'_{e_max} = 0$: pure electric mode-engine speed is not high enough to close the clutch

$T'_{e_min} = T'_{e_max} \geq 0$: the desired torque $T_{wh}(k)$ should be equal to the maximum torque of the powertrain determined by i_{gb}

$T'_{e_min} \geq T'_{e_max}$: the desired torque $T_{wh}(k)$ is greater than the powertrain torque capability

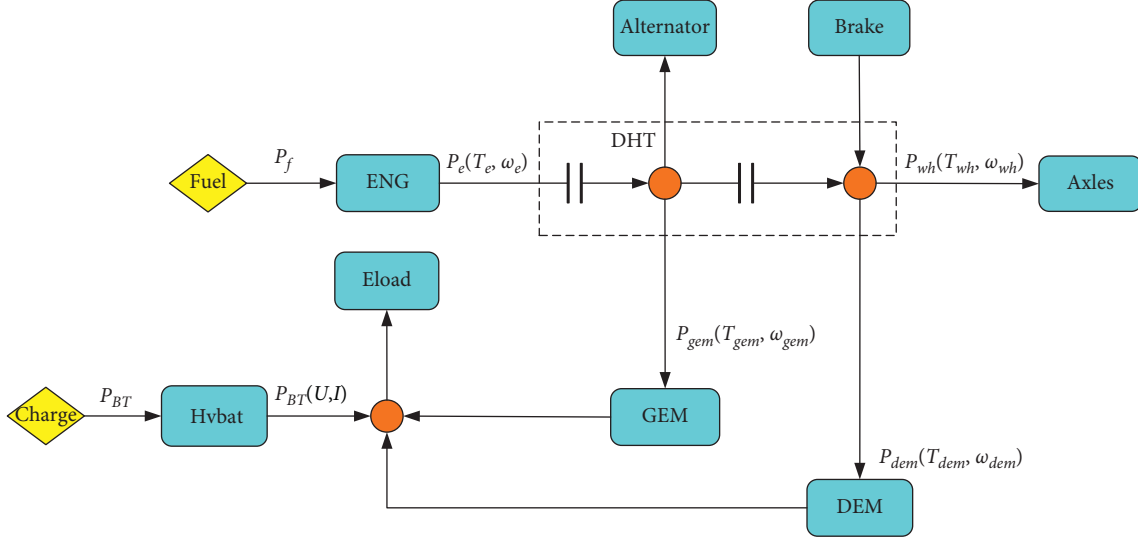


FIGURE 3: Power flows of the hybrid vehicle powertrain. The arrows indicate the direction of the positive power flow.

TABLE 1: Powertrain parameters.

Components	Parameters	Values
ENG	Displacement (L)	1.5
	Peak power (Kw)	103
	Maximum speed (r·min ⁻¹)	5500
	Peak torque (N·m)	220
GEM	Peak power (Kw)	9.5
	Peak torque (N·m)	50
DEM	Peak power (Kw)	17
	Peak torque (N·m)	62
DHT	Engine gears number (—)	6
	Motor gears number (—)	2
Hvbat	Capacity (Ah)	20
	Energy (kWh)	2
	Nominal voltage (V)	46
	Maximum current (A)	400

$T'_{e-\min} \leq T'_{e-\max}$: desired torque $T_{wh}(k)$ can be produced by both motor and engine

3.1. DP Formulation. Dynamic programming (DP) is a multistep decision process, which uses Bellman's optimal principle for making hierarchical decisions and solving optimal controls [19].

For an optimal decision, regardless of the initial state and initial decision (*stage cost*) $d(x_k, x_{k-1,i})$, the remaining decisions (*cost-to-go*) $J_{k-1}(x_{k-1,i})$ must be optimal for the first decision. That is, the second section of the optimal trajectory is also the optimal trajectory.

The following is the equation of the multistep decision process:

$$J_k(x_k) = \min_{u_{k,i}} [d(x_k, x_{k-1,i}) + J_{k-1}(x_{k-1,i})], \quad (17)$$

where $J_k(x_k)$ is the optimal value function of k -stage decision process starting state x_k to the end state x_f and $u_{k,i}$ is the control strategy at starting state x_k of k -stage decision

process so that the state is transferred to next state. In this paper, reverse solution is used.

Figure 4 shows the optimal path of WLTC using DP reverse solution (Figure 4(a)) and the cumulative fuel consumption of the corresponding optimal path (Figure 4(b)).

3.2. ECMS Formulation. After dividing by $\eta_e q_{LHV}$, this results in the following objective function:

$$J = \frac{1}{\eta_e q_{LHV}} \sum_{k=0}^{N-1} P_e(T_e(k), \omega_e(k)) \Delta t. \quad (18)$$

Introducing the Lagrangian parameter $\lambda(k)$, the Hamiltonian function can be written as

$$H = \frac{1}{\eta_e q_{LHV}} P_e(T_e(k), \omega_e(k)) + \lambda(k) \eta_{BT} T_m(k) \omega_{dem}(k). \quad (19)$$

In order to avoid exceeding the boundary value of the constraint condition, introducing an additional cost function, then, (19) can be rewritten as

$$H = \frac{1}{\eta_e q_{LHV}} P_e(T_e(k), \omega_e(k)) + (\lambda(k) + \gamma(k)) \eta_{BT} T_m(k) \omega_{dem}(k), \quad (20)$$

where

$$\gamma(k) = \begin{cases} 0 & \text{if constraints are not active,} \\ -K & \text{if upper constraints are active,} \\ K & \text{if lower constraints are active.} \end{cases} \quad (21)$$

In order to make the SoC meet the constraint condition (12), a penalty function is introduced:

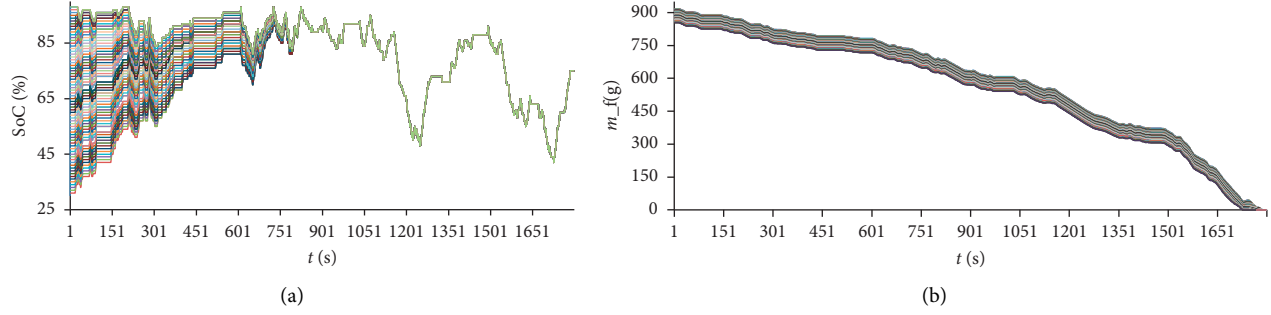


FIGURE 4: The optimal results of WLTC using DP.

$$p(x(k)) = 1 - \left(\frac{x(k) - x_{xf}(k)}{(x_{\max} - x_{\min})/2} \right)^a. \quad (22)$$

Then, the Hamiltonian function can be rewritten as

$$H = \frac{1}{\eta_e q_{\text{LHV}}} P_e(T_e(k), \omega_e(k)) + (\lambda(k) + \gamma(k)) \eta_{\text{BT}} T_m(k) \omega_{\text{dem}}(k) p(x(k)), \quad (23)$$

where

$$s(k) = \lambda(k) + \gamma(k). \quad (24)$$

$s(k)$ is the equivalent factor.

According to Pontryagin's minimum principle, the optimal controls are obtained by solving the minimum value of Hamiltonian function, shown as follows:

$$T_m^* = \arg \min H(s(k), x(k), T_m(k), \omega_{\text{dem}}(k)). \quad (25)$$

3.2.1. ECMS Algorithm. The following steps must be executed to implement ECMS, as also illustrated in Figure 5:

- (1) Identify the acceptable range of control $[T_{\text{gem}, \min}(k), T_{\text{gem}, \max}(k)]$ and $[T_{\text{dem}, \min}(k), T_{\text{dem}, \max}(k)]$ which satisfies the instantaneous torque constraints
- (2) Discretize the intervals $[T_{\text{gem}, \min}(k), T_{\text{gem}, \max}(k)]$ and $[T_{\text{dem}, \min}(k), T_{\text{dem}, \max}(k)]$ into a finite number of controls $\{T_{dm,i}\}$ and $\{T_{gm,i}\}$, where $i = 1, 2, \dots, q$ and $j = 1, 2, \dots, p$, a total of $q \times p$ control candidates
- (3) Calculate the equivalent fuel consumption H corresponding to each control candidate
- (4) Select the control values $T_{\text{gem}}(k)$ and $T_{\text{dem}}(k)$ that minimize H

Steps 1 to 4 are computed at each instant of time over the entire duration of the driving cycle. This approach has been shown to closely approximate the global optimal solution.

4. Control Design

In order to reduce the amount of memory use and improve the calculation speed, the offline simulation is used to

calculate the fuel cost in series mode and mode selection for a given combination $(T_w, \omega_w, \text{SoC})$ [7, 19, 25]. Because the efficiency of the battery does not change greatly with the change of SoC in the desired operating region, the SoC is found to have minor effects on the optimal solution, so that effect is ignored.

However, not only are all control variables stored in tables, but also some insights can be gained from the kinematic relations in (1)–(3) to reduce the amount of memory used:

Mode 1 and mode 2: T_m can be directly calculated from T_{req} . Therefore, no tables are required.

Mode 3: we only need to store the optimal line of $\omega_{\text{APU-opt}}(1\text{-D})$ and $T_{e\text{-opt}}(1\text{-D})$ as shown in Figure 6.

The above maps are approximate estimates of the optimal controls of DP, which can be generated with the help of the Model-Based Calibration (MBC) toolbox of MathWorks.

Mode 4 is implemented using ECMS algorithm, and the algorithm flow is shown in Figure 4. There could be instances where an engine torque command produces the minimum cost but differs greatly from the previously selected engine torque. This can occur when higher engine torque and lower engine torque produce minimum costs that are close in value, which causes the Min function to alternate between higher and lower engine torque outputs. Therefore, the difference between the current engine power vector $(P_e^*(k))$ and the previously selected engine power $(P_e^*(k-1))$ is introduced into the Hamiltonian function and will help limit the rate at which the engine power (and torque) can change from time step to time step, and the Hamiltonian function (23) can be rewritten as

$$H = \frac{1}{\eta_e q_{\text{LHV}}} P_e(T_e(k), \omega_e(k)) + s(k) \eta_{\text{BT}} T_m(k) \omega_{\text{dem}}(k) p(x(k)) + (P_e^*(k) - P_e^*(k-1)). \quad (26)$$

4.1. Controller. The structure of the controller is shown in a block diagram in Figure 7, which consists of three main subsystems. The first subsystem is the operation mode detection, combined with formulas (14)–(16) as the boundary

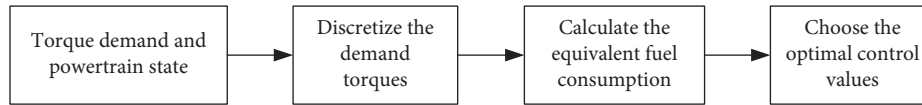


FIGURE 5: ECMS algorithm flow.

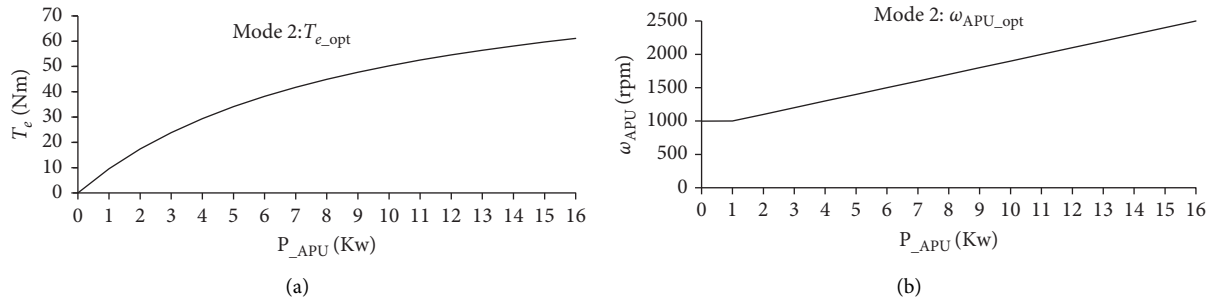


FIGURE 6: The optimal line of APU.

condition of the mode selection; the second subsystem is operation mode management, which mainly realizes the transition of the four modes by the state machine; the third subsystem is torque distribution amnagement, which mainly realizes the torque distribution of pure electric mode (modes 1 and 2), series mode (mode 3), and parallel hybrid mode (mode 4).

5. Energy Management

Charge-depleting charge-sustaining strategy (CDCS) is to make use of all the stored electric energy in the battery. The PHEV is run as an electric vehicle until the SoC is under a certain limit and then operates as a hybrid in the charge-sustaining mode. It is guaranteed to make use of the stored electric energy, and it does not need information about the future driving mission, which is the main advantage of this strategy. Global optimal strategy based on DP is to mix usage of fuel and electricity throughout the driving cycle. Comparing the optimization-based strategies with the CDCS-based strategies, the optimization-based strategies may result in a lower fuel consumption than the CDCS-based strategies [24]. However, in order to use all the energy in the battery for the global optimal strategy, the distance of the driving cycle must be known.

In order to make full use of the electric energy in the battery, in this paper a mix between global optimal strategy and CDCS strategies is implemented, and in order to reduce the application of maps and avoid manual adjustment of parameters, parallel HEV is implemented based on ECMS algorithm.

5.1. Charge-Discharge Reaction. In order to extend the life cycle of the battery, the charge and discharge reaction (CDR) of the battery is taken into account in the energy management strategy.

The CDR of the battery is divided into 5 states: discharging, effective (Eff) discharging, normal, effective (Eff) charging, and critical (Crit) charging, as shown in Figure 8. When the SoC is close to the maximum boundary value, the CDR is in discharging state. With the SoC gradual decrease, the CDR will be in the effective discharging state and the normal state and then in the effective charging state, and when the SoC is close to its minimum boundary value, the CDR will be in the critical charging state to avoid the voltage of the battery and the discharge depth of the battery into the nonlinear region [22, 23].

In Figure 9, with SoC as the feedback variable, a feedback energy management system (FEMS) is established to maintain the SoC within an allowable interval, as shown in Figure 10(d). When the SoC decreases, the CDR also decreases accordingly; then, the FEMS will select charging maps, shown in Figure 11; when the SoC increases, the CDR also increases; then, the system will select the discharging maps. Each map is approximate estimates of the corresponding optimal trajectory of DP, which can be generated with the help of the Model-Based Calibration (MBC) toolbox of MathWorks.

5.2. Reference SoC. In order to make full use of all the energy stored in the battery, a blended strategy that the instantaneous optimal strategy based on ECMS is combined with CDCS strategy is implemented. In order to avoid SoC not reaching the final value of the reference SoC, when the end is reached, the strategy is to underestimate the approximate distance by 15% and use it as the horizon for the blended strategy and then switch to CS mode. This is achieved by setting a reference SoC [25], x_{rf} , which is linear in the ratio of traveled distance versus expected distance according to equation (27). Minimum x_{rf} is set to 0.3 in order to ensure that the final SoC is 0.3. The shape of x_{rf} is shown in Figure 12.

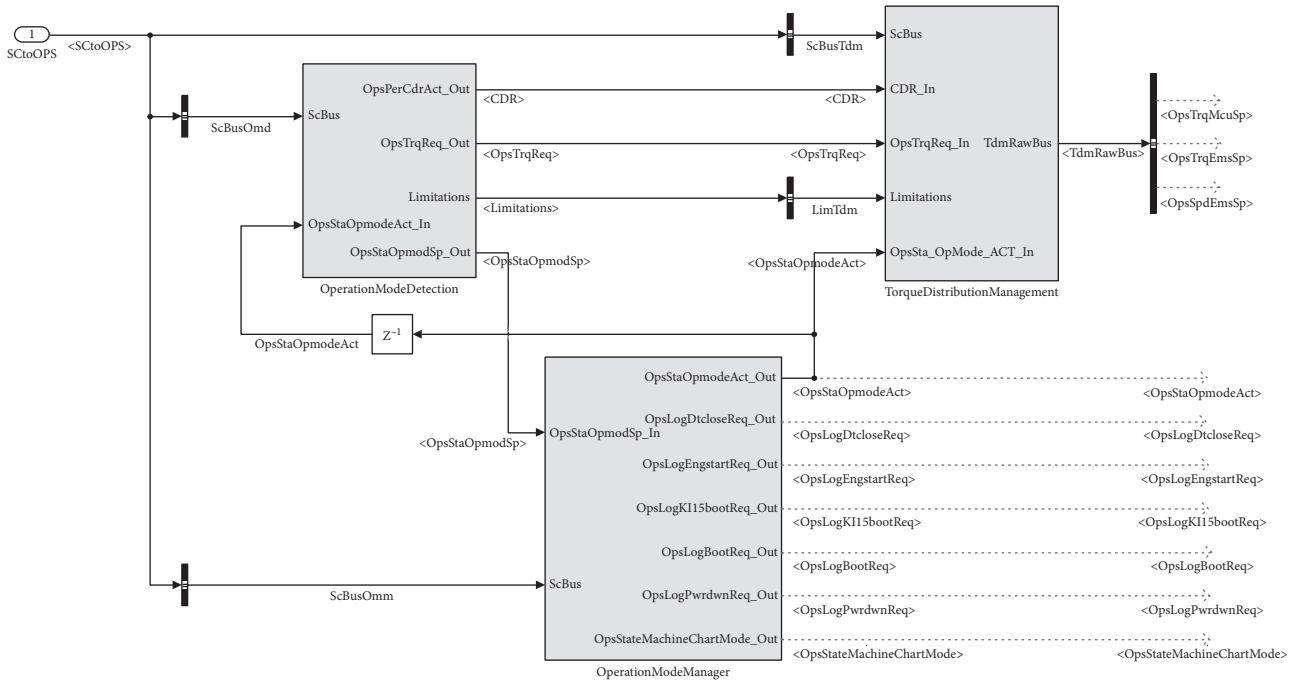


FIGURE 7: The structure of the controller.

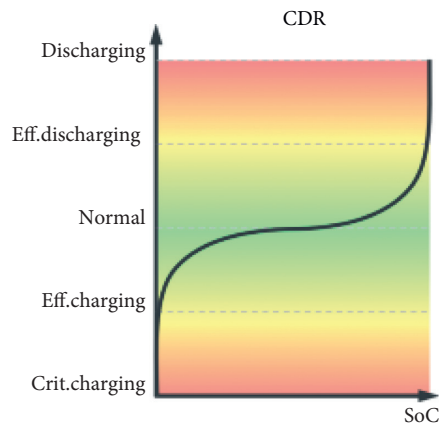


FIGURE 8: Charge and discharge reaction.

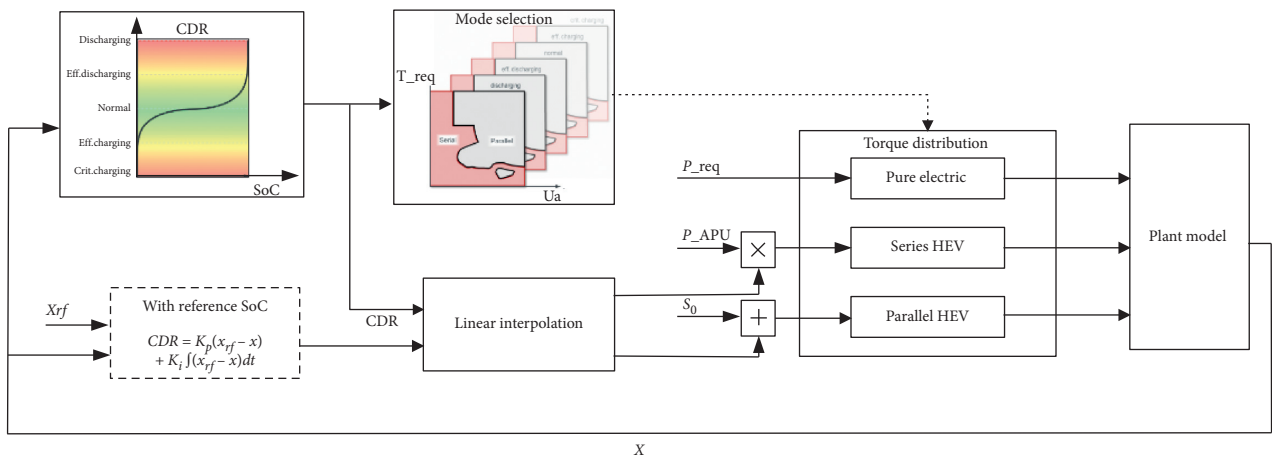


FIGURE 9: Feedback energy management system.

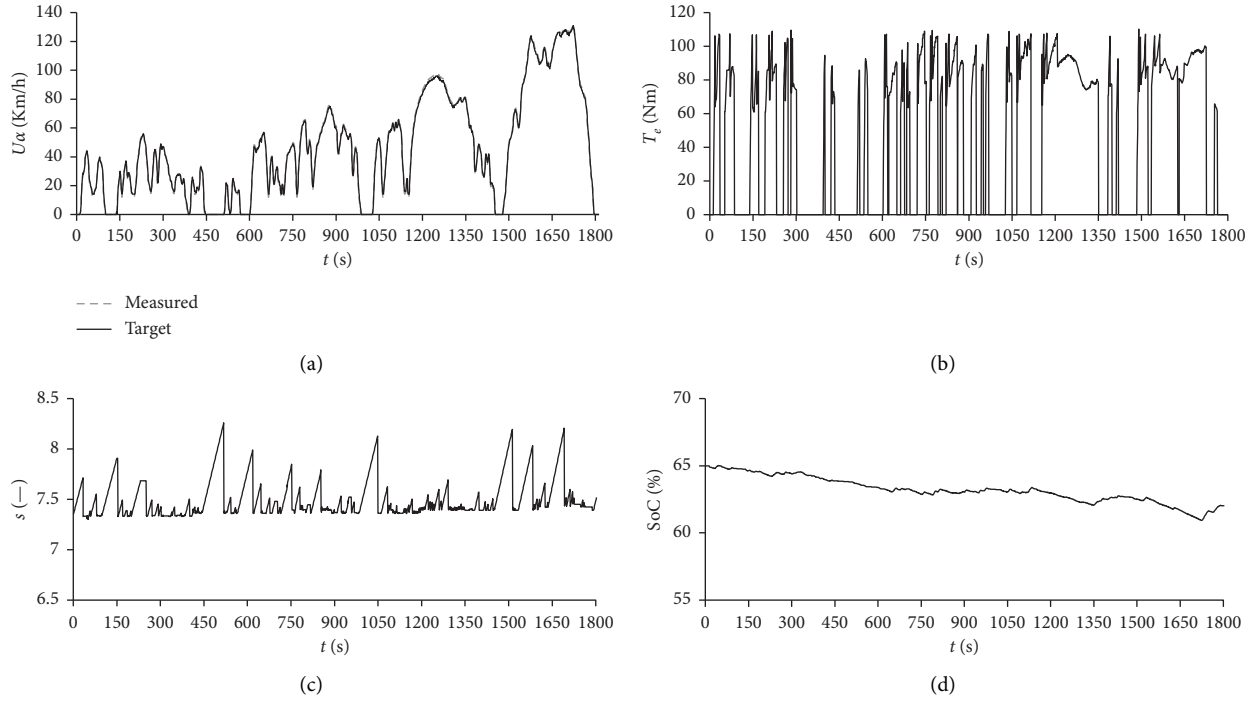


FIGURE 10: The simulation results of WLTC without reference SoC.

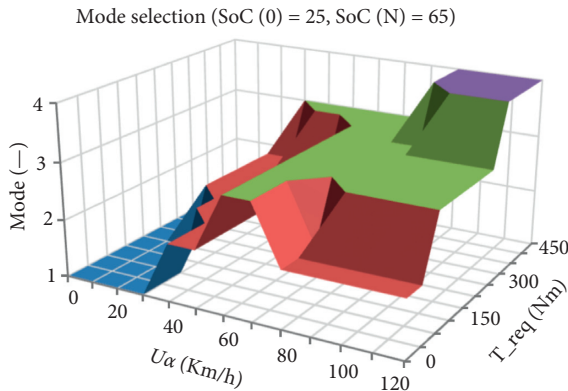


FIGURE 11: The mode selection for effective charging.

$$\begin{cases} D_t = \frac{D_{\text{real}}}{0.85D_{\text{cycle}}}, \\ x_{\text{rf}} = (x_f - x(0))D_t + x(0), \\ x_{\text{min}} \leq x_{\text{rf}} \leq x_{\text{max}}, \end{cases} \quad (27)$$

where x_f is the minimum reference SoC.

In order to improve the robustness of the system, the PI controller is designed according to the following formula:

$$\text{CDR} = K_p(x_{\text{rf}} - x) + K_i \int (x_{\text{rf}} - x) dt. \quad (28)$$

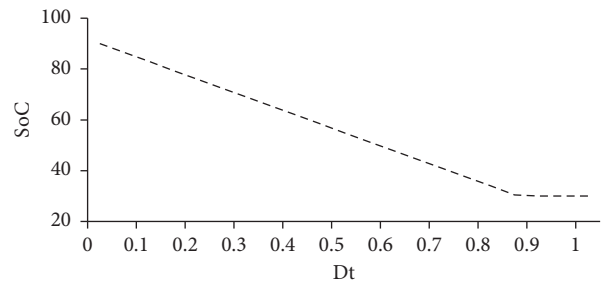


FIGURE 12: The outline of the reference SoC shape.

5.3. Adaptive Optimal Supervisory Control. The adaptive optimal supervisory control is designed based on SoC feedback, which is to dynamically change $s(k)$ (without using past driving information or trying to predict future driving behavior) to compare SoC changes and maintain its value near the reference value [26–28].

An adaptation law based on the PI controller of the type:

$$s = s_0 + K_p(x_{\text{rf}} - x) + K_i \int (x_{\text{rf}} - x) dt. \quad (29)$$

In (29), s_0 represents the initial value of s at time $t=0$, and K_p and K_i are the proportional and integral gains of the adaptation law. The initialization of this algorithm, i.e., the choice of s_0 , is arbitrary, and it can be done by averaging different optimal initial values obtained offline [28, 29].

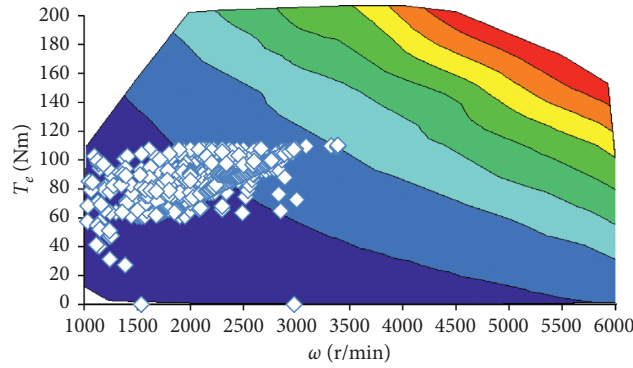


FIGURE 13: Engine operating points' distribution of WLTC.

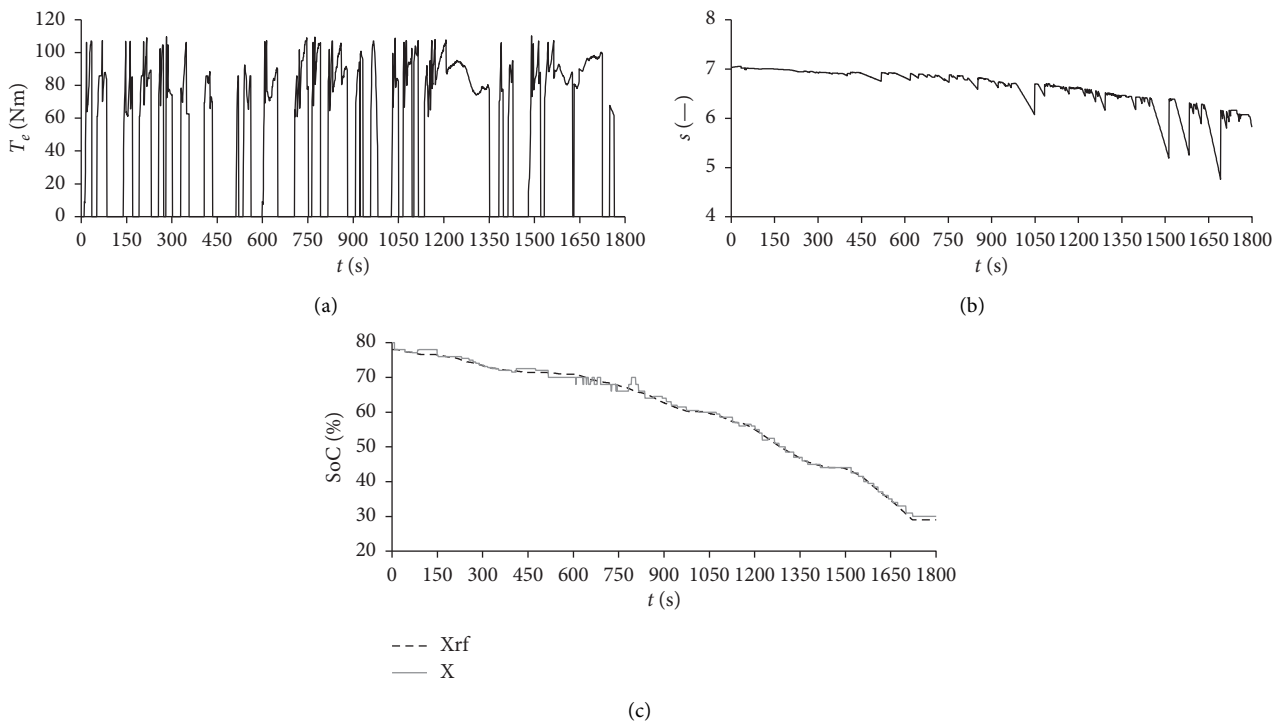


FIGURE 14: The simulation results of WLTC with reference SoC.

6. Simulation Result in MATLAB-Simulink

The controller is evaluated in a closed loop together with PM, and the simulation results are compared with the global optimal results of DP offline simulation.

The offline simulation results of using DP reverse to solve WLTC are presented in Figure 4. Figure 4(a) shows the optimal paths with different SoC initial values, and the cumulative fuel consumption of the corresponding optimal path is shown in Figure 4(b), and the SoC constraints are

$$\begin{aligned} 25\% \leq x \leq 100\%, \\ x(N) = 75\%. \end{aligned} \tag{30}$$

In Figure 4, the optimal paths with different SoC initial values converge to one path at 900 s, and the fluctuation range of SoC is in a larger interval [30, 95]; the average fuel

consumption of all optimal paths after the WLTC is 820 g, corresponding to the one-hundred-kilometer fuel consumption which is 4.69 L.

Figure 13 shows that the engine operating points are concentrated in the low fuel consumption area of the engine and the speed is in the interval [1000 r/min, 3500 r/min]. It can also be seen from Figures 10(b) and 14(a) that the engine torque is mostly concentrated around 80 Nm, and the number of engine starts with the reference SoC (27 times) is lower than the number of engine starts without the reference SoC (31 times). Figure 10(c) is the trajectory of the equivalent factor, and the overall trend of the equivalent factor is stable with the peak upward. The larger the peak value, the greater the desire for engine power. Conversely, as shown in Figure 14(b), the equivalent fuel factor decreases with the decrease of the reference SoC, the peak is down, and the smaller the peak value, the greater the desire for motor

TABLE 2: Driving cycles' simulation results.

Cycle info		WLTC	CUDC	NEDC
Without reference SoC	m_f	4.81	3.53	4.71
	$x(N)$	63	61	59
	n_{on}	31	7	16
With reference SoC	m_f	4.21	3.23	4.23
	$x(N)$	31	29	31
	n_{on}	27	6	13
Δm_f		0.61	0.2	0.48
D_{cycle}		23.16	5.9	10.95

power. The resulting SoC trajectories for the tested cycle are shown in Figures 10(d) and 14(c). In Figure 10(d), the SoC fluctuation range of the tested cycle is narrower than the DP offline simulation result in Figure 4(a), which is located in the interval [61, 65]. Compared with Figure 14(c), SoC can better follow the reference SoC, and the range of SoC variation is relatively large, indicating that the energy stored in the battery can be fully utilized. As shown in Figure 10(a), the measured vehicle speed can follow the target vehicle speed very well.

In order to verify the adaptability of the controller to different tested cycles, in addition to the WLTC tested cycle, two tested cycles, China Urban Driving Cycle (CUDC) and NEDC, are also selected for simulation comparison. The results for the 3 tested cycles are shown in Table 2.

In fact, in WLTC testing, the final SoC may not reach exactly the target value (75%) of DP; therefore, in order to fairly compare fuel consumption results, a linear correlation between final SoC and fuel consumption is visible, which is easily approximated by the linear expression [30].

$$m_f \approx m_{f0} + \sigma \Delta \text{SoC}, \quad (31)$$

where m_f is the actual fuel consumption, m_{f0} is the value that would correspond to a zero SoC variation, and σ is a curve fitting coefficient that translates ΔSoC into a corresponding amount of fuel; here, $\sigma \approx s$.

In Table 2, the fuel consumption of the WLTC without reference SoC is 4.81 L/100 km with the final SoC 63%. After correction, the fuel consumption is 4.83 L/100 km, which is 0.14 higher than the average fuel consumption of DP simulation with the final SoC value 75%. For the 3 test cycles, the fuel consumption without the reference SoC is higher than the fuel consumption with the reference SoC; the final value of the SoC without the reference SoC is close to the target value of 75%; the final value of the SoC with the reference SoC is close to 30%.

7. Conclusion

This study proposes a real-time control of PHEV based on DP and ECMS. In order to fully exploit the potential of the battery, combined with the CDR and CDCS, the FEMS was established, and the controller was evaluated by closed-loop simulation. The conclusion is as follows:

- (1) This study proposes a real-time control of PHEV based on DP-ECMS, which is a suboptimal solution,

and the results show that the real-time controller has good control ability and better robustness, and the fuel consumption value of the real-time controller is close to the offline simulation results of DP.

- (2) The engine operating points are concentrated in the low fuel consumption area of the engine, and the engine starts and stops are evenly distributed. They effectively avoid alternating output between higher and lower engine torques.
- (3) When the future driving distance is unknown, the controller can make the SoC within a admissible interval, but the SoC change range is relatively small, and the system cannot make full use of the energy stored in the battery. When the future driving distance is known, the system can make the SoC better follow the reference SoC, which can make full use of the energy stored in the battery; therefore, fuel economy is effectively improved.

Nomenclature

q_{LHV} :	Fuel lower heating value (J/Kg)
U_a :	Vehicle speed (Km/h)
T :	Torque (Nm)
i :	Gear ratio (—)
η :	Efficiency (—)
ρ :	Air density (kg/m ³)
g :	Gravitational acceleration (m/s ²)
Δt :	Sample time (s)
Q :	Battery capacity (As)
P :	Power (W)
ω :	Angular velocity (rad/s)
b_h :	Fuel consumption (Kg/h)
x :	State of charge (—)
\dot{m}_f :	Fuel mass flow (g/s)
m_f :	Fuel consumption (L/100 km)
m_{f-xf} :	Fuel consumption with reference SoC (L/100 km)
D_{real} :	Actual distance traveled (km)
D_{cycle} :	Estimated driving cycle distance (km)
λ :	Lagrangian parameter (—)
s :	Equivalent factor (—)

Subscripts

wh:	Wheel
req:	Requirement
gb:	Gear box
elec:	Electricity
e:	Engine
m:	Motor
gem:	Generator electric motor
dem:	Drive electric motor
red:	Reducer
opt:	Optimal
rf:	Reference
BT:	Battery
APU:	Auxiliary power unit

Acronyms

ENG:	Engine
Eload:	Electronic load

HvBat: High-voltage battery
 DHT: Dedicated hybrid transmission
 SoC: State of charge
 DEM: Drive electric motor
 GEM: Generator electric motor
 Eff: Effective
 Crit: Critical.

Data Availability

The Models.slx data used to support the findings of this study are currently under embargo while the research findings are commercialized. Requests for data 6 months after publication of this article will be considered by the corresponding author.

Conflicts of Interest

The authors declare that they have no conflicts of interest.

References

- [1] S. Ke, X. Wang, F. Li, M. Sorrentino, and B. Zheng, "Pontryagin's minimum principle-based real-time energy management strategy for fuel cell hybrid electric vehicle considering both fuel economy and power source durability," *Energy*, vol. 205, Article ID 118064, 2020.
- [2] R. Schmid, J. Bürger, and N. Bajcinca, "A comparison of PMP-based energy management strategies for plug-in-hybrid electric vehicles," *IFAC-PapersOnLine*, vol. 52, no. 5, pp. 592–597, 2019.
- [3] W. v. Harselaar, N. Schreuders, T. Hofman, and S. Rinderknecht, "Improved implementation of dynamic programming on the example of hybrid electric vehicle control," *IFAC-PapersOnLine*, vol. 52, no. 5, pp. 147–152, 2019.
- [4] A. Pam, A. Bouscayrol, P. Fiani, F. Faval, and P. Barrade, "Integration of the road slope in the optimization of the energy management strategy of a parallel HEV," *IFAC-PapersOnLine*, vol. 52, no. 5, pp. 28–33, 2019.
- [5] Y. Yang, H. Pei, X. Hu, Y. Liu, C. Hou, and D. Cao, "Fuel economy optimization of power split hybrid vehicles: a rapid dynamic programming approach," *Energy*, vol. 166, no. 1, pp. 929–938, 2019.
- [6] Q. Feiyan, *Research on Stochastic Dynamic Programming Based Energy Management Strategy of Hybrid Vehicles*, University of Chinese Academy of Sciences, Beijing, China, 2018.
- [7] B. Bader, O. Torres, and J. A. Ortega, "Predictive real-time energy management strategy for PHEV using lookup-table-based dynamic programmings," in *Proceedings of the 2013 World Electric Vehicle Symposium and Exhibition*, Barcelona, Spain, 2013.
- [8] N. Ding, K. Prasad, and T. T. Lie, "Design of a hybrid energy management system using designed rule-based control strategy and genetic algorithm for the series-parallel plug-in hybrid electric vehicle," *International Journal of Energy Research*, vol. 45, pp. 1627–1645, 2020.
- [9] M. Montazeri-Gh and M. Mahmoodi-k, "Development a new power management strategy for power split hybrid electric vehicles," *Transportation Research Part D: Transport and Environment*, vol. 37, pp. 79–96, 2015.
- [10] J. Hu, X. Niu, X. Jiang, and G. Zu, "Energy management strategy based on driving pattern recognition for a dual-motor battery electric vehicle," *International Journal of Energy Research*, vol. 43, pp. 3346–3364, 2019.
- [11] T. C. J. Romijn, T. H. Pham, and S. Wilkins, "Modular ECMS framework for hybrid vehicles," *IFAC-PapersOnLine*, vol. 52, no. 5, pp. 128–133, 2019.
- [12] S. Antonio and G. Lino, "Control of hybrid electric vehicles," *IEEE Control Systems Magazine*, vol. 4, pp. 60–70, 2007.
- [13] T. Nesch, A. Ceroflini, G. Mancini et al., "Equivalent consumption minimization strategy for the control of real driving nox emissions of a diesel hybrid electric vehicle," *Energies*, vol. 7, no. 5, pp. 3148–3178, 2014.
- [14] J. Han, Y. Park, and D. Kum, "Optimal adaptation of equivalent factor of equivalent consumption minimization strategy for fuel cell hybrid electric vehicles under active state inequality constraints," *Journal of Power Sources*, vol. 267, no. 4, pp. 491–502, 2014.
- [15] C. Sun, F. Sun, and H. He, "Investigating adaptive-ECMS with velocity forecast ability for hybrid electric vehicles," *Applied Energy*, vol. 185, no. 2, pp. 1644–1653, 2017.
- [16] J. Park and J. H. Park, "Development of equivalent fuel consumption minimization strategy for hybrid electric vehicles," *International Journal of Automotive Technology*, vol. 13, pp. 835–843, 2012.
- [17] Z. Chen, W. Liu, Y. Yang, and W. Chen, "Online energy management of plug-in hybrid electric vehicles for prolongation of all-electric range based on dynamic programming," *Mathematical Problems in Engineering*, vol. 2015, Article ID 368769, 11 pages, 2015.
- [18] C. Zheng, C. C. Mi, J. Xu, X. Gong, and C. You, "Energy management for a power-split plug-in hybrid electric vehicle based on dynamic programming and neural networks," *IEEE Transactions on Vehicular Technology*, vol. 63, no. 4, pp. 1567–1580, 2013.
- [19] J. A. Chekan and S. Bashash, "Dynamic programming-based approximate real-time control policies for plug in hybrid electric vehicles," in *Proceedings of the 2017 IEEE Conference on Control Technology and Applications (CCTA)*, IEEE, Mauna Lani, HI, USA, 2017.
- [20] S. Onori, L. Serrao, and G. Rizzoni, "Adaptive equivalent consumption minimization strategy for hybrid electric vehicles," in *Proceedings of ASME 2010 Dynamic Systems and Control Conference*, pp. 499–505, Cambridge, MA, USA, 2010.
- [21] D. Zhu, E. G. D. Pritchard, and L. M. Silverberg, "A new system development framework driven by a model-based testing approach bridged by information flow," *IEEE Systems Journal*, vol. 12, no. 3, pp. 2917–2924, 2016.
- [22] H. Hongwen, S. Fengchun, Z. Chenguang et al., "An experimental study on the charging and discharging characteristics of Li-ion traction battery," *Journal of Beijing Institute of Technology*, vol. 22, no. 5, pp. 578–581, 2002.
- [23] G. Suri and S. Onori, "A control-oriented cycle-life model for hybrid electric vehicle lithium-ion batteries," *Energy*, vol. 96, pp. 644–653, 2016.
- [24] V. Larsson, L. Johannesson, and B. Egardt, "Impact of trip length uncertainty on optimal discharging strategies for phev," in *Proceedings of the IFAC Symposium on Advances in Automotive Control*, Munich, Germany, 2010.
- [25] M. Sivertsson and L. Eriksson, "Design and evaluation of energy management using map-based ECMS for the PHEV benchmark," *Oil & Gas Science and Technology*, vol. 70, no. 1, pp. 195–211, 2015.

- [26] A. García, P. Carlucci, J. Monsalve-Serrano, A. Valletta, and S. Martínez-Boggio, “Energy management strategies comparison for a parallel full hybrid electric vehicle using reactivity controlled compression ignition combustion,” *Applied Energy*, vol. 272, Article ID 115191, 2020.
- [27] C. Yang, S. Du, L. Li, S. You, Y. Yang, and Y. Zhao, “Adaptive real-time optimal energy management strategy based on equivalent factors optimization for plug-in hybrid electric vehicle,” *Applied Energy*, vol. 203, pp. 883–896, 2017.
- [28] C. Musardo, G. Rizzoni, Y. Guezennec, and B. Staccia, “A-ECMS: an adaptive algorithm for hybrid electric vehicle energy management,” *European Journal of Control*, vol. 11, no. 4-5, pp. 509–524, 2005.
- [29] J. T. B. A. Kessels, M. W. T. Koot, P. P. J. van den Bosch, and D. B. Kok, “Online energy management for hybrid electric vehicles,” *IEEE Transactions on Vehicular Technology*, vol. 57, no. 6, pp. 3428–3440, 2008.
- [30] G. Paganelli, M. Tateno, A. Brahma, G. Rizzoni, and Y. Guezennec, “Control development for a hybrid-electric sport-utility vehicle: strategy, implementation and field test results,” in *Proceedings of the 2002 American Control Conference*, Anchorage, AK, USA, 2002.